Instability of Immunoglobulin G (IgG) Monoclonal Antibodies Induced by Redox-Active Metal Ions and Photo-Irradiation

By

Shuxia Zhou

Submitted to the Department of Pharmaceutical Chemistry and the Faculty of the Graduate School of the University of Kansas in partial fulfillment of the requirements for the degree of Doctor of Philosophy.

Dissertation Committee Members

_____
Chairman: Dr. Christian Schöneich

_____
Dr. John Stobaugh

_____
Dr. David Volkin

_____
Dr. Teruna Siahaan

_____
Dr. Heather Desaire

Date defended: Aug 13, 2012

The Dissertation Committee for Shuxia Zhou certifies that this is the approved version of the following dissertation:

Instability of Immunoglobulin G (IgG) Monoclonal Antibodies Induced by Redox-Active Metal Ions and Photo-Irradiation

_____

Chairperson: Dr. Christian Schöneich

Date approved: Aug 31, 2012

ABSTRACT

Since the approval of the first monoclonal antibody (mAb) drug in 1986, mAbs have developed into a major class of therapeutic agents due to their unique properties. Compared to traditional small molecule drug products, the actions of the antibodies are more specific leading to generally fewer off-target related side effects. Also antibodies may be conjugated to another therapeutic entity for efficient delivery of this entity to a target site, thus reducing potential side effects. On the other hand, due to the structural complexity and the dependence of stability of the antibodies on the conformation and structure, antibodies are subject to multiple degradation pathways induced by a variety of factors encountered during antibody production, purification, development, manufacturing, storage, shipping and delivery to the patients. The exposure of antibodies to redox-active metal ions and/or light during processing and use is inevitable, and may result in antibody degradation. Although abundant information on metal-catalyzed oxidation (MCO) and photo-degradation of peptides and small proteins is documented in the literature, very limited research has been performed on IgG oxidative modifications and physical instability. The research covered in this dissertation focused on two major degradation mechanisms for IgG therapeutic mAbs: chemical and physical instability induced by redox-active metal ions and photo-degradation. Redox-active metal ion-induced instability was first examined by a comprehensive study of IgG oxidation induced by MCO. The oxidation of the amino acids, especially Phe and Tyr in IgG1 was first identified, and subsequently a fluorogenic derivatization methodology was developed for their detection. Secondly, a systematic study of the conformational change and intrinsic thermal stability of IgG revealed that metal ions perturbed IgG tertiary structure resulting in decreased intrinsic thermal stability. Lastly, metal chelators were examined to protect the IgG from MCO-induced degradation. This dissertation

also documents the formation of carbon-centered radicals due to homolytic cleavage of disulfide bonds upon photo-irradiation and an UPLC-MS method was developed to simultaneously separate and characterize IgG1 photo-degradants. The ultimate goal of this research is to gain better understanding of IgG degradation mechanism, thereof, providing guidance to develop a therapeutic mAb drug product with desired attributes for unmet medical needs.

ACKNOWLEDGEMENTS

First of all, I would like to thank my research advisor Dr. Christian Schöneich from the bottom of my heart, for his insightful guidance and continuous support throughout the sojourn of my graduate study. I have learned so much from him not only in academic research but also the nature of being a genuine researcher. Among all my learning, the most impressed has been the quality of the research. This gift is the one for which I will forever benefit. Additionally, it has been my privilege to work with and learn from the researchers and graduate students in Dr. Schöneich's research group, Dr. Olivier Mozziconacci, Dr. Yelena Dremina, Dr. Victor Sharov, Dr. Daniel Steinmann, Asha Hewarathna, Maria Feeney, Jessica Haywood and Christopher Asmus. I would like to thank them for the numerous scientific discussions and also the inclusive learning environment. I would like to give my special thanks to Dr. Olivier Mozziconacci for his sacrifice of his weekends/ evening hours to provide me constant support during my last year research at University of Kansas.

I would like to thank my committee members: Dr. David Volkin, Dr. John Stobaugh, Dr. Teruna Siahaan and Dr. Heather Desaire for their time and constructive feedback. Special thanks go to Dr. David Volkin and Dr. Teruna Siahaan for reading through my thesis and their valuable input for improvement.

I would like to thank all the faculty members of Pharmaceutical Chemistry Department, who made my dream of pursuing doctoral degree come true. I would like to give my special thanks to Dr. John Stobaugh and Dr. Christian Schöneich for their efforts and openness. I also would like to thank Nancy Helm for her administrative support during my entire graduate study.

I would like to acknowledge my research advisors at Pfizer Inc., Dr. Satish K. Singh and Dr. Dirk Teagarden and other colleagues for their support and valuable input to my research work. I would like to give my special thanks to Dr. Satish K. Singh not only for his continuous guidance for my research but also as a great mentor for my career and personal development.

I would like to thank Mass Spectrometry/ Applied Proteomics Laboratory at the University of Kansas, in particular Dr. Todd Williams and Dr. Nadzena Galeva for their help with the mass spectrometry analysis of the fluorogenic derivatized IgG1 monoclonal antibody.

I must acknowledge those who have personally nurtured me over years. I dedicate this dissertation to my loving parents, Zunwei Zhou and Guiyue Hao, my husband, Guotao Song and my daughter, Yang Song who have always been there for me regardless. Without their support, understanding, and patience, I would have never been able to achieve this. I must give my special thanks to my lovely daughter, Yang Song for her courage and sacrifices. It was her to encourage me to pursue my dream. I cannot image if I could have done the same as she did, especially at this young age. Thank you, my darling for being so mature and understanding.

Finally, I would like to acknowledge Pfizer Inc. and Amgen Inc. for their financial support.

This doctoral dissertation is dedicated to my loving parents, Zunwei Zhou and Guiyue Hao and my dear husband, Guotao Song and our lovely daughter, Yang Song

Instability of Immunoglobulin G (IgG) Monoclonal Antibodies Induced by Redox-Active Metal Ions and Photo-Irradiation

Table of Contents

List of Acronyms

ABS	4-(aminomethyl)-benzenesulfonic acid
ACN	acetonitrile
CD	circular dichroism
DOE	design of experiments
DOPA	3,4-hydroxyphenylalanine
DPK	diketopiperazine
DSC	dynamic scanning calorimetry
DTPA	diethylenetriaminepentaacetic acid
DTT	dithiothreitol
EDTA	ethylenediaminetetraacetic acid
ESI	electron spray ionization
FDA	Food and Drug Administration
FT-ICR	Fourier transform ion cyclotron resonance
IAM	iodoacetamide
iCE	imaged capillary isoelectric focusing
ICH	International conference of harmonization
ICP-MS	inductively coupled plasma – mass spectrometry
IgG	immunoglobulin
ITC	isothermal titration calorimetry
$K_3Fe(CN)_6$	potassium ferricyanide
LOD	limit of detection

mAb	monoclonal antibody
MCO	metal-catalyzed oxidation
MS	mass spectrometry
m/z	mass to charge ratio
QbD	quality by design
Q-TOF	quadrupole-time-of-flight
RMSE	root mean square error
RPLC	reverse phase liquid chromatography
SDS-PAGE	sodium dodecyl sulfate–polyacrylamide gel electrophoresis
SEC	size exclusion chromatography
SS	stainless steel
TIC	total ion counts
USP	United States Pharmacopeia
UV	ultra-violet
WHO	World Health Organization

Part I: Introduction to IgG instability induced by redox-active metal ions and photo-irradiation

Part I: Introduction

Table of Contents

1.1 Introduction

Since the approval of the first monoclonal antibody (mAb) product, OKT-3 in 1986, IgG antibodies represent a rapidly growing biotherapeutic class in the biopharmaceutical industry for the treatment and prevention of diseases by recognizing and eliminating pathogenic and disease antigens [1-3]. Prior to delivery of a therapeutic IgG product to the patients, the antibody undergoes a variety of stresses during each step of antibody production, purification, development, manufacturing, shipping, storage and delivery. These stresses include but are not limited to pH, temperature, leachables, freeze/thaw, shaking, shearing, absorption, ionic strength, reactive oxygen species, impurities from the exicipients and/or light exposure, etc. Each stress may induce IgG physical and chemical instability, resulting in potentially significant negative consequences, such as reduced potency [4], formation of subvisible/visible particles [5], and immunogenicity [6]. Among these stresses, the exposure of IgG to the contamination of redox-active metal ions and/or light is inevitable in developing a biotherapeutic drug product, which is the focus of this dissertation.

Abundant information on the degradation mechanisms of metal-catalyzed oxidation (MCO) of peptides and small proteins, especially the oxidative modifications of His, Cys, Met and Trp can be found in the literature [7-15]. However, few studies have focused on the impact of metal ions on IgG conformation / thermal instability and chemical instability, especially the oxidative modifications of Phe and Tyr.

Light testing is an integral part of stress testing for submission in registration application for new molecular entities and associated drug products by regulatory agencies [16]. The current literature has focused on investigating the degradation mechanisms of photo-instability on model

peptides and/or small proteins [17-20]. Due to the structural complexity of IgG, so far, very limited knowledge on photo-initiated degradation mechanism(s) of IgG can are available.

The limited understanding of IgG degradation mechanism(s) leads to less efficient design of stable antibodies and/or formulations to provide first-class therapeutic IgG products to the patients. The focus of this dissertation is to investigate IgG with respect to i) physical and chemical instability induced by redox-active metal ions and formulation strategies to prevent metal-catalyzed degradation, and ii) photo-degradation mechanism(s) by studying the formation of carbon-centered (C-centered) radicals upon photo-irradiation and developing a methodology allowing simultaneous separation and characterization of IgG photo-degradation products. The ultimate goal is to address these two major concerns encountered in developing IgG therapeutic agents. Prior to introducing any detailed aspects of these two projects, it is necessary to review IgG structure, therapeutic significance, instability and development challenges in general.

1.1.1. Overview of IgG

1.1.1.1 Structure

IgG antibody is a protein, composed of primary sequence and higher order secondary, tertiary and quaternary structure. Primary sequence is defined as the amino acid sequence composed of 20 amino acids. Different regions of the primary sequence form local regular secondary structure consisting of α helices, β strands and/or random coils. The tertiary structure is formed by packing the secondary structure into one or several compact globular domains. The final protein may contain several polypeptide chains arranged in quaternary structure. Protein stability and its functions depend not only on its primary sequence but also on its high order structures.

Antibodies belong to a family of globular proteins called immunoglobulins. Immunoglobulins comprise antibody molecules and molecules having patterns of molecular structure (antigenic determinants) in common with antibodies. They are roughly Y-shaped molecules or combination of such molecules, consisting of variable region (Fv) defining antigen-binding properties and constant region (Fc) interacting with effector cells and molecules. Based on the differences in the Fc region, immunoglobulins are divided into five classes of IgA, IgD, IgE, IgM and IgG. IgGs (~150 kDa) contain two identical heavy chains (~50 kDa) and two identical light chains (~25 kDa). IgGs are further divided into four subclasses of IgG1, IgG2, IgG3 and IgG4 based on the number and location of the inter-chain disulfide bonds and the length of the hinge region.

The IgG light chain consists of two domains and the heavy chain contains four domains, respectively. Each domain is of about 110 amino acids (~12 kDa in size) [21]. All these domains display similar folded structures of β barrels, which comprise the immunoglobulin fold. Each domain is stabilized by a disulfide bond and hydrophobic interactions. These individual domains interact with one another and fold into three equal-sized spherical shapes linked by a flexible hinge region. The stability of the antibody is a result of balance between destabilizing and stabilizing forces. The destabilizing forces are mainly due to the large increase in entropy of unfolding, and the stabilizing forces are provided by covalent/non-covalent interactions. The presence of a significant number of disulfide bonds and intimate domain-domain interactions in antibodies make them relatively more stable and resistant to moderate thermal stress compared to other proteins. Unlike small-molecule drugs, the large size, compositional variety, and amphipathic characteristics of the IgG constitute specific behavior such as folding, conformational stability and unfolding/denaturation.

1.1.1.2 Therapeutic significance

Since the first IgG product, OKT-3 came on the US market in 1986, approximately 30 antibodies have been approved by Food and Drug Administration (FDA) to become commercially available therapeutic products in the US alone by 2011. Antibodies have gained popularity for commercial development as therapeutic agents because i) compared to small molecule drugs, mAbs are highly specific, thereby reducing side effects or having fewer; ii) antibodies may be conjugated to other therapeutic entities for efficient delivery of these entities to the target sites, thus reducing potential side effects [22]; iii) antibodies may be conjugated to radioisotopes for specific diagnostic purposes; and iv) technology advancement has made fully human mAbs available, which are less immunogenic. On the other side, mAbs exhibit significantly lower stability due to the strong dependence of their physical-chemical properties on the structure and conformation. Like other proteins, antibodies are prone to a variety of physical and chemical degradation pathways. Their instability can be observed in liquid, frozen and lyophilized states. In many cases, multiple degradation pathways can occur at the same time and the degradation mechanisms may change depending on the stress conditions [23].

1.1.1.3 Chemical and physical instability

Even though multiple degradation pathways are present, in general, the degradation pathways are divided into two major categories: chemical and physical instability. Chemical instability is defined as any process that involves covalent bond formation and/or breakage, yielding new chemical entity whereas physical instability does not involve any covalent modification. However, chemical degradation can also lead to physical instability. Both chemical and physical instability can be induced by a variety of factors, such as pH, reactive oxygen species, temperature, shaking, ionic strength, vortexing, and surface/interface adsorption, etc.

Chemical instabilities reported for proteins of therapeutic interest are deamidation, Asp-isoAsp interconversion, racemization, proteolysis, β-elimination, oxidation, disulfide exchange, formation of diketopiperazine (DPK) ring, condensation reaction, formation of pyroGlu (pGlu) and hydrolysis [24]. Any protein containing His, Met, Cys, Trp, Tyr and Phe amino acids can be potentially damaged by reactive oxygen species (ROS) [13, 25-26].

Physical instability refers to the changes in the antibody high order structure of secondary, tertiary and/or quaternary due to the polymeric nature and ability of antibody in adapting to different forms without alteration in its chemical compositions. This includes denaturation, aggregation, precipitation, and surface absorption. Denaturation denotes the loss of the globular or three-dimensional structure that most proteins adopt, that is, a disruption of the tertiary and secondary structure. Once unfolded, the polypeptide chains can undergo further inactivation by association with surfaces (absorption), aggregation with other protein molecules, or some chemical reactions. The process by which aggregation leads to macroscopic ensembles is termed “precipitation”. Aggregation may result from chemical degradations or modifications and subsequently exposure of the hydrophobic surface(s). Physical and chemical aggregation may occur simultaneously. The most common physical instability is protein aggregation.

1.1.1.4 Challenges in developing IgG therapeutics

One of the most challenging tasks in the development of protein pharmaceuticals is to deal with physical and chemical instability. During biotherapeutic product development, manufacturing, shipping, storage and delivery process, the biotherapeutic products inevitably experience various stresses, resulting in degradation. Aggregation and oxidation represent two prominent degradation pathways [7, 12-13, 15, 27-30].

Aggregation has received much attention from industry, academia, as well as regulatory agencies for a number of reasons. First, aggregates may have reduced activity and more importantly, have the potential to induce immunogenicity [31-32]. Immunoglobulin aggregates have been reported to cause serious renal failure [33] and anaphylactoid reactions, such as headache, fever, and chills [34]. Second, the presence of aggregates may reduce the potency of the products, since their biological activity may be compromised due to conformational change. Lastly, aggregates, especially insoluble aggregates, can form subvisible and visible particles to make a solution turbid or physically precipitate from the solution, thus reducing its pharmaceutical elegance and resulting in a loss of quality of the product.

Oxidation is another major concern. Oxidative modifications of the amino acid residues may have significant impact on protein functions. A loss of binding and biological activity was observed for IgG monoclonal antibodies due to light oxidative modifications [35-36]. Oxidation can further induce formation of aggregates [35, 37]. Oxidation of proteins can be classified into two general categories: i) site specific reactions, i.e. metal-catalyzed oxidation; and ii) non-site specific reactions, i.e. photo-oxidation and free radical cascades. Metal-catalyzed oxidation can induce both physical and chemical instability [11, 13].

1.2. Overview of this dissertation

Instability of IgG induced by redox-active metal ions and photo-exposure is commonly encountered during the production and use of biotherapeutic products. Understanding the underlying degradation mechanisms would provide valuable insights to stabilize protein pharmaceuticals and/or to design more stable proteins. In light of the above discussion, specifics of this study will now be addressed. In this dissertation, seven themes are discernible throughout the research presented in Chapters 1 through 8 to help address these two major concerns. The

dissertation covers Part I: chemical and physical instability of IgG by redox-active meta ions by examining i) the origin of metal leachables, ii) chemical modifications and their detection/characterization, iii) physical instability, conformational change and aggregation, iv) thermal instability and v) formulation strategy to protect IgG from degradation; and Part II: photo-instability by studying vi) formation of carbon-centered radicals in IgG and vii) developing a methodology to allow simultaneous separation and characterization IgG photo-degradants. The first five themes in Part I are designed to address the IgG instability concerns induced by redox-active metal ions and the last two to gain understanding in IgG photo-instability. Finally, Chapter 9 offers general conclusions as well as a critical assessment of the research presented, and suggestions for future research directions.

1.2.1. Instability of an IgG1 mAb induced by redox-active metal ions

1.2.1.1. Origin of metal ions

Metal ions can be inadvertently introduced into biotherapeutic products from different resources, such as excipients, and/or leachables from the contact materials. The level of metal ions present in parenteral grade excipients is generally at part per billion (ppb) or below. In this dissertation, metal leachables from the stainless steel are the major focus. Chapter 1 and 2 evaluate the capacity of the biologic formulation factors in leaching metal ions from stainless steel by first studying the impact of the commonly used individual formulation factors and then the combination of the formulation factors by the approach of design of experiments (DOE).

1.2.1.2. Chemical and physical instability of an IgG1 induced by metal ions

Metal ion induced chemical and physical instability of an IgG1 is the main focus through Chapters 3-5. Chapter 3 addresses the chemical instability, more specifically the oxidative modifications induced by MCO and their detection/characterization. Chapter 4 focuses on the

physical instability, mainly the conformation instability and the resulting aggregation whereas Chapter 5 targets another aspect of physical instability, that is, thermal instability. Chapter 6 examines the practical aspects of formulation in evaluating the metal chelators to prevent metal-catalyzed degradation which would be directly applicable to biotherapeutic product development.

Chapters 3-6 are designed in a way to systematically address an IgG1 physical and chemical instability induced by metal ions encountered in developing biotherapeutic products and formulation strategies.

1.2.2. Photo-instability

Photo-irradiation induced instability is the second subject of this dissertation. Photo-instability is first examined by investigating the formation of carbon-centered radicals in IgG1 and IgG2 exposed to ultra-violet (UV) irradiation (chapter 7) and then chapter 8 focuses on developing a method capable of simultaneous detection and characterization of IgG1 photo-degradants.

1.3. Remarks

IgG mAbs represent an important class of biotherapeutic agents. Since the exposure of IgG to redox-active metal ions and/or photo-irradiation is inevitable, understanding of degradation mechanisms of IgG mAb induced by the two stresses would have significant impact in developing first-class biotherapeutic products to cure the patients in need.

1.4. References

1. Brekke, O.H., et al., *Therapeutic antibodies for human diseases at the dawn of the twenty-first century*. Nat Rev Drug Discov, 2003. **2**(1): p. 52-62.

2. Bebbington, C., et al., *Antibodies for the treatment of bacterial infections: current experience and future prospects.* Curr Opin Biotechnol, 2008. **19**(6): p. 613-9.

3. Schrama, D., et al., *Antibody targeted drugs as cancer therapeutics.* Nat Rev Drug Discov, 2006. **5**(2): p. 147-59.

4. Rehder, D.S., et al., *Isomerization of a single aspartyl residue of anti-epidermal growth factor receptor immunoglobulin gamma2 antibody highlights the role avidity plays in antibody activity.* Biochemistry, 2008. **47**(8): p. 2518-30.

5. Singh, S.K., et al., *An industry perspective on the monitoring of subvisible particles as a quality attribute for protein therapeutics.* J Pharm Sci, 2010. **99**(8): p. 3302-21.

6. Rosenberg, A.S., *Effects of protein aggregates: an immunologic perspective.* AAPS J, 2006. **8**(3): p. E501-7.

7. Li, S., et al., *Aggregation and precipitation of human relaxin induced by metal-catalyzed oxidation.* Biochemistry, 1995. **34**(17): p. 5762-72.

8. Luo, Q., et al., *Chemical modifications in therapeutic protein aggregates generated under different stress conditions.* J Biol Chem, 2011. **286**(28): p. 25134-44.

9. Schöneich, C., *Selective Cu2+/ascorbate-dependent oxidation of alzheimer's disease beta-amyloid peptides.* Ann N Y Acad Sci, 2004. **1012**: p. 164-70.

10. Schöneich, C., et al., *Cu(II)-catalyzed oxidation of beta-amyloid peptide targets His13 and His14 over His6: Detection of 2-Oxo-histidine by HPLC-MS/MS.* Chem Res Toxicol, 2002. **15**(5): p. 717-22.

11. Schöneich, C., et al.,*CU(II)-catalyzed oxidation of Alzheimer's disease beta-amyloid peptide and related sequences: remarkably different selectivities of neurotoxic betaAP1-40 and non-toxic betaAP40-1.* Cell Mol Biol (Noisy-le-grand), 2003. **49**(5): p. 753-61.

12. Stadtman, E.R., *Metal ion-catalyzed oxidation of proteins: biochemical mechanism and biological consequences.* Free Radic Biol Med, 1990. **9**(4): p. 315-25.

13. Stadtman, E.R., *Oxidation of free amino acids and amino acid residues in proteins by radiolysis and by metal-catalyzed reactions.* Annu Rev Biochem, 1993. **62**: p. 797-821.

14. Stadtman, E.R., et al., *Metal-catalyzed oxidation of proteins. Physiological consequences.* J Biol Chem, 1991. **266**(4): p. 2005-8.

15. Zhao, F., et al., *Metal-catalyzed oxidation of histidine in human growth hormone. Mechanism, isotope effects, and inhibition by a mild denaturing alcohol.* J Biol Chem, 1997. **272**(14): p. 9019-29.

16. *ICH harmonised tripartite guideline: guideline for the Photostability Testing of New Drug Substances and products.* J Postgrad Med 2001. **47**: p. 264.

17. Creed, D., *Photochemical probes for biological interactions.* Photochem Photobiol, 1974. **19**(6): p. 459-62.

18. Mozziconacci, O., et al., *Photolysis of an intrachain peptide disulfide bond: primary and secondary processes, formation of H2S, and hydrogen transfer reactions.* J Phys Chem B, 2010. **114**(10): p. 3668-88.

19. Mozziconacci, O., et al., *Peptide cysteine thiyl radicals abstract hydrogen atoms from surrounding amino acids: the photolysis of a cystine containing model peptide.* J Phys Chem B, 2008. **112**(30): p. 9250-7.

20. Mozziconacci, O., et al., *Reversible intramolecular hydrogen transfer between protein cysteine thiyl radicals and alpha C-H bonds in insulin: control of selectivity by secondary structure.* J Phys Chem B, 2008. **112**(49): p. 15921-32.

21. Ramsland, P.A., et al., *Crystal structures of human antibodies: a detailed and unfinished tapestry of immunoglobulin gene products.* J Mol Recognit, 2002. **15**(5): p. 248-59.

22. Martsev, S.P., et al., *Fusion of the antiferritin antibody VL domain to barnase results in enhanced solubility and altered pH stability.* Protein Eng Des Sel, 2004. **17**(1): p. 85-93.

23. Paborji, M., et al., *Chemical and physical stability of chimeric L6, a mouse-human monoclonal antibody.* Pharm Res, 1994. **11**(5): p. 764-71.

24. Manning, M.C., et al., *Stability of protein pharmaceuticals.* Pharmaceutical Research, 1989. **6**: p. 903-918.

25. Hovorka, S., et al.,*Oxidative degradation of pharmaceuticals: theory, mechanisms and inhibition.* J Pharm Sci, 2001. **90**(3): p. 253-69.

26. Torosantucci, R., et al., *Chemical Modifications in Aggregates of Recombinant Human Insulin Induced by Metal-Catalyzed Oxidation: Covalent Cross-Linking via Michael Addition to Tyrosine Oxidation Products.* Pharm Res, 2012.

27. Bee, J.S., et al., *Precipitation of a monoclonal antibody by soluble tungsten.* J Pharm Sci, 2009. **98**(9): p. 3290-301.

28. Li, S., et al., *Chemical pathways of peptide degradation. V. Ascorbic acid promotes rather than inhibits the oxidation of methionine to methionine sulfoxide in small model peptides.* Pharm Res, 1993. **10**(11): p. 1572-9.

29. Uversky, V.N., et al., *Metal-triggered structural transformations, aggregation, and fibrillation of human alpha-synuclein. A possible molecular NK between Parkinson's disease and heavy metal exposure.* J Biol Chem, 2001. **276**(47): p. 44284-96.

30. Zhou, S., et al., *Comparative evaluation of disodium edetate and diethylenetriaminepentaacetic acid as iron chelators to prevent metal-catalyzed destabilization of a therapeutic monoclonal antibody.* J Pharm Sci, 2010. **99**(10): p. 4239-50.

31. Braun, A., et al., *Protein aggregates seem to play a key role among the parameters influencing the antigenicity of interferon alpha (IFN-alpha) in normal and transgenic mice.* Pharm Res, 1997. **14**(10): p. 1472-8.

32. Hermeling, S., et al., *Structure-immunogenicity relationships of therapeutic proteins.* Pharm Res, 2004. **21**(6): p. 897-903.

33. Demeule, B., et al.,*Where disease pathogenesis meets protein formulation: renal deposition of immunoglobulin aggregates.* Eur J Pharm Biopharm, 2006. **62**(2): p. 121-30.

34. Ryan, M..E., et al., *Adverse effects of intravenous immunoglobulin therapy.* Clin Pediatr (Phila), 1996. **35**(1): p. 23-31.

35. Qi, P., et al., *Characterization of the photodegradation of a human IgG1 monoclonal antibody formulated as a high-concentration liquid dosage form.* J Pharm Sci, 2009. **98**(9): p. 3117-30.

36. Wei, Z., et al., *Identification of a single tryptophan residue as critical for binding activity in a humanized monoclonal antibody against respiratory syncytial virus.* Anal Chem, 2007. **79**(7): p. 2797-805.

37. Lorenz, C.M., et al., *The effect of low intensity ultraviolet-C light on monoclonal antibodies.* Biotechnol Prog, 2009. **25**(2): p. 476-82.

Part II: Chemical and Physical Instability of IgG1 Induced by Redox-Active Metal Ions

Chapter 1: Metal Ion leachables Induced by Individual Biologics Formulation Factors

Table of Contents

1.1 Introduction

Metal ions occur widely in association with proteins both in vivo and in vitro via direct covalent binding or electrostatic interactions. Alkali and alkaline earth metals bind proteins primarily through electrostatic interactions while the transition metals, such as Fe(II/III), Co(II), Cu(II), Al(III), and Mn(II), bind covalently to proteins [1] because the protein ligands donate an electron pair to form coordinate covalent bond with transition metals. The most common metal-binding amino acids are cysteine, histidine, aspartate, glutamate, and more rarely, glutamine, serine, methionine, threonine, and tyrosine because they contain electron donor elements, such as sulfur, nitrogen, or oxygen. The coordination numbers vary from one to eight among different metals. The solution pH and ionization state of the amino acid residue play an important role in determining the coordination number. Metal ions mediate in vivo biological functions of about one third of the known proteins via directly binding to either protein catalytic sites or structural sites [1]. Metal ions in proteins serve a variety of functions, including stabilizing protein structure and assisting protein function by inducing conformational changes. On the other hand, excessive metal ions introduced into biological systems have been implicated in the aggregation of proteins responsible for the pathophysiology of several neurodegenerative diseases, such as Alzheimer and Parkinson disease [2].

Although metal ions play a critical role in modulating physiological functions through binding to proteins in vivo, they can have a profound negative impact on biotherapeutic products when present as inadvertent contaminants. Trace levels of metal ions can induce biotherapeutic product degradation which potentially jeopardizes the quality of the products by altering physicochemical properties as well as reducing stability and shelf life. Metal ions migrating from

rubber stoppers into a therapeutic protein liquid formulation have been reported to induce N-terminal degradation [3]. Barium leached from glass vials reacted with sulfate in the formulation to form visible particles [3]. Salts of tungsten oxide were shown to migrate from prefilled syringes into the drug product, where they triggered protein oxidation followed by aggregation to produce visible particles [4].

Contamination by leachables raises concerns about the safety and efficacy of the product due to the potential to cause acute toxicity or long-term health issues through chronic exposure. In the USA, the requirement for the proper evaluation of extractables and leachables (E&Ls) is governed by the FD&C Act as codified in 21 Code of Federal Regulations parts 210 and 211. Current Good Manufacturing Practice in Manufacturing, Processing, Packing or Holding of Drugs: General and Current Good Manufacturing Practice for Finished Pharmaceuticals, Subpart D-211.65 which states that "equipment shall be constructed so that surfaces that contact components, in-process materials, drug products shall not be reactive, additive, or adsorptive so as to alter the safety, identity, strength, quality, or purity of the drug product beyond the official or other established requirements."

Specific guidance has been issued for monitoring and control of leachables as part of requirement for the documentation of primary packaging of drug product [5–9]. Orally inhaled and nasal drug products as well as injection (solution and powder) products are of the highest degree of concern. The likelihood of interaction between packaging and dosage form is considered high for solutions or suspensions and medium for powders. Biological products are predominately formulated as liquid or freeze-dried products delivered by injection, which fall into the category of highest concern.

In biopharmaceutical drug product manufacturing and storage processes, the contact materials can be classified into three main categories: plastics/elastomers, glass, and stainless steel. Plastics/elastomers are by far the biggest source of extractables and leachables. Extensive research has been devoted to leachables/extractables from plastic materials [10–19]. The strategy and guidance for selecting, evaluating, and qualifying appropriate container closures as well as strategies for safety evaluation have been reported [20–23]. Other leachables/extractables from glass have also been studied [21, 22]. However, very limited research has been carried out on metal leachables/extractables. Metals can leach out from drug substance and/or product contacting equipment in the manufacturing, packaging, shipping, and storage process, especially from stainless steel surfaces. Some plastic packages, glass vials, and/or rubber stoppers can also be the sources of metal leachates [24]. Stainless steel is a typical contact material used for biologics product manufacturing, shipping, and storage. The stainless steel commonly used in biopharmaceutical applications is of the grade 316L and is an alloy containing mainly iron, nickel, and chromium with minor amounts of manganese and molybdenum. The grade 316L is a low-carbon formulation of austenitic stainless steel 316, and this modified chemistry is designed to reduce the propensity of the alloy to sensitize. Sensitization is the precipitation of chromium carbides (actually mixed iron/chromium carbides) along grain boundaries of stainless steel. This precipitation depletes the volume of metal near the grain boundaries of chromium in solution, thereby diminishing its corrosion resistance. The precipitation rate can be reduced by keeping carbon below 0.03%. The objective of this work is to elucidate the effect of various biologics formulation factors (e.g., buffer species, fill volume per unit stainless steel contact surface area, metal chelators, and pH) on the quantity of metal leachables from 316L stainless steel over time at different storage conditions.

1.2 Materials and methods

1.2.1 Materials

As shown in Fig. 1, the rectangular shape 316L stainless steel defined as coupons were utilized for this study. Prior to use, the coupons were chemically passivated by first immersing them in the solution of 1:4 (v/v) of CitruSurf solution (50%; Stellar Solution, McHenry, IL, USA; http://www.citrisurf.com) to milliQ water for 30 mins at 50–70°C and then were autoclaved after thorough rinsing with water. Two different sizes of stainless steel coupons were utilized, defined as type A and B. Type A had a surface area of 3.52 cm^2 with the dimensions of 1.55 cm (length) × 0.7 cm (width) × 0.3 cm (thickness) while type B had a surface area of 6.0 cm^2 with the dimensions of 2.5 cm (length) × 1.0 cm (width) × 0.15 cm (thickness). The 30-mL type I glass vials with 20 mm neck were purchased from Abbott Laboratories (Chicago, IL, USA). The 10-mL type I glass vials with 20 mm neck and serum stoppers were obtained from West Pharmaceutical Services (Lionville, PA, USA). USP/EP grade L-histidine and L-histidine mono hydrochloride, analytical grade acetate acid, monobasic sodium phosphate, dibasic sodium phosphate, citric acid (anhydrous), and sodium citrate dihydrate, acetate acid and sodium acetate trihydrate, succinic acid, $FeCl_3$, disodium edentate (Na_2EDTA), and diethylenetriaminepentaacetic acid (DTPA) were obtained from Sigma-Aldrich Chemical Co. (St. Louis, MO, USA). Polyvinylidene fluoride, 0.22 μm, filters were obtained from Millipore Inc. (Billerica, MA, USA).

1.2.2 Methods

1.2.2.1 Inductively coupled plasma-mass spectrometry (ICP-MS)

Metal ion concentrations in the testing solutions were quantitated by an inductively coupled plasma–mass spectrometry (ICP-MS) method which utilized an Agilent 7500 CX ICP-

MS system equipped with an autosampler. The instrument was qualified and calibrated with certified standard multi-element solution (BDH 10 ppm-Aristar) and maintained regularly. The accuracy of the method was evaluated by spiking recovery and inter-lab comparison with external GLP lab in Galbraith Laboratories, Inc. (Knoxville, TN, USA). All vessels, pipettes, and other laboratory equipment that came in direct contact with solutions used in the analysis were made of plastic. Samples were analyzed in the "hydrogen mode" and 10× diluted certified standard multi-element solution (BDH10 ppm-Aristar) was used as the internal standard. An external calibration curve for each element measured was established before analyzing the samples. A linear response curve between 1 and 500 ppb was established for iron, and 1–100 ppb for chromium and nickel. The limit of quantitation of iron, chromium and nickel was 1 ppb. A 50-ppb iron standard was analyzed every six samples to ensure the system performance. Samples were injected directly without dilution unless the metal ion concentration was outside the linear range as specified above. The sample volume required was 3.0 mL, and 1.5 mL aliquots were injected.

1.2.2.2 RP-HPLC analyses for chelator concentration

The concentrations of both Na_2EDTA and DTPA in the formulations were determined using an Agilent 1100 system coupled to a diode array detector. The system was calibrated and maintained regularly. The method accuracy was evaluated by spiking recovery. The separation was achieved isocratically on an Agilent Eclipse XDB-C18 column (5 μm, 4.6 × 150 mm) at a flow rate of 1 mL/min at ambient temperature. The mobile phase consisted of 30 mM sodium acetate, 2 mM tetrabutylammonium hydroxide, and 5% (v/v) methanol in water (pH 3.15). Excessive $FeCl_3$ (5 mM final concentration) was added to both samples and standards. External calibration was established with varying levels of Na_2EDTA and DPTA simultaneously. Of the

sample, 20 μL was injected onto the column and the separation was monitored by UV detection at 254 nm.

1.3 Experiments

To assess the effect of the five buffers on metal leachates from passivated 316L stainless steel at storage temperatures of −40°C to 25°C, the relationship between the testing solution volume (mL) and the coupon surface area (cm^2) was controlled at 5 mL/cm^2. All buffer solutions were prepared at 20 mM (pH 5.5) and sterile filtered with 0.22 μm polyvinylidene fluoride filters. Aliquots of 17.6 mL of the filtered buffer solutions were added into 30 mL type I glass vials with or without type A stainless steel coupons and sealed with serum stoppers and flip-off aluminum seals. The vials were stored in the stability chamber at either −40°C, −20°C, 2–8°C, or 25°C/60%RH separately for over 34 weeks. The vials without type A stainless steel coupons served as negative controls. The testing solutions and storage conditions are summarized in Table 1. The selected buffer types, concentration, pH, and storage conditions were chosen because these are commonly used conditions in biotherapeutic drug substance and/or product development. To evaluate the impact of contact surface area on metal leachates, commonly used 20 mM histidine–HCl buffer at pH 5.5 was selected as a testing solution. The testing solution volume (mL) per unit stainless steel contact surface area (cm^2) was selected to be between 1 and 5 mL/cm^2, with 1 mL/cm^2 as the worst case scenario for a stainless steel minitank used as a model for stability studies. The testing solution was prepared and processed as previously discussed. Aliquots of the testing solution of 17.6 mL for 5 mL/cm^2, 14.08 mL for 4 mL/cm^2, 10.56 mL for 3 mL/cm^2, 7.04 mL for 2 mL/cm^2, and 3.25 mL for 1 mL/cm^2 were individually added to the vials with or without type A stainless steel coupons and stored at 25°C/60% RH in a

stability chamber over the time period of 26 weeks. The vials without stainless steel coupons served as negative controls.

Many parenteral biologics drug products include metal chelators to improve product stability. To assess the effect of chelators on metal leachates, DTPA and Na_2EDTA were tested as chelators at three concentrations of 0.0, 0.134, and 0.268 mM in 20 mM histidine–acetate buffer at pH 6. At this pH, DTPA (H_5A), polyamino polycarboxylic acid, exists in equilibrium between H_2A^{3-} and H_3A^{2-}; however, in presence of metal ions, DTPA forms the metal complexes of MA^{3-}/MA^{2-} at equal molar ratios. For simplicity, the term DTPA and Na_2EDTA are used in the text, regardless of their ionization forms. Here, the concentration of 0.134 mM is equivalent to 0.05 mg/mL Na_2EDTA and 0.053 mg/mL DTPA. Similarly, the concentration of 0.268 mM is equivalent to 0.1 mg/mL Na_2EDTA and 0.106 mg/mL DTPA. These two concentrations were selected because they are typical concentrations applied in parenteral formulations. The samples without chelators served as controls. The stainless steel coupons utilized in this experiment were of type B due to unavailability of the previously used type A coupons. In order for the coupons to be fully immersed in the solution, 10 mL type I glass vials were used as the sample containers. The fill volume of the testing solutions (mL) per unit stainless steel contact surface area (cm^2) was controlled at 1 mL/cm^2. The testing vials were filled with 6.0 mL of solution in glass vials with or without stainless steel coupons and were then stored in a 25°C/60% RH stability chamber for 34 weeks. The vials without stainless steel coupons served as negative controls.

It is well known that pH plays a major role in protein stability. To evaluate the effect of pH on metal leachates, 20 mM histidine–acetate solutions, of pH values ranging from 5.0 to 9.0, were tested. The stainless steel coupons, glass vials and fill volumes were the same as those

utilized for the chelator evaluation in the previous experiment. The vials filled with testing solutions (6.0 mL) with or without stainless steel coupons (type B) were stored in a 25°C/60 RH stability chamber over the time period of 34 weeks. The vials without stainless steel coupons served as negative controls.

1.4 Results

The amount of metal ions leaching into biologics products is subject to multiple variables, such as formulation components, pH, contact materials, drug substance/drug product contact surface area with stainless steel, surface area processing procedure, contact duration and temperature, etc. In this paper, commonly utilized buffers, the relationship of the solution volume and contact surface area, chelators, and pH were studied individually to explore their impact, if any, on metal leachates from 316L stainless steel coupons. 316L (US: S31603) is an alloy, mainly composed of iron (62–72%), Cr (16–18.5%), and Ni (10–14%) [25]. Thus, in this study, all these three metals in the testing solutions were monitored by ICP-MS to evaluate the concentrations of metal ions potentially introduced into the products. Each measured metal ion concentration in the testing solution was corrected by subtracting the average amount detected in negative control solutions not containing stainless steel coupons. This allowed compensation for any metals possibly introduced from the glass and raw materials [26]. Each sample was tested in triplicate and the relative standard deviation (RSD) for the triplicate measure was within 0.5%, thus the average was utilized here.

1.4.1 Effect of buffers

Buffers are added to a formulation to adjust the pH to optimize protein solubility and stability. Phosphate, citrate, acetate, histidine, and succinate are the most commonly used buffers in parenteral products. In this study, in order to compare the effect of the buffer species on metal

leachates from stainless steel with time and storage conditions, the buffer concentration and pH were fixed at 20 mM and 5.5, respectively. Iron, nickel, and chromium were monitored in the media in contact or no contact with stainless steel coupons over 34 weeks. The sample storage temperatures were −40°C, −20°C, 2–8°C, and 25°C at 60% RH, the commonly accepted DS/DP storage or stressed conditions. At each time point, an individual vial was pulled for metal ion determination. The vials containing no stainless steel coupons served as negative controls. Due to glass vial breakage, the metal leachables data for 20 mM succinate buffer at the time points of 26 and 34 weeks stored at −40°C are not available. The concentrations of iron, nickel, and chromium leached from stainless steel coupons were very low. Nickel was not measurable quantitatively since its concentrations were below its limit of quantitation. Chromium was only determined quantitatively in the samples stored at 25°C at 60%RH. Among these three metal ions, iron was the most abundant and its concentrations were quantitatively determined by ICP-MS in all samples as shown in Fig. 2. Each buffer exhibited a different pattern on iron leachates. To further explore the differences in the impact of each buffer, the iron leachable data in each tested buffer were analyzed individually with the aid of John's Macintosh Project (JMP; SAS Institute Inc., Cary, NC, USA), a statistical data analysis software.

1.4.2 Effect of contact surface area

During drug substance manufacturing and the storage process, drug substances are in contact with stainless steel at different fill volume per unit contact surface area. In this study, the worst scenario has been chosen as 1 mL/cm^2. Most practical situations will be significantly better than this, i.e., larger volume per unit surface area. The metal leachable data for iron, nickel, and chromium after 26 weeks at controlled room temperature are shown in Fig. 3.

1.4.3 Effect of metal chelators

The metal chelator Na_2EDTA has been commonly used in parenteral formulations. DTPA has also been used in several approved parenteral products. The efficiency of Na_2EDTA and DTPA at inhibiting iron-induced degradation of an antibody was reported to be equivalent [27]. Thus, in this study, the effect of the two chelators on metal leachates at two concentrations was explored. The testing solutions containing no chelators served as controls. The iron concentration data are plotted in Fig. 4 and that for chromium in Fig. 5. No data analysis was performed on nickel since the observed levels were either below or at the limit of quantitation.

1.4.4 Effect of pH

In this study, the typical pH values of 5.0, 6.0, 7.0, and 9.0 were chosen as testing conditions to evaluate the impact of pH on metal leachates. The storage temperatures were 2–8°C and 25°C/60%RH. The amounts of iron, chromium, and nickel leaching out from the stainless steel coupons at 25°C are shown in Fig. 6 while data for 2–8°C are presented in Fig. 7. A comparison of the amounts of iron, chromium, and nickel leaching out from stainless steel at storage temperatures of 2–8°C vs. 25°C for 34 weeks is shown in Fig. 8.

1.5 Discussion

1.5.1 Effect of buffers on metal leachables

Chromium was quantitatively determined only at 25°C/60%RH storage over 34 weeks. Histidine–HCl, histidine–acetate, and phosphate behaved similarly (about 3.5 ppb Cr), and better than succinate buffer (4.6 ppb Cr). The highest levels of leachables are observed for citrate buffer (7.1 ppb Cr). The leached amount of Cr did not exhibit direct relationship with its corresponding salt solubility in the buffers. Cr(III) phosphate salt is slightly soluble in water and Cr salt of histidine, succinate, and citrate are water soluble. Similarly, the leached amount of Nickel ion did not exhibit dependence on its salt solubility. Ni(II) phosphate salt is insoluble in

water with solubility product constant of 4.74×10^{-32} at 25°C while its salt of histidine, citrate, and succinate are water soluble [28]. Nickel levels were below the limit of quantitation for all tested conditions. Among three monitored metal ions, iron was the most abundant even though the highest concentration observed is less than 40 ppb over 34 weeks. Therefore, in this section, only the iron data were analyzed to explore each buffer behavior. As indicated in Fig. 2, each buffer exhibited its own properties over the time course of 34 weeks studied here. Thus, temperature/time impact on iron leachates is discussed for each individual buffer first, followed by a discussion of the comparison among the five buffers.

For histidine–acetate buffer at pH 5.5 (Fig. 2a), temperature seemed to exert an effect on iron leachables. Storage temperature of -20°C exhibited the highest levels of iron leachates followed by 25°C, −40°C, and 2–8°C at time points of 12 and 22 weeks. No good explanation can be provided for this counterintuitive result. However, when the storage time increased to 34 weeks, the temperature effect diminished. Further statistical data analysis was performed by JMP to explore whether temperature or time makes a significant contribution to iron leachates. With a 95% confidence level, the probability factor of less than 0.05 indicates that the factor is significant. The calculated probability factor for time is 0.0262 while the calculated probability factor for temperature is 0.9029 which indicates that within a 95% confidence level, time is the significant factor that impacts the iron leachates.

For histidine–HCl buffer at pH 5.5 (Fig. 2b), the levels of iron leakage for the storage temperature of 25°C are significantly higher than those for lower storage temperatures of −40°C, −20°C, and 2–8°C, which was further confirmed by JMP statistical data analysis. The calculated probability factor of 0.0178 means a significant difference at the 95% confidence level. However, no significant difference in iron leachates was observed when storage temperatures

range from −40°C to 2–8°C. Further data analysis by JMP indicated that, again, time plays a significant role in affecting iron leaching from the stainless steel because the calculated significant factor is 0.0909.

For 20 mM phosphate buffer at pH 5.5 (Fig. 2c), leached iron amounts at 25°C storage temperature exhibited the highest level over the tested time period, as expected, followed by the levels for a storage temperature of −40°C. The iron amount leached at the storage temperature of 2–8°C is the lowest among the tested conditions. That the iron amount detected for storage at −40°C is much higher than for storage at 2–8°C is probably due to the fact that the pH of phosphate buffer can drop significantly upon freezing [29]. The significance of the temperature impact on iron leachates cannot be calculated by JMP because the iron leachates concentrations are similar for temperature of 25°C and −20°C. However, as Fig. 2c indicates, the iron leachates at 25°C or −20°C are significantly higher than those at −40°C and 2–8°C. Also, iron leachates at −40°C are three times of that at 2–8°C. The iron leachates at −40°C, 2–8°C, and 25°C did not significantly increase over the tested time course, which was confirmed by JMP data analysis. However, iron leachates at the storage temperature of −20°C increased about 2.5 times over the time period of 22 weeks. The trend is significantly different from the other three tested conditions.

For citrate buffer at pH 5.5 (Fig. 2d), the highest iron levels were seen at 25°C, followed by −20°C, 2–8°C, and −40°C. With 95% confidence level, time makes significant contribution to iron leachates observed for the four tested conditions, especially at the storage temperature of 25°C, which was suggested by JMP calculated probability factor of 0.0148.

For succinate buffer, because of the sample loss at −40°C due to vial breakage, this temperature was not evaluated. Storage temperature had a significant impact on the iron

leachates: levels of iron leachates at 25°C were highest, followed by those for 2–8°C, and then −20°C (Fig. 2e). Further data analysis by JMP (probability factor of 0.0265) suggested that at the 95% confidence level, temperature is a major factor in affecting iron leaching from stainless steel. Here, within the 95% confidence level, time has no major impact on iron leachates for succinate buffer over all the tested conditions since the calculated probability factor is 0.7476.

All five buffers were tested at four different storage temperatures to explore the difference of their capacity at affecting iron leaching from stainless steel. The comparison was performed for each individual condition by calculating probability factors based on buffer species using SAS data analysis. Within the 95% confidence level, a probability factor of less than 0.05 indicates that a significant difference is observed. Over the tested time course of 34 weeks, at −40°C storage temperature, a calculated probability factor of 0.002 indicates that significant differences exists among the four buffers (no data for succinate buffer). Phosphate buffer shows the highest impact on iron leachates, followed by citrate buffer, and histidine–acetate buffer. Histidine–HCl buffer exhibited the least impact at leaching iron from stainless steel at −40°C. Similarly, significant differences with a probability factor of 0.013 was observed among five buffers at the storage temperature of 25°C. The ability to induce iron leaching from stainless steel decreases in the following order: citrate buffer >phosphate buffer, succinate buffer > histidine–HCl buffer >histidine–acetate buffer. This trend is not consistent with iron salt solubility in water at 25°C. Fe (II)/(III) phosphate salt is least soluble (Ksp for FePO4 is 1.3×10^{-22} and $Fe_3(PO4)_2$ is 10^{-36}) while its citrate, histidine, and succinate salt are water soluble [28]. However, at storage temperatures of −20°C and 2–8°C, no clear trend was observed. Thus, the effect of buffer on iron leachates is determined by multiple factors, such as buffer species, storage temperature, and contact time, etc.

1.5.2 Effect of contact surface area on metal leachables

Solution fill volume per unit contact surface area between 1 and 5 mL/cm^2 were investigated in this study. Fig. 3 shows that, as expected, the lower the fill volume (mL) per unit stainless steel contact surface area (cm^2), the higher the relative levels of metal ions leached. However, no linearity was observed at the studied relationship range between fill volume and contact surface area over the tested time period of 26 weeks. A plateau was observed when the fill volume per unit stainless steel contact surface area reached 3 mL/cm^2.

1.5.3 Effect of metal chelators on metal leachables

The effect of the metal chelators Na_2EDTA and DTPA on metal leachables was explored for the storage temperature of 25°C over 34 weeks. Both chelators at the concentrations of 0.134 and 0.268 mM showed a dramatic impact on iron leachates as shown in Fig. 4. Compared to the solutions without chelator, the concentration of leached iron from stainless steel in the buffer with Na_2EDTA increased more than 20-fold over the 17 weeks, and increased more than 10-fold over 34 weeks (Fig. 4a). It was reported previously that EDTA facilitated the migration of metal ions into the solution from metal contact surfaces [30]. A similar trend was observed for DTPA. Compared to the solutions without any chelator, leached iron ion concentrations in the buffer containing DTPA increased more than 10-fold for both the 17 and 34 weeks time period (Fig. 4b). However, increase in concentration of Na_2EDTA did not have a significant impact on leached iron ion concentrations over 34 weeks unlike increased DTPA levels which exhibited a significant effect on iron leaching. Doubling the concentration of DTPA from 0.134 to 0.268 mM increased the concentration of leached iron ions by a factor of 1.7. A linear increase in leached iron ion concentration with the increased concentration of DTPA was also observed in

both cases (R^2 is 0.9971 when the solutions contain 0.134 mM DTPA while R^2 is 0.9829 when DTPA is 0.268 mM).

The data in Fig. 5a suggest that the presence of Na_2EDTA in the solutions increased chromium ions leaching from stainless steel but the concentration of the chelator did not make a difference under the tested conditions. An effect of DTPA on chromium leachates was not observed until 34 weeks (Fig. 5b). Similar to Na_2EDTA, no DTPA concentration effect was observed for chromium leachates.

Since iron is the major metal leachate compared to chromium and nickel, it was used to explore the capacity difference affecting metal leachates between Na_2EDTA and DTPA. At equal molar concentrations of Na_2EDTA and DTPA over 34 weeks at 25°C, Na_2EDTA facilitated iron leaching from stainless steel faster than DTPA as shown in Fig. 9. This can be of concern since it has been shown that Na_2EDTA and DTPA cannot protect protein degradation if the ratio of the molar concentration of the metal chelators to iron in solution is less than 1:1 [27].

1.5.4 Effect of pH on metal leachables

Similar to previously discussed results, the major leached metal ions at the tested pH of 5.0, 6.0, 7.0, and 9.0 is iron, at temperatures of 2–8°C and 25°C. At 25°C, chromium and nickel could not be quantitated (levels were below the limit of quantitation) until a contact time with stainless steel of over 17 weeks. Thus, in Fig. 6b and c, only the data for 17 and 34 weeks time points were plotted. Fig. 6 suggests that iron, chromium, and nickel leached most at pH 5.0 while between pH 6.0 and 9.0, no pH effect was observed. At 2–8°C, pH affected metal leaching from stainless steel differently compared to 25°C. For iron, the sequence of impact from high to low is pH 5.0 >> pH 9.0 > pH 6.0 ~pH 7.0 (Fig. 7a). Acidic conditions of pH 5.0 produced about 4-fold higher iron leachate compared to pH 9.0. It has been reported that ferric/ferrous salts of

sulfate, gluconate, and citrate exhibit much higher solubility in acidic conditions than neutral and basic conditions [31]. At close to neutral and neutral conditions, no pH impact was observed. The effect of pH on chromium shows decreasing leakage in the following order: pH 9.0 > pH 5.0 > pH 6.0 > pH 7.0, that is, both basic and acidic conditions have impact on chromium leachables but not at neutral pH 7.0 conditions as shown in Fig. 7b. Similar to chromium, basic condition (pH 9.0) produced strongest impact on nickel leachables, followed by pH 5.0, then pH 6.0 (Fig. 7c). At neutral pH 7.0, no pH impact was observed over 34 weeks.

To further explore the temperature impact at pH 5.0–9.0, the concentrations of each leachate were compared using the 34 weeks time point as shown in Fig. 8. For iron, at the acidic pH 5.0, the lower temperature of 2–8°C storage produced a stronger impact than at 25°C while for neutral conditions of pH 7.0, the 25°C storage condition impact was stronger than 2–8°C. At pH 6.0 and 9.0, no temperature impact was observed. For chromium leachables, at acidic to neutral condition of pH 5.0–7.0, the higher temperature of 25°C exerted a stronger impact. In contrast, at basic condition of pH 9.0, the lower temperature of 2–8°C produced more leachables. For nickel leachables, lower temperatures produced much more metal leachates except at neutral condition of pH 7.0 which had no obvious impact.

1.6 Conclusions

Among the three monitored metal leachates of iron, chromium, and nickel, iron is the most abundant. However, overall metal leachates observed are at the ppb level. Multiple factors such as buffer species, the amount of testing media fill volume per unit stainless steel contact surface area, formulation excipients such as metal chelator type and/or concentration, pH, storage temperature, and contact duration with stainless steel, play an important role in affecting the concentrations of metal ions leaching from contact with stainless steel. Each studied factor

exhibited its own capacity at leaching metal ions from contact with stainless steel. The commonly used buffers of histidine–acetate, histidine–HCl, phosphate, citrate, and succinate exhibited different properties at storage conditions of −40°C to 25°C with time at same concentration and pH. Furthermore, with the same buffer species and concentration, pH impacted the capacity to leach metal ions from stainless steel. Solution fill volume per unit stainless steel contact surface area above 3 mL/cm^2 did not further decrease the concentration of metal iron leachates. Compared to the other factors tested in this study, commonly present metal chelators in parenteral formulations, metal chelator Na_2EDTA and DTPA, produced the most significant impact on metal leachates, especially iron leachates. However, Na_2EDTA and DTPA behaved differently. Na_2EDTA produced a much stronger impact compared to DTPA over the tested 34 weeks at 25°C. Increase in concentration of Na_2EDTA present in the formulations did not increase iron leachates. In contrast, the concentration of iron leachates increased significantly with an increase of DTPA concentration. Therefore, to minimize metal leaching from stainless steel during drug substance and/or drug product manufacturing, storage, and shipping processes, multiple factors have to be evaluated to balance the risk and benefit to achieve the desired drug product shelf life. Large-scale production tanks generally have much higher volume per unit surface areas than those tested here (of the order of 10 mL/cm^2 or higher), which significantly reduces the risk if proper maintenance procedures are followed.

1.7 Acknowledgements

The 316L stainless steel coupons utilized in this study were supplied courtesy of Boehringer Ingelheim Pharma. We gratefully acknowledge Parag Kolhe (Biotherapeutic Pharmaceutical Science, Pfizer Inc.) for his help in calculating the probability factor using the

JMP data analysis software and Bo Zhang (Biotherapeutic Pharmaceutical Science, Pfizer Inc.) for his help in analyzing the samples.

1.8 References

1. Passerini A et al. *Identifying cysteines and histidines in transition-metal-binding sites using support vector machines and neural networks.* Proteins. 2006;65(2):305–16.
2. Uversky V.N., et al., *Metal-triggered structural transformations, aggregation, and fibrillation of human alpha-synuclein. A possible molecular link between Parkinson's disease and heavy metal exposure.* J Biol Chem. 2001;276(47):44284–96.
3. Markovic I. *Challenges associated with extractables and/or leachables substances in therapeutic biologic protein products.* Am Pharm Rev. 2006;9(6):20–7.
4. Bee J.S., et al., *Precipitation of a monoclonal antibody by soluble tungsten.* J Pharm Sci. 2009;98(9):3290–301.
5. ICH, *International conference on harmonization of technical requirements for registration of pharmaceuticals for human use (ICH). Guideline for industry: impurities in new drug substances*, ICH Q3A
6. *CDER Guidance Document: container closure systems for packaging human drugs and biologics*. 1999.
7. *EMEA, Harmonized guideline (EMEA and health Canada) on the pharmaceutical quality of inhalation and nasal products.* 2005.
8. ICH, *International conference on harmonization of technical requirements for registration of pharmaceuticals for human use. Guideline for industry: Good manufacturing practices,* ICH Q6A.

9. ICH, *International conference on harmonization of technical requirements for registration of pharmaceuticals for human use. Guidance for industry: impurities in new drug substances,* ICH Q3B.
10. Arbin A., et al., *Studies on contamination of intravenous solutions from PVC bags with dynamic headspace GC-MS and LC-diode array techniques.* J Pharm Sci. 1986;28:211–8.
11. Goydan R., et al., *High-temperature migration of antioxidants from polyolefins.* Food Addit Contam. 1990;7(3):323–37.
12. Jenke D., *Extractable/leachable substances from plastic materials used as pharmaceutical product containers/devices.* PDA J Pharm Sci Technol. 2002;56(6):332–71.
13. Jenke R.D., et al., *Performance characteristics of an ion chromatographic method for the quantitation of citrate and phosphate in pharmaceutical solutions.* J Chromatogr Sci. 2007;45(1):50–6.
14. Jenke R.D., et al., *Strategy for assessing the leachables impact of a material change made in a container/closure system.* PDA J Pharm Sci Technol. 2005;59(6):360–80.
15. Jenke R.D., et al., *Model for estimating the accumulation of solutes leaching from polymeric containers into parenteral solutions.* Int J Pharm Sci. 1992; 78:115–22.
16. Jenke R.D., et al., *Modeling of the leachables impact on the engineering of parenteral product container systems.* Int J Pharm. 1994;108:1–9.
17. Kim K., et al., *Enzymatic cleavage of proteins by reactive oxygen species generated by dithiothreitol and iron.* J Biol Chem. 1985;260(29):15394–7.
18. Reif O.W., et al., *Analysis and evaluation of filter cartridge extractables for validation in pharmaceutical downstream processing.* PDA J Pharm Sci Technol. 1996;50(6):399–410.

19. Sanga S.V., *Review of glass types available for packaging parenteral solutions.* J Parenter Drug Assoc. 1979;33(2):61–7.

20. Jenke D.R., et al., *Extractables/leachables from plastic tubing used in product manufacturing.* Int J Pharm. 2006;315(1–2):75–92.

21. Nicholas K., *Extractables and leachables determination: a systematic approach to select and qualify a container closure system for a pharmaceutical product.* Am Pharm Rev. 2006;9 (3):21–7.

22. Osterberg R.E., *Potential toxicity of extractables and leachables in drug product.* Am Pharm Rev. 2005;8(2):64–7.

23. Taborsky C.J., et al., *A critical approach to the evaluation of packaging components and the regulatory and scientific considerations in developing a testing strategy.* Am Pharm Rev. 2006;9:146–50.

24. Allain L., et al., *Impact of package leachables on the stability of pharmaceutical products.* Am Pharm Rev. 2007;10(4):38, 40, 42-44.

25. *316/316L Stainless steel product data sheet.* Cited 2007; available from: www.aksteel.com.

26. Waterman K.C., et al., *Stabilization of pharmaceuticals to oxidative degradation.* Pharm Dev Technol. 2002;7(1):1–32.

27. Zhou S., et al., *Comparative evaluation of disodium EDTA and DTPA as iron chelators to prevent metal catalyzed destabilization of a therapeutic monoclonal antibody.* J Pharm Sci. 2010;99(10):4239–50.

28. Rubinson, K.A., ed. *Chemical Analysis.* 1st ed. 1987, Little, Brown and Company, Boston.

29. Kolhe P., et al., *Impact of freezing on pH of buffered solutions and consequences for monoclonal antibody aggregation.* Biotech Progr. 2009. doi:10.1002/btpr.377.

30. Kocijan A., et al., *The influence of complexing agent and proteins on the corrosion of stainless steels and their metal components.* J Mater Sci Mater Med. 2003;14(1):69–77.

31. Jacobs A., et al., *Role of gastric secretion in iron absorption.* Gut. 1969;10(3):226–9.

Table 1. Experimental conditions to assess the effect of buffer species and storage conditions on metal leachates from 316 L stainless steel coupons with a surface area of 3.52 cm^2 in 30 mL type I glass Vials

Storage condition (^oC)/ Test solutions	-40^{o}C	-20^{o}C	2-8^{o}C	25^{o}C
20 mM Histidine-Acetate at pH 5.5	1 vial w/ ss	1 vial w/ ss	1 vial w/ ss	1 vial w/ ss
	1 vial w/o ss	1 vial w/o ss	1 vial w/o ss	1 vial w/o ss
20 mM Histidine-HCl at pH 5.5	1 vial w/ ss	1 vial w/ ss	1 vial w/ ss	1 vial w/ ss
	1 vial w/o ss	1 vial w/o ss	1 vial w/o ss	1 vial w/o ss
20 mM Phosphate at pH 5.5	1 vial w/ ss	1 vial w/ ss	1 vial w/ ss	1 vial w/ ss
	1 vial w/o ss	1 vial w/o ss	1 vial w/o ss	1 vial w/o ss
20 mM Citrate at pH5.5	1 vial w/ ss	1 vial w/ ss	1 vial w/ ss	1 vial w/ ss
	1 vial w/o ss	1 vial w/o ss	1 vial w/o ss	1 vial w/o ss
20 mM Succinate at pH 5.5	1 vial w/ ss	1 vial w/ ss	1 vial w/ ss	1 vial w/ ss
	1 vial w/o ss	1 vial w/o ss	1 vial w/o ss	1 vial w/o ss
20 mM Acetate at pH 5.5	1 vial w/ ss	1 vial w/ ss	1 vial w/ ss	1 vial w/ ss
	1 vial w/o ss	1 vial w/o ss	1 vial w/o ss	1 vial w/o ss

Note:
1. The test solution fill volume is 17.6 mL
2. ss stands for stainless steel coupon

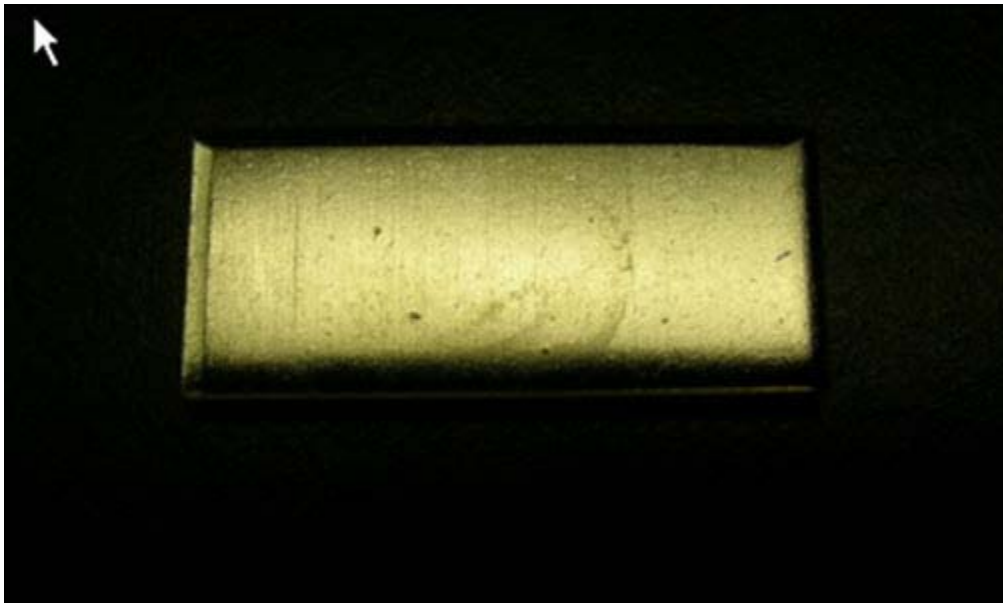

Fig. 1. Appearance of stainless steel coupons used

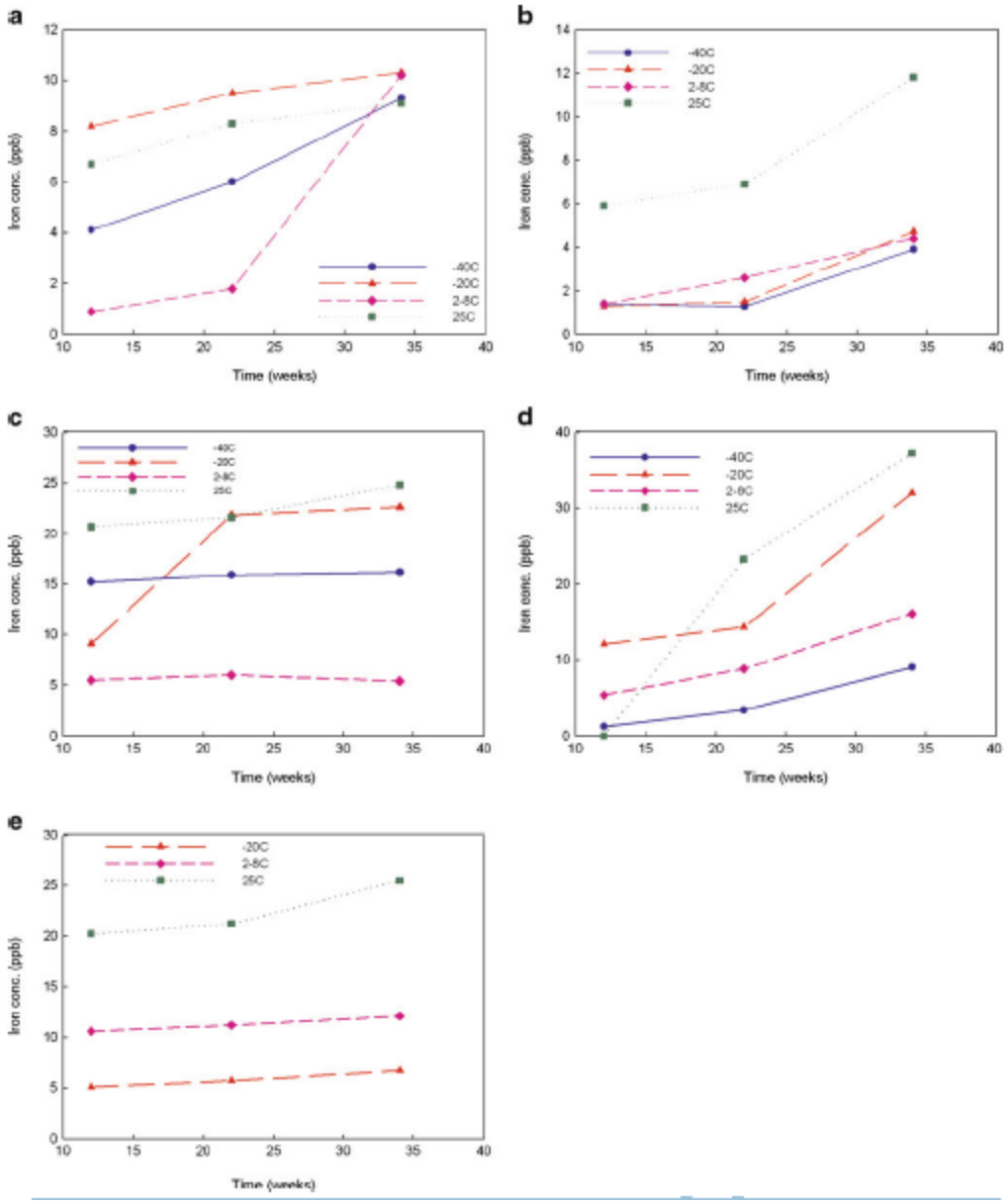

Fig. 2. Iron leachate average concentrations for five different buffers (20 mM) at pH 5.5 stored at −40°C, −20°C, 2–8°C, and 25°C over 34 weeks (triplicate measurement with RSD of 0.5%). a for histidine-acetate, b for histidine–HCl, c for phosphate, d for citrate, and e for succinate buffer

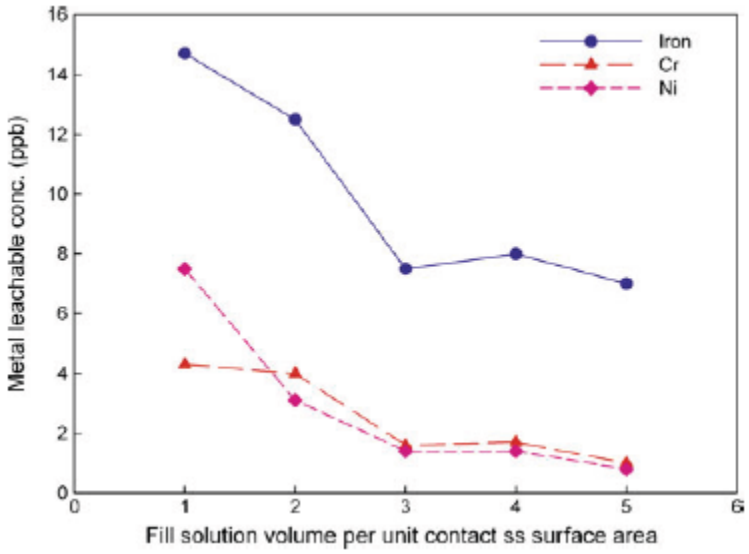

Fig. 3. Metal leachates average concentrations in 20 mM histidine–HCl buffer solution at pH 5.5 at different solution fill volumes per unit contact ss surface area (triplicate measurement with RSD of 0.5%)

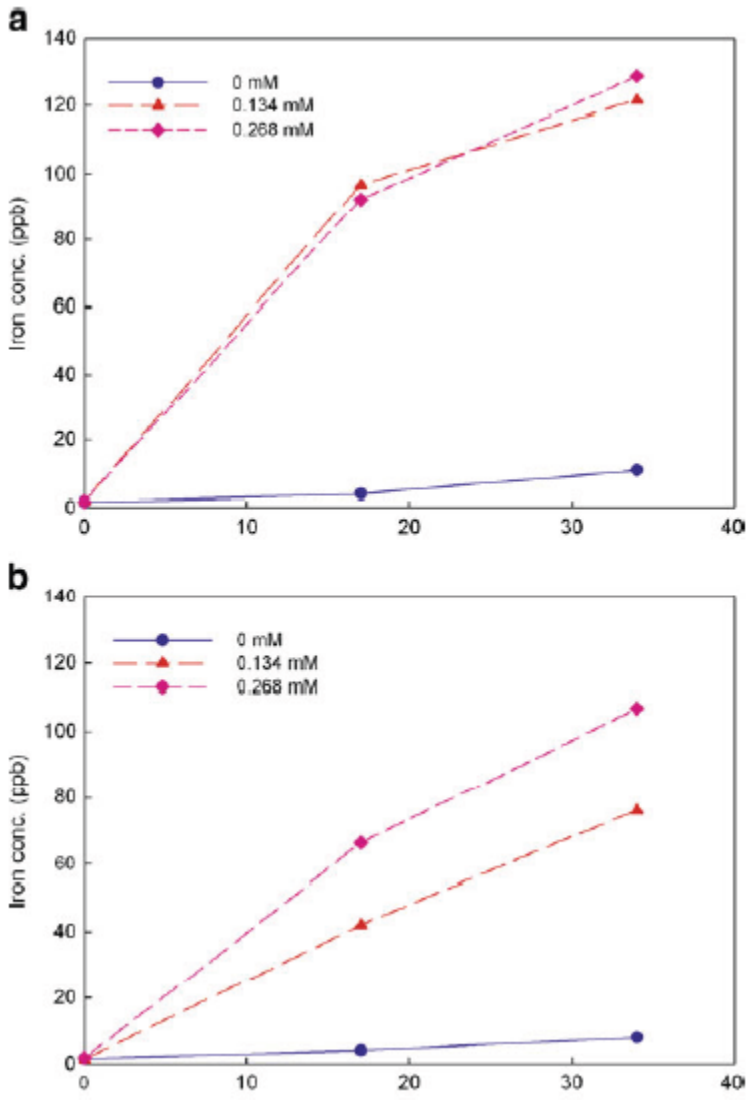

Fig. 4. Iron leachate average concentrations in 20 mM histidine–acetate buffer solutions (pH 6.0) containing Na_2EDTA and DTPA at the concentrations of 0, 0.134, and 0.268 mM over 34 weeks stored at 25°C (triplicate measurement with RSD of 0.5%). a for Na_2EDTA and b for DTPA

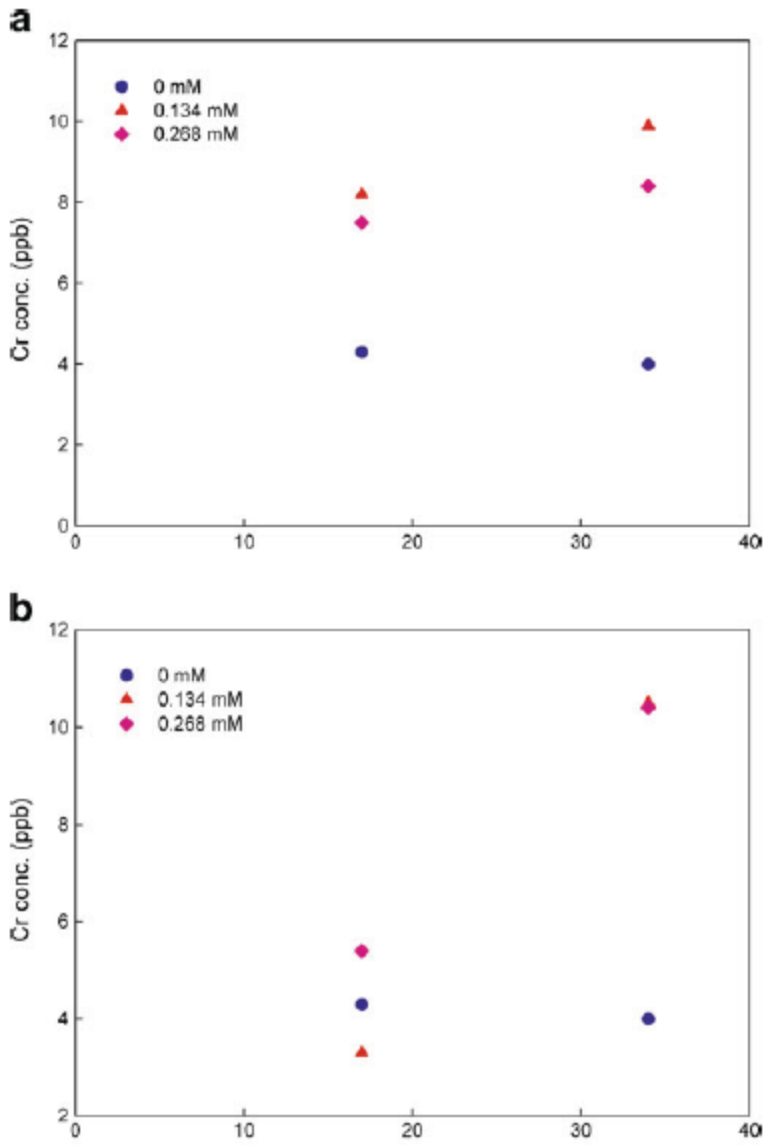

Fig. 5. Chromium leachate average concentrations in 20 mM histidine–acetate buffer solutions (pH 6.0) containing Na_2EDTA and DTPA at the concentrations of 0, 0.134, and 0.268 mM over 34 weeks stored at 25°C (triplicate measurement with RSD of 0.5%). a for Na_2EDTA and b for DTPA

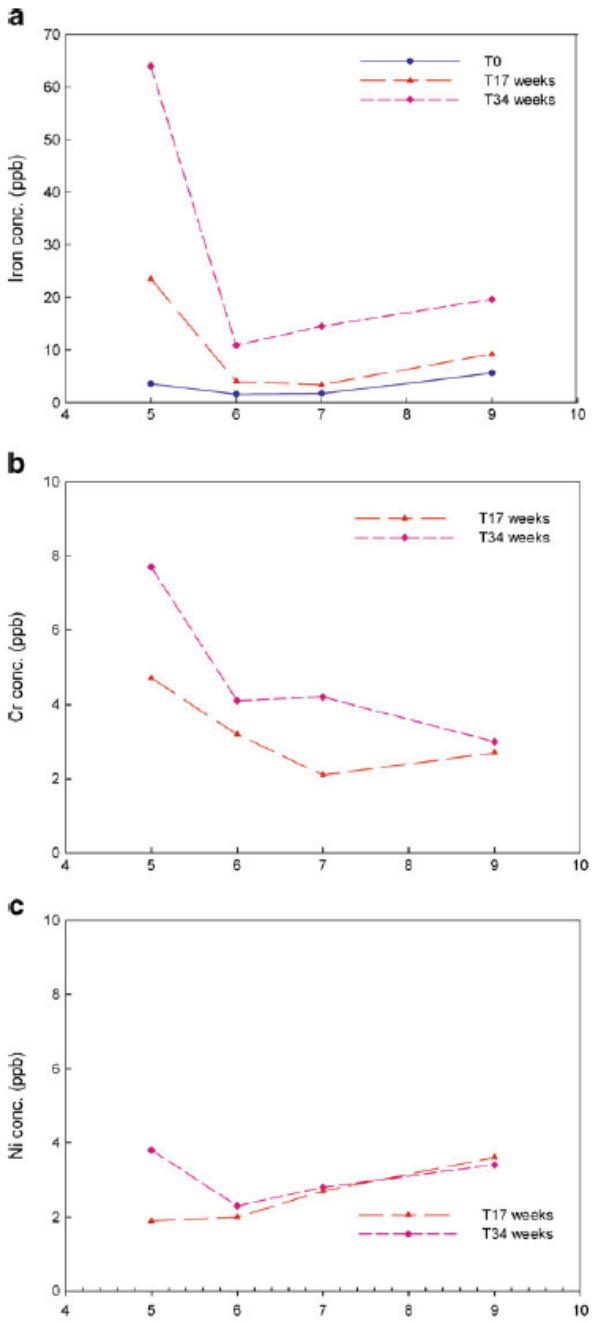

Fig. 6. a–c Iron, chromium and nickel leachates average concentration in 20 mM histidine–acetate buffer solution at pH 5.0, 6.0, 7.0, and 9.0 stored at 25°C over 34 weeks (triplicate measurement with RSD of 0.5%)

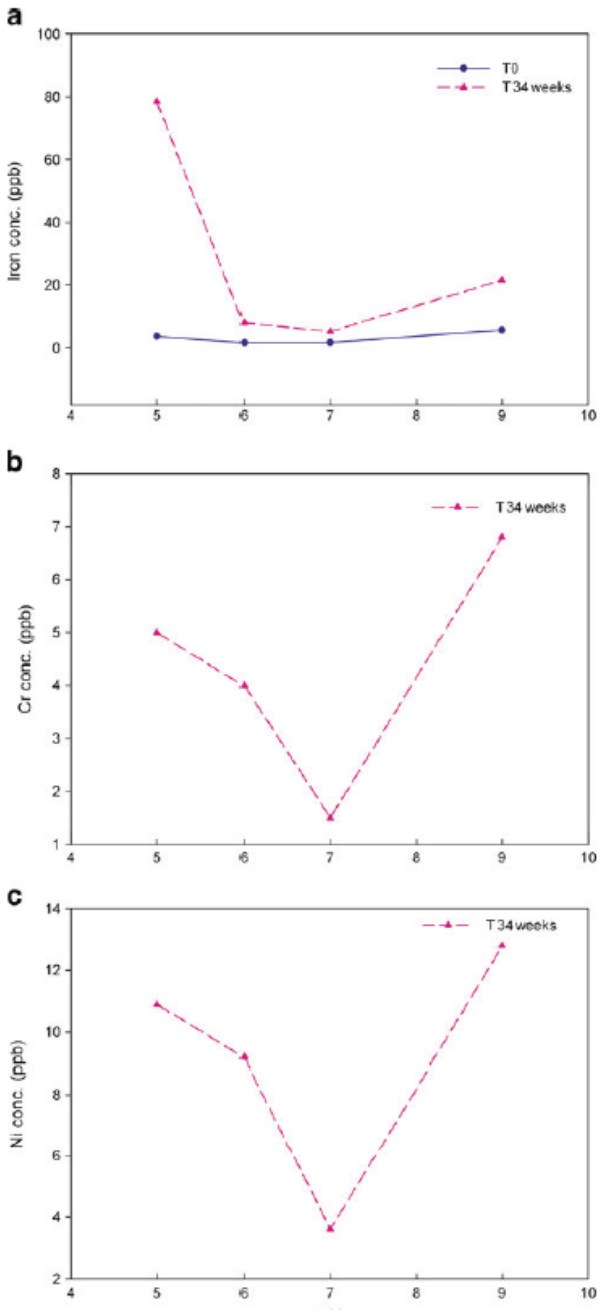

Fig. 7. a–c Iron, chromium, and nickel leachates average concentration in 20 mM histidine–acetate buffer solution at pH 5.0, 6.0, 7.0, and 9.0 stored at 2–8°C over 34 weeks (triplicate measurement with RSD of 0.5%)

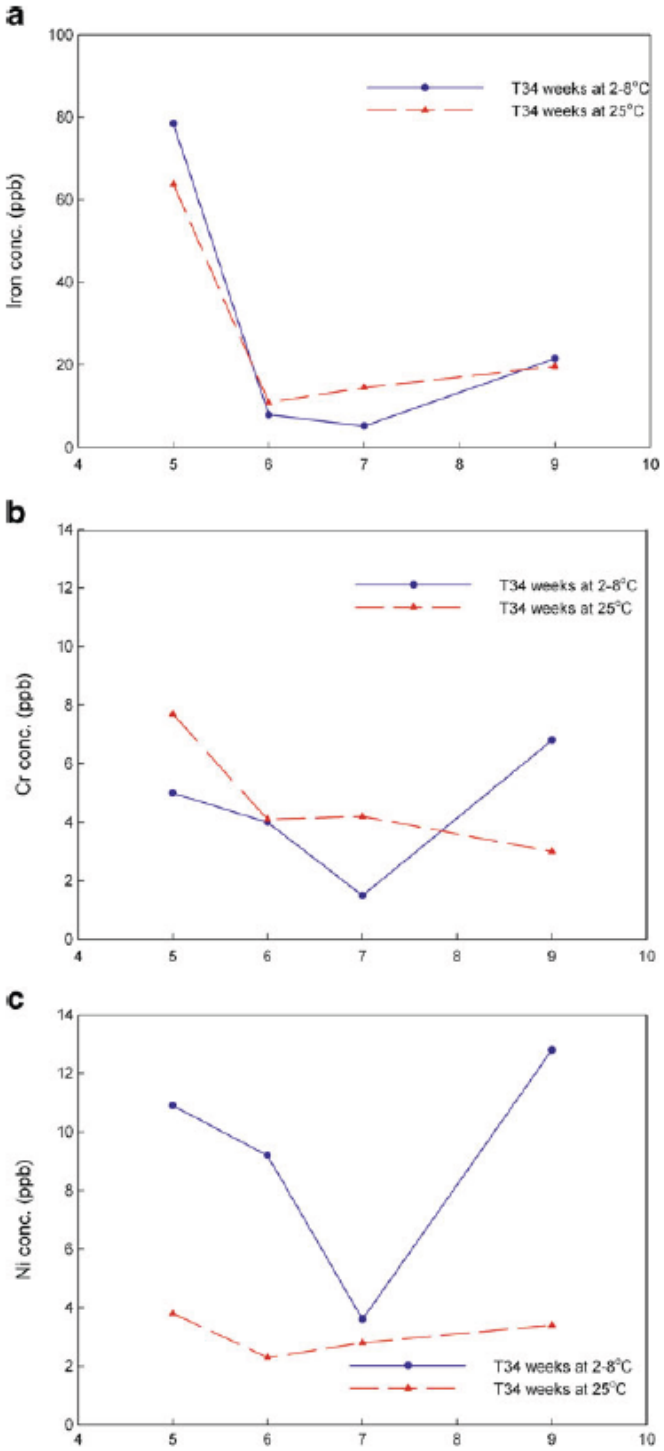

Fig. 8. a–c Comparisons of the average concentrations of metal leachates of iron, chromium and nickel in 20 mM histidine buffer at pH 5.0, 6.0, 7.0, and 9.0 when stored at 2–8° vs. 25°C over 34 weeks time points (triplicate measurement with RSD of 0.5%)

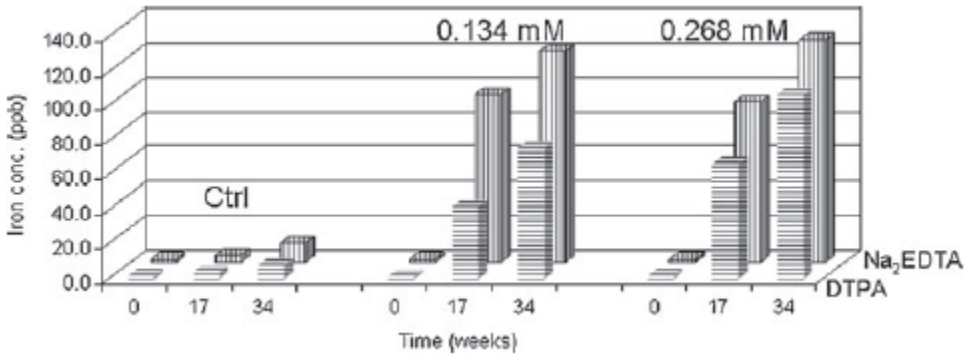

Fig. 9. Iron leachates average concentration comparison between Na_2EDTA and DTPA in 20 mM histidine-acetate buffer solutions (pH 6.0) when metal chelator concentrations at 0, 0.134, and 0.268mMstored at 25°C over 34 weeks (triplicate measurement with RSD of 0.5%)

Chapter 2: Metal Ion Leachables Induced by Combined Biologics Formulation Factors by Design of Experiment

Table of Contents

2.1. Introduction

Biotherapeutic products are predominately formulated as liquids or freeze-dried products delivered by injection, and therefore fall into the category of parenteral formulations. In order to develop a stable formulation with an acceptable shelf life, excipients such as solvents/cosolvents, polymeric and surface-active compounds, chelating agents, anti-oxidants, preservatives, buffers, bulking agents, protectants, and tonicity adjusters, have been used in parenteral formulations. The majority of biologics products consist of a buffer, a tonicity modifier, a cryo- or lyoprotectant, and a surfactant [1–4]. In some cases, a metal chelator and an antioxidant are also added to the formulation to protect the protein from oxidation. Polysorbate 80 and 20 are the most commonly used surface-active compounds. The concentration of polysorbate 80 employed in most biologics formulations is ≤ 0.2 mg/mL. To complex the trace amount of metal ions inadvertently present in parenteral formulations, salts of EDTA (mainly sodium edentate; $Na_2EDTA.2H_2O$), have been used as chelating agents. The content of $Na_2EDTA.2H_2O$ in pharmaceutical preparations is generally between 0.005% and 0.1% (w/v, 0.05–1 mg/mL) [5]. Diethylenetriaminepentaacetic acid (DTPA) is an alternative metal chelator approved for parenteral use and has demonstrated a comparable capacity to inhibit metal-induced mAb instability [6]. L-methionine has been used as an antioxidant to protect labile methionine residues in proteins from oxidation. L-histidine buffer is commonly used to adjust the formulation pH for optimal stability and solubility.

Trace amounts of metal ions are invariably introduced into biotherapeutic bulk solution during drug substance and/or drug product manufacturing, shipping, and storage. The metal ions inadvertently introduced into products either arise from the excipients or leach into solution from contact with manufacturing equipment. Even though parenteral grade excipients are used,

residual amounts of metal ions are present, mostly at part per billion (ppb) levels or below. Some plastic packages, glass vials, and/or rubber stoppers can also be the sources of metal leachates [7]. Salts of tungsten oxide were reported to migrate from prefilled syringes into a biotherapeutic protein product [8]. Barium was also observed leaching from glass vials [9]. However, the major source of the metal contamination in biotherapeutic drug products is the contact with stainless steel during drug substance and/or drug product manufacturing, as well as during shipping and storage processes, such as transfer tanks, cryotanks, compounding tanks, stainless steel piping, header tanks, and filling needles.

Trace amount of metals can have a profound negative impact on the stability of the product. Site specific metal-protein binding can induce secondary and tertiary structural changes resulting in the formation of protein aggregates [10, 11]. Metals can induce product degradation reactions, such as oxidation [6, 12–14], fragmentation [6, 13], and aggregation [6, 12, 15]. Such degradation reactions can potentially jeopardize the quality of the products by altering physicochemical properties as well as reducing stability and shelf life. In addition, excessive metal ions, especially heavy metal ions, introduced into a biological system may lead to safety concerns. Although metal ions are too small to induce an immune response, they can conjugate with proteins to form metal–protein complexes, potentially resulting in immunogenicity [16]. Iron has been implicated in the aggregation of proteins responsible for the pathophysiology of several neurodegenerative diseases, such as Alzheimer and Parkinsons [15].

Biotherapeutic products are predominately delivered by intravenous injection. Additionally, the majority of biological products are formulated as a liquid or as a lyophilized dry powder and packaged in vials. The likelihood of an interaction between packaging and a liquid solution dosage form is considered high and considered medium for a powder product.

Therefore, biotherapeutic products fall into the category of highest concern from an extractables and leachables perspective [17–19]. In the USA, the requirement for the proper evaluation of extractables and leachables is governed by the Federal Food, Drug, and Cosmetic Act as codified in 21 Code of Federal Regulations, parts 210 and 211. Furthermore, specific guidance for monitoring and control of leachables as part of requirements for the primary packaging of drug products has been issued by the regulatory authorities [17, 19].

The stainless steel grade commonly used in biopharmaceutical applications is called 316L, a low-carbon (<0.03%) alloy containing mainly iron, nickel, and chromium. This grade is called austenitic stainless steel and the alloy is designed to reduce its propensity for corroding by reducing the precipitation of chromium carbides (actually mixed iron/chromium carbides) along grain boundaries of stainless steel by keeping carbon below 0.03%.

Since the biologic drug product in solution interacts with the manufacturing equipment, it is useful to understand their role in the leaching process. The impact of individual biotherapeutic formulation factors, commonly utilized buffers, the relationship of the solution volume and contact surface area, metal chelating agent concentration and type, and solution pH, on metal leachables from 316L stainless steel was studied, respectively [20]. In this paper, six major formulation factors: protein concentration, solution pH controlled by L-histidine, metal chelator concentration and type ($Na_2EDTA.2H_2O$ vs. DTPA), antioxidant (methionine), and surfactant (polysorbate 80), were investigated to elucidate the effect of the biotherapeutic formulation component in the presence of other components on the quantity of metal leachables from 316L stainless steel over time at storage temperatures of −40°C, 2–8°C, and 25°C. The presence of multiple factors makes it efficient to study their impact by a design of experiments (DOE) approach. Such DOE studies are in accordance with the principles of quality by design as

suggested in ICH Q8 [21] since the impact of multiple factors and their potential interaction can be evaluated, thus providing an understanding of product during all phases of production and enhance the probability of developing a robust formulation.

2.2. Materials and Methods

2.2.1. Materials

As in our previous work [20], rectangular 316L stainless steel coupons were utilized for this study. Prior to use, the coupons were chemically passivated as described earlier [20]. The dimensions of the coupons were 2 cm (length) ×1 cm (width) × 0.1651 cm (thickness) with a surface area of ~5 cm^2. The 10-mL type I Schott glass vials and serum stoppers (West 4432/50 Gray B2-40 and Flurotec coated, West Pharmaceutical Services, Lionville, PA, USA) were used after they were cleaned and autoclaved. An IgG2 monoclonal antibody produced in-house was used in this study. The mAb was formulated in 20 mM histidine at pH 5.5. USP/EP grade L-histidine and L-histidine hydrochloride monohydrate, analytical grade $FeCl_3$, Na_2EDTA dihydrate, and DTPA were obtained from Sigma-Aldrich Chemical Co. (St. Louis, MO, USA). EP/USP grade polysorbate 80 was obtained from J. T. Baker (Meriden, CT, USA). USP/F.C.C. grade L-methionine was obtained from J. T. Baker (Phillipsburg, NJ, USA) and parenteral grade α,α-trehalose dihydrate (low endotoxin) was obtained from Ferro Pfanstiehl Laboratories, Inc (Cleveland, OH, USA). Polyvinylidene fluoride (PVDF), 0.22 μm, filters were obtained from Millipore Inc. (Billerica, MA, USA).

2.2.2. Methods

2.2.2.1. Inductively coupled plasma - mass spectrometry

Metal ion concentrations in the testing solutions were quantitated by an inductively coupled plasma-mass spectrometry (ICP-MS) method which utilized an Agilent 7500 CX ICP-

MS system equipped with an auto-sampler according to our published method [20]. The instrument was qualified, calibrated, and maintained regularly to ensure the system suitability. Prior to analyzing the samples at each time point, an external calibration curve for each element measured was revalidated. The same linear range as in previous work [20], 1–500 ppb for iron and 1–100 ppb for chromium and nickel, was maintained.

2.2.2.2. UV spectrophotometer for mAb concentration

The mAb concentrations in the formulations were determined using a Cary UV spectrophotometer coupled with a diode-array detector (Varian Inc., Lake Forest, CA, USA). The extinction coefficient of 1.43 (1 mg/mL at 280 nm) was determined by the Edelhoch method [22]. The system was calibrated and maintained regularly. Quartz cuvettes with a 1 cm path length were utilized. The formulations were gravimetrically diluted to 0.5 mg/mL using the corresponding placebo and then equilibrated to room temperature before testing. The corresponding placebo was used as the reference solution to zero the instrument. The absorptions for the formulations were measured at the fixed wavelength of 280 nm.

2.2.2.3. RP-HPLC analysis for chelator concentration

The concentrations of both Na_2EDTA and DTPA in the formulations were determined using an Agilent 1100 system coupled to a diode array detector [6, 20]. The system was calibrated and maintained regularly to ensure the system suitability. The method accuracy was evaluated by a spike recovery test. Prior to sample analysis, external calibration was reestablished with varying levels of Na_2EDTA and DPTA simultaneously. The separation was monitored by UV detection at 254 nm.

2.2.2.4. Experimental design

The experiment was designed by StatEase Design Expert® (v7.1.6) (Stat-Ease Inc., Minneapolis, MN, USA). In this study, six formulation factors of protein concentration, pH, anti-oxidation agent, metal chelator, metal chelator concentration, and surfactant concentration were investigated. In order to reduce the substantial resources needed for the full design of 2^6 (64) formulations, a fractional factorial design, $2^{(6-2)}$, of 16 formulations was adopted. This design is shown in Table 1. Five of the formulation factors (factors A–E) are continuous while factor F, chelator type, is a categorical factor. The design incorporated 16 boundary runs (F1–F16) along with seven additional formulations, five of which were center points (F17–F21), and the other two formulations (F22–F23) were controls not containing any protein while other components at center points. The drawback for this design is that there could be aliasing between the significant factors which would require additional knowledge or experiments to deconvolute as to which interaction is actually significant.

The formulations were prepared in 20 mM histidine buffer with 84 mg/mL α,α-trehalose dihydrate, except the formulations F20 and 21, which were included to explore the effect of sugar. The mAb concentration ranged from 5.0 to 20.0 mg/mL with 12.5 mg/mL as center point. These concentrations were confirmed by UV absorption at 280 nm. The formulation pH was controlled at 5.5–6.5 (due to consideration of protein stability) with the center point at pH 6.0, and these were confirmed by a pH meter at ambient room temperature. The concentrations of methionine ranged from 0.0 to 0.1 mg/mL with 0.05 mg/mL as the center point. The surfactant (polysorbate 80) concentration ranged from 0.0 to 0.2 mg/mL with the center point of 0.1 mg/mL. The metal chelator concentration ranged from 0.0 to 0.1 mg/mL with 0.05 mg/mL as the center point, as confirmed by RP-HPLC. The chelator was either Na_2EDTA or DTPA. At a pH

of 5.5–6.5, DTPA (H_5A) exists in equilibrium between H_2A^{3-} and H_3A^{2-} [23]. For simplicity, from here on, the term DTPA is used regardless of its ionization form.

The formulations were sterile filtered through a 0.22 μm PVDF filter. Aliquots of 5 mL were filled into 10 mL autoclaved glass vials containing stainless steel coupons as the samples accompanied by the vials containing no coupons as negative controls. The vials were sealed with the autoclaved stoppers and placed upright in stability chambers maintained at −40°C over 6 months, as well as 2–8°C and 25°C over 3 months. During storage, the testing solutions were not allowed to come into contact with the stoppers eliminating the potential leachables from the stoppers confounding the study.

ICP-MS was performed on each formulation sample at the initial time point and 3 months for the storage temperature of 2–8°C and 25°C, and at both 3 and 6 months for storage temperature of −40°C to explore the impact of the formulation components on metal leachables from 316L stainless steel.

2.3. Results and Discussion

The amount of metal ions leaching into biological products is dependent on many variables, such as formulation components, solution pH, contact materials, drug substance/drug product contact surface area with stainless steel, surface area processing procedure, contact duration and temperature, etc. The leaching capacity of individual biotherapeutic formulation factor, commonly utilized histidine/HCl, histidine/acetate, succinate, acetate and citrate buffers, the relationship of the solution volume and contact surface area of 1–5 mL/cm^2, metal chelator Na_2EDTA vs. DTPA at the concentration of 0.0–0.1 mg/mL, solution pH 5.0–9.0, on metal leachables from 316L stainless steel was studied, respectively [20]. In this paper, the focus was to investigate the effect of each formulation component in the presence of others, as described in

Table 1, on metal leachables from 316L stainless steel. All stainless steel coupons used in this study were made from the same sheet of stainless steel to ensure consistency of the material. The 316L stainless steel was made in the USA (US: S31603), composed of 62–72% iron, 16–18.5% chromium, and 10–14% nickel, along with a trace amount of carbon, magnesium, manganese, silicon, nitrogen, phosphate, and sulfur [24]. Three major components, iron, chromium, and nickel in the testing solutions were quantified by ICP-MS to evaluate the amounts of metal ions introduced into the product. The other elements such as magnesium, manganese, silicon, phosphate, and sulfur were not monitored in this study because our feasibility study suggested that the amount of these leached into solution was several order of magnitudes lower than that of three major elements (iron, chromium, and nickel). Silicon can also arise from packaging such as stoppers in greater amounts than via leaching from stainless steel containers and was thus not monitored.

At each time point, both the sample vial (containing the stainless steel coupon) and its negative control (containing no stainless steel coupon) were pulled for metal ion determination. Prior to ICP-MS analysis, the samples were equilibrated to ambient room temperature by storing them in the laminar airflow hood overnight at ambient room temperature. In order to eliminate the interference of any metals possibly introduced from the glass and raw materials [25], each measured metal ion concentration in the testing solution was corrected by subtracting the amount detected in the negative control. All the samples were tested in triplicate and the relative standard deviation was within 0.5%, thus the average was utilized here.

Analysis of variance was used to explore the impact of the experimental factors on the metal ions. For each of the tested metals at their individual storage temperatures, a mathematical model was fitted to the experimental data. Formulation factors not included in the predictive

equations were either not statistically significant or were concluded to be of far lesser importance than the included factors. The relative impact of the statistically significant factors over the range tested can be assessed by the magnitude and sign of their coefficients. The magnitude is the indication of their relative impact and the sign is the indication of the impact direction relative to that of variables. A positive sign indicates that the impact changed in the same direction as the change of the variables and the negative sign indicated the opposite trend.

The equation provides a quantitative prediction tool in assessing metal amounts of the untested formulations given the formulation components are within the specified testing ranges. The visual representations as well as the coefficients make it easy to compare the relative impact of the significant factors within the ranges tested. Given the need for higher protein concentration formulations and longer storage time, caution must be taken in applying the prediction model to the formulations outside of the tested ranges since the models may no longer hold true. In each data analysis, adjusted R^2 and root mean square error (RMSE) are also provided. The adjusted R^2 is used to indicate the percentage of the total variation in the data explained by the model, adjusted for the number of terms in the model. The closer the adjusted R^2 is to 1.00, the better the model fits the experimental data. The RMSE is calculated from the difference between the experimental and predicted values (residuals). This number can be interpreted as the standard deviation of the residuals. For most of the models, we would expect about 95% of the observed values to lie within ±2 times the RMSE of the predicted values. The data on each storage condition are addressed individually.

2.3.1. Six months storage at -40^{o}C

Over 6 months in contact with the coupons at −40°C, iron ions leaching into the testing solutions ranged from 3 to 276 ppb with a mean value of 49 ppb. Chromium ions ranged from

below limit of quantitation to 17 ppb with a mean value of 5 ppb, while nickel ions increased from below limit of quantitation to 13 ppb with a mean value of 5 ppb. As expected, iron ions are the most abundant leachates among the three monitored metal ions, consistent with our previous findings [20].

A natural logarithmic transformation was applied to the data for iron, chromium, and nickel leachates as these data at 6 months were significantly higher and more variable compared to those at the initial time point. The prediction equations with the adjusted R^2 and RMSE (in natural logarithmic scale) for all three leachates are provided in Table 2. The adjusted R^2, 70% with RMSE of 0.57% for iron leachates, 73% with RMSE of 0.45% for chromium, and 90% with RMSE of 0.35% for nickel, suggest that the models fit the experimental data reasonably well. The factors included in the models are only the statistically significant factors: metal chelator concentration, protein concentration, and contact time for iron leachates while protein concentration and contact time for chromium and nickel leachates. Other formulation factors, namely solution pH, the presence of methionine and polysorbate 80, and the metal chelator type (for iron leachates), or metal chelator concentration (for chromium and nickel) leachates, are not statistically significant. The coefficients of each significant factor for iron, chromium, and nickel leachates are positive, indicating that the amount of all three metal leachates increased accordingly with the increased amount of the significant factors. The impact of respective response surface plots: Fig. 1a, b for iron leachates, Fig. 1c for chromium, and Fig. 1d for nickel. Because no curvature and no interactions are observed among the significant factors, the models for all three metal leachates are additive. Consequently, the relative impact of the individual significant factor can be compared quantitatively over the range studied.

For iron leachates, the impact (per unit) of metal chelator is 19-fold of that of contact time and 91-fold of that of protein concentration within all ranges tested. The overall impact of contact time was about twice as much as that of protein concentration and three times of that of metal chelator concentration as shown in Fig. 1a, b. Note these magnitudes are relative to ranges tested. Fig. 1a shows the impact of contact time and protein concentration in the formulations without any chelating agent while Fig. 1b shows the effects in the formulations with 0.1 mg/mL metal chelator. The highest levels would be predicted at 6 months, for the highest protein concentration tested (20 mg/mL) and the highest chelator concentration (0.1 mg/mL). This is represented by the elevation of the surface towards the back on the right side in Fig. 1b.

For chromium leachates, the impact of contact time is three times of that of protein concentration in per unit term within the ranges tested. However, over the tested ranges, the overall impact of contact time is approximately equal to that of the protein concentration as shown in Fig. 1c. The highest amounts of chromium leachates would be predicted for 6 months in formulations containing 20 mg/mL protein, as represented by the elevated surfaces towards the back on the right side in Fig. 1c.

As with iron and chromium, the impact on leached nickel by contact duration of the solution with stainless steel is thirteen times as much as that by protein concentration in per unit terms. In relative terms, the overall impact of contact time is about five times as high as that of protein over the ranges tested as shown in the response surface plot displayed in Fig. 1d. The highest amount of nickel leachates occurred in formulations containing the highest concentration of protein (20 mg/mL) over 6 months contact with stainless steel, represented by the elevated surface towards the back on the right side in Fig. 1d.

Compared to the iron leachates in the solutions, the concentrations of chromium and nickel were significantly lower, by about 1 order of magnitude. Considering all three metals, potentially migrating from stainless steel into the drug substance and/or product from the contact stainless steel, we see that contact time and protein concentration, as well as metal chelator concentration for iron leachates are the statistically significant factors. Their contribution to the total amount of metal leachates in the final products depends on the formulation compositions and contact duration. Ranked by the contribution per unit, milligram per milliliter for concentration and months for contact time, metal chelator concentration is the most significant factor, followed by contact time and protein concentration for leaching iron, while contact time followed by protein concentration is the most significant parameter for chromium and nickel leachates.

2.3.2. Three months storage at 2-8^{o}C

The iron leachates ranged from 3 to 229 ppb with a mean of 69 ppb. The chromium ion leachates increased from below limit of quantitation to 17 ppb with a mean of 5 ppb and nickel increased from below limit of quantitation to 23 ppb with a mean of 5 ppb. The overall levels of all three metal leachates are higher than those at −40°C. As stated previously, due to higher and more variable values at the 3 months compared to initial time point, a natural logarithmic transformation was utilized for the data analysis.

The prediction equations with the adjusted R^2 and RMSE (in the natural logarithmic scale) for all three leachates at 2–8°C are also listed in Table 2. The adjusted R^2, 82% with RMSE of 0.51% for iron leachates, 77% with RMSE of 0.42% for chromium, and 94% with RMSE of 0.31% for nickel are better than those observed at −40°C. The enhanced-adjusted R^2 and RMSE suggest that the models fit experimental data very well. As discussed previously, only

the statistically significant factors are included in the models. Other formulation factors are not statistically significant. The models for all three metal leachates of iron, chromium, and nickel are additive and the combined impacts of significant factors on metal leachates are presented in the response surface plots: Fig. 2a, b for iron leachates, Fig. 2c for chromium, and Fig. 2d for nickel.

As shown for the analysis of storage at −40°C, the significant effects for the three metal leachates at 2–8°C also arise from protein concentration and contact time, and includes metal chelator concentration for iron leachates. All three have positive coefficients: metal leachates increase as any of these factors and/or the combination thereof increases.

For iron leachates, as shown in Fig. 2a and b, the impact coefficient (per unit) of metal chelator concentration is about 110-fold of that of protein concentration and 9-fold of contact time. Over the ranges tested, the relative contributions for leaching iron decrease in the following order: contact time was about 2.5 times of that of protein concentration, and 3 times of that of chelator concentration. This is the same trend as observed for −40°C storage except that the magnitudes are higher. The highest amounts of ion leachates occurred in the formulation containing 20 mg/mL protein and 0.1 mg/mL metal chelator over 3 months contact with the stainless steel, as indicated by the elevation of the surface towards the back on the right side in Fig. 2b (note that Fig. 2a shows the impact of time and protein concentration in formulations containing no metal chelator while 2b shows the same effect in formulations with 0.1 mg/mL metal chelator.)

For chromium leachates, as shown in Fig. 2c, the impact (per unit) of contact time was about 7-fold that of protein concentration. Within the tested ranges, the overall impact of the contact time is 1.3 times that of protein concentration. The highest levels occurred at 3 months in

the formulations containing 20 mg/mL protein, represented by the elevation of the surface towards the back on the right side in Fig. 2c.

For nickel leachates, the contribution of the contact duration (per month) of the solution with stainless steel is about 20-fold that of protein concentration (per milligram/per milliliter). Within the tested ranges, the overall impact of contact time is about 4 times of that of protein concentration as shown in the response surface plot in Fig. 2d. The formulation containing 20 mg/mL protein stored over 3 months exhibited the highest levels of nickel leachates, represented by the elevation of the surface towards the back on the right side in Fig. 2d.

Similar to the results at −40°C, iron leaching occurs to a much higher extent than the leaching of chromium and nickel. In the parameter ranges studied, the impact coefficient (impact per unit) indicated that metal chelator concentration showed the most significant contribution for the leaching of iron from stainless steel, followed by contact time and then protein concentration, while contact time followed by protein concentration was most important for chromium and nickel leachates.

2.3.3. Three months storage at 25°C

As expected, iron ion leaching increased much more at 25°C compared to that at −40°C or 2–8°C. The iron leachates ranged from 3 to 550 ppb with a mean of 165 ppb, almost twice the amount of iron leachates at −40°C and 2–8°C. The chromium leachates increased from below the limit of quantitation to 27 ppb with a mean of 8 ppb, and nickel increased from below the limit of quantitation to 23 ppb with a mean of 8 ppb, a slight increase compared to the data at −40°C and 2–8°C. A natural logarithmic transformation was utilized for data analysis. The prediction equations along their R^2 and RMSE (in natural logarithmic scale) at 25°C are presented in Table 2. The R^2, 96% with RMSE of 0.34% for iron leachates, 95% with RMSE of 0.28% for

chromium, and 98% with RMSE of 0.22% for nickel suggest that the models fit experimental data with high accuracy.

As discussed previously, only the statistically significant factors are included in the models. Even though protein concentration, metal chelator concentration, and contact time of the tested solutions with the stainless steel are still the only three statistically significant factors within the testing parameter ranges, interactions between contact time and protein concentration, and metal chelator concentration are observed for all three metal leachates. The interactions greatly increased the prediction model complexity because of the inherent inadequacy due to the partial factorial design of $2^{(6-2)}$ (16 formulations) instead of the full factorial design of 2^6 (64 formulations). This partial DOE design was adopted to balance the required resources and the benefit. In this design, the individual contribution of the interacting factors cannot be separated from the combined effect as the interactions are present. In order to mathematically quantify the dependency of one factor on another, a more thorough investigation is needed which is outside the scope of the work reported here. Therefore, in our data analysis, the interactions of the contact time with the protein concentration, and metal chelator concentration do not allow ranking of the relative contribution of the three major factors affecting three metal ion leachates.

For iron leachates, protein concentration, metal chelator concentration, and contact time are the three statistically significant factors and their individual impact coefficients are positive. However, interactions between metal chelator concentration and contact time, and between protein concentration and contact time are also observed. The combined effect of metal chelator concentration and contact time enhanced metal ion leaching, comparable to their individual effects. Thus, the overall effect of increased metal chelator concentration was to increase metal iron leachates in the solution, as shown in Fig. 3a and b. In contrast, the interaction between

protein concentration and contact was opposite to the direction of their individual impact so that it is hard to quantify the individual final impact. However, the overall contribution of each parameter is qualitatively presented in Fig. 3a and b. The overall consequences of contact time were to increase metal ion leachates over the increased contact duration while no significant impact from protein concentration was observed. Despite the complexity of the interactions in the models, the overall impact of metal chelator concentration is more significant than that of contact time and protein concentration, that is, the amount of iron ion leachates increased much more dramatically in the formulations containing 0.1 mg/mL metal chelator (Fig. 3b) than the formulations containing no metal chelator (Fig. 3a). The highest amounts of iron leachates occurred in the formulations containing 5 mg/mL protein (lowest studied level) and 0.1 mg/mL metal chelator (the highest studied levels) over 3 months, represented by the elevation of the surface towards the front on the right side in Fig. 3b.

For chromium leachates, the model shown in Table 2 suggests that within the tested parameter ranges, besides protein concentration, metal chelator concentration and contact time as the significant factors, solution pH also played an important role. The lower pH of 5.5 increased chromium leaching more than pH 6.5. The interactions of contact time with protein concentration and with metal chelator concentration make it infeasible to quantify the individual contributions of protein concentration, metal chelator concentration, and contact time. However, over the tested ranges, an increased contact time and metal chelator concentration increased chromium leachates as shown in Fig. 3c–f. As a consequence of the combined effects, the amount of chromium leachates increased most significantly in the formulations at pH 5.5 (lowest tested pH) containing 0.1mg/mL metal chelators (highest tested level), as shown in Fig. 3f. This indicates that a decrease of pH and an increase in metal chelator concentration increase the

capacity of the formulation for leaching chromium from stainless steel. The highest amount of chromium leachates occurred in the formulations at pH 5.5 containing the lowest protein concentration of 5 mg/mL protein, and 0.1 mg/mL metal chelator over 3 months, represented by the elevation of the surface towards the front on the right side in Fig. 3f, the worst case scenario. The chromium leaching pattern observed at 25°C is dramatically different from that observed at lower storage temperatures of −40°C and 2–8°C.

For nickel ion leachates, protein concentration, metal chelator concentration, and contact time are still the three statistically most significant factors. As for iron and chromium leachates, the complicated interactions between the contact time and protein concentration, and the interaction with metal chelator concentration make it infeasible to quantify each individual impact. However, the overall impact of the significant factors as exhibited in Fig. 3g and h, the increased contact duration and metal chelator concentration increased nickel leachates in the formulations. The nickel leachates changed more significantly in the formulations containing 0.1 mg/mL metal chelators as shown in Fig. 3h which indicates that the metal chelator plays an important role. The highest amount of nickel leachates occurred in the formulations containing the lowest protein concentration of 5 mg/mL protein, and highest metal chelator concentration of 0.1 mg/mL over 3 months, represented by the elevation of the surface towards the front on right side in Fig. 3h. Analogous to the data for chromium leachates, the observed nickel leaching pattern from stainless steel at 25°C is also dramatically different from that observed for lower storage temperatures of −40°C and 2–8°C.

Compared to the leaching patterns of iron, chromium, and nickel at −40°C and 2–8°C, more complex metal leaching patterns were observed at 25°C, which indicates that temperature plays an important role. Regardless of the interactions, under the three tested storage conditions,

metal chelator concentration, protein concentration, and contact time are the three major statistically significant factors for leaching iron, chromium, and nickel from stainless steel. The statistically significant and insignificant formulation components affecting metal ion leachates at storage temperature of −40°C, 2–8°C, and 25°C are summarized in Table 3.

Protein concentration ranges vary widely in biopharmaceutical products. Our observation that protein concentration controls the capacity for metal leaching from stainless steel is consistent with previous findings [26–28]. It was reported that the presence of proteins had a significant impact on the passivation behavior of the metals and alloys [26–28]. Acting as complexing agents for dissolved metal ions, the protein stimulated the dissolution rate of a base metal in a structure-dependent manner, and, consequently, suppressed the formation of the protective oxide layer [27]. Brown and Merritt reported that the presence of protein produced pitting corrosion on the surface of stainless steel [26]. The same phenomenon was also observed by us during protein drug product storage in 316L stainless steel minitanks. Woodman demonstrated that in the presence of protein, the leached nickel and chromium predominately formed metallo-organic complexes with the protein [28]. In addition, serum protein in vivo and in vitro fluids also showed a significant capacity at increasing cobalt, chromium and nickel leaching from 316L stainless steel [28] and the leaching pattern was quantitatively fitted into a mathematical model.

In approved biotherapeutic drug products, metal chelators such as Na_2EDTA and DTPA are present at relatively low concentrations. EDTA was reported to facilitate metal leaching from contact stainless steel into solution [20, 27], consistent with the present study. However, our observation of no significant difference between Na_2EDTA and DTPA is different from previous observations when the leaching capacity was investigated only in 20 mM histidine buffer [20].

The impact of contact time was reported to play a significant role in leaching metal ions from stainless steel when the impact of individual component of buffer species, and metal chelator in 20 mM histidine was investigated [20], a similar phenomenon as observed in this study.

We note here that this study was performed with histidine buffer which is commonly used in biotherapeutics drug products. Histidine buffer has a significant temperature coefficient (~0.022 K^{-1}) such that formulations prepared at ambient room temperature (~25°C) will experience a pH approximately 0.4 units higher at 2–8°C [29]. Thus samples at 2–8°C actually underwent leaching at a slightly higher pH than stated. However, this represents exactly the situation that would occur in practice.

In the current competitive market, the need for high concentration biotherapeutic drug products has increased dramatically to improve dosing and storage convenience. A protein concentration of 100 mg/mL and higher has been seen in some approved biotherapeutic products. In most cases, protein concentration in drug substance has to be even higher than the finished drug product due to the dilution effect of excipients which must be added afterwards. Also, the storage duration of the drug substance can be over 24 months. Therefore, the overall impact of protein concentration, metal chelator concentration, and contact time needs to be carefully evaluated with respect to the formulation composition and the storage duration. We expect that if different ranges of the factors had been studied, the relative magnitudes of impact would not be the same. However, it can be generally expected that the presence of metal chelators and long contact time at higher temperatures will always contribute to more leaching of metal ions.

2.4. Conclusions

Biotherapeutic formulation factors of protein concentration, metal chelator concentration/type, solution pH, the presence of methionine and surfactant of polysorbate 80, and contact time were studied for their capacity to promote metal leaching from contact stainless steel in a defined formulation matrix. Among them, metal chelator concentration, protein concentration, and contact time are the three statistically most significant parameters affecting metal leaching from the contact with 316L stainless steel at storage temperatures of −40°C, 2–8°C, and 25°C. Furthermore, temperature is an important factor affecting metal leaching pattern. Increased temperature dramatically increased metal leaching amount, probably simply because of higher mobility of ions and reduced viscosity of the disaccharide solutions. The higher mobility enables leached ions to be transported away from the metal surface and thus maintains a higher driving force for leaching compared to that at lower temperatures. Regardless of the interactions among factors, increased metal chelator concentration and contact duration enhanced metal leaching into the solution for all three tested conditions. However, the complexity caused by the interactions makes the impact of protein concentration more complicated at storage temperature of 25°C. At −40°C and 2–8°C, the increased protein concentration increased the metal leachates. Within the tested pH range of 5.5–6.5, solution pH played a minor role for facilitating chromium leaching from stainless steel into the product only at 25°C. No statistically significant impact is observed for anti-oxidant (methionine) and the surfactant (polysorbate 80). During biotherapeutic product development, each formulation component, and potential storage duration and temperature must be carefully evaluated for its impact to reduce the risk, consequently, to optimize the biotherapeutics formulation to achieve the target drug product shelf life with acceptable quality.

2.5. Acknowledgments

The 316L stainless steel coupons utilized in this study were supplied by CSI Design (Springfield, MO, USA).We gratefully acknowledge Bo Zhang for his help in analyzing the samples.

2.6. References

1. Carpenter, J.F., et al., *Rational design of stable lyophilized protein formulations: some practical advice.* Pharm Res, 1997. **14**(8): p. 969-75.
2. Daugherty, A.L., et al., *Formulation and delivery issues for monoclonal antibody therapeutics.* Adv Drug Deliv Rev, 2006. **58**(5-6): p. 686-706.
3. Parkins, D.A., et al., *The formulation of biopharmaceutical products.* Pharm Sci Technolo Today, 2000. **3**(4): p. 129-137.
4. Wang, W., et al., *Antibody structure, instability, and formulation.* J Pharm Sci, 2007. **96**(1): p. 1-26.
5. Rowe, R., et al.,. *Handbook of Pharmaceutical Excipients*. 4th ed. 2003, Phamaceutical press: Chicago. 225-228.
6. Zhou, S., et al., *Comparative evaluation of disodium edetate and diethylenetriaminepentaacetic acid as iron chelators to prevent metal-catalyzed destabilization of a therapeutic monoclonal antibody.* J Pharm Sci, 2010. **99**(10): p. 4239-50.
7. Allain, L., et al., *Impact of package leachables on the stability of pharmaceutical products.* American Pharmaceutical Review, 2007. **10**(4): p. 38, 40, 42-44.
8. Bee, J.S., et al., *Precipitation of a monoclonal antibody by soluble tungsten.* J Pharm Sci, 2009. **98**(9): p. 3290-301.

9. Markovic, I., *Challenges associated with extractables and/or leachables substances in therapeutic biologic protein products.* American Pharmaceutical Review, 2006. **9**(6): p. 20-27.

10. Cleland, J.L., et al., *The development of stable protein formulations: a close look at protein aggregation, deamidation, and oxidation.* Crit Rev Ther Drug Carrier Syst, 1993. **10**(4): p. 307-77.

11. Stadtman, E.R., *Metal ion-catalyzed oxidation of proteins: biochemical mechanism and biological consequences.* Free Radic Biol Med, 1990. **9**(4): p. 315-25.

12. Li, S., et al., *Aggregation and precipitation of human relaxin induced by metal-catalyzed oxidation.* Biochemistry, 1995. **34**(17): p. 5762-72.

13. Marx, G., et al., *Site-specific modification of albumin by free radicals. Reaction with copper(II) and ascorbate.* Biochem J, 1986. **236**(2): p. 397-400.

14. Uchida, K., et al., *Identification of oxidized histidine generated at the active site of Cu,Zn-superoxide dismutase exposed to H2O2. Selective generation of 2-oxo-histidine at the histidine 118.* J Biol Chem, 1994. **269**(4): p. 2405-10.

15. Uversky, V.N., et al., *Metal-triggered structural transformations, aggregation, and fibrillation of human alpha-synuclein. A possible molecular link between Parkinson's disease and heavy metal exposure.* J Biol Chem, 2001. **276**(47): p. 44284-96.

16. Golub, E.S., et al., *The nature of antigens. In: Immunology, A Synthesis*. 2nd ed. 1992, Sinauer Associates, Sunderlandm, MA. 21-41.

17. *International conference on harmonization of technical requirements for registration of pharmaceuticals for human use (ICH). Guideline for industry: impurities in new drug substances, ICH Q3A, Q3B and Q6A.*

18. *CDER Guidance Document: container closure systems for packaging human drugs and biologics.* 1999.

19. EMEA, *Harmonized guideline (EMEA and health Canada) on the pharmaceutical quality of inhalation and nasal products.* 2005.

20. Zhou, S., et al., *Biologics formulation factors affecting metal leachables from stainless steel.* AAPS PharmSciTech, 2011. **12**(1): p. 411-21.

21. Pace, C.N., et al., *How to measure and predict the molar absorption coefficient of a protein.* Protein Sci, 1995. **4**(11): p. 2411-23.

22. Vandegaer, et al., *Iron chelates of diethylenetriaminepentaacetic acid.* J. Inorg. Nucl. Chem., 1959. **11**: p. 210-221.

23. *316/316L stainless steel product data sheet.* www.aksteel.com, 2007.

24. Waterman, K.C., et al., *Stabilization of pharmaceuticals to oxidative degradation.* Pharm Dev Technol, 2002. **7**(1): p. 1-32.

25. Brown, S.A., et al., *Electrochemical corrosion in saline and serum.* Journal of Biomedical Materials Research, 1980. **14**(2): p. 173-175.

26. Kocijan, A., et al., *The influence of complexing agent and proteins on the corrosion of stainless steels and their metal components.* J Mater Sci Mater Med, 2003. **14**(1): p. 69-77.

27. Woodman, J.L., et al., *Isolation of serum protein organometallic corrosion products from 316L SS and HS-21 in vitro and in vivo.* J Biomed Mater Res, 1984. **18**(1): p. 99-114.

Table 1. Biotherapeutic formulation components studied to explore their capacity in leaching metal ions from 316L stainless steel

Formulation ID	A	B	C	D	E	F	Comment: Sugar
	mAb Conc. (mg/mL)	pH	Chelate Conc. (mg/mL)	Methionine Conc. (mg/mL)	Polysorbate 80 (mg/mL)	Chelator type	
F1	5.0	5.5	0.0	0.0	0.0	DTPA	Trehalose
F2	5.0	5.5	0.0	0.1	0.0	Na_2EDTA	Trehalose
F3	20.0	5.5	0.0	0.1	0.2	Na_2EDTA	Trehalose
F4	20.0	5.5	0.0	0.0	0.2	DTPA	Trehalose
F5	20.0	5.5	0.1	0.0	0.0	Na_2EDTA	Trehalose
F6	20.0	5.5	0.1	0.1	0.0	DTPA	Trehalose
F7	5.0	5.5	0.1	0.1	0.2	DTPA	Trehalose
F8	5.0	5.5	0.1	0.0	0.2	Na_2EDTA	Trehalose
F9	20.0	6.5	0.0	0.1	0.0	DTPA	Trehalose
F10	20.0	6.5	0.0	0.0	0.0	Na_2EDTA	Trehalose
F11	5.0	6.5	0.0	0.1	0.2	DTPA	Trehalose
F12	5.0	6.5	0.0	0.0	0.2	Na_2EDTA	Trehalose
F13	5.0	6.5	0.1	0.1	0.0	Na_2EDTA	Trehalose
F14	5.0	6.5	0.1	0.0	0.0	DTPA	Trehalose
F15	20.0	6.5	0.1	0.0	0.2	DTPA	Trehalose
F16	20.0	6.5	0.1	0.1	0.2	Na_2EDTA	Trehalose
F17	12.5	6.0	0.0	0.05	0.1	Na_2EDTA	Trehalose
F18	12.5	6.0	0.05	0.05	0.1	DTPA	Trehalose
F19	12.5	6.0	0.05	0.05	0.1	Na_2EDTA	Trehalose
F20	12.5	6.0	0.05	0.05	0.1	DTPA	None
F21	12.5	6.0	0.05	0.05	0.1	Na_2EDTA	None
F22	0.0	6.0	0.05	0.05	0.1	DTPA	Trehalose
F23	0.0	6.0	0.05	0.05	0.1	Na_2EDTA	Trehalose

Table 2. Three metal ions of iron, chromium and nickel leaching prediction model along with adjusted R-squared (R^2) and root mean square error (RMSE) in natural logarithmic scale

Storage Temperature (^oC)	Metal leachates	Prediction Models	Adjusted R^2 (%)	RMSE (%)
-40^{o}C	Iron	Ln (Fe) = 1.827 + 0.0525 * [protein conc.] + 4.812 * [metal chelator conc.] + 0.251 * contact time	70	0.57
	Chromium	Ln (Cr) = -0.0825 + 0.0628 * [protein conc.] + 0.195 * contact time	73	0.45
	Nickel	Ln (Ni) = -0.364 + 0.0262 * [protein conc.] + 0.353 * contact time	90	0.35
2-8^{o}C	Iron	Ln (Fe) = 1.754 + 0.0539 * [protein conc.]+ 5.998 * [metal chelator conc.] + 0.657 * contact time	82	0.51
	Chromium	Ln (Cr) = -0.0746 + 0.0621 * [protein conc.] + 0.410 * contact time	77	0.42
	Nickel	Ln (Ni) = -0.493 + 0.0374 * [protein conc.] + 0.755 * contact time	94	0.31
25^{o}C	Iron	Ln (Fe) = 1.476 + 0.0906 * [protein conc.] + 3.035* [metal chelator conc.] + 1.164 * contact time - 0.0327 * contact time *[protein conc.] + 3.553 * [metal chelator conc.]* contact time	96	0.34
	Chromium	Ln (Cr) = 2.098 + 0.0887 * [protein conc.] – 0.404 * pH - 1.031 * [chelator conc.] + 0.901 * contact time – 0.0306 * [protein] * contact time + 3.064 * [chelator conc.] * contact time	95	0.28
	Nickel	Ln (Ni) = -0.721+ 0.0601 * [protein conc.] - 0.649 * [chelator conc.] + 1.106 * contact time – 0.0217 * [protein conc.] * contact time + 1.170 * [chelator conc.] * contact time	98	0.22

Note:

1) Unit for protein and metal chelator concentration: mg/mL;
2) Unit for contact time: month

Table 3. Summary presentation of statistically significant and insignificant factors impacting metal leachability at storage temperatures of -40°C, 2-8°C and 25°C

Storage Temperature (°C)	Leachables	Significant factors	Insignificant factors
-40°C	Iron	Protein conc., metal chelator conc. and contact time	pH, metal chelator type, anti-oxidant and surfactant
	Chromium	Protein conc. and contact time	pH, metal chelator conc. /type, anti-oxidant and surfactant
	Nickel		
2-8°C	Iron	Protein conc., metal chelator conc. and contact time	pH, metal chelator type, anti-oxidant and surfactant
	Chromium	Protein conc. and contact time	pH, metal chelator conc. /type, anti-oxidant and surfactant
	Nickel		
25°C	Iron	Protein conc., metal chelator conc. and contact time	pH, metal chelator type, anti-oxidant and surfactant
	Chromium	Protein conc., metal chelator conc., contact time and pH	Metal chelator type, anti-oxidant and surfactant
	Nickel	Protein conc., metal chelator conc. and contact time	Metal chelator type, pH, anti-oxidant and surfactant

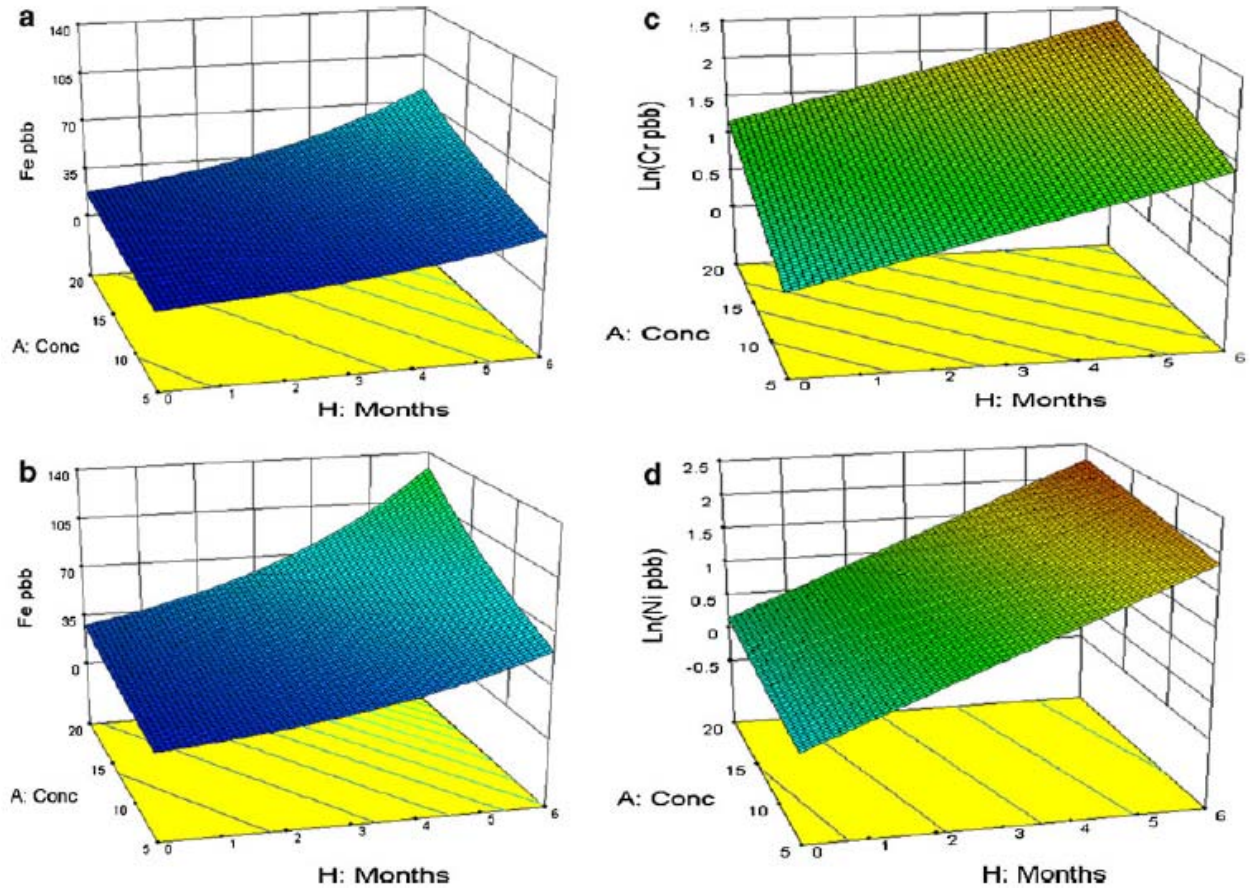

Fig. 1. The impact of the statistically significant formulation factors on metal ion leachates from stainless steel at the storage temperature of −40°C (a and b the impact on iron ion leachates: a for the formulations containing no metal chelator and b for the formulations containing 0.1 mg/mL metal chelator; c for the impact on chromium ion leachates in natural logarithmic scale and d for the impact on nickel ion leachates in natural logarithmic scale)

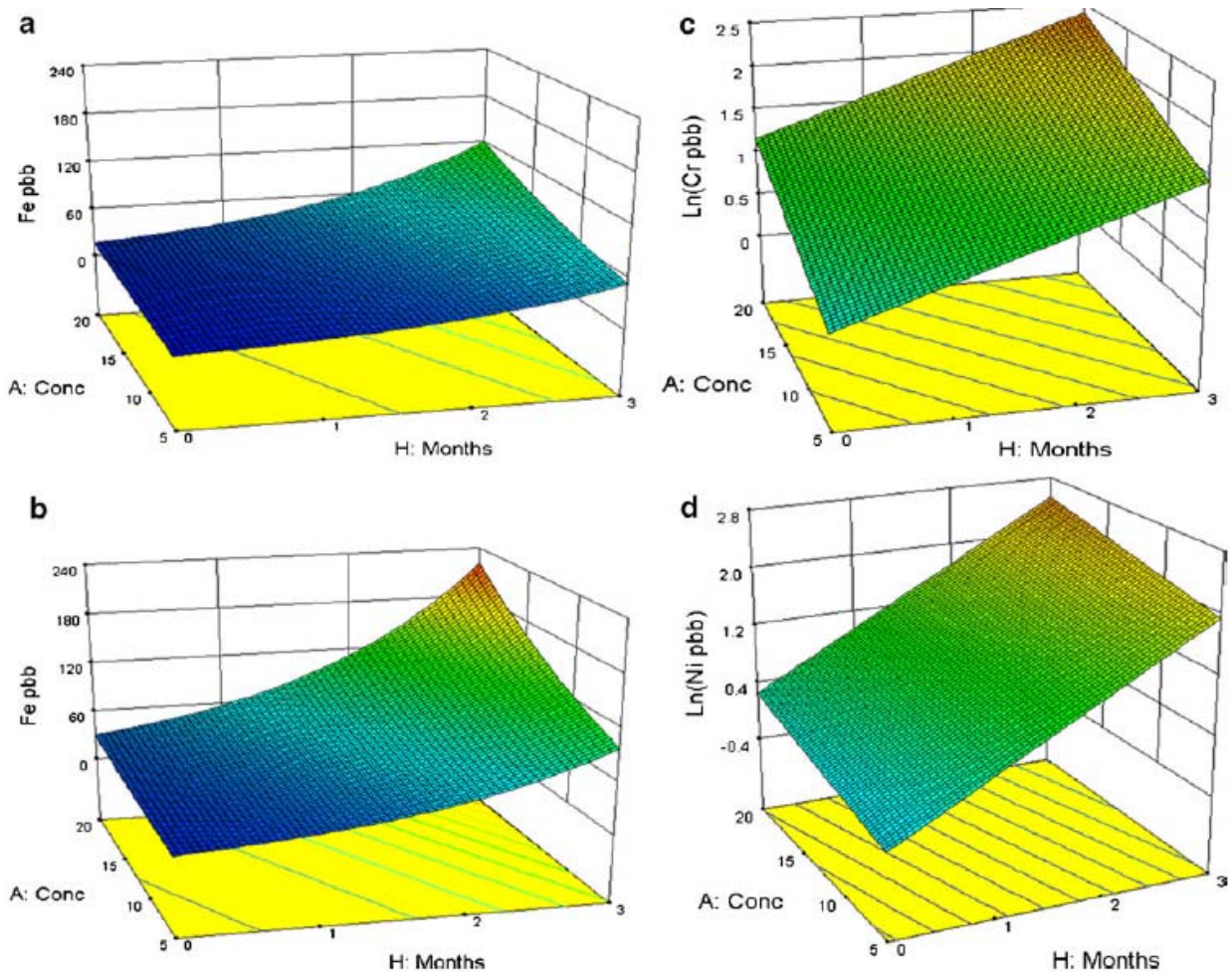

Fig. 2. The impact of the statistically significant formulation factors on metal ion leachates from stainless steel at the storage temperature of 2–8°C (a and b the impact on iron ion leachates: a for the formulations containing no metal chelator and b for the formulations containing 0.1 mg/mL metal chelator; c for the impact on chromium ion leachates in natural logarithmic scale; and d for the impact on nickel ion leachates in natural logarithmic scale)

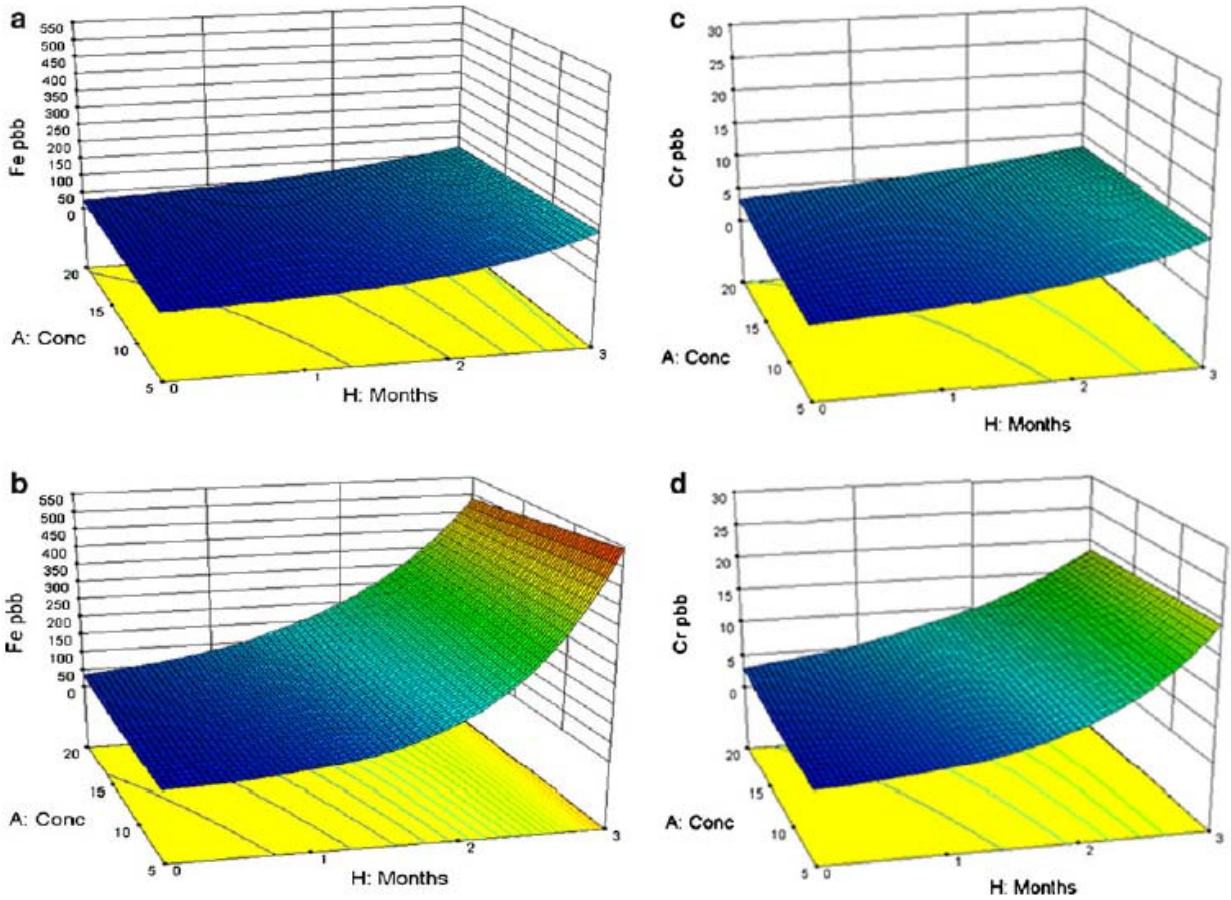

Fig. 3. The impact of the statistically significant formulation factors on metal ion leachates from stainless steel at the storage temperature of 25°C (a and b the impact on iron leachates: a for the formulations containing no metal chelator and b for the formulations containing 0.1 mg/mL metal chelator; c–f the impact on chromium ion leachates: c for the formulations at pH 6.5 containing no metal chelator, d for the formulations at pH 6.5 containing 0.1 mg/mL metal chelator, e for the formulations at pH 5.5 containing no metal chelator, and f for the formulations at pH 5.5 containing 0.1 mg/mL metal chelator; g and h the impact on nickel ion leachates: g for the formulations containing no metal chelator and h for the formulations containing 0.1 mg/mL metal chelator)

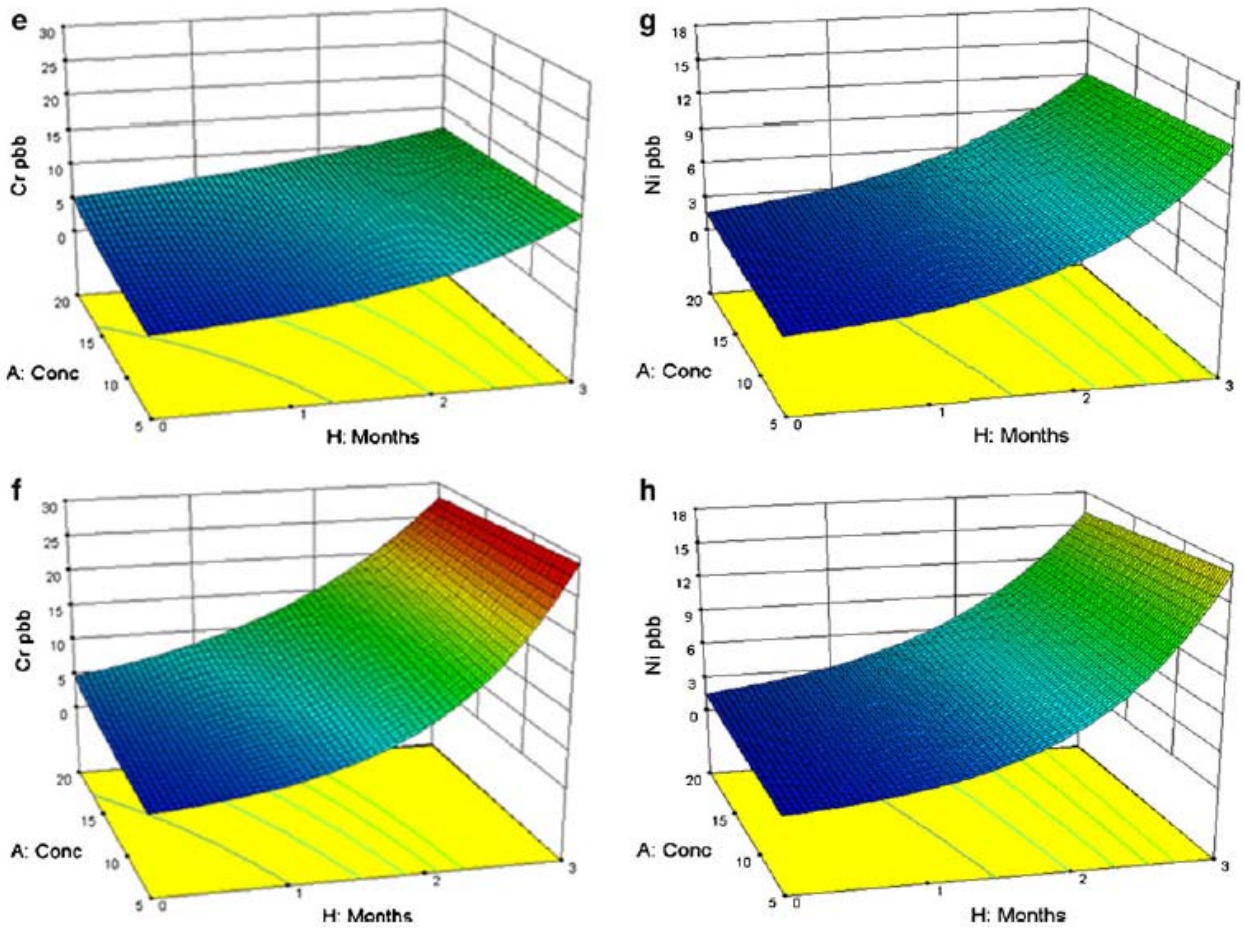

Fig. 3. continued

Chapter 3: Chemical instability of IgG1 induced by metal-catalyzed oxidation: fluorogenic tagging methodology applied to characterize oxidized tyrosine and phenylalanine in an immunoglobulin monoclonal antibody

Table of Contents

3.1 Introduction

Immunoglobulin G (IgG) monoclonal antibodies (mAbs) represent a rapidly growing biotherapeutic class in the biopharmaceutical industry for the treatment and prevention of diseases by recognizing and eliminating pathogenic antigens [1-3]. Compared to small-molecule drugs, mAbs are highly specific, reducing potential side effects. On the other side, mAbs exhibit significantly lower stability due to the strong dependence of their physical-chemical properties on conformation. Oxidation represents a prominent degradation pathway of proteins [4-11], potentially changing potency or causing other undesired pharmaceutical consequences.

The detection and identification of oxidized proteins has been an analytical challenge due to their potentially low abundance and structural complexity. With high demands for the development of biotherapeutic products, the need for an efficient and sensitive analytical tool to detect and identify oxidative protein modification(s) is becoming imperative.

Currently, in proteomic research and the biopharmaceutical industry, mass spectrometry (MS) is a dominant tool to characterize protein structural features, including amino acid sequences, disulfide bond linkages, carbohydrate structures and profiles, post-translational modifications, and in-process and in-storage degradation. Reverse-phase liquid chromatography (RPLC), size exclusion chromatography (SEC) and sodium dodecyl sulfate polyacrylamide gel electrophoresis (SDS-PAGE) are generally used to separate proteins prior to MS analysis. Despite the advantages of mass spectrometry, sample separation, purification and digestion, and data analysis and interpretation are very time-consuming and resource-intensive processes. The complexity of these processes and the expertise necessary to utilize mass spectrometry for protein analysis, in general, require a dedicated expert team. In the pharmaceutical industry, RP-

HPLC coupled to UV detection has served as a routine analytical method to monitor Met oxidation as an indicator of IgG oxidation. However, this method does not provide a complete picture of oxidation, or may mislead the assessment of protein degradation; for example, in the heavy chain Met is not the best representative residue to monitor mAb oxidation.

In biotherapeutic product development, manufacturing and during storage, trace amounts of metal ions are inadvertently and inevitably introduced into the product from excipients and contact materials. Even trace amount of metal ions can be sufficient to induce metal-catalyzed oxidation (MCO) [10]. Generally, for the evaluation of a protein's susceptibility towards MCO, a combination of L-ascorbic acid/Cu(II)/O_2 or L-ascorbic acid/Fe(III)/O_2 has been used as a model system, to predominately study reaction mechanisms and to identify oxidation-sensitive amino acids [5, 10, 12-17] . Protein primary sequence, structure and the geometry of the metal-binding sites, as well as the particular oxidation mechanisms inherent to various oxidizing species, play important roles in transitional metal-induced oxidative modifications. The predominantly oxidized amino acids are either directly involved in metal-binding or located at or in close vicinity of metal-binding sites [5, 10, 12, 13, 15]; thus, the reaction sites are not necessarily exposed to the surface. Amino acids sensitive to MCO are mainly Met, His, Trp, Cys, Lys and Arg [5, 10, 13, 14]. The chemical modifications generated in an IgG2 mAb were thoroughly studied under different stress conditions, including MCO [14], and only oxidative modifications of Met, Trp and His were identified. No oxidative modifications of Tyr and Phe in IgGs are reported to date, even though Tyr oxidation in small proteins and peptides was reported [18-20]. Under MCO, Tyr was oxidized to different products, such as Tyr hydroxylation (DOPA) and 2-amino-3-(3,4-dioxocyclohexa-1,5-dienlyl) propanoic acid (DOCH) [18] and dityrosine [19, 20]. Tyr and Phe oxidation was also identified in covalent aggregates of insulin induced by

MCO [18]. Despite the fact that Tyr can be oxidized to different products, Tyr oxidation in IgG and its detection have not received much attention in accelerated stability studies of protein pharmaceuticals.

Specific oxidation products of Tyr and Phe, DOPA and DOCH, can be successfully derivatized with 4-(aminomethyl)-benzenesulfonic acid (ABS), where the resulting benzoxazole [21] exhibits a characteristic fluorescence with excitation and emission maxima at 360±2 nm and 490±2 nm, respectively [18]. Thus, fluorescence can serve as a fast and sensitive approach to detect and characterize Tyr and/or Phe oxidation because of the specificity of the resulting benzoxazole derivatives. To date, no study has been reported to utilize this fluorogenic tagging method to monitor and characterize oxidative degradation of IgG mAbs.

Since IgG mAbs represent a major class of biopharmaceutical products, and the exposure of antibodies to redox-active metal ions is inevitable and inadvertent, the screening for oxidative modifications induced by MCO would provide a valuable approach in evaluating antibody instability during biotherapeutic product development. Here, we provide a fluorogenic derivatization methodology to detect oxidized Phe and Tyr in IgG1 to monitor IgG1 oxidation induced by MCO.

3.2 Experimental

3.2.1 Materials

IgG1 mAb stock solution at 37 mg/mL was supplied by Amgen Inc. (Seattle, WA, USA). The purified antibody was stored in formulation buffer at -80^{o}C. Dithiothreitol (DTT), iodoacetamide (IAM), sodium phosphate dibasic (Na_2HPO_4), sodium phosphate monobasic (NaH_2PO_4), copper dichloride ($CuCl_2$), L-ascorbic acid, potassium ferricyanide ($K_3Fe(CN)_6$), and sodium chloride (NaCl) were purchased from Sigma Aldrich (St. Louis, MO, USA).

FabRICTATOR® was purchased from Bulldog Bio, Inc. (Portsmouth, NH, USA), a distributor of Genovis (Lund, Sweden). All analytical and HPLC grade organic solvents were purchased from Sigma (St. Louis, MO, USA) or VWR Scientific (West Chester, PA, USA). SDS-PAGE running buffer (100 mM Tris, 1.92 M Glycine and 0.1% (w/v) SDS at pH 8.3), sample buffer (100 mM Tris, 100 mM Tricine, and 0.1% (w/w) SDS at pH 8.25) and Precision Plus Protein dual color standards were purchased from Bio-Rad (Hercules, CA, USA). Sequencing-grade trypsin and Glu-C were obtained from Promega Corp. (Madison, WI, USA). ABS was synthesized according to a published protocol [21].

3.2.2 Metal-catalyzed oxidation (MCO)

The IgG1 stock solution was exchanged into milliQ H_2O at 2-8^oC using an Amicon® ultra-0.5 centrifugal filter device with a 10 kDa filter membrane (Millipore Inc., Bedford, MA, USA). An aliquot of the IgG1 stock solution in water was diluted to 1.5 mg/mL with 20 mM sodium phosphate buffer (pH6.5). IgG1 oxidation was induced by MCO under air in the presence of Cu(II)/L-ascorbic acid. The concentration of Cu(II) varied from 10 μM to 5 mM [14, 16]. Considering the relevance to biological and biopharmaceutical conditions [12, 22-24], most experiments were performed with 10 μM of Cu (II) and 1 mM L-ascorbic acid. An aliquot (1.5 mL) of 1.5 mg/mL IgG1 in 20 mM phosphate (pH6.5) was incubated with 10 μM $CuCl_2$ and 1 mM L-ascorbic acid over 6 hours in a 2 mL Eppendorf vial at 37^oC in a water bath. An aliquot of oxidized IgG1 solution was sampled at 0, 2, 4, and 6 hours. The reaction was quenched by the addition of 100 μM disodium EDTA. In this paper, we will use several terms that need to be explicitly defined. First, the term “control” will refer to an IgG1 sample, which was treated identically as the MCO sample, but without the addition of $CuCl_2$ and L-ascorbic acid. Second, the term “reference standard” will refer to an IgG1 solution which was freshly diluted from the

IgG1 stock solution and not subject to any manipulation related to MCO. The control and the reference standard, respectively, were used to evaluate i) the impact, if any, of the in-process manipulation on IgG1 instability and ii) the method to monitor the IgG1 quality. In the discussion, the same definitions were applied to the control and reference standard.

3.2.3 MCO monitored by size exclusion chromatography (SEC)

The MCO of IgG1 was monitored by SEC coupled to a diode array detector. The separation of monomer and degradation products, aggregates (high molecular weight species, soluble aggregates) and fragments (low molecular weight species), was achieved by an isocratic elution at 0.7 mL/min over 40 minutes with a Shimadzu ultra performance liquid chromatography (UPLC) system equipped with TSK-GEL® G3000SWXL and G2000SWXL columns (7.8 x 300 mm, 5 μm) (Tosoh Biosciences, King of Prussia, PA, USA) connected in line. The mobile phase consisted of 200 mM phosphate and 50 mM NaCl at pH 7.0. An aliquot of 20 μL of the IgG1 sample was injected onto the column. The IgG1 stock solution was diluted to 1.5 mg/mL with the mobile phase and used as the reference standard to evaluate the system performance. The elution was monitored by a diode array detector, allowing for the recording of UV spectra in the region between 200-800 nm.

3.2.4 Cleavage, reduction and alkylation of IgG1

An aliquot of the MCO-treated IgG1 was cleaved at the hinge region using FabRICATOR® at a ratio of 1:1 (w/w) (IgG1/ FabRICATOR®) for 30 minutes at 37°C. Then the disulfide bonds were reduced by DTT (4 mM) by incubating the samples for another 30 minutes at 37°C. The thiols resulting from the reduction of the disulfide bonds were alkylated with 10 mM iodoacetamide for 45 minutes, in the dark, at room temperature. An aliquot (20 μL) was sampled for RPLC/MS analysis. The remaining solution was used for ABS derivatization (see

below). The IgG1 reference standard and the control were cleaved, reduced and alkylated according to the same protocol to evaluate the impact, if any, on IgG1 instability in the absence of MCO reagents.

3.2.5 Analysis of MCO-induced degradation by RPLC-mass spectrometry (RPLC-MS)

A 20 μL aliquot of IgG1 as well as its control and reference standard after cleavage, reduction and alkylation, were purified by an Amicon® ultra-0.5 centrifugal filter device (Millipore Corp., Bedford, MA, USA) with 50 mM NH_4HCO_3 (pH8.0). The purified samples were analyzed to evaluate IgG1 degradation induced by MCO using RPLC-MS according to our developed procedure (unpublished data). Briefly, an aliquot of 10 μL purified sample was injected onto a non-porous column (15 cm x 0.5 mm C18, 2 μm) (Imtakt Corp., Philadelphia, PA, USA) on an Acquity RPLC chromatography system (Water Corp., Milford, MA, USA). The chromatographic separation was achieved by a combination of several linear gradients of H_2O and acetonitrile (ACN) containing 0.1% formic acid: a linear increase of from 15% to 25% B between 0 and 3 min and from 25% to 35% B between 3 and 20 min at a flow rate of 5 μL/min; and a further increases from 35% to 65% B between 20 and 35 min and from 65% to 95% B between 35 and 45 min at a flow rate of 7 μL/min. Each chromatographically separated component was analyzed by means of a SYNAPT G2 high definition mass spectrometer (Waters Corp. Milford, MA, USA). The spectra were acquired using a mass range of 900-3000 amu (amu: atomic mass unit). The data were accumulated for 0.7 sec per cycle and processed using the software MassLynx (Waters Corp. Milford, MA, USA). To characterize the polypeptides, the mass-to-charge *(m/z)* ratio distributions were analyzed by maximum entropy (MaxEnt) processing.

3.2.6 Feasibility and optimization of fluorogenic tagging of intact and cleaved IgG1

After MCO, the intact IgG1 as well as the control and reference standard were dialyzed into 100 mM sodium phosphate buffer (pH 9.0) using Amicon® ultra-0.5 centrifugal filter devices (Millipore Corp. Bedford, MA, USA) for ABS fluorogenic tagging. The feasibility and optimization of ABS tagging of oxidized IgG1 were performed by incubating the oxidized IgG1 with ABS derivatization reagents in the dark at room temperature under the following conditions: i) molar ratios of $K_3Fe(CN)_6$/ IgG1 ranged from 5:1 to 30:1; ii) concentrations of ABS were 2 and 10 mM ; and iii) the reaction time spanned over 200 minutes. An aliquot was sampled at time points of 0, 60, 90, 150 and 200 min. The formation of the resulting fluorescent benzoxazole derivatives of oxidized IgG1 was monitored by a steady-state fluorescence spectrometer and SEC coupled to a fluorescence detector. Similar derivatizing conditions were applied to the reference standard and the control to monitor any potential derivatization not due to MCO. The optimized ABS-derivatization conditions were applied to oxidized IgG1 as well as its control and reference standard after cleavage, reduction and alkylation for SDS-PAGE and in-gel digestion to identify the oxidized amino acids, and the benzoxazole derivatives of the oxidized Tyr and Phe residues.

3.2.7 Steady-state fluorescence spectrometry

The benzoxazole fluorescence of the ABS-derivatized IgG1 samples was measured by a Shimadzu RF-5000U fluorescence spectrophotometer (Kyoto, Japan) equipped with a 1-cm quartz cuvette and a 96-well plate model, respectively. The emission and excitation spectra were acquired in a 0.5 mL 1-cm quartz cuvette (Hellma, Plainview, NY, USA), and the fluorescence intensities at λ_{em} = 490 nm (λ_{ex} = 360 nm) for the ABS derivatized samples as well as the reference standards and controls were measured in a 96-well plate. For both modes, the excitation and emission slit was set at 5 nm.

3.2.8 Sodium dodecyl sulfate polyacrylamide gel electrophoresis (SDS-PAGE)

After cleavage, reduction and alkylation, the oxidized IgG1, its control, reference standard and their ABS-derivatized samples were independently mixed with SDS-PAGE sample buffer containing 100 mM Tris, 100 mM Tricine, and 0.1% (w/w) SDS at pH 8.25. The samples were boiled at 100^{o}C for 2 mins after mixing. An aliquot of 20 µL of each sample was loaded onto a Novex 4-20% polyacrylamide gel from Invitrogen Inc. (Carlsbad, CA, USA). Molecular Weight Standards, precision plus protein dual color standards from Bio-Rad (Hercules, CA, USA), were also loaded onto the same gel as the samples. The gel electrophoresis was run under a difference of potential of 250 V for 60 mins using 10-fold diluted running buffer at a temperature maintained at 6^{o}C. Fluorescence visualization of ABS-tagged proteins was recorded by a UV Transilluminator from Fotodyne Inc. (Hartland, WI, USA). Fluorescent bands of interest were excised for in-gel digestion.

3.2.9 In-gel digestion

The proteins present in the excised fluorescent bands were digested according to the in-gel digestion protocol described by Shevchenko *et al* [25]. Briefly, the gel slices were first rinsed twice with 100 mM NH_4HCO_3 (pH 7.8) in ACN (1:1 v/v) and then rinsed with 100% ACN at room temperature. The gel slices were dried using a SpeedVac from Labconco Corp. (Kansas City, MO, USA). The dried gel slices were incubated for 1 hour at 4^{o}C in 125 µL of a Promega® reconstitution buffer for trypsin, containing 5 µg of sequencing-grade trypsin and 2 µg of Glu-C in 1.5-mL Eppendorf vials. An aliquot of 275 µL of 100 mM NH_4HCO_3 (pH 7.8) was then added to the samples prior to protein digestion at 37^{o}C overnight. Upon the completion of digestion, the digested protein solutions were transferred into new 1.5-mL Eppendorf vials. The gel slices were rinsed three times with 100% ACN and the rinsing solutions were combined with the digested

protein solutions in the new Eppendorf vials. The samples were concentrated using the SpeedVac to reach a final volume of 20 µL for LC-MS/MS analysis.

3.2.10 CapLC-ESI-TQ-FT-MS analysis

The in-gel digested protein samples were subjected to capillary LC-MS/MS experiments using an LTQ-FT mass spectrometer (ThermoFinnigan, Bremen, Germany) under conditions described by Ikehata *et al* [26]. In short, peptides were separated on a reverse-phase LC Packings PepMap C18 column (0.300 × 150 mm) (Dionex, Sunnyvale, CA, USA) at a flow rate 10 µL/min with a linear gradient rising from 0 to 65% ACN in 0.06% aqueous formic acid over a period of 55 minute s using a LC Packing Ultimate Chromatograph (Dionex, Sunnyvale, CA, USA). LC-MS experiments were performed in a data-dependent acquisition mode using the Xcalibur 2.0 software (Thermo Scientific, Waltham, MA, USA). The five most intense precursor ions in a survey MS^1 mass spectrum acquired in the FT-ICR over a mass range of 300–2000 amu were selected and fragmented in the linear ion trap by collision-induced dissociation. The ion selection threshold was 500 counts.

The MS/MS analysis was performed using MassMatrix [27-29]. The theoretical fragments from the parent ions were generated by MassMatrix and then compared to the experimental MS/MS spectra to validate the structures, which were taken into account only when the difference between the theoretical and the experimental *m/z* of the parent ion was within 0.1 Da. The oxidation of Met (+16, 32 and 48 amu) and Trp (+4, 16, 20, 32 and 48 amu), Phe (+16 and 32 amu), and Tyr (+14 and 16 amu) and the benzoxazole derivatives of oxidized Tyr and Phe (listed in Table 1) were built in a customized IgG1 database for identification of the chemical modifications. The elementary compositions of the benzoxazole derivatives of the oxidized Tyr and Phe residues are also listed in Table 1.

3.3 Results

3.3.1 Degradation of IgG1 induced by MCO

In a 2-mL Eppendorf vial, 1.5 mL of IgG1 at a concentration of 1.5 mg/mL in 20 mM sodium phosphate buffer (pH 6.5) was incubated with 10 μM $CuCl_2$ and 1 mM L-ascorbic acid over 6 hours at 37°C. IgG1 degradation induced by MCO was monitored at 0, 2, 4, and 6 hours by SEC coupled to a diode array detector (Fig. 1). Soluble aggregates (t_R = 18.0 min) were eluted first, followed by monomers (t_R = 21.5 min) and fragments (t_R = 26.0 min) (Fig. 1). The control (Fig. 1, pink) exhibits the same profile as our reference standard (Fig. 1, black). Thus, the processing of IgG1 did not induce additional soluble aggregates and fragments. A prolonged exposure (over 6 hours) of IgG1 to MCO reagents ($CuCl_2$ /L-ascorbic acid under air) led to the formation of more soluble aggregates and fragments as monitored by UV detection at 214 nm (Fig. 1, blue, dark red and green).

To further characterize the MCO of IgG1, the reference standard, control and oxidized IgG1 were cleaved, reduced and alkylated as described in the Experimental, section 3.2.4, to form Fc-HC, Fab-HC and LC. The resulting polypeptides were analyzed by RPLC-MS. The chromatograms, monitored by MS analysis of the reference standard, control, and oxidized IgG1 are shown in Fig. 2. The chromatograms of the reference standard (Fig. 2A) and the control (Fig. 2B) exhibited the same pattern, which is different from that of the oxidized IgG1 (Fig. 2C). Masses of the polypeptides observed in the control (Fig. 3A) and reference standard (Fig. 3B) confirm that the processing of the IgG1 (in the absence of MCO) did not induce detectable degradation. Indeed, the acquired molecular weights of 22,982 Da for the LC and 24,457 Da for Fab-HC, respectively, match their expected masses after alkylation. Also, the acquired molecular weights of 24,996 Da, 25,200 Da and 25,362 Da match the expected masses taking into account

the glycosylation heterogeneity of the IgG1 Fc-HC (unpublished data). The MCO of IgG1 results in a mass increase of 32 Da (25,201 Da to 25,233 Da and 25,364 Da to 25,396 Da) for the Fc-HC (Fig. 4A). Similarly, new species with mass increases of 16 Da and 34 Da (22,983 Da to 22,999 Da, and 22,983 Da to 23,017 Da) along other products were observed for the IgG1 LC (Fig. 4B). No significant new species were observed for the Fab-HC resulting from MCO (Fig. 4C). The mass spectrometric analysis of the oxidized IgG1 (Fig. 4) indicates that several amino acids may be targeted for oxidative modifications, although the MS^1 analysis alone cannot detail which amino acid is oxidized. The analysis of oxidized IgG1 as well as its control (Fig. 5) indicate that MCO induced not only oxidative modifications in the IgG1 primary sequence, as described above, but also induced the formation of fragments and/or aggregates, consistent with the data obtained by SEC-UV analysis. For example, a fragment with a mass of 11,492 Da and multiple aggregates with masses of 33,212 Da, 45,998 Da and 68,948 Da etc., were formed due to MCO.

3.3.2 ABS derivatization of oxidized IgG1: feasibility and optimization

$CuCl_2$ and L-ascorbic acid were removed after oxidation of IgG1 by centrifugation through a 10 kDa centrifugal filter (as described in the Experimental, section 3.2.3) prior to ABS derivatization. The same procedure was applied to the control. Oxidized IgG1 and its control were incubated with 10 mM ABS and 100 μM of $K_3Fe(CN)_6$ (molar ratio of 10:1 of $K_3Fe(CN)_6$: IgG1) for 1 hour in the dark at room temperature. Prior to and post ABS derivatization, the fluorescence emission (370 to 650 nm at λ_{ex} = 360 nm) and excitation (220 to 470 nm at λ_{em} = 490 nm) spectra (Fig. 6) were recorded. For oxidized IgG1 alone, a maximal emission at λ_{em} = 410 nm (λ_{ex} = 360 nm) was observed prior to ABS derivatization (Fig. 6A, dotted line). A maximal emission at λ_{em} = 490 nm with a significantly increased intensity emerged after ABS derivatization (Fig. 6A, solid line). Likewise, at λ_{em} = 490 nm, a maximal excitation at λ_{ex} = 360

nm (Fig. 6B, solid line) was observed after ABS derivatization besides the maximal excitation at λ_{ex} = 245 nm that was present prior to ABS derivatization (Fig. 6B, dotted line). No change in maximal fluorescence emission and excitation wavelengths was observed for the control after and prior to ABS derivatization (data not shown). Additionally, we observed that the fluorescence emission intensity increased at least by 10-fold (Fig. 6A, solid line) after ABS-derivatization in comparison to the non-ABS derivatized oxidized IgG1 (Fig. 6A, dotted line). The increase of fluorescence intensity observed at λ_{em} = 490 nm (λ_{ex} = 360 nm) of the ABS-tagged sample is consistent with the formation of a benzoxazole derivative as presented in Scheme 1 [18]. Met, His, and Trp are subject to MCO [5, 10, 13, 14]. However, Tyr and Phe are also prone to oxidation. In the presence of $K_3Fe(CN)_6$ and ABS, DOPA and DOCH can be transformed into benzoxazole derivatives via the reactions summarized in Scheme 1. Thus, the characteristic fluorescence (λ_{em}= 490 nm / λ_{ex} = 360 nm) observed after ABS derivatization of the oxidized IgG1 can be rationalized by the formation of ABS derivatives of DOPA and/or DOCH resulting from the oxidation of Phe and Tyr.

Sharov *et al,* optimized the ABS derivatization conditions for 3-aminotyrosine (3-AT), that is, the optimal molar ratio of $K_3Fe(CN)_6$ to the peptide was ≥ 5:1 in the presence of 2 mM ABS at room temperature for the peptide concentrations between 0.1, 1 and 10 μM [21]. However, this peptide contained only one 3-AT residue for derivatization. Since IgG1 contains twenty seven Tyr and sixteen Phe residues and MS analysis indicated the presence of several oxidized amino acids, it was necessary to optimize the ABS derivatization conditions specifically for the oxidized IgG1. Samples containing the oxidized IgG1 were mixed with different amounts of $K_3Fe(CN)_6$ and ABS. The molar concentration of IgG1 was maintained at 10 μM. The fluorescence intensity of the samples was monitored over 200 minutes at λ_{em} = 490 nm (λ_{ex} =

360 nm) (Fig. 7A). At fixed molar ratios of $K_3Fe(CN)_6$/IgG1 of 5:1 and 15:1, the concentrations of ABS at 2 mM and 10 mM did not show significantly different fluorescence, indicating that the ABS concentration was sufficient for derivatization of the oxidized protein. However, an increase of the molar ratio of $K_3Fe(CN)_6$/IgG1 resulted in a significant increase of the fluorescence intensity. The latter can be rationalized by the fact that multiple oxidized Tyr and Phe residues are available for ABS derivatization. The derivatization time also affected the fluorescence intensity. A plateau was reached after 150 minutes. Importantly, the incubation of the oxidized IgG1 with either ABS or $K_3Fe(CN)_6$ did not produce any additional fluorescence background monitored by fluorescence spectrometer. Thus, the optimized ABS derivatization conditions for oxidized IgG1 are achieved with a molar ratio $K_3Fe(CN)_6$/IgG1 of 30:1, and 10 mM ABS. The derivatization reaction was performed at room temperature in the dark for 60-90 minutes.

To confirm the optimized ABS derivatization conditions, SEC coupled to a fluorescence detector was employed to analyze oxidized IgG1, a mixture of oxidized IgG1 and $K_3Fe(CN)_6$, a mixture of oxidized IgG1 and ABS, and ABS-derivatized IgG1 after 90 minutes storage in the dark at room temperature. The fluorescence (Fig. 7B) was monitored at λ_{em} = 490 nm with λ_{ex} = 360 nm. Consistent with our previous results obtained by fluorescence spectroscopy, the optimized molar ratio of 30:1 of $K_3Fe(CN)_6$/IgG1 resulted in a significant increase of the fluorescence intensity (Fig. 7B, dotted line). Moreover, the incubation of IgG1 with either $K_3Fe(CN)_6$ or ABS alone under the same conditions did not generate additional fluorescent products (Fig. 7B. solid lines), consistent with the results obtained by fluorescence spectroscopy.

3.3.3 ABS derivatization to monitor time-dependent IgG1 oxidation

IgG1 was exposed to MCO and an aliquot of the solution was sampled at 0, 2, 4, and 6 hours to evaluate the reaction progress of MCO through ABS derivatization. The control protein was processed in the same way as the oxidized protein. At each time point, the MCO was terminated by the addition of EDTA. Prior to ABS derivatization, the reaction mixtures were dialyzed into sodium phosphate buffer (100 mM, pH 9.0). The progress of MCO was monitored by tagging the IgG1 with ABS using our optimized conditions (see above). The fluorescence intensity at λ_{em} = 490 nm (λ_{ex} = 360 nm) was measured prior to and after ABS derivatization of the oxidized IgG1 samples and their respective controls. The controls as well as their respective ABS treated controls did not exhibit fluorescence. The fluorescence intensities obtained prior to and after ABS derivatization of the oxidized IgG1 were plotted against the reaction time (Fig. 8). Prior to ABS derivatization, the oxidized IgG1 exhibited very low intrinsic fluorescence. The fact that the fluorescence intensity increased significantly after ABS derivatization of the oxidized IgG1, indicates that the residues of Tyr and/or Phe were oxidized and subsequently derivatized by ABS. Our data show that oxidation of Phe and Tyr occurred within 2 hours of MCO.

3.3.4 SDS-PAGE visualization of ABS-derivatized oxidized IgG1

SDS-PAGE analysis was performed to visualize ABS derivatization of the oxidized IgG1 prior to in-gel digestion. The oxidized IgG1, and the control as well as the reference standard were first cleaved, reduced and alkylated. An aliquot of each sample was incubated with ABS and $K_3Fe(CN)_6$ at the optimized conditions for ABS derivatization. An aliquot of 5 μL of the Molecular Weight Standards was loaded into lane 1 of the SDS-PAGE gel. Lane 2, 7 and 10 were left blank to monitor the background. An aliquot of 20 μL of each of the following IgG1 was loaded onto the gel: i) reference standard prior to and after ABS derivatization, ii) control

prior to and after ABS derivatization, and iii) oxidized IgG1 prior to and after ABS derivatization. The fluorescence was recorded by an UV Transilluminator (Fotodyne Inc., Hartland, WI, USA) as presented in Fig. 9. Clearly, only ABS derivatization of the oxidized IgG1 (lane 9) exhibited a strong fluorescence. This observation confirms our results obtained by fluorescence spectroscopy and SEC analysis coupled to fluorescence detection. The fluorescent lane 9 in Fig. 9 was excised from the gel for in-gel digestion to identify the oxidized amino acids and the benzoxazole derivatives of the oxidized Phe and Tyr residues. The fact that no fluorescence was observed for ABS derivatized IgG1 reference standard and control is consistent with the results obtained by RPLC/MS analysis. That is, the processing of IgG1 did not induce any oxidative modifications. Therefore, we can conclude that any oxidative modifications in the oxidized IgG1 were induced by MCO.

3.3.5 Identification of ABS derivatives and oxidized amino acids

The fluorescent lane 9 from the SDS-PAGE (Fig. 9) was excised and subjected to in-gel digestion. The resulting proteolytic peptides were analyzed by means of capillary LC-ESI-LTQ-FT-MS. The purpose of this analysis was to map the oxidative modifications and benzoxazole derivatives in the primary sequence of oxidized IgG1. The oxidized amino acids identified in oxidized IgG1 are summarized in Table 2. Besides the oxidation of His, Met and Trp, we report the oxidation of Tyr and Phe residues. In fact, three out of eleven Tyr, two out of three Trp, and one out of four Phe residues located in the IgG1 LC, and six out of sixteen Tyr, three out of ten Trp, nine out of twelve Phe, five out of ten His and one out of eleven Met residues in the IgG1 HC were oxidized by MCO when IgG1 was incubated with 10 μM $CuCl_2$/ 1 mM ascorbic acid at 37^{o}C over 6 hours.

Four MS/MS spectra are presented below to illustrate how the oxidative modifications were rationalized from the MS/MS analysis of the proteolytic peptides obtained after digestion of oxidized IgG1. The b and y fragments used in the discussion below for MS/MS analysis refer to the cleavage sites defined by Roepstorff [30].

i. *Hydroxylation of Phe.* MS/MS data displayed in Fig. 10 indicate that Phe [103] in IgG1 LC is hydroxylated. The b2 fragment shows a mass increase of 16 Da compared to the b2 fragment of non-oxidized IgG1 indicating that the addition of one oxygen atom is located either to Val or Phe. The series of the fragment ions of b4-b6 and y2-y5 show that none of the amino acids in the sequence GTGTK, C-terminal to Phe is oxidized. The mass increase of 163 Da (147 Da for Phe + 16 Da) from the y5 fragment to y6 confirms that Phe in the tryptic peptide VFGTGTK is oxidized. We cannot determine the position of the hydroxylation from the information obtained here since Phe hydroxylation can occur in ortho, meta or para position [31]. Only hydroxylation of Phe at the para position leads to the formation of Tyr.

ii. *ABS derivatization of oxidized Phe.* The formation of benzoxazole derivative of oxidized Phe [166] in HC in the sequence of TFPAVLQ is indicated by the MS/MS data presented in Fig. 11. The fragment ions y3 and y4 indicate that the sequence of AVLQ is not oxidized and derivatized. The presence of the fragment ion y5+16 Da suggests the formation of a hydroxyl group at Pro in the HC [32]. Therefore, the additional mass increase of 181 Da is localized to the sequence TF. The series of b3-b6 fragment ions also confirm a mass increase of 197 Da in the original sequence TFP. The loss of two molecules of H_2O from the b4 fragment ion is likely due to the presence of two hydroxyl functions within the sequence of the b4 fragment ion. Because the non-oxidized peptide generates a b4 fragment ion with only one Thr, the loss of the second molecule of H_2O from the b4 fragment ion of the oxidized peptide is therefore likely

due to the presence of the hydroxylated Pro. Therefore, we can assign the mass increase of 181 Da to Phe corresponding to the addition of one molecule of ABS. The reaction mechanism allowing for the formation of the benzoxazole group is possibly facilitated by the amide between the original Phe and the Pro residue. The analysis of the fragment ions is completed by the assignment of the fragment ion TF(+181 amu)P(+16 amu)AL with *m/z* of 743.40 and the one with *m/z* of 725.41 corresponding the loss of one molecular of H_2O from TF(+181 amu)P(+16 amu)AL, respectively. These two fragments are likely formed by neutral lose of Val from b6 and b6-H_2O, respectively.

iii. *ABS derivatization of oxidized Tyr.* ABS derivatization of oxidized Tyr [403] in IgG1 HC is characterized by the MS/MS fragmentation of the parent ion DSDGSFFLY(+196 amu) (Fig. 12). The presence of the y1 and y2 fragment ions indicates a mass increase of 196 Da on the C-terminal Tyr residue. The fragment ion b8 confirms that none of the amino acids in the sequence DSDGSFFL is oxidized. The observation of a mass increase of 196 Da suggests that Tyr was oxidized and subsequently derivatized by ABS. The structure of the benzoxazole derivative is presented in Fig. 12, which contains an amino substituted in the 6-position, consistent with the data of Sharov *et al* [21].

iv. *ABS derivatization of oxidized Tyr.* MS/MS spectra presented in Fig. 13 demonstrate that Tyr [315] in HC is oxidized and subsequently derivatized by ABS. The MS/MS spectrum of the tryptic peptide W(+16 amu)LNGKEY(+179 amu)K shows a mass increase of 179 Da located at Tyr and 16 Da increase located at Trp. Such peptide should have a *m/z* of 1232.50. The presence of the ion with *m/z* of 607.99 (assigned to the $[M+2H-H_2O]^{++}$ ion) along with the observation of the series of y2-y6 and b4-b6 fragment ions suggest that i) the oxidized Tyr is derivatized by ABS, and ii) the formation of a cyclic product involving Lys [316] (Fig. 13, A). The structure

involving the C-terminal Lys [316] is also supported by the formation of the internal fragment NGKE (*m/z* 412.20). Meanwhile, the series of b4, b7 and y4-y6 fragment ions, and internal fragment of ABS-derivatized GKEY (*m/z* 576.36), with a loss of 80 Da (SO_3H), suggest that ABS derivatization of the oxidized Tyr can also form a cyclic product with Lys [313] (Fig. 13, B). This intra-molecular crosslink is the result of the addition of the primary amine ($-NH_2$) from the side chain of Lys [316] or Lys [313] to the benzoxazole group located on the original Tyr [315]. This observed structure of benzoxazole derivative formed through intramolecular crosslink to primary amino functional group in the 6-position is consistent with data of Sharov *et al* [21].

MS/MS analysis of the tryptic peptides containing Phe [103] (Fig. 10) in the LC confirms that Phe is oxidized to hydroxyphenylalanine. MS/MS analyses of the tryptic peptides containing Phe [166, HC] (Fig. 11), Tyr [403, HC] (Fig. 12) and Tyr [315, HC] (Fig. 13) confirm that Phe and Tyr residues are oxidized and subsequently derivatized by ABS.

3.4 Discussion

Oxidative modifications of Trp, His and Met residues induced by MCO are well documented [5, 12-14, 16, 17, 33], and specifically His has been identified as a target for MCO [12, 13, 16, 17]. Luo *et al* reported the degradation of IgG2 under different conditions of chemical and physical stresses. The authors demonstrated that the residues Met, Trp, and His were oxidized by MCO [14]. Consistent with this report, we also observed the oxidation of Met, His and Trp residues during the MCO of IgG1. The MS/MS spectra were not presented here for a more detailed analysis since they are well known oxidation products.

To the best of our knowledge, the oxidation of Tyr and Phe residues in IgG has not been reported. Furthermore, the feasibility of using a fluorogenic tag to detect the oxidized Tyr and

Phe in a mAb is also first reported here. We are able to obtain MS/MS confirmation of benzoxazole derivatives of Tyr [315, HC], Tyr [403, HC] and Phe [166, HC], consistent with the observed significant fluorescence increase at λ_{em} = 490 nm (λ_{ex} = 360 nm) after ABS-derivatization. The abundance of other ABS-tagged Tyr and Phe residues may be sufficiently high for fluorescence detection, but too low for MS/MS analysis. The mapping of oxidized amino acids in the primary sequence of IgG1 indicates that no modifications are identified in the IgG1 complementarity determining regions (CDRs) for antigen binding.

Noteworthy, the quantification of the monomer by SEC-UV has been a well-accepted practice to evaluate protein stability in the biopharmaceutical industry. However, as revealed by our ABS derivatization procedure, we noticed that the fluorescence signal (due to the benzoxazole formation) increased not only for the fragments and soluble aggregates, but also for the monomers monitored by SEC-fluorescence detection (Fig. 7B). These observations suggest that the monomers also incorporate oxidized Tyr and/or Phe that are derivatized with ABS. Therefore, the coupling of our ABS-tagging procedure with SEC-fluorescence analysis provides additional information on protein integrity. That is, a stability study monitored by SEC-UV analysis does not provide sufficient information to assess the stability of IgG1. Here, the application of a variety of techniques of SEC-UV/fluorescence, SDS-PAGE, RPLC-MS and MS/MS allowed us to develop a practical fluorogenic tagging approach to monitor and characterize oxidized Tyr and Phe amino acids to evaluate IgG1 stability.

3.5 Conclusions

Oxidation represents a prominent protein degradation pathway. In this paper, we applied fluorogenic tagging approach to detect the oxidized Phe and Tyr in IgG. Fluorescence detection

alone and/or SEC combined with a fluorescence detector would provide a rapid alternative approach for additional information to evaluate protein stability.

3.6 Acknowledgments

This research was supported by Amgen Incorporation. The authors thank Dr. Nadya Galeva from the Mass Spectrometry Laboratory at University of Kansas for performing MS measurements on the FT-ICR.

3.7 References

1. Brekke, O.H., et al., *Therapeutic antibodies for human diseases at the dawn of the twenty-first century.* Nat Rev Drug Discov, 2003. **2**(1): p. 52-62.
2. Bebbington, C., et al., *Antibodies for the treatment of bacterial infections: current experience and future prospects.* Curr Opin Biotechnol, 2008. **19**(6): p. 613-9.
3. Schrama, D., et al., *Antibody targeted drugs as cancer therapeutics.* Nat Rev Drug Discov, 2006. **5**(2): p. 147-59.
4. Bee, J.S., et al., *Precipitation of a monoclonal antibody by soluble tungsten.* J Pharm Sci, 2009. **98**(9): p. 3290-301.
5. Li, S., et al., *Aggregation and precipitation of human relaxin induced by metal-catalyzed oxidation.* Biochemistry, 1995. **34**(17): p. 5762-72.
6. Li, S., et al., *Chemical pathways of peptide degradation. V. Ascorbic acid promotes rather than inhibits the oxidation of methionine to methionine sulfoxide in small model peptides.* Pharm Res, 1993. **10**(11): p. 1572-9.
7. Stadtman, E.R., *Metal ion-catalyzed oxidation of proteins: biochemical mechanism and biological consequences.* Free Radic Biol Med, 1990. **9**(4): p. 315-25.

8. Stadtman, E.R., *Oxidation of free amino acids and amino acid residues in proteins by radiolysis and by metal-catalyzed reactions.* Annu Rev Biochem, 1993. **62**: p. 797-821.
9. Uversky, V.N., et al., *Metal-triggered structural transformations, aggregation, and fibrillation of human alpha-synuclein. A possible molecular link between Parkinson's disease and heavy metal exposure.* J Biol Chem, 2001. **276**(47): p. 44284-96.
10. Zhao, F., et al., *Metal-catalyzed oxidation of histidine in human growth hormone. Mechanism, isotope effects, and inhibition by a mild denaturing alcohol.* J Biol Chem, 1997. **272**(14): p. 9019-29.
11. Zhou, S., et al., *Comparative evaluation of disodium edetate and diethylenetriaminepentaacetic acid as iron chelators to prevent metal-catalyzed destabilization of a therapeutic monoclonal antibody.* J Pharm Sci, 2010. **99**(10): p. 4239-50.
12. Schöneich, C., *Selective Cu2+/ascorbate-dependent oxidation of alzheimer's disease beta-amyloid peptides.* Ann N Y Acad Sci, 2004. **1012**: p. 164-70.
13. Schöneich, C., *Mechanisms of metal-catalyzed oxidation of histidine to 2-oxo-histidine in peptides and proteins.* J Pharm Biomed Anal, 2000. **21**(6): p. 1093-7.
14. Luo, Q., et al., *Chemical modifications in therapeutic protein aggregates generated under different stress conditions.* J Biol Chem, 2011. **286**(28): p. 25134-44.
15. Lim, J., et al., *Development of a methodology based on metal-catalyzed oxidation reactions and mass spectrometry to determine the metal binding sites in copper metalloproteins.* Anal Chem, 2003. **75**(5): p. 1164-72.
16. Schöneich, C., et al., *Cu(II)-catalyzed oxidation of beta-amyloid peptide targets His13 and His14 over His6: Detection of 2-Oxo-histidine by HPLC-MS/MS.* Chem Res Toxicol, 2002. **15**(5): p. 717-22.

17. Schöneich, C., et al., *Cu(II)-catalyzed oxidation of Alzheimer's disease beta-amyloid peptide and related sequences: remarkably different selectivities of neurotoxic betaAP1-40 and non-toxic betaAP40-1.* Cell Mol Biol (Noisy-le-grand), 2003. **49**(5): p. 753-61.
18. Torosantucci, R., et al., *Chemical Modifications in Aggregates of Recombinant Human Insulin Induced by Metal-Catalyzed Oxidation: Covalent Cross-Linking via Michael Addition to Tyrosine Oxidation Products.* Pharm Res, 2012.
19. Dubinina, E.E., et al., *Oxidative modification of proteins: oxidation of tryptophan and production of dityrosine in purified proteins using Fenton's system.* Biochemistry (Mosc), 2002. **67**(3): p. 343-50.
20. Huggins, T.G., et al., *Formation of o-tyrosine and dityrosine in proteins during radiolytic and metal-catalyzed oxidation.* J Biol Chem, 1993. **268**(17): p. 12341-7.
21. Sharov, V.S., et al., *Fluorogenic Tagging of Peptide and Protein 3-Nitrotyrosine with 4-(Aminomethyl)-benzenesulfonic Acid for Quantitative Analysis of Protein Tyrosine Nitration.* Chromatographia, 2010. **71**(1-2): p. 37-53.
22. Zhou, S., et al., *Biotherapeutic formulation factors affecting metal leachables from stainless steel studied by design of experiments.* AAPS PharmSciTech, 2012. **13**(1): p. 284-94.
23. Zhou, S., et al., *Biologics formulation factors affecting metal leachables from stainless steel.* AAPS PharmSciTech, 2011. **12**(1): p. 411-21.
24. Zhou, S., et al., *Metal leachables in therapeutic biologic products: origin, impact and detection.* Am. Pharm. Rev., 2010. **13**(4): p. 76-80.
25. Shevchenko, A., et al., *Mass Spectrometric Sequencing of Proteins from Silver-Stained Polyacrylamide Gels.* Anal. Chem., 1996. **68**(Copyright (C) 2012 American Chemical Society (ACS). All Rights Reserved.): p. 850-8.

26. Ikehata, K., et al., *Protein Targets of Reactive Metabolites of Thiobenzamide in Rat Liver in Vivo.* Chem. Res. Toxicol., 2008. **21**(Copyright (C) 2012 American Chemical Society (ACS). All Rights Reserved.): p. 1432-1442.
27. Xu, H., et al., *A mass accuracy sensitive probability based scoring algorithm for database searching of tandem mass spectrometry data.* BMC Bioinformatics, 2007. **8**: p. 133.
28. Xu, H., et al., M*assMatrix: a database search program for rapid characterization of proteins and peptides from tandem mass spectrometry data.* Proteomics, 2009. **9**(6): p. 1548-55.
29. Xu, H., et al., *A robust linear regression based algorithm for automated evaluation of peptide identifications from shotgun proteomics by use of reversed-phase liquid chromatography retention time.* BMC Bioinformatics, 2008. **9**: p. 347.
30. Roepstorff, P., et al., *Proposal for a common nomenclature for sequence ions in mass spectra of peptides.* Biomed Mass Spectrom, 1984. **11**(11): p. 601.
31. Kaur, H., et al., *Aromatic hydroxylation of phenylalanine as an assay for hydroxyl radicals: Application to activated human neutrophils and to the heme protein leghemoglobin.* Analytical Biochemistry, 1988. **172**(2): p. 360-367.
32. Shacter, E., *Quantification and significance of protein oxidation in biological samples.* Drug Metab Rev, 2000. **32**(3-4): p. 307-26.
33. Schöneich, C., et al, *mass spectrometry of protein modifications by reactive oxygen and nitrogen species.* Free radical biology & medicine 41 (10):1507-1520. doi:10.1016/j.freeradbiomed.2006.08.013

Scheme 1. ABS derivatization of oxidized Phe and Tyr to form fluorogenic benzoxazole derivatives

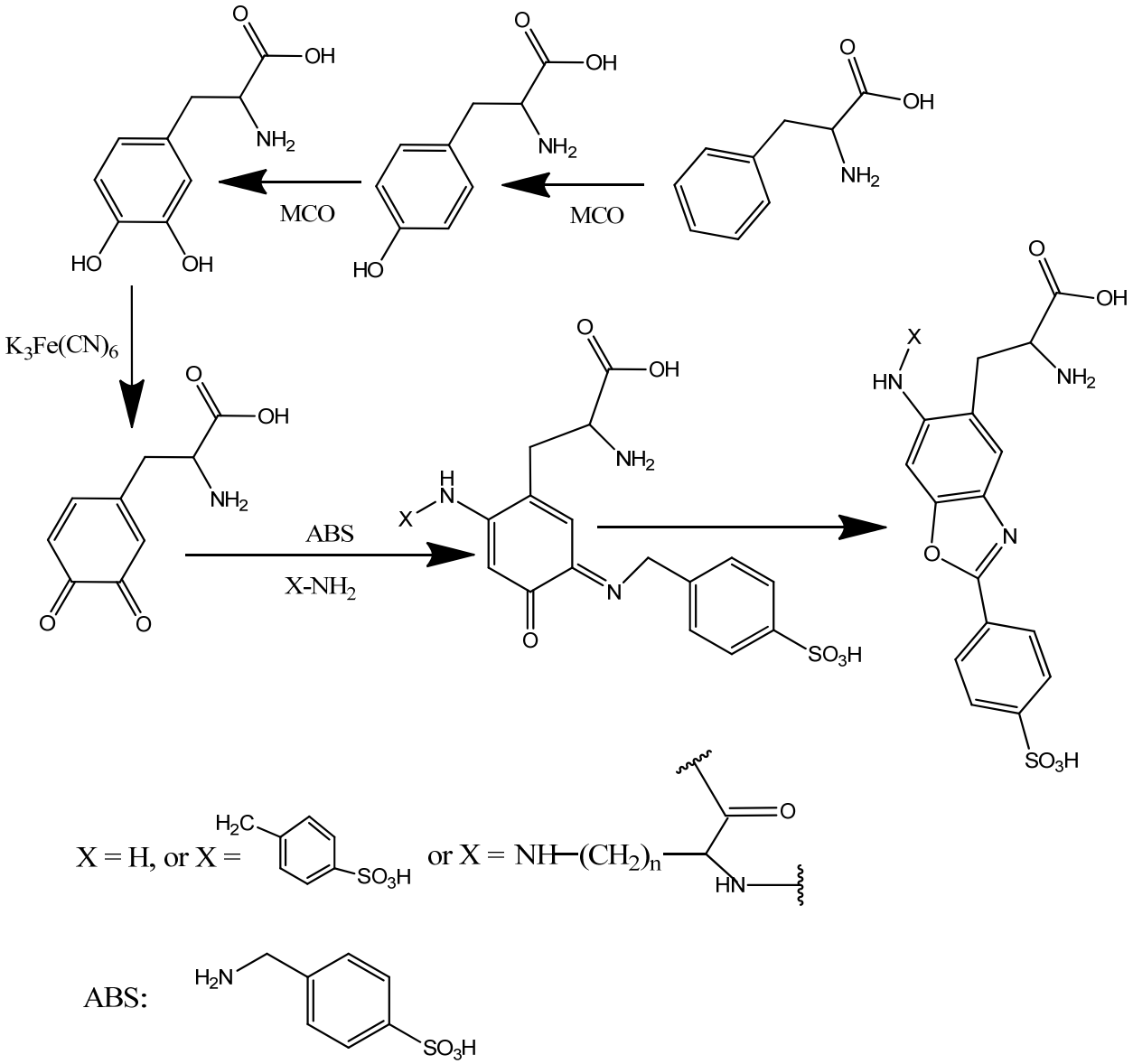

Table 1. Structure, elementary composition of the modified amino acids and mass shift for the non-oxidized residue which are taken into account for peptide mapping searching of ABS derivatives of oxidized Tyr in IgG1 (the structures for ABS derivatives of oxidized Phe are the same as listed in the table with additional +16 Da mass shift for one atom of oxygen)

Structure	Elementary compositions of modifications	Mass shift (Da)
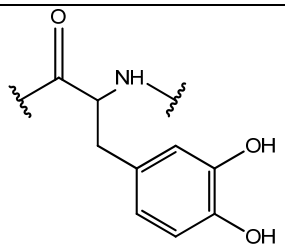 DOPA	O_1	+16
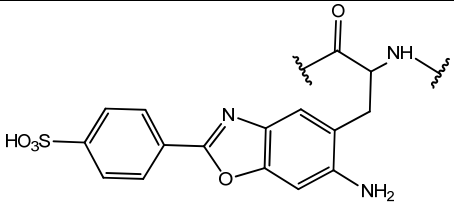 ABS-NH_2 derivative	$C_7H_4N_2O_3S$	+196
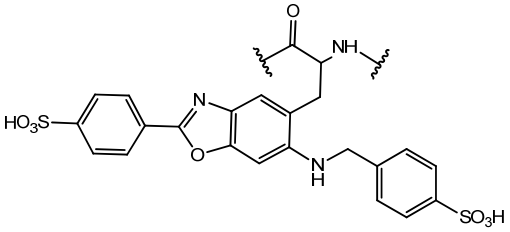 $(ABS)_2$ derivative	$C_{14}H_{10}N_2O_6S_2$	+366
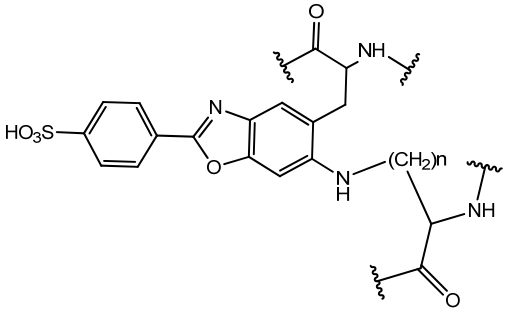 ABS-NH_2 crosslink	C_7HO_3NS	+179

Table 2. The oxidized amino acids in oxidized IgG1 by MCO, their oxidation products, positions in primary sequence and probability of the oxidized amino acids compared to the same amino acids in the primary sequence

Oxidized residues	Oxidation products	Location	Position	Oxidized probability
Tyr	3,4-hydroxyphenylalanine (DOPA), quinone	LC	38, 88, 101	3/11
		HC	60, 94, 95, 274, 315, 403	6/16
Phe	hydroxyphenylalanine, DOPA, quinone	LC	103	1/4
		HC	79, 122, 146, 166, 237, 239, 271, 401, 419	9/12
Trp	kynurenine, hydroxyl-Trp, 3-hydroxy kynurenine	LC	37, 191	2/3
		HC	48, 273, 413	3/10
His	2-ox-histidine	HC	54, 220, 281, 306, 431	5/10
Met	methionine sulfoxide, methionine sulfone	HC	248	1/11

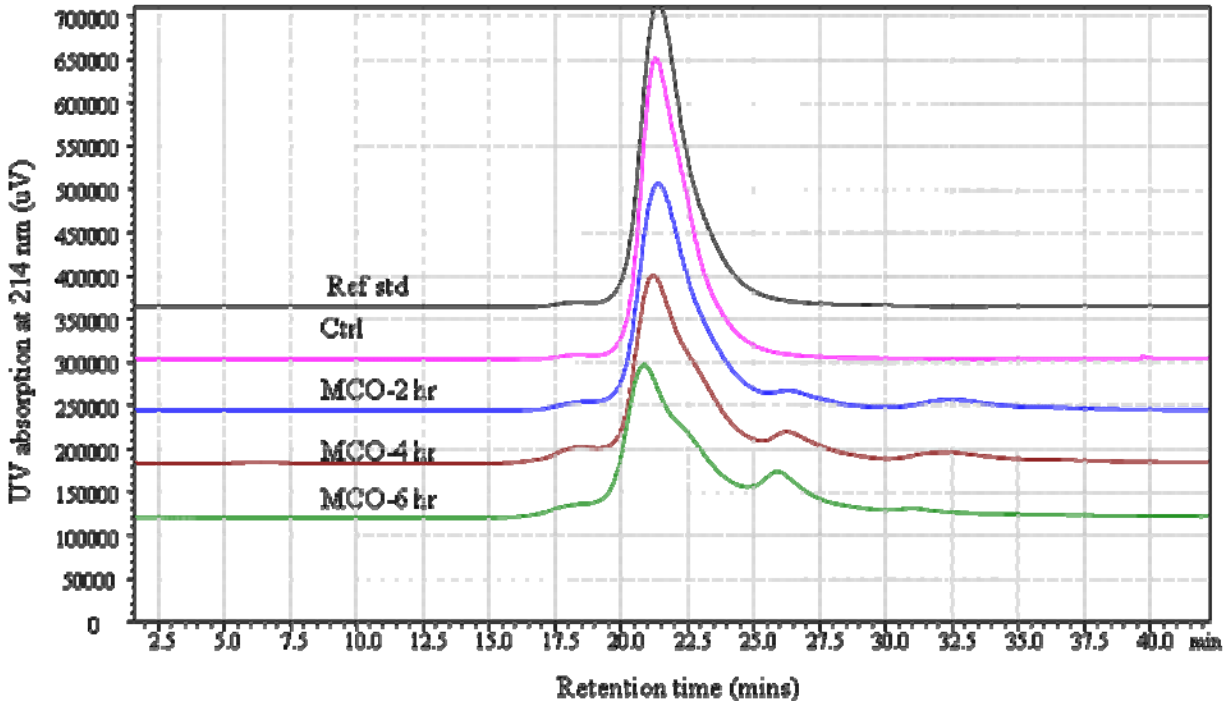

Fig. 1. SEC-UV Chromatograms (λ = 214 nm) to monitor IgG1 degradation induced by metal-catalyzed oxidation (MCO) using $CuCl_2$/L-ascorbic acid/O_2 system.

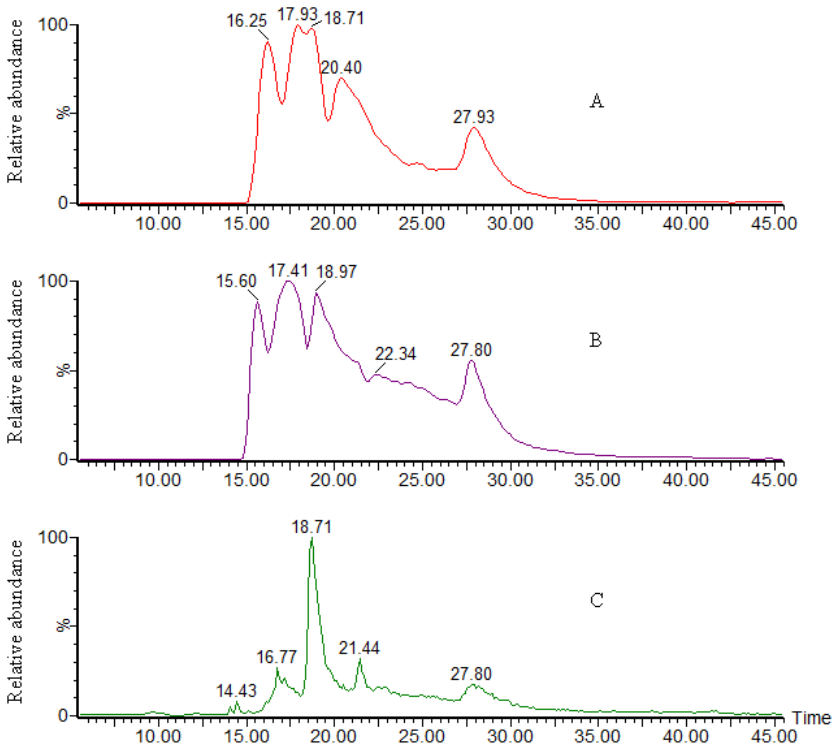

Fig. 2. RPLC-MS chromatograms of IgG1 reference standard (A), and the control (B) as well as oxidized IgG1 (C) after cleavage, reduction and alkylation.

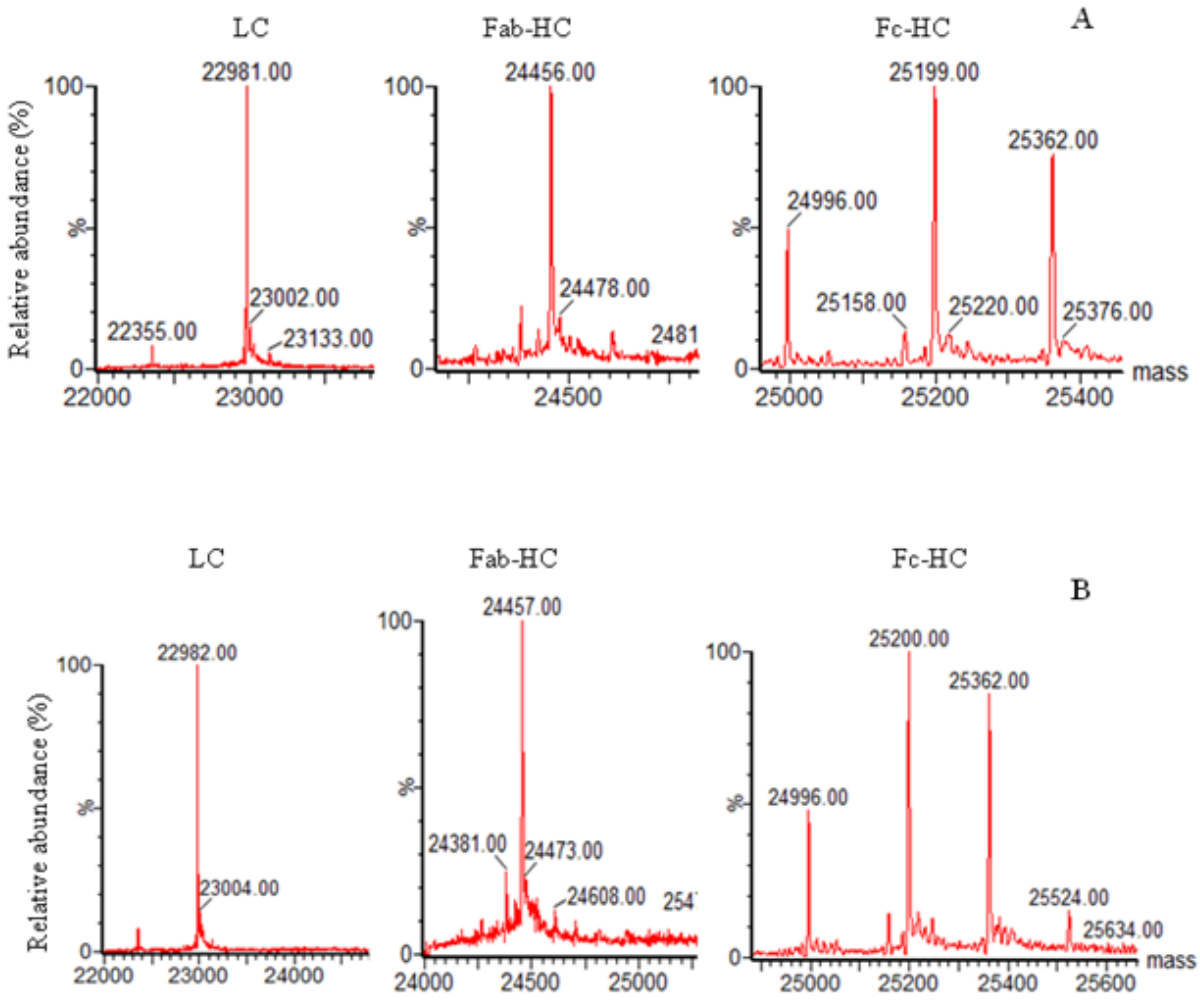

Fig. 3. Identification of the components detected by RPLC-MS for IgG1 reference standard (Fig. 2A) and the control (Fig. 2B). IgG1 was cleaved at hinge region and disulfide bonds were reduced and alkylated. The mass for each detected component was obtained by deconvolution of the respective mass to charge *(m/z)* ion distribution using MaxEntropy.

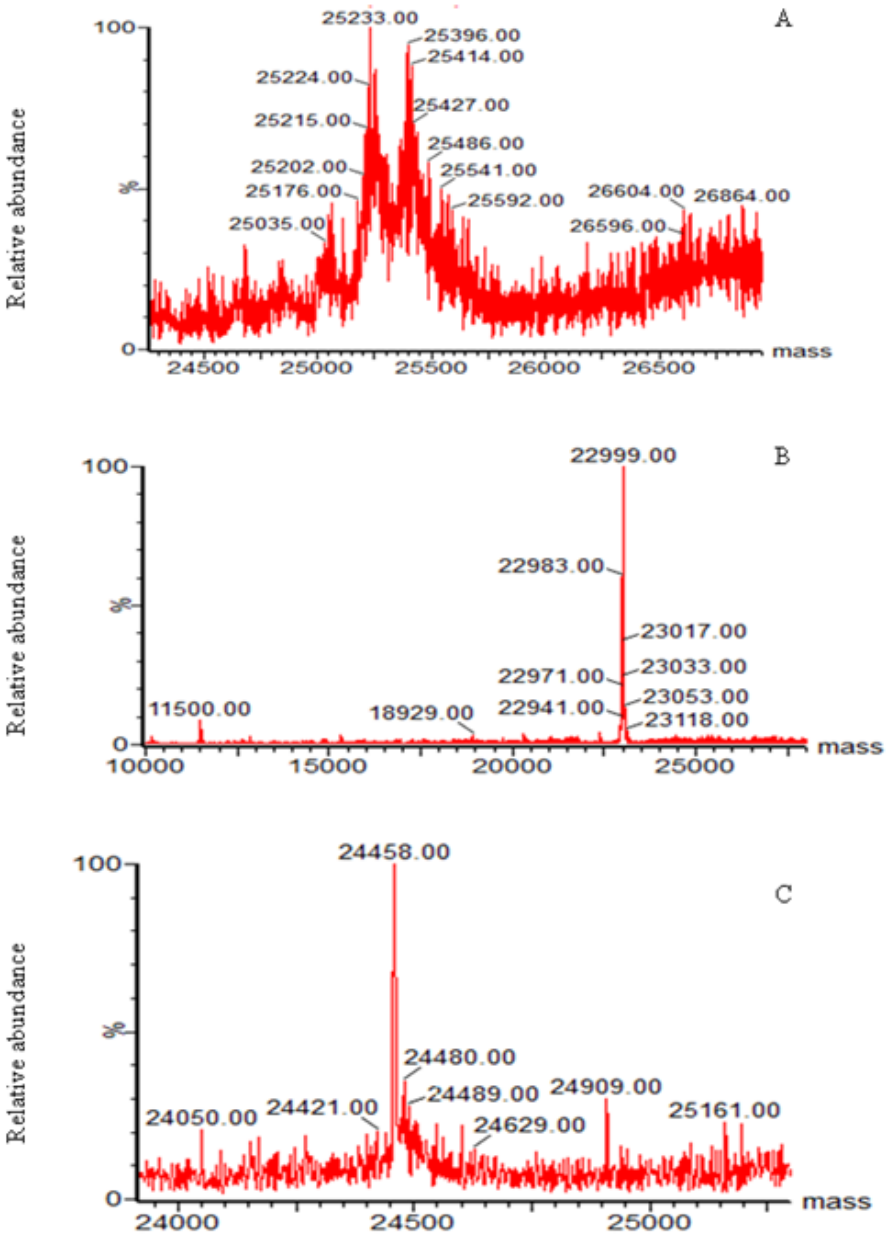

Fig. 4. Identification of the components detected by RPLC-MS for oxidized IgG1 (Fig. 2C). IgG1 was cleaved at hinge region and disulfide bonds were reduced and alkylated. The mass for each detected component was obtained by deconvolution of the respective mass to charge *(m/z)* ion distribution using MaxEntropy.

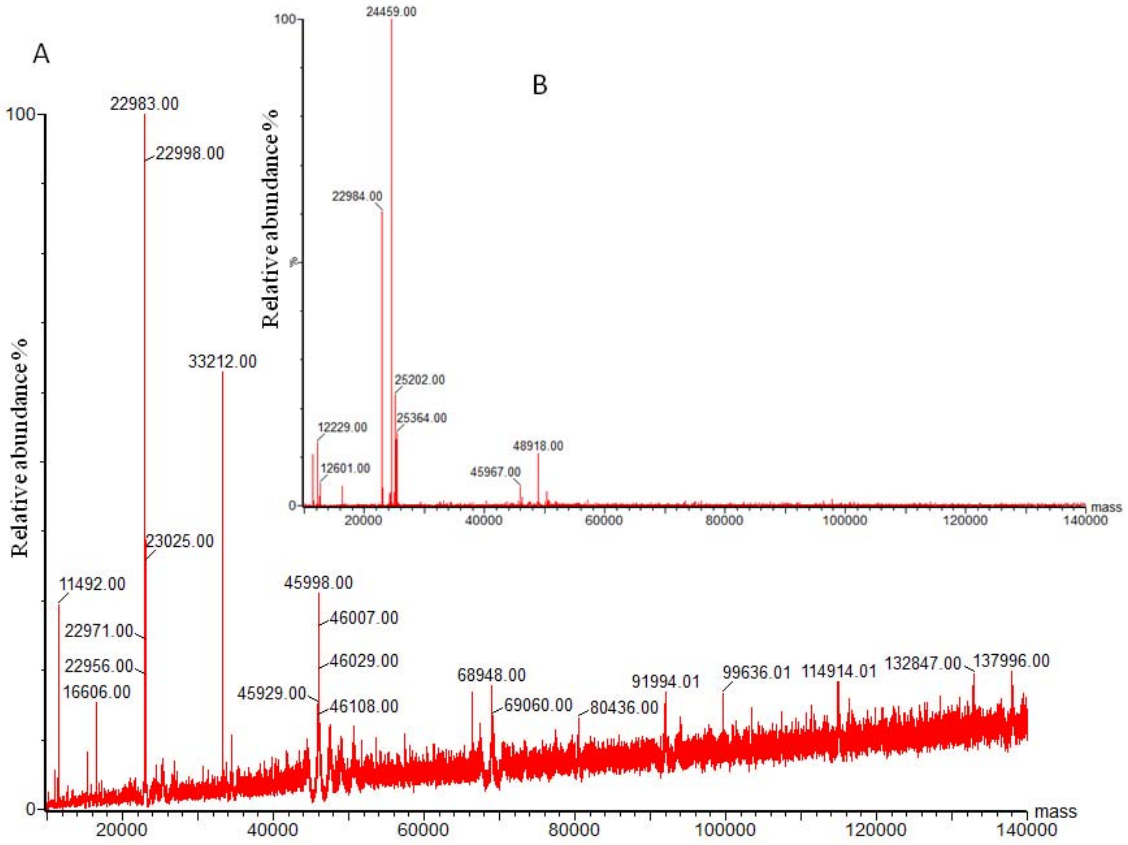

Fig. 5. Combination of all the MS scans of oxidized IgG1 (A) and non-oxidized IgG1 (B).

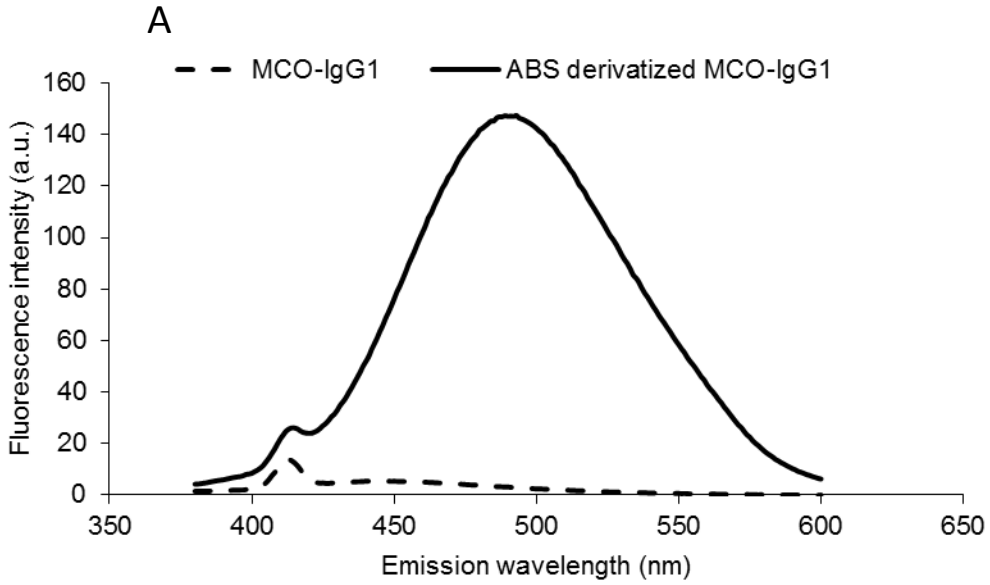

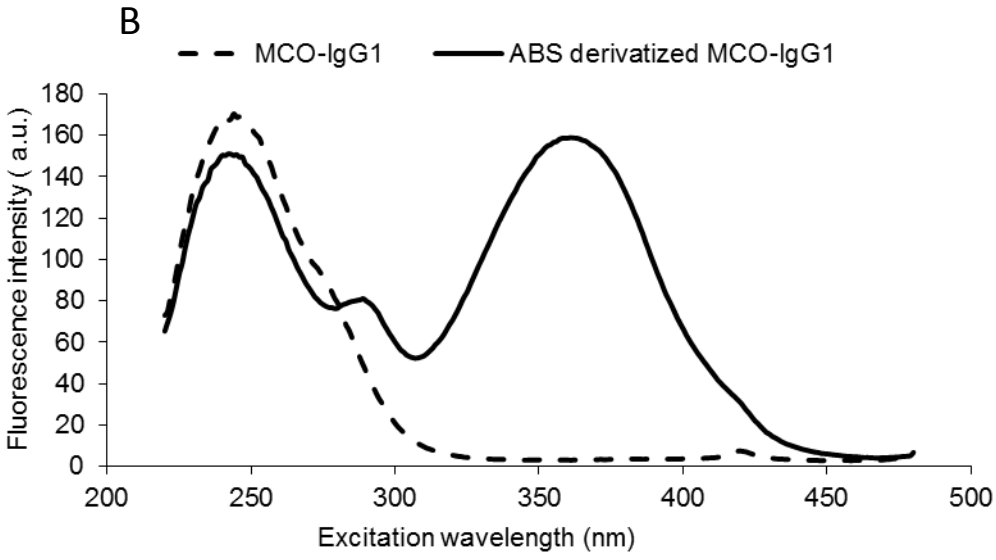

ization: emission

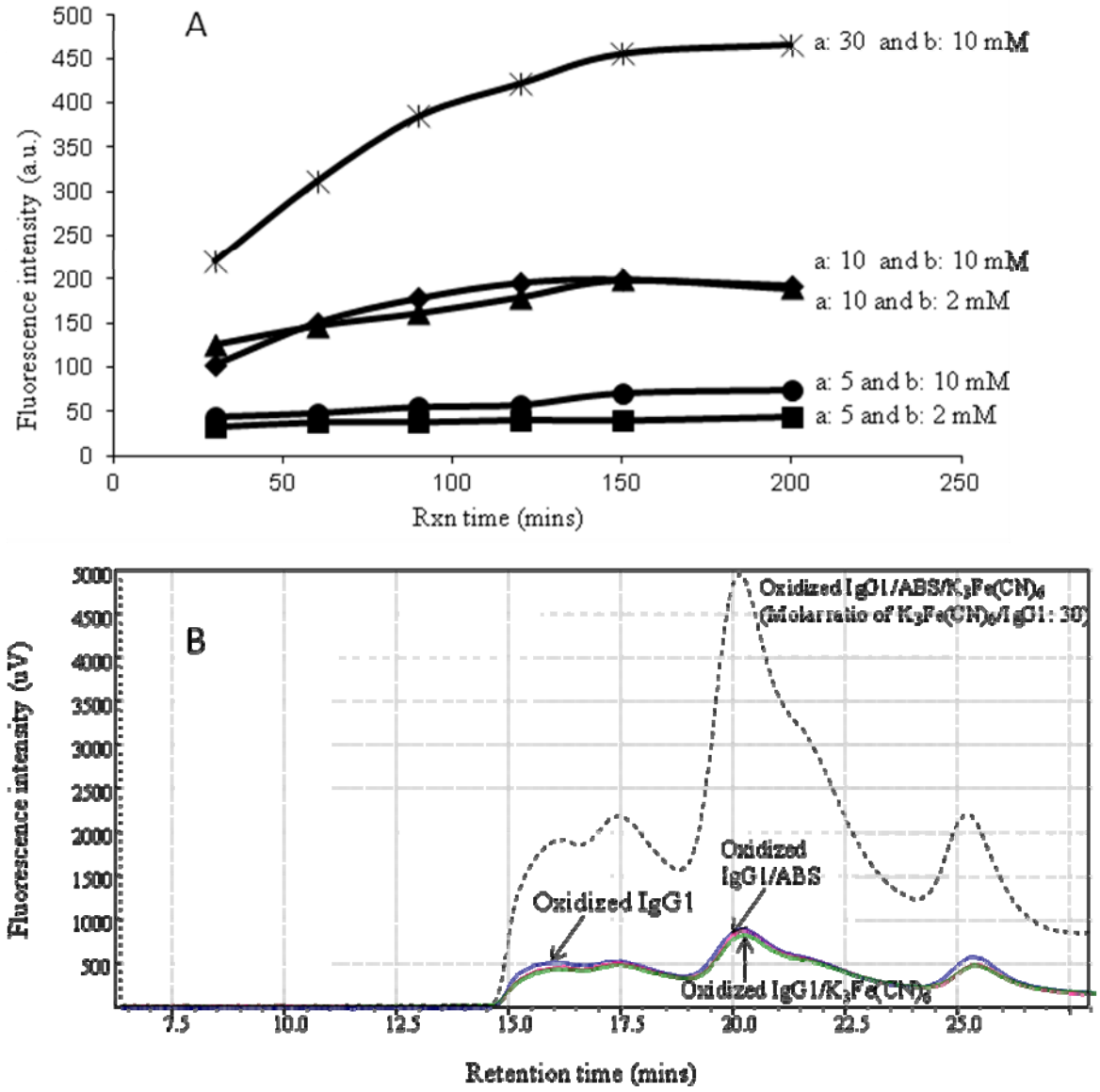

Fig. 7. Optimization of ABS derivatization of oxidized IgG1 by fluorescence at λ_{em} = 490 nm (λ_{ex} = 360 nm) at different molar ratios of $K_3Fe(CN)_6$ to IgG1 (a) and ABS concentrations (b) over the time course of 200 mins (A) and SEC-Fluorescence chromatograms (λ_{em}/ λ_{ex} = 490 nm/360 nm) (B) (the %RSD is within 0.5% with triplicate measurements)

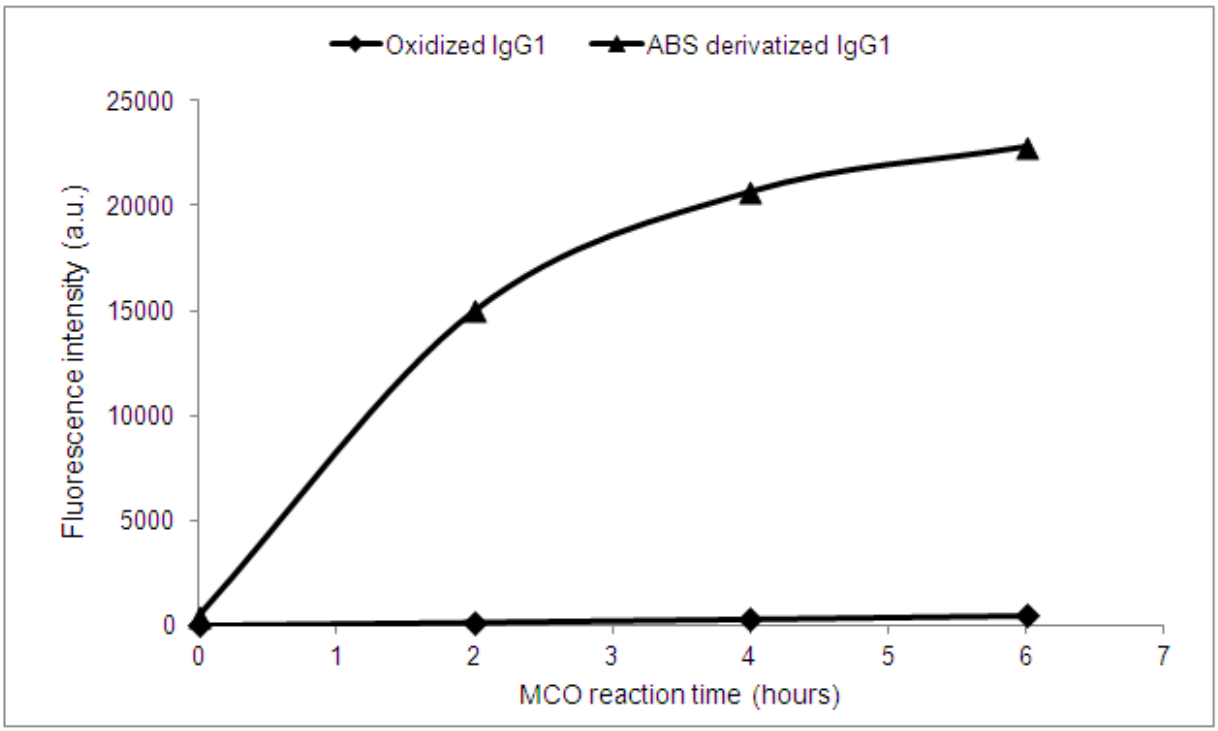

Fig. 8. Fluorescence intensity at λ_{em} = 490 nm (λ_{ex} = 360 nm) acquired by fluorescence spectrometer to monitor IgG1 degradation over the time course of 6 hours induced by metal catalyzed oxidation by using the optimized ABS derivatization condition: molar ratio of 30:1 of $K_3Fe(CN)_6$ to IgG1 at presence of 10 mM ABS at room temperature in the dark (%RSD is within 0.5% for triplicate measurements).

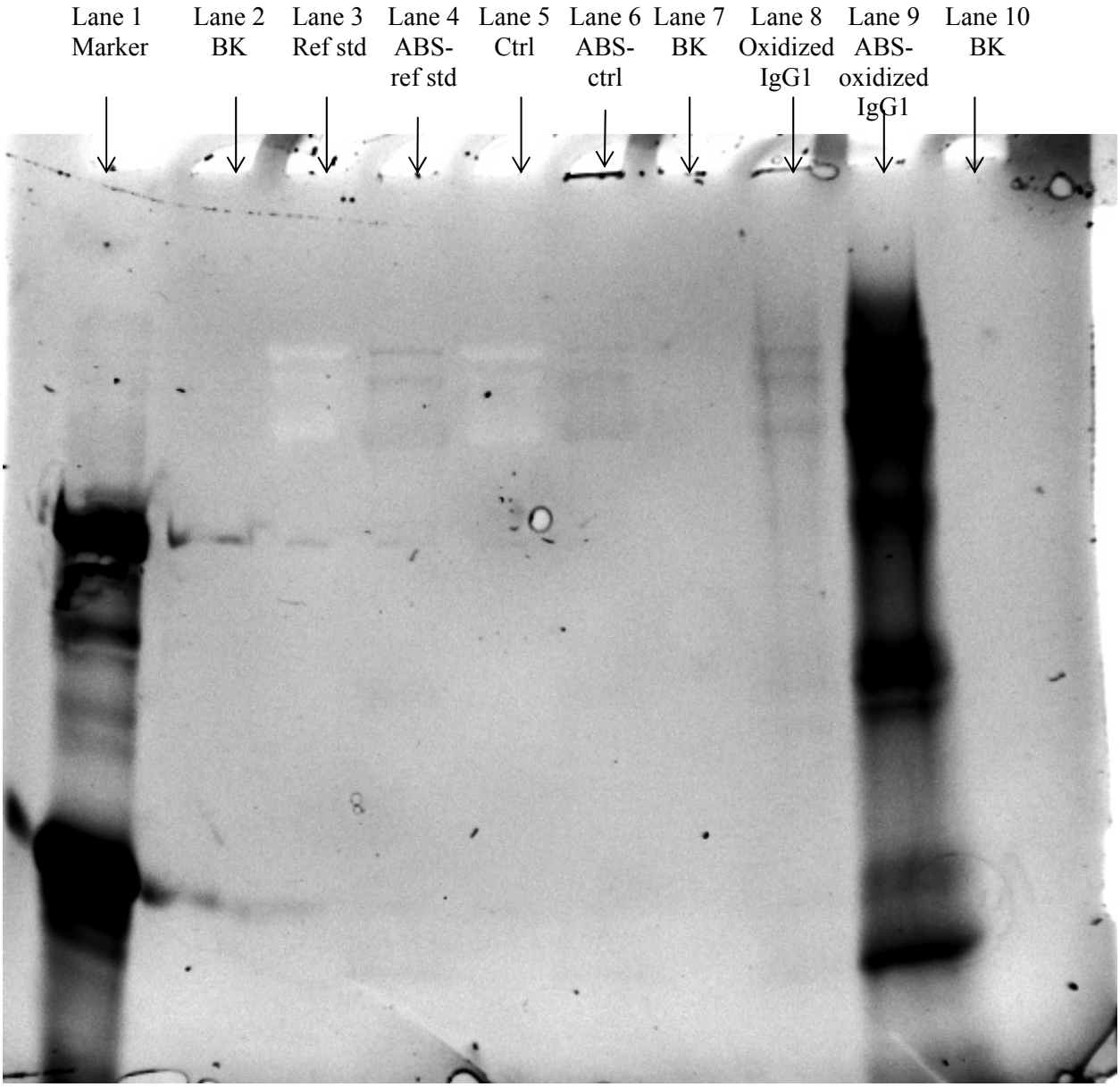
Lane 1
Marker
Lane 2
BK
Lane 3
Ref std
Lane 4
ABS-
ref std
Lane 5
Ctrl
Lane 6
ABS-
ctrl
Lane 7
BK
Lane 8
Oxidized
IgG1
Lane 9
ABS-
oxidized
IgG1
Lane 10
BK

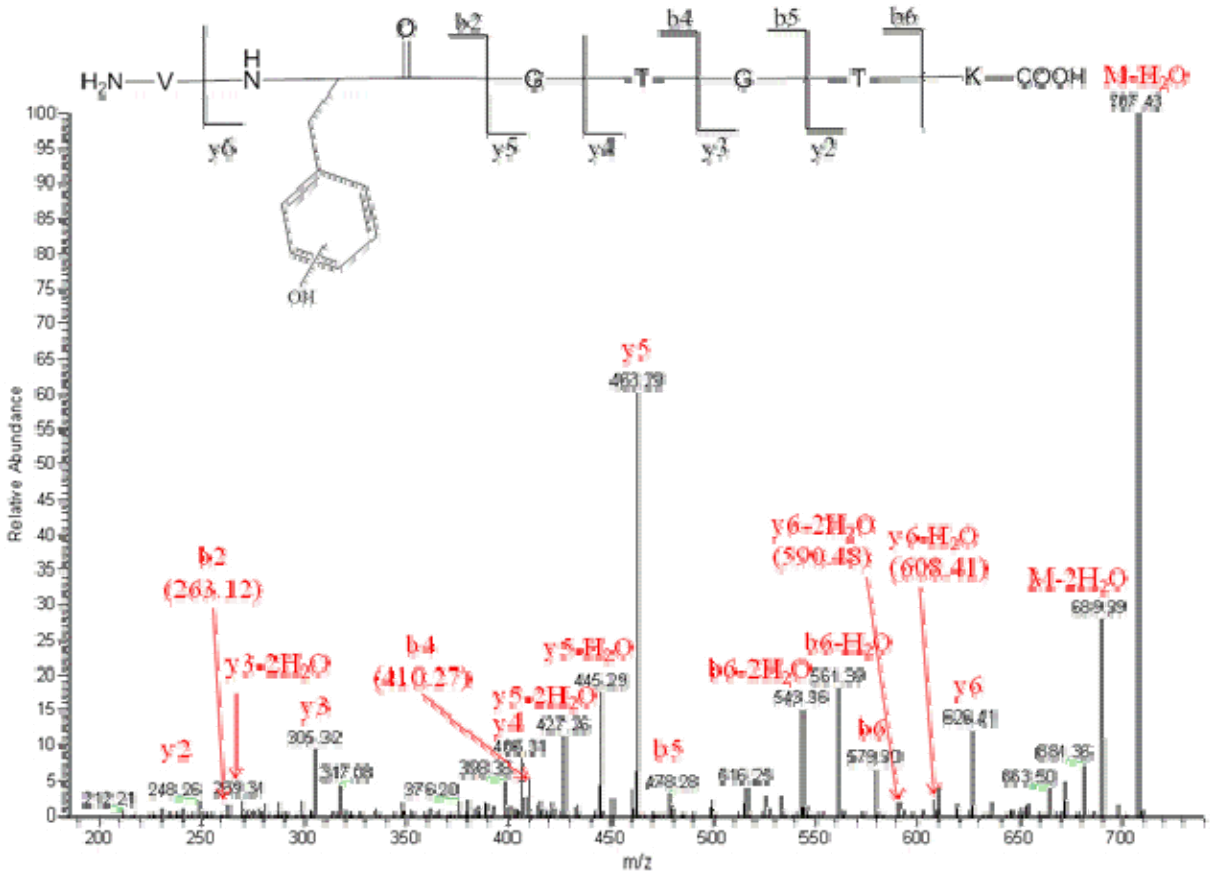

Fig. 10. Collision induced dissociation (CID) obtained by a FT-ICR MS for the peptide VF(+16 amu)GTGTK [102:108]. The peptide is the result of the tryptic digestion of oxidized IgG1 after ABS derivatization.

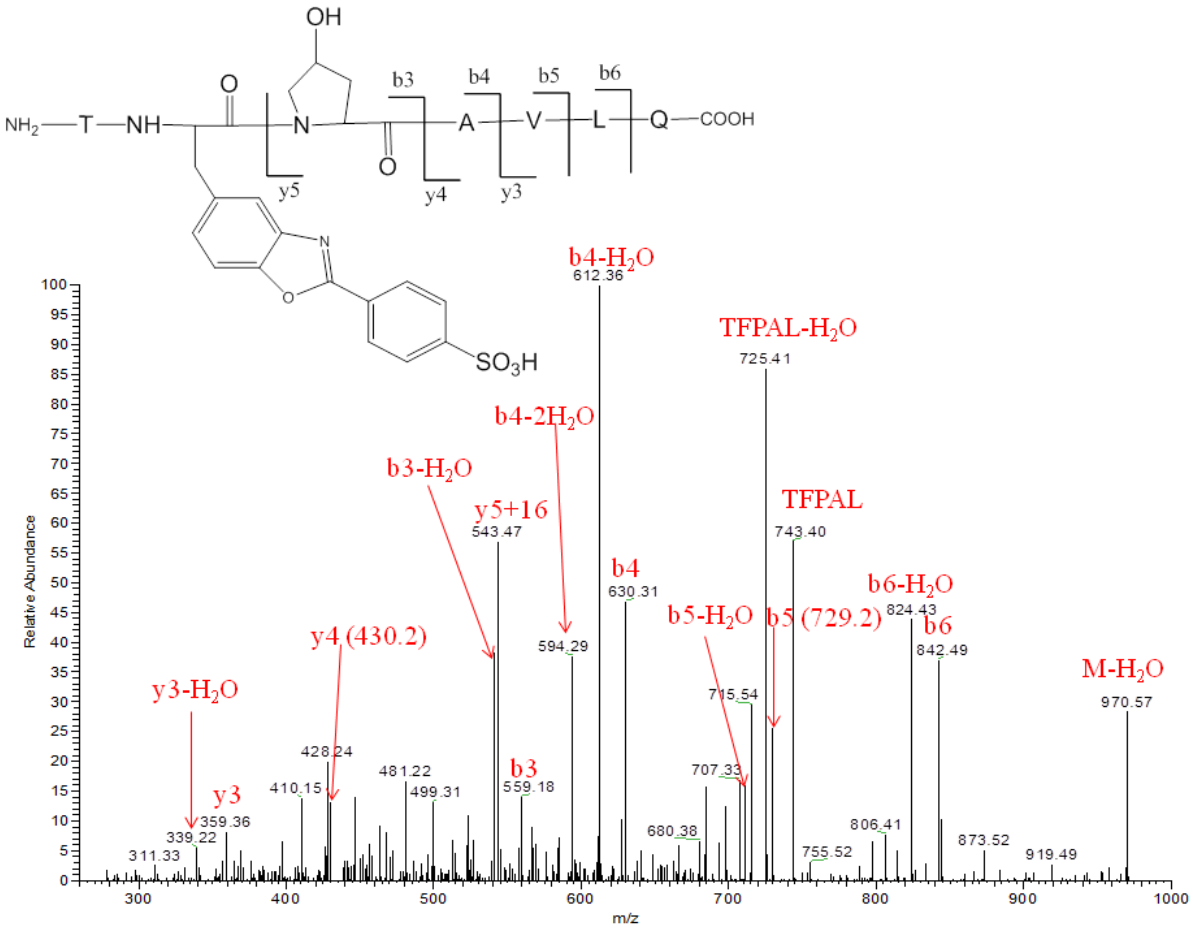

Fig. 11. Collision induced dissociation (CID) obtained by a FT-ICR MS for the peptide TF(+181 amu)P(+16 amu)AVLQ. The peptide is the result of the tryptic digestion of oxidized IgG1 after ABS derivatization.

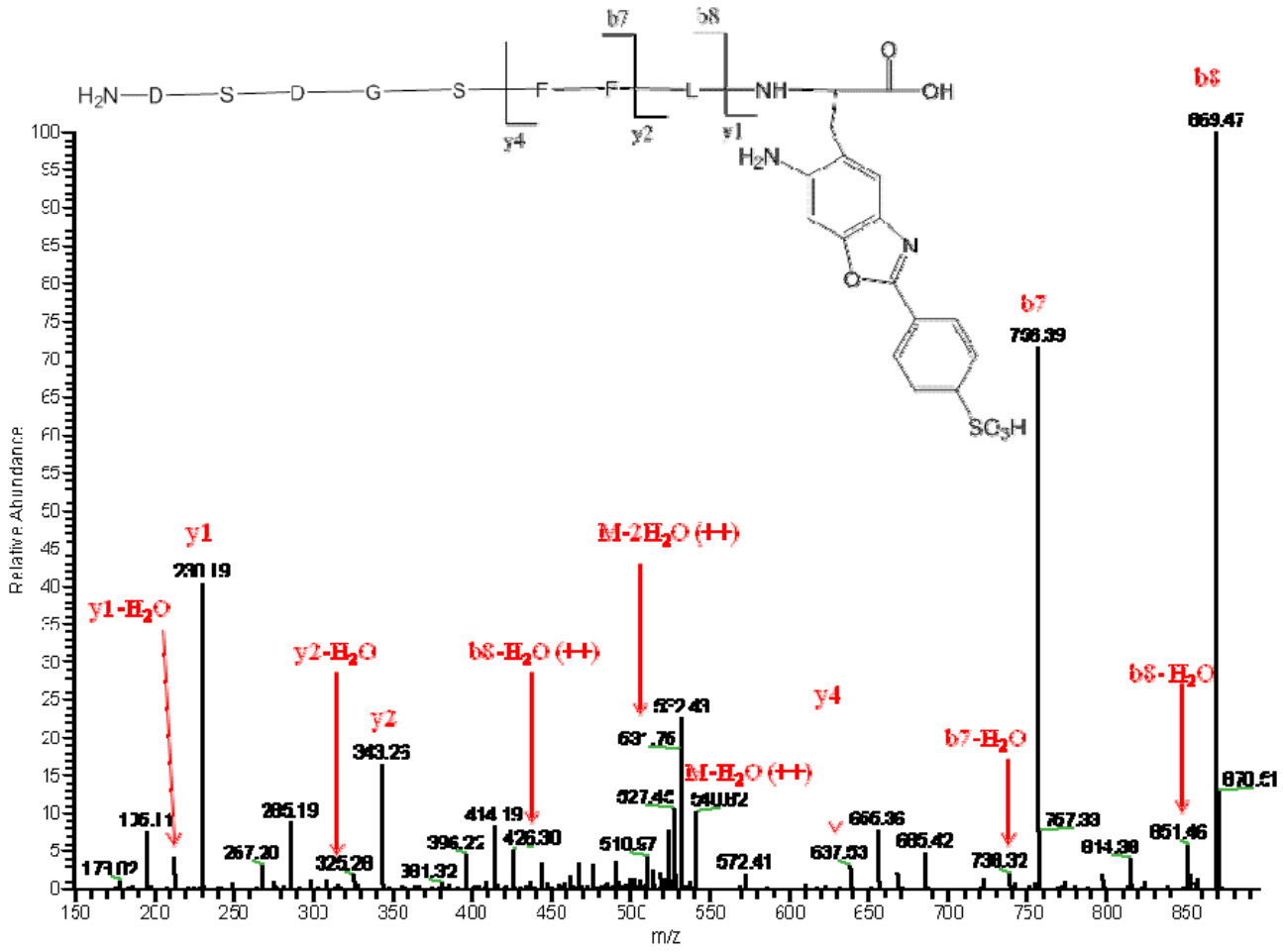

Fig. 12. Collision induced dissociation obtained by a FT-ICR MS for the peptide, DSDGSFFLY(+196 amu). The peptide is the result of the tryptic digestion of oxidized IgG1 after ABS derivatization.

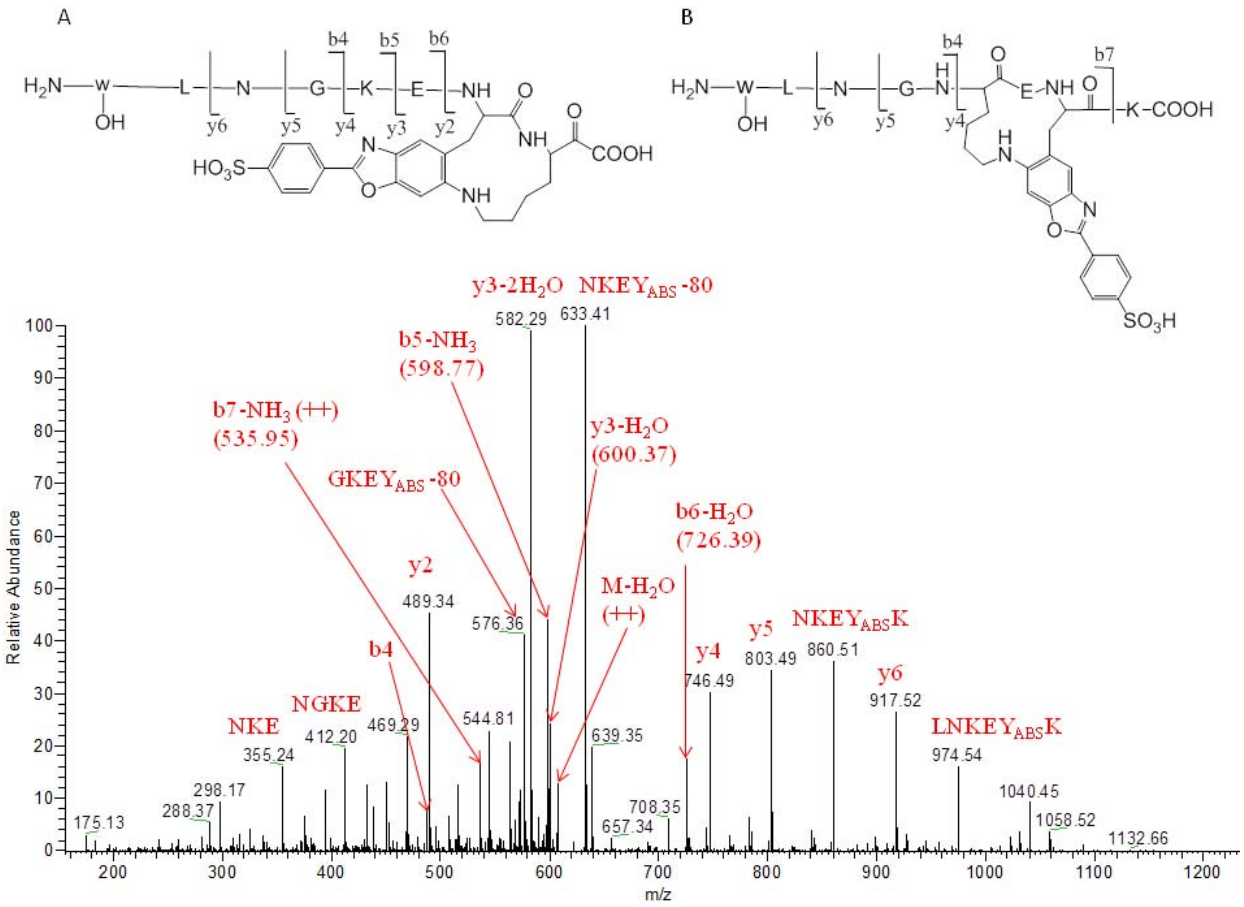

Fig. 13. Collision induced dissociation obtained by a FT-ICR MS for the peptide W(+16 amu)LNGKEY(+195 amu)K. The peptide is the result of the tryptic digestion of oxidized IgG1 after ABS derivatization.

Chapter 4: Physical Instability: Impact of Metal Ions on IgG1 Conformation and Aggregation

Table of Contents

4.1 Introduction

Trace levels of metal ions are inadvertently but inevitably present in biotherapeutic products. They either arise from the excipients and/or leach from the contact materials during product manufacturing, shipping and/or storage process. Metal ions such as tungsten, iron, nickel, zinc, barium, manganese, and chromium can leach from prefilled syringes, glass vials, plastic container, rubber stoppers and/or stainless steel [1-7]. In our earlier reports, the leaching of iron, chromium and nickel from stainless steel has been systemically examined [7-8]. It is well known that trace levels of metal ions can induce protein degradation such as oxidation, aggregation, fragmentation and the formation of insoluble particles [9-17].

In vivo, it is believed that one third of the proteins bind to metal ions such as calcium and iron as cofactors in their native conformation so that the proteins are stabilized and/or perform their functions properly [18-22]. Excessive metal ions present in biological systems have been reported to be related to neurodegenerative diseases, with the associated protein aggregation potentially induced by metal ions [10, 15]. Protein conformational change induced by metal ions is a viable protein degradation route *in vitro* [10, 15, 17, 23-24]. The structure of recombinant human factor VIII was affected by the presence of metal ions such as Al^{3+}, Tb^{3+}, Co^{2+} and Fe^{3+}, resulting in the acceleration of protein aggregation and inactivation [23]. It was proposed that the detectable structural change was a result of binding of metal ion to the protein. Serum transferring protein exhibited a different tertiary structure upon binding of Fe^{3+} compared to its native state, characterized by ultraviolet-visible (UV) spectroscopy, near UV-circular dichroism (CD) spectroscopy, and small-angle x-ray scatting [24]. A conformational change of α-synuclein was observed to be correlated with aggregation and fibril formation due to the presence of metal ions such as Al^{3+}, Cu^{2+}, Fe^{3+}, Co^{2+} or Mg^{2+}

[15]. Chen, *et al* observed that Al^{3+} and Zn^{2+}, but not Cu^{2+} and Fe^{3+}, induced amyloid-β (Aβ) conformational change, exposing a larger hydrophobic area [55]. The authors concluded that this conformational change destabilized αβ, resulting in the acceleration of aggregation. Previously, we had evaluated the effect of disodium edetate (Na_2EDTA) and diethylenetriaminepentaacetic acid (DTPA) as iron chelators to prevent metal-catalyzed destabilization of a monoclonal antibody (mAb) [17]. We found that the mAb tertiary structure was perturbed when the amount of chelators was not sufficient to bind all the metal ions. Even though the tertiary structure perturbation was subtle, it was sufficient to induce protein oxidation, aggregation, deamidation and fragmentation. Isothermal titration calorimetry (ITC) experiments showed that Fe^{3+} bound to mAb at a molar stoichiometry of 20 ±1 per mAb with a Kd of 0.18 mM [17]. The binding was suggested to be responsible for mAb tertiary structure perturbation. To further explore the conformational impact of Fe^{3+} on the mAb and the resulting degradation mechanism, we have systematically investigated the changes in mAb conformation via Far-UV CD, intrinsic/extrinsic fluorescence, and chemical denaturation by guanidine hydrochloride (GdnHCl). Also, the resulting degradation products of aggregation were studied in a real-time stability manner. Furthermore, we built a homology model of the full length antibody and identified potential Fe^{3+} binding sites in the mAb native structure and their surface exposure. These studies provided us insights into the mechanism(s) of mAb and Fe^{3+} interaction. For simplicity, the testing solution was only composed of the mAb and Fe^{3+} in 20 mM histidine buffer at pH5.5 under deaerated conditions. The same therapeutic quality IgG2 mAb as in our previous study [17] was chosen as the model compound in this study.

Here we report that increasing levels of Fe^{3+} in the mAb solutions result in greater levels of mAb degradation, as monitored by aggregation. The mAb tertiary and quaternary structure were perturbed, but not secondary structure. Chemical denaturation of the mAb by GdnHCl suggested that the unfolding process changed from a two-step transition to a broad single step transition at high molar ratios of Fe^{3+} to mAb. A homology model of the mAb was built. The model showed that Fe^{3+} binding residue clusters (putative Fe^{3+} binding sites) are spatially and sequentially proximal to aromatic residues and aggregation prone regions (APRs) located in the complementarity determining regions (CDRs) of the mAb. Putative Fe^{3+} binding sites were also identified in other parts of the mAb, including the hinge region and CH2:CH3 domain interfaces. These molecular level observations help us rationalize the experimental results on aggregation of the mAb upon Fe^{3+} binding.

4.2 Materials and Methods

4.2.1 Materials

An in-house produced therapeutic quality IgG2 mAb in 20 mM histidine (pH5.5) was utilized. USP/Ph.Eur. grade L-histidine, analytical grade ferric chloride ($FeCl_3$), bis-ANS (4,4'-dianilino-1,1'-binaphthyl-5,5'-disulfonic acid, dipotassium salt), 8M GdnHCl stock solution and concentrated hydrochloride acid (HCl) were purchased from Sigma-Aldrich Chemical Co. (St. Louis, MO, USA). Polyvinylidene fluoride (PVDF), 0.22 µm, syringe filter (33 mm) was obtained from Millipore Inc. (Bedford, MA, USA).

4.2.2 Preparation of the test solutions

The mAb solution in 20 mM histidine buffer at pH5.5 was first concentrated to 31.7 mg/mL using a lab-scale tangential flow filtration (TFF) unit with 50 kDa cut-off membrane (Millipore Inc., Barrington, IL, USA). An appropriate amount of 31.7 mg/mL mAb stock

solution and 1 mg/mL $FeCl_3$ stock solutions in 20 mM histidine (pH5.5) were compounded so that a series of test solutions were obtained at discrete molar ratios of Fe^{3+} to mAb of 0, 10, 20, 40, 60 and 80. The mAb concentration in all test solutions was maintained at 5 mg/mL. The formulations were sterile filtered through a 0.22 μm PVDF filter. The actual mAb concentrations in the solutions were measured by UV spectrometry at 280 nm using an extinction coefficient of 1.43 au. mL per mg per cm (1 mg/mL at 280 nm) determined by the Edelhoch method [25]. 2 mL aliquots of the formulations were filled into 2-mL type I glass vials (washed and autoclaved), purged with nitrogen and stopper-sealed. The vials were stored in stability chambers maintained at 25ºC over 35 days. At designated time points, aggregate quantification and biophysical characterization were performed on the samples using three individual vials, to explore the effects of Fe^{3+} on mAb stability and its structure over the monitored time course. An aliquot of 1 mL of the test solutions was filled into 2-mL type I glass vials for chemical denaturation by GdnHCl.

4.2.3 Aggregation determined by size exclusion chromatography (SEC)

The aggregation of the mAb was monitored by SEC. The separation of monomer, aggregates (high molecular weight species, soluble aggregates) and fragments (low molecular weight species) were achieved by isocratic elution over 40 minutes (0.7 mL/min) on an Agilent 1100 system equipped with G3000SWXL and G2000SWXL columns (7.8 x 300 mm, Tosoh Biosciences or equivalent) in tandem. The mobile phase consisted of 200 mM phosphate and 50 mM NaCl at pH 7.0. The mAb was diluted to 1 mg/mL using the mobile phase and an aliquot of 20 μL was injected into column. An in-house reference standard was injected at the beginning, after every 6 samples, and at the end of the sequence to ensure system performance by monitoring both peak area count and monomer elution

time. The elution was monitored at 214 nm and the relative percentage of the monomers, soluble aggregates and fragments was reported. The soluble aggregates are the total percent of high molecule weight species including primarily dimeric and higher order species. The limit of quantitation (LOQ) for soluble aggregates was determined to be 0.5% with a variability of 0.2%. For each time point, three individual samples were analyzed and the results were averaged.

4.2.4 Sodium sulfate-polyacrylamide gel electrophoresis (SDS-PAGE)

SDS-PAGE was employed to evaluate the identity and purity of the mAb. The mAb concentration was diluted to 0.8 mg/mL using 2x sample buffer for non-reducing SDS-PAGE. Mark 12 molecular weight standard was used as the reference standard. An aliquot of 5 µL of the reference standard, and 10 µL of samples and blanks were loaded onto gel. The separation was performed on precast polyacrylamide gels (NuPAGE 4-12% Bis-Tris, 1.0 mm x 12 well) using a mini-gel apparatus (Invitrogen Cell SureLock^{TM}) using NuPAGE$^{®}$ MES SDS running buffer for 35-45 minutes at a voltage of 200 V. The gel was fixed for 10 minutes, stained using Colloidal Blue for 12 hours and then destained with MilliQ water for 4 hours. All reagents and gels utilized here were purchased from Invitrogen (Carlsbad, CA, USA). The bands were analyzed using the molecular dynamics personal densitometer (PDQC-90) with the FragmeNT software.

4.2.5 Inductively coupled plasma – mass spectrometry (ICP-MS)

The concentrations of Fe^{3+} in the test solutions were measured by ICP-MS utilizing an Agilent 7500 CX ICP-MS system equipped with an autosampler. An aliquot of 50 µL of mAb samples were hydrolyzed using 70% nitric acid (Omnitrace-NX0407) (EMD Chemicals Inc, Gibbstown, NJ, USA) at a volume ratio of 1:3 (sample: nitric acid) for 15 minutes at 80-

90°C in a water bath. Upon completion of hydrolysis, the samples were cooled to ambient temperature and then diluted to 5 mL with 1% (v/v) nitric acid before analysis. The blanks were treated using the same procedure as described above. Scandium (45) was used as the internal standard and the "hydrogen mode" was utilized to analyze the samples. Prior to sample analysis, an external calibration curve was established, giving a linear range of 1-500 ppb with a LOD of 1 ppb. A 50 ppb standard was analyzed every 6 samples to ensure system performance.

4.2.6 Circular dichroism spectroscopy (CD)

Far UV-CD spectra for all the samples were acquired on a ChiraScan^{TM} (Applied Photophysics, Leatherhead, Surrey, UK) at ambient room temperature. Samples were diluted to 0.2 mg/mL using milliQ water. The blanks were diluted in the same way as the samples. A 1 mm quartz cuvette was used. The sample volume needed for analysis was 400 μL. The spectra of the samples and of the respective blanks were acquired by scanning from 200 to 260 nm with a scan rate of 20 nm / minute, a resolution of 0.5 nm and a response time of 1 second. Each acquired spectrum was the average of three individual samples (three accumulations for each sample). Sample spectra were corrected by subtracting the corresponding blank spectra.

4.2.7 Intrinsic and extrinsic fluorescence

Intrinsic and extrinsic fluorescence were studied using a Cary Eclipse Fluorescence Spectrometer (Varian Inc, Lake Forest, CA, USA). A 1 cm rectangular cuvette was used. For intrinsic fluorescence, the mAb samples were diluted to 0.2 mg/mL using 20 mM histidine buffer at pH5.5. The protein was excited at 295 nm and the Trp-dominated emission was recorded from 300 to 450 nm. For extrinsic fluorescence, bis-ANS was used as the

fluorescence dye. The sample was diluted to 1 mg/mL in 20 mM histidine (pH5.5) containing 50 μM bis-ANS. The mAb was excited at 385 nm and extrinsic bis-ANS fluorescence was recorded from 400 to 600 nm. The excitation and emission slits were set at 5 nm. All the spectra were analyzed using the Microcal Origin 7.0 (Piscataway, NJ, USA) software. Both Trp-dominated intrinsic and bis-ANS fluorescence spectra of the respective blanks were acquired using the same methods as the mAb samples. Each sample spectrum was corrected by subtracting its respective blank control spectrum to eliminate the contribution of the formulation matrix. At each time point, the spectra reported represent the average of three independent samples with three runs for each sample.

4.2.8 Chemical denaturation of the mAb by GdnHCl

The mAb chemical denaturation was studied with GdnHCl. 8M GdnHCl stock solution in water was spiked into mAb solution and then diluted with 20 mM histidine (pH5.5), resulting in a series of test solutions containing 0.4 mg/mL mAb with GdnHCl at the concentrations of 0.0, 0.5, 1.0, 1.5, 2.0, 2.5, 3.0, 3.5, 4.0, and 4.5M, respectively. The solutions were shaken for 10 minutes at 200 rpm and then incubated for 1 hour at 37°C to reach equilibrium. A feasibility study demonstrated that fluorescence intensity did not change for incubations up to 48 hours. Denaturation was monitored by intrinsic fluorescence using a plate reader of 96-well plate format (Spectra Max M5, Molecular Devices, Sunnyvale, CA, USA). The 96-well plate was an optical black plate with clear bottom from Nalge Nunc International (Rochester, NY, USA). The mAb was excited at 295 nm and the fluorescence was recorded from 310 to 400 nm, 2 nm per step. Before the measurement, the solutions on the plate were automatically mixed for 5 second and the settling time was set at 100

milliseconds. The plate was incubated at 37^{o}C. The denaturation experiment was repeated twice.

4.2.9 Homology based model building for full length mAb

The mAb used in this study was a humanized IgG2 mAb. The crystal structure of a full length murine IgG2a antibody from the Protein Data Bank (PDB) (www.pdb.org, 1IGT) was used as an overall template for this mAb, after replacing its hinge region with that found in human IgG2 mAbs [26]. The murine IgG2a structure (1IGT) was chosen over that of a full length human IgG1 antibody (1HZH) because its hinge region is more similar in sequence to the human IgG2 hinge region. Moreover, all the inter-chain disulfide bonds are intact in 1IGT and the coordinates of all heavy (non hydrogen) atoms in this region are available. A separate model for the Fv (fragment variable) portion of the mAb in this study was built using Antibody Modeler under MOE2010.10 and superimposed onto the Fv portion of the modified 1IGT template. The high resolution (1.6 Å) crystal structure for the Fc (fragment constant) portion of the human IgG (PDB entry 1L6X) was also superimposed onto the one of the modified 1IGT template. These superimpositions enabled construction of a chimeric template which retained the overall spatial disposition of the domains seen in the murine IgG2a mAb. However, some of the individual domains (Fv and Fc) were replaced with the human ones.

One thousand (100 backbone models and 10 side chain models per backbone model) intermediate homology models were generated and optimized *via* energy minimization using the homology model module in MOE2010.10. In the calculations, all-atom AMBER99 force field was used. A cut off of 12 Å with switching starting at 10 Å was applied to non-bonded interactions. Generalized Born implicit solvation was employed and interior and exterior

dielectric values were 4 and 80, respectively. The one thousand intermediate models were ranked using Generalized Born Volume Integral (GB/VI) score and the best ranked model was selected for further optimizations. The final model was checked for stereo-chemical precision and was found to be of high quality. This model was used to identify potential Fe^{3+} binding residues and their clusters. Inter-chain disulfide bonds in human IgG2 undergo scrambling when subjected to redox potential. A recent molecular dynamic study indicated that conformational heterogeneity of human IgG2 hinge region results in potential non-canonical inter-chain disulfide bond pairings [26]. However, for the purpose of this study, the canonical IgG2 disulfide bonding scheme [27] was retained and models with non-canonical inter-chain disulfide schemes were not created.

4.2.10 Prediction of APR

Potential APRs in this mAb sequences were identified using a combination of Tango (Fernandez-Escamilla, 2004) and PAGE (Tartaglia, 2005) as described in an earlier publication from our group [28]. To complement the predictions from Tango and PAGE, we have also used a relatively new aggregation prediction program, Waltz (VIB, 2010). It uses position-specific scoring matrices and performs better at recognizing polar APRs [29].

4.2.11 Identification of putative Fe^{3+} chelating sites

Goyal and Mande [30] have surveyed a large number of protein structures to study the characteristics of metal binding residues which coordinate divalent and trivalent metal ions. Their survey indicates that Fe^{3+} primarily binds to Glu, Asp and His residues. Thus, to identify potential Fe^{3+} coordinating sites, we looked for Asp, Glu and His residues in the mAb sequence and structure as the primary sites. In the mAb homology model, all Cys residues are disulfide bonded. In the disulfide bonded form, Cys is not a major residue

involved in Fe^{3+} binding [56]. However, if the disulfide bonds are broken, Cys residues can also bind Fe^{3+}. The primary Fe^{3+} binding sites, identified in the mAb structure, were expanded into Fe^{3+} binding hot spots by including Cys, Asp, Glu and His residues that are spatially proximal (neighboring) to a primary site residue. The criterion for selecting spatially proximal residues is as following: a pair of amino acid residues, A and B, are considered to be spatially proximal if at least one non-hydrogen (heavy) atom belonging to residue A is within 4.5 Å distance from a heavy atom in the residue B. For our purpose, residue A is a primary Fe^{3+} binding residue (Asp, Glu or His) [39]. The expansion of a primary site continued until all Fe^{3+} binding residues spatially proximal to the primary residue were accounted for. Two Fe^{3+} binding hotspots were merged together if they contained at least one common residue. The Fe^{3+} binding hotspots thus obtained are the putative Fe^{3+} chelating sites in the mAb structure and are expected to bind multiple Fe^{3+} ions. Each putative Fe^{3+} chelating site was evaluated for its solvent exposure to measure its location in the mAb surface. The solvent exposure of a putative Fe^{3+} chelating site was measured by averaging the solvent accessible surface areas (SASA) of its residues. A putative Fe^{3+} chelating site was considered to be on surface if its average SASA $\geq$ 20%.

4.3 Results and Discussion

Various levels of Fe^{3+} were spiked into a mAb solution in 20 mM histidine at pH5.5 to obtain a series of solutions containing 5 mg/mL mAb with discrete molar ratios of Fe^{3+} to mAb. The actual molar ratios of Fe^{3+} to mAb (ICP-MS and UV280 determinations) were: 0, 8, 18, 35, 54 and 75. The solution without Fe^{3+} served as a negative control. Three individual vials for each molar ratio were pulled for aggregate analysis at defined time points from storage at 25°C. Intrinsic fluorescence was monitored at each tested time point. Extrinsic

(bis-ANS) fluorescence was recorded for samples at the initial and last time points. Similarly, far UV-CD spectra were also recorded at initial and final time points.

4.3.1 Antibody degradation by aggregation

The levels of aggregates monitored by SEC over 819 hours in the solutions containing different molar ratios of Fe^{3+} to the mAb are shown in Fig. 1. The results are plotted as % soluble aggregates *versus* duration of incubation. At each time point, the reported level of soluble aggregates represents the average of three individual samples with its relative standard deviation (RSD) shown by an error bar. It appears that at 2 hours after formulation preparation, the presence of Fe^{3+} causes an increase in the levels of soluble aggregates. The amounts of aggregates increased over time when molar ratios of Fe^{3+} to mAb increased.

To further explore the nature of aggregation, SDS-PAGE was performed on the samples at two selected time points of 75 and 819 hour exposure. SDS-PAGE at the time point of 75 hours (Fig. 2) clearly indicates an increasing molar ratios of Fe^{3+} to mAb induced an increasing levels of aggregates. For molar ratios of Fe^{3+} to mAb $\geq$35, multiple high molecular weight assemblies of aggregates were formed. The SDS-PAGE results at the last time point (data not shown) are similar to those at 75 hour time point. With further incubation at 25°C over another 30 days, the aggregation pattern did not change (data not shown).

4.3.2 Impact on mAb conformation: secondary and higher order tertiary structures

The impact of Fe^{3+} on the mAb secondary structure was explored by Far-UV CD on the stability samples at initial and final time points. The spectra obtained on the stability samples at final time point are presented in Fig. 3. These spectra are identical to those

collected at the initial time point (data not shown). This result indicates that increasing molar ratios of Fe^{3+} to mAb do not have any significant impact on the mAb secondary structure. The impact of Fe^{3+} on mAb higher order tertiary and quaternary structures was studied by both intrinsic and extrinsic fluorescence over twenty six days when stored at 25°C. The intrinsic fluorescence spectra are shown in Fig. 4A. The fluorescence spectra represent the normalized averages of three samples with three runs of each sample after background subtraction. No clear blue to red shift in the wavelength of maximal fluorescence intensity is observed, but the Trp/Tyr fluorescence intensity decreased with increased molar ratios of Fe^{3+} to the mAb. However, as shown in Fig. 4B, no further significant decrease in maximal fluorescence intensity over the incubation period of twenty six days is observed, suggesting that the impact of the Fe^{3+} binding on mAb conformation is rapid and not affected by further changes in aggregation levels. The change in intensity is thus likely related to the initial rapid change in aggregation levels. In order to further explore the impact of Fe^{3+} on tertiary structure, bis-ANS extrinsic fluorescence was utilized which characterizes hydrophobic pockets or surfaces in the mAb [31]. The fluorescence properties of bis-ANS strongly depend on their interactions with protein molecules [32]. The bis-ANS fluorescence emission is sensitive to the polarity of the environment. In hydrophobic environment, an increase in quantum yield and a blue shift in the maximum are detected. The extrinsic fluorescence spectra acquired are shown in Fig. 5A. Each spectrum represents the average of three samples, each with three runs after background correction. Bis-ANS extrinsic fluorescence exhibits a similar pattern as observed for Trp/Tyr intrinsic fluorescence: no significant blue or red shift in the maximal wavelength, but a decrease in fluorescence intensity for increasing molar ratios of Fe^{3+} to mAb (Fig. 5B). The intensity was reduced by 50% for a molar ratio of

18. This corresponds to the 50% reduction of intrinsic fluorescence intensity observed for a molar ratio of 18 in Fig. 4B. Unlike the intrinsic fluorescence, the decrease in bis-ANS fluorescence intensity reaches a plateau when the molar ratio of Fe^{3+} to mAb reaches 54. The leveling in bis-ANS fluorescence intensity with increased molar ratios of Fe^{3+} to mAb shows that above a certain level of Fe^{3+}, the tertiary structure is disrupted to such a complete extent that further increase in Fe^{3+} amount cannot lead to any further changes. Together, the results from SEC, SDS-PAGE, intrinsic and extrinsic fluorescence experiments show that the binding of Fe^{3+} perturbs mAb structure accompanied by the formation of aggregates. The perturbation of mAb conformation is seen in Fig. 4 and Fig. 5. The intrinsic (Fig. 4) and extrinsic fluorescence (Fig. 5) intensity decrease is observed immediately after the addition of Fe^{3+}, indicating that the metal binding-induced structural changes are rapid.

4.3.3 Chemical denaturation by GdnHCl

The impact of Fe^{3+} on chemical denaturation of the mAb was explored by addition of GdnHCl at concentrations of 0 - 4.5M. Chemical denaturation studies have been used to study the folding-unfolding transitions in proteins and to gain insight into stabilizing and destabilizing interactions [33-34]. The mAb denaturation was completed after 1 hour of incubation at 37^{o}C. Intrinsic fluorescence is used to monitor the chemical denaturation. The maximal fluorescence intensity for the solution containing no GdnHCl is observed at 346 nm with excitation at 295 nm (data not shown), corresponding to Trp/Tyr fluorescence. At increasing concentrations of GdnHCl, a progressive red shift in the maximal wavelength is observed for all tested molar ratios of Fe^{3+} to mAb (data not shown). This observation suggests the loss of compact structure around some of the Trp/Tyr residues and a progressive exposure of these hydrophobic regions to a hydrophilic environment. The intrinsic

fluorescence emission at 354 nm was chosen to plot fluorescence intensity against the concentrations of GdnHCl, as shown in Fig. 6. The negative control not containing any Fe^{3+}, shows a two-transition unfolding process, where the first transition occurs in the range of 0 – 2M and the second transition in the range of 2 – 3.5M. A similar behavior was also observed for the molar ratio of Fe^{3+} to mAb at 8. For the molar ratios of Fe^{3+} to mAb > 8, the two-step unfolding process changes to a single broad transition. Two-step unfolding in the absence of Fe^{3+}or at the molar ratio of Fe^{3+} to mAb at 8 is also observed in the differential scanning calorimetry (DSC) melting curve [17] as well as by differential scanning fluorometry (DSF) in our another study (unpublished data). At higher molar ratios of Fe^{3+} to mAb, increased tertiary and higher order structure perturbation (as demonstrated by intrinsic/extrinsic fluorescence in Fig. 4 and Fig. 5) reduces the overall stability of the mAb, producing the observed broad single transition. The above noted change in mAb unfolding pattern from double to single transition is also observed in the wavelength shift of the maximal intensity (Fig.7A) and the calculated fractions of unfolded mAb (Fig.7B). This observed unfolding pattern change strongly suggests that the mAb tertiary structure is perturbed by the addition of Fe^{3+}. The chemical denaturation by GdnHCl also offers further insight for the aggregation pattern induced by Fe^{3+}. When the molar ratio of Fe^{3+} to mAb is 8 or less, the aggregates are formed probably due to interactions among the perturbed region(s), which are only marginally stable. In the solutions containing higher molar ratios of Fe^{3+} to mAb, the least stable domain of the mAb is rapidly unfolded to expose hydrophobic APRs, which, in turn, facilitate aggregation. There could also be a second explanation. The destabilization of mAb higher order structure may originate from two different structural domains at low molar ratios of Fe^{3+} to mAb. However, at high molar ratios of Fe^{3+} to mAb, the domains may be

destabilized simultaneously leading to a single broad transition. To locate the potential APRs, sequence and structural features of the mAb were analyzed.

4.3.4 Sequence and structural analysis of mAb

A full length homology-based three dimensional structural model of the mAb was built. This model was used to identify putative Fe^{3+} chelating sites in the mAb structure (see materials and methods). Fig. 8 shows the putative Fe^{3+} chelating sites in the mAb structure. Tables 1 and 2 list all putative Fe^{3+} chelating sites in the mAb, along with their average SASA values which indicate their location in the mAb three dimensional structure. Several putative Fe^{3+} chelating sites could be identified throughout the mAb structure including in the CDRs, hinge regions and CH2: CH3 domain interfaces. Fig. 9 maps the potential Fe^{3+} binding residues on the sequences of the mAb light and heavy chains along with predicted APR, CDRs, aromatic residues (Trp, Tyr and Phe) and auto/metal catalyzed hydrolysis sites. The putative Fe^{3+} chelating sites in hinge region involve Glu and Asp residues that are vicinal to inter-chain disulfide bonds.

APR prediction is shown in the Fig. 10 and Fig. 11, for the mAb heavy and light chains, respectively. Predicted APRs, aromatic residues and putative Fe^{3+} chelating sites are co-localized in the CDRs and adjacent framework regions (the sequence regions separating the CDRs in the Fv portion) of the mAb. The following APRs were found to overlap with the CDRs and adjacent framework regions: (i) 45-KLLIYAA-51 in framework region 2 and CDR loop 2 in the light chains, (ii) 87-YCQQYYS-93 in framework region 3 and CDR loop 3 in the light chains, (iii) 47- WVAVIWY-53 in framework region 2 and CDR loop 2 in the heavy chains and (iv) 103- ATLYYYYYG-111 (Kabat positions 99–100G) in CDR loop 3 in the heavy chains. All these APRs are strongly predicted by Tango/Page combination (Fig. 10

and Fig. 11) and Waltz. Several Fe^{3+} binding residues are also present in the CDRs of the mAb. These residues are Asp34 in CDR loop 1 in the light chains, His35 in CDR loop 1 in the heavy chains, Asp54 and Asp62 in CDR loop 2 in the heavy chains, Asp99 (Kabat position 95) in the framework region 3 in the heavy chains, and Asp113 (Kabat position 101) in CDR loop 3 in the heavy chains. Some of these residues are vicinal to aromatic residues, Trp and Tyr, in sequence and structure. For example, Asp34 precedes Trp35 and Tyr36 in the CDR loop 1 of the light chains. Similarly, His35 precedes Trp36 in CDR loop 1 of the heavy chain. Glu46 in framework 2 region of heavy chains precedes the APR, 47-WVAVIWY–53. Asp54 succeeds this APR. Three of the seven residues in this APR are Trp and Tyr. Glu46 is also part of a putative Fe^{3+} chelating site (Glu46, Glu89 and Asp90) in both the heavy chains and is solvent exposed in one heavy chain but not in the other. On the other hand, Asp54 is alone and solvent exposed in both heavy chains. Asp62 in the CDR loop 2 is also solvent exposed in both heavy chains. Asp113 (Kabat position 101) is located close to a five-Tyr residue cluster in the APR 103-ATLYYYYYG–111 in the CDR 3 of the heavy chains and also to Trp115 (Kabat position 103). Asp113 is buried in both heavy chains. Accessible surface area calculations show that most of the residues in APR 47-WVAVIWY–53 are buried and thus protected from solvent. A majority of the residues in the APR 103-ATLYYYYYG–111 are solvent exposed and this APR is partially on surface. These observations are consistent in both the heavy chains. Accessible surface areas for the Fe^{3+} binding residues that are proximal to the aromatic residues (Trp, Tyr and Phe) in the CDRs and adjoining framework regions are summarized in Table 3. Fig. 12 shows solvent accessible Fe^{3+} binding residues along with their proximal aromatic residues in Fv region of the mAb. These Fe^{3+} binding residues may serve as initial anchor sites for Fe^{3+} and the

nearby aromatic residues may report the conformational changes in the fluorescence experiments. As stated above, there are APRs in vicinity and Trp47, Trp52, Tyr53 and Tyr106 are located within these APRs. Physico-chemical degradations initiated by Fe^{3+} binding in the CDR regions may perturb the mAb tertiary structure and cause additional buried residues to become solvent-exposed, thereby, leading to further degradation. These observations correlate very well with the experimental observations of perturbation of tertiary structures and increased aggregates upon increasing molar ratios of Fe^{3+} to mAb, and indicate that destabilization of Fab/Fv regions may underpin the experimental observations.

Overall, most of the experimental observations on the mAb in this study could be rationalized when its molecular sequence and structural properties were taken into account. However, collapse of the double transition step in to a single broad transition step at higher molar ratios of Fe^{3+} to mAb in the chemical denaturation studies could not be readily explained. The two transitions at the lower molar ratios of Fe^{3+} to mAb may be due to the differences in conformational stabilities of Fc and Fab portions of the mAb. At higher molar ratios of Fe^{3+} to mAb, both Fab and Fc portions may be destabilized simultaneously leading to a single broad transition. There could also be a second possibility. The two transition steps seen at lower molar ratios of Fe^{3+} to mAb may be due to the marginal differences in the stabilities of two Fab or Fv portions in the mAb. Crystal structures for the full length mAbs available in the PDB [35] (PDB entries, 1IGY, 1IGT and 1HZH) show that the two Fabs in the antibody structure are oriented asymmetrically with respect to the Fc Portion. This results in imperfect T or Y configurations for the overall mAb three-dimensional structure [29, 36]. Moreover, there are conformational differences between the two Fabs even though both the Fabs have identical sequences (our unpublished data) [37]. These conformational differences

also result in the differences among the putative Fe^{3+} chelating sites (Tables 1 and 2). Thus, at low molar ratios of Fe^{3+} to mAb, the two Fab/Fv regions may be destabilized to marginally different extents. But at the higher molar ratios of Fe^{3+} to mAb, both Fabs are destabilized to similar extents and a single broad transition is observed instead of two. Clearly, this question will require further investigation.

4.4 Conclusions

The impact of Fe^{3+} on an IgG2 mAb and its degradation mechanism were investigated in solutions which did not contain fenton reagents or fenton-like reagents. Aggregation and structural change were monitored in this study. Both modes of degradation were correlated with the molar ratios of Fe^{3+} to mAb.

The impact of the Fe^{3+} on mAb conformation studied by far UV-CD, intrinsic/ extrinsic fluorescence and chemical denaturation by GdnHCl indicates that the mAb secondary structure is not impacted by the presence of Fe^{3+} but its tertiary and higher order oligomeric structures are perturbed. The intrinsic/extrinsic fluorescence intensity significantly decreases with increased molar ratios of Fe^{3+} to mAb even though no detectable red or blue shift in the wavelength of the maximum intensity is observed. The perturbation of the tertiary structure and the resulting enhanced aggregation is due to the binding of Fe^{3+} to the mAb. An impact on the tertiary and quaternary structures is seen immediately after addition of Fe^{3+}, suggesting that the binding occurs at specific regions in such a way that the local environment of the aromatic residues, especially, Trp/Tyr, is altered. These experimentally measured ‘macroscopic’ observations of the mAb in this study could be rationalized on the basis of its ‘microscopic’ sequence and structural properties. Homology model of the mAb indicates presence of putative Fe^{3+} chelating sites throughout the mAb

structure, both in the variable (Fv) and constant (Fc) regions. In particular, these putative Fe^{3+} chelating sites are in close sequence and spatial proximity with the aromatic residues, especially Trp and Tyr, and APRs located in the CDRs and adjacent framework regions of the mAb. This study also demonstrates the utility of predictive methods towards understanding degradation of biotherapeutics from a formulation perspective.

4.5 References

1. Allain, L., et al., *Impact of package leachables on the stability of pharmaceutical products.* American Pharmaceutical Review, 2007. **10**(4): p. 38, 40, 42-44.
2. Fliszar, K.A., et al., *Profiling of metal ions leached from pharmaceutical packaging materials.* PDA J Pharm Sci Technol, 2006. **60**(6): p. 337-42.
3. Markovic, I., *Challenges associated with extractables and/or leachables substances in therapeutic biologic protein products.* American Pharmaceutical Review, 2006. **9**(6): p. 20-27.
4. Markovic, I., *Evaluation of safety and quality impact of extractable and leachable substances in therapeutic biologic protein products: a risk-based perspective.* Expert Opin Drug Saf, 2007. **6**(5): p. 487-91.
5. Osterberg, R.E., *Potential toxicity of extractables and leachables in drug product.* American Pharmaceutical Review, 2005. **8**(2): p. 64-67.
6. Waterman, K.C., et al., *Stabilization of pharmaceuticals to oxidative degradation.* Pharm Dev Technol, 2002. **7**(1): p. 1-32.
7. Zhou, S., et al., *Biologics formulation factors affecting metal leachables from stainless steel.* AAPS PharmSciTech, 2011. **12**(1): p. 411-21.

8. Zhou, S., et al., *Biotherapeutic Formulation Factors Affecting Metal Leachables from Stainless Steel Studies by Design of Experiments.* AAPS PharmSciTech, 2011.
9. Bee, J.S., et al., *Precipitation of a monoclonal antibody by soluble tungsten.* J Pharm Sci, 2009. **98**(9): p. 3290-301.
10. Chen, W.T., et al., *Distinct effects of Zn^{2+}, Cu^{2+}, Fe^{3+}, and Al^{3+} on amyloid-beta stability, oligomerization, and aggregation: amyloid-beta destabilization promotes annular protofibril formation.* J Biol Chem, 2011. **286**(11): p. 9646-56.
11. Dufield, D.R., et al., *Selective site-specific fenton oxidation of methionine in model peptides: evidence for a metal-bound oxidant.* J Pharm Sci, 2004. **93**(5): p. 1122-30.
12. Kim, K., et al., *Nonenzymatic cleavage of proteins by reactive oxygen species generated by dithiothreitol and iron.* J Biol Chem, 1985. **260**(29): p. 15394-7.
13. Li, S., et al., *Aggregation and precipitation of human relaxin induced by metal-catalyzed oxidation.* Biochemistry, 1995. **34**(17): p. 5762-72.
14. Stadtman, E.R., *Metal ion-catalyzed oxidation of proteins: biochemical mechanism and biological consequences.* Free Radic Biol Med, 1990. **9**(4): p. 315-25.
15. Uversky, V.N., et al., *Metal-triggered structural transformations, aggregation, and fibrillation of human alpha-synuclein. A possible molecular link between Parkinson's disease and heavy metal exposure.* J Biol Chem, 2001. **276**(47): p. 44284-96.
16. Zhao, F., et al., *Metal-catalyzed oxidation of histidine in human growth hormone. Mechanism, isotope effects, and inhibition by a mild denaturing alcohol.* J Biol Chem, 1997. **272**(14): p. 9019-29.
17. Zhou, S., et al., *Comparative evaluation of disodium edetate and diethylenetriaminepentaacetic acid as iron chelators to prevent metal-catalyzed*

destabilization of a therapeutic monoclonal antibody. J Pharm Sci, 2010. **99**(10): p. 4239-50.

18. Akke, M., et al., *Three-dimensional solution structure of Ca(2+)-loaded porcine calbindin D9k determined by nuclear magnetic resonance spectroscopy.* Biochemistry, 1992. **31**(4): p. 1011-20.
19. Banci, L., et al., *A prokaryotic superoxide dismutase paralog lacking two Cu ligands: from largely unstructured in solution to ordered in the crystal.* Proc Natl Acad Sci U S A, 2005. **102**(21): p. 7541-6.
20. Degtyarenko, K., *Bioinorganic motifs: towards functional classification of metalloproteins.* Bioinformatics, 2000. **16**(10): p. 851-64.
21. Sun, H., et al.,, *Transferrin as a metal ion mediator.* Chem Rev, 1999. **99**(9): p. 2817-42.
22. Tainer, J.A., et al., *Metal-binding sites in proteins.* Curr Opin Biotechnol, 1991. **2**(4): p. 582-91.
23. Derrick, T.S., et al., *Effect of metal cations on the conformation and inactivation of recombinant human factor VIII.* J Pharm Sci, 2004. **93**(10): p. 2549-57.
24. Thakurta, P.G., et al., *Tertiary structural changes associated with iron binding and release in hen serum transferrin: a crystallographic and spectroscopic study.* Biochem Biophys Res Commun, 2004. **316**(4): p. 1124-31.
25. Pace, C.N., et al., *How to measure and predict the molar absorption coefficient of a protein.* Protein Sci, 1995. **4**(11): p. 2411-23.
26. Wang, X., et al., *Disulfide scrambling in IgG2 monoclonal antibodies: insights from molecular dynamics simulations.* Pharm Res, 2011. **28**(12): p. 3128-44.

27. Milstein, C., et al., *Disulphide bridges of the heavy chain of human immunoglobulin G2.* Biochem J, 1971. **121**(2): p. 217-25.

28. Wang, X., et al., *Potential aggregation-prone regions in complementarity-determining regions of antibodies and their contribution towards antigen recognition: a computational analysis.* Pharm Res, 2010. **27**(8): p. 1512-29.

29. Maurer-Stroh, S., et al., *Exploring the sequence determinants of amyloid structure using position-specific scoring matrices.* Nat Methods, 2010. **7**(3): p. 237-42.

30. Goyal, K., et al., *Exploiting 3D structural templates for detection of metal-binding sites in protein structures.* Proteins, 2008. **70**(4): p. 1206-18.

31. Togashi, D.M., et al., *A fluorescence analysis of ANS bound to bovine serum albumin: binding properties revisited by using energy transfer.* J Fluoresc, 2008. **18**(2): p. 519-26.

32. Matulis, D., et al., *1-Anilino-8-naphthalene sulfonate anion-protein binding depends primarily on ion pair formation.* Biophys J, 1998. **74**(1): p. 422-9.

33. Jennings, P.A., et al., *Formation of a molten globule intermediate early in the kinetic folding pathway of apomyoglobin.* Science, 1993. **262**(5135): p. 892-6.

34. Kim, P.S., et al., *Intermediates in the folding reactions of small proteins.* Annu Rev Biochem, 1990. **59**: p. 631-60.

35. Dutta, S., et al., *Promoting a structural view of biology for varied audiences: an overview of RCSB PDB resources and experiences.* J Appl Crystallogr, 2010. **43**(Pt 5): p. 1224-1229.

36. Harris, L.J., et al., *Comparison of the conformations of two intact monoclonal antibodies with hinges.* Immunol Rev, 1998. **163**: p. 35-43.

37. Zhou, S., et al., *Simultaneous separation and identification of IgG1, IgG1 fragments and photodegradation product by reverse phase liquid chromatography/ mass spectrometry (LC/MS) submitted*, 2012.

Table 1. Putative Fe^{3+} chelating sites in the heavy chains of the mAb

Residue clusters in heavy chain 1 (HC1)	Structural Location	Average SASA (μ±σ)	Residue clusters in heavy chain 2 (HC2)	Structural Location	Average SASA (μ±σ)
HC1.E6, HC1.C22, HC1.H35, HC1.C96, HC1.D99, HC1.D113	V_H	3.69 ± 7.32	HC2.E6, HC2.C22, HC2.H35, HC2.C96, HC2.D99, HC2.D113	V_H	2.77 ± 6.79
HC1.E46, HC1.E89, HC1.D90	V_H	17.17 ± 14.93	HC2.E46, HC2.E89, HC2.D90	V_H	11.52 ± 16.71
HC1.D54	V_H	49.48	HC2.D54	V_H	49.35
HC1.D62, LC1.D1	V_H:V_L	44.42	HC2.D62, LC2.D1	V_H:V_L	42.57
HC1.D73	V_H	24.61	HC2.D73	V_H	23.65
HC1.E145	C_H1	74.08	HC2.E145	C_H1	71.33
HC1.D156	C_H1	33.51	HC2.D156	C_H1	13.21
HC1.E160, HC1.D211, HC1.H212	C_H1	12.06 ± 20.89	HC2.E160	C_H1	2.219
HC1.H176, LC1.D167, LC1.E165	C_H1:C_L	9.10 ± 13.08	HC2.H176, LC2.E165, LC2.D167	C_H1:C_L	3.20 ± 5.31
None			HC2.D211, HC2.H212	C_H1	10.09
LC1.E123, HC1.C208, HC1.D220	C_H1:C_L	18.82 ± 22.25	HC2.D220, LC2.E123	C_H1:C_L	36.09
HC1.E224, LC1.D122	C_H1:C_L	32.7	HC2.E224, LC2.D122, HC2.E230, HC2.C228, HC2.C231, HC2.C234, HC1.C234	Hinge	6.11 ± 7.73
HC1.E230, HC2.C227, HC1.C228, HC1.C231, HC2.C228, HC2.C231"	Hinge	17.13 ± 16.76	None		
HC1.D253, HC1.E262, HC1.H314, HC1.D316, HC1.E349, HC1.D380, HC1.H433, HC1.E434, HC1.H437, HC1.H439	C_H2:C_H3	23.07 ± 27.39	HC2.D253, HC2.E262, HC2.H314, HC2.D316, HC2.E349, HC2.D380, HC2.H433, HC2.E434, HC2.H437, HC2.H439	C_H2:C_H3	18.53 ± 25.89
HC1.D269	C_H2	7.632	HC2.D269	C_H2	6.8
HC1.C234, HC1.H272, HC1.E273, HC1.D274, HC1.E276, HC1.E297, HC1.E298	C_H2	23.28 ± 19.39	HC2.H272, HC2.E273, HC2.D274, HC2.E276, HC2.E297, HC2.E298	C_H2	49.56 ± 21.41
HC1.D284, HC1.E322	C_H2:C_H3	34.7	HC2.D284, HC2.E322	C_H2:C_H3	42.32
HC1.E287, HC1.H289	C_H2	50.46	HC2.E287, HC2.H289	C_H2	47.34
HC1.E337, HC1.C325	C_H3	15.765	HC2.E337, HC2.C325	C_H3	19.89
HC1.E360, HC1.E361	C_H3	13.73	HC2.E360, HC2.E361	C_H3	10.83
HC1.E384, HC1.E386, HC1.E392, HC1.C429	C_H3	9.61 ± 8.29	HC2.E384, HC2.E386, HC2.E392, HC2.C429	C_H3	9.68 ± 7.55
HC1.D403, HC1.D405	C_H3	27.55	HC2.D403, HC2.D405	C_H3	29.55
HC1.D417	C_H3	34.8	HC2.D417	C_H3	36.22

Table 2. Putative Fe^{3+} chelating sites in the light chains of the mAb

LC1			LC2		
Residue clusters in light chain 1 (LC1)	Structural Location	Average AASA ($\mu \pm \sigma$)	Residue clusters in light chain 2 (LC2)	Structural Location	Average AASA ($\mu \pm \sigma$)
LC1.D1, HC1.D62	V_H:V_L	44.42	LC2.D1, HC2.D62	V_H:V_L	42.57
LC1.D17	V_L	39.75	LC2.D17	V_L	40.04
LC1.D34, LC1.C88	V_L	0	LC2.D34, LC2.C88	V_L	0
LC1.D70, LC1.C23	V_L	26.84	LC2.D70, LC2.C23	V_L	27.1
LC1.E81, LC1.D82	V_L	20.46	LC2.E81, LC2.D82, LC2.E105, LC2.E165, LC2.D167, LC2.D170, HC2.H176	V_L	10.94 ± 12.77
LC1.E105	V_L	2.702	None		
LC1.D122,LC1.E123, LC1.E213, LC1.C214, HC1.D220, HC1.E224, HC1.C227	C_L:C_H1	27.88 ± 18.63	LC2.D122, LC2.E123, LC2.D151, LC2.D185, LC2.E187, LC2.H189, HC2.D220, HC2.E224	C_L:C_H1	25.98 ± 19.46
LC1.143, LC1.H198	C_L	20.33	LC2.143, LC2.H198	C_L	26.7
LC1.D151, LC1.H189, LC1.D185, LC1.D187	C_L	26.23 ± 9.41			
LC1.E161	C_L	42.15	LC2.E161	C_L	47.23
LC1.E165, LC1.D167, LC1.D170, HC1.H176	C_L	13.78 ± 14.20			
LC1.E195, LC1.C194	C_L	4.24	LC2.E195, LC2.C194	C_L	9.65
LC1.E213, LC1.C214, HC1.E224, HC1.C227	C_L:C_H1	33.43 ± 18.35	LC2.E213, LC2.C214, HC2.C139	C_L:C_H1	21.49 ± 22.63

Table 3. Fe^{3+} ion binding residues in the neighborhood of aromatic residues in CDRs and adjoining framework regions

Residue and structural location	Spatially vicinal aromatic residues	SASA (%)
D 34 in L1 loop in LC1	LC1: W35, Y36, Y49, Y87, Y91 HC1: Y109	0
D 34 in L1 loop in LC2	LC1: W35, Y36, Y49, Y87, Y91 HC1: Y109, Y110	0
E46 in FR2 region of HC1	HC1: W47 LC1: F98	24.4
E46 in FR2 region of HC2	HC2: W47 LC2: F98	3.9
D54 in H2 loop of HC1	HC1: W52, Y53, Y106	49.5
D54 in H2 loop of HC2	HC2: W52, Y53, Y106	49.4
D62 in H2 loop of HC1	HC1: W47, Y60	41.8
D62 in H2 loop of HC2	HC2: W47, Y60	30.4
D99 in H3 loop of HC1	HC1: Y32, Y108, Y109, Y110	0
D99 in H3 loop of HC2	HC2: F27, Y32, Y108, Y110	0
D113 in H3 loop of HC1	HC1: W115	18.3
D113 in H3 loop of HC2	HC2: W115	16.6

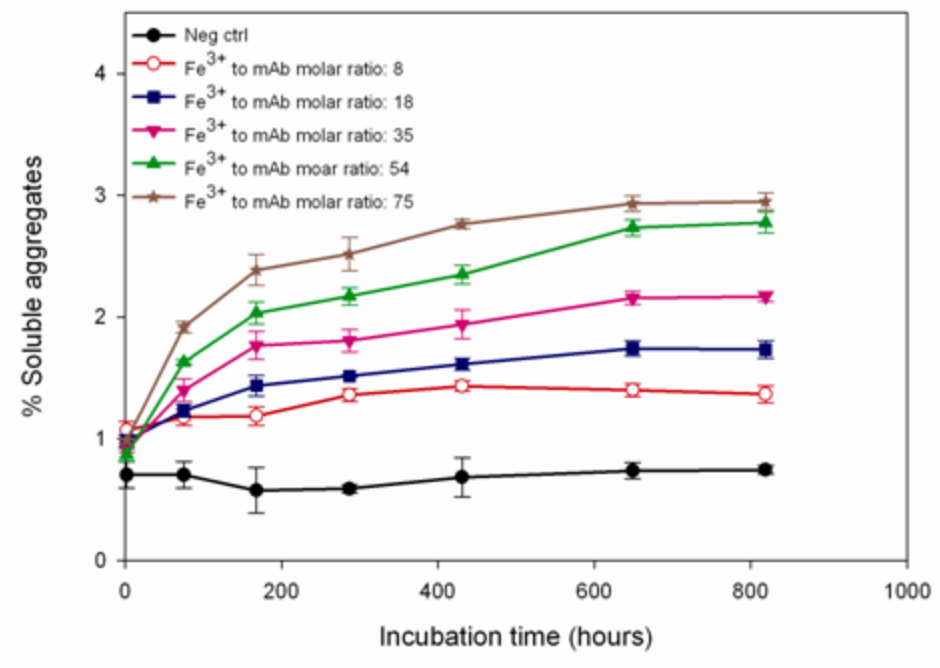

Fig. 1. Yield (%) of soluble aggregates of mAb in the formulations containing discrete molar ratios of Fe^{3+} to mAb when incubated at 25^{o}C are plotted *versus* incubation time. % soluble aggregates are the total percent of high molecule weight species quantitated by SEC. The values represent the average of three individual samples at each time point.

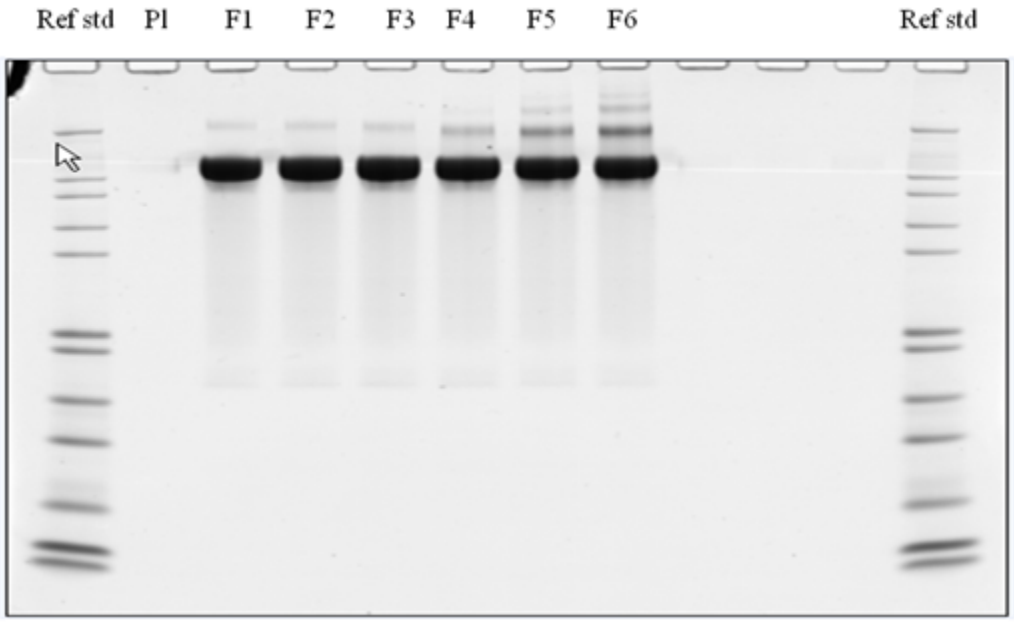

Fig. 2. SDS-PAGE of the mAb formulations at different molar ratios of Fe^{3+} to mAb (Pl means placebo, F1 for negative ctrl and F2-F6 stand for the formulations at molar ratios of Fe^{3+} to mAb of 8, 18, 35, 54 and 75) at a time point of 75 hours

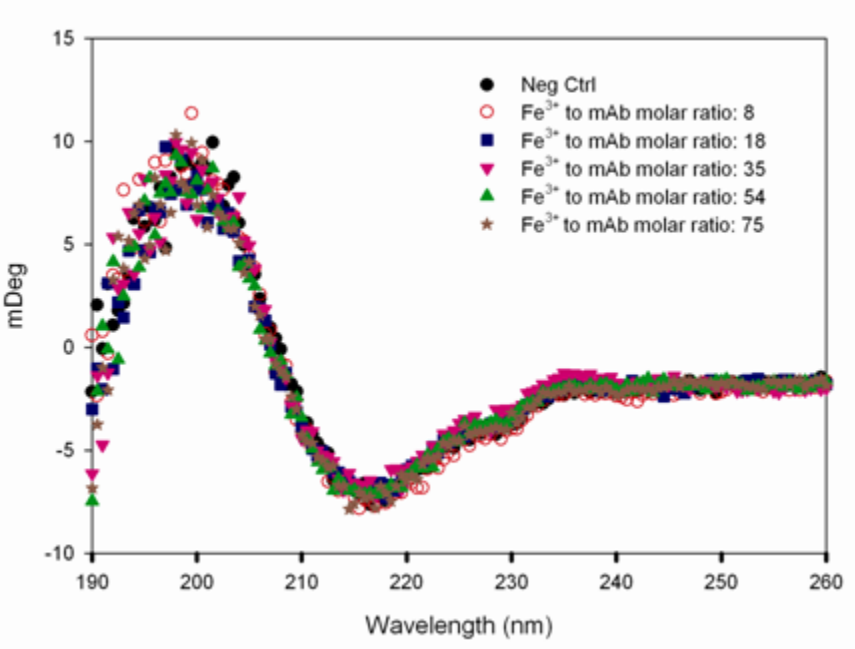

Fig. 3. Secondary structure of the formulations containing different molar ratios of Fe^{3+} to mAb when incubated at 25°C over 35 days by Far UV CD from 190-200 nm at ambient temperature. The mAb conc. was at 0.2 mg/mL. The spectra represent the average of three samples with RSD < 0.05%

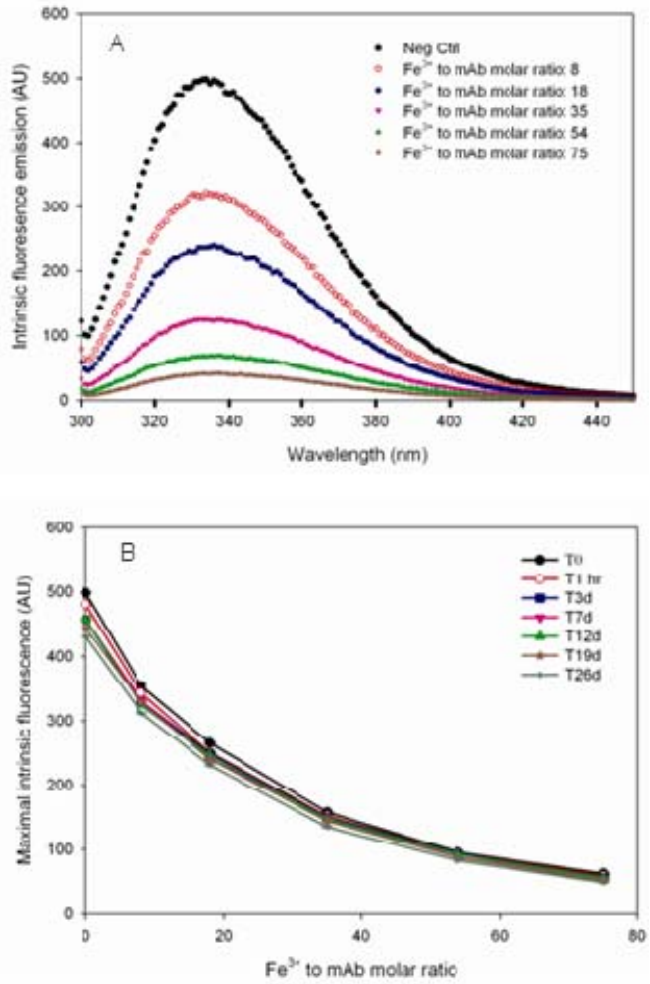

Fig. 4. Intrinsic fluorescence (excitation was set at 295 nm) of the solutions containing discrete molar ratios of Fe^{3+} to mAb is presented. (A) Fluorescence spectra at initial time points (the spectra represent the average of three individual samples with RSD <0.5%); and (B) Maximal intrinsic fluorescence change of the formulations with the molar ratios of Fe^{3+} to mAb over the different incubation period at 25^{o}C. The mAb conc. for all the tested solutions was 0.2 mg/mL and experiment was performed at ambient temperature.

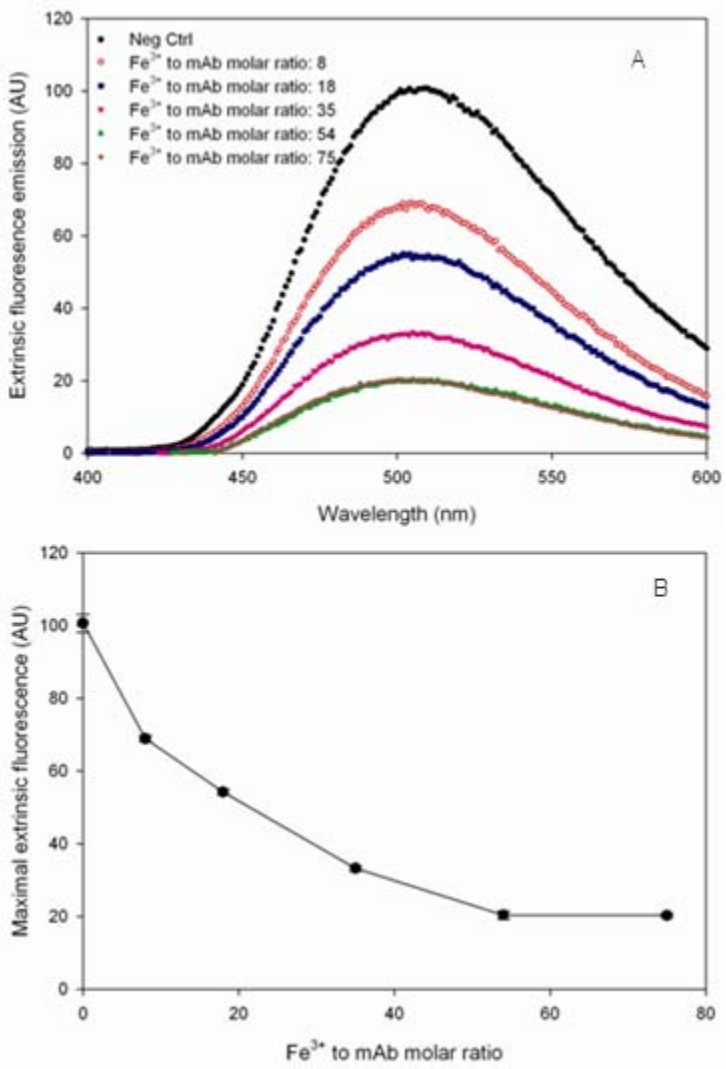

Fig. 5. Bis-ANS extrinsic fluorescence (excitation wavelength was set at 385 nm) of the formulations containing different molar ratios of Fe^{3+} to mAb is shown. (A) Bis-ANS extrinsic fluorescence spectra at final time point (the spectra represent the average of three individual samples with RSD < 0.5%); and (B) Maximal bis-ANS extrinsic fluorescence change with the molar ratios of Fe^{3+} to mAb over the incubation at 25°C. The mAb conc. for all the tested solutions was 1 mg/mL and the experiment was performed at ambient temperature.

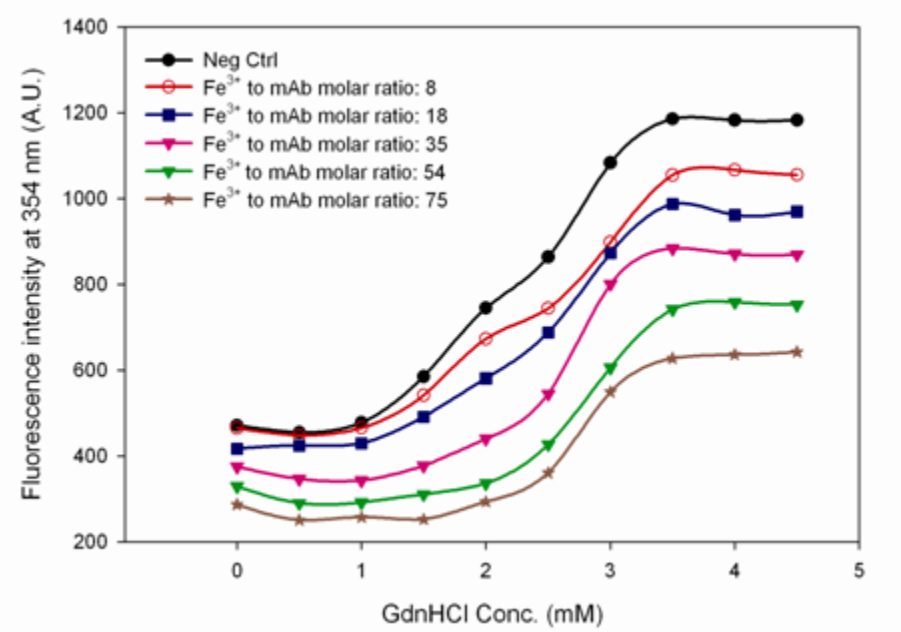

Fig. 6. Chemical denaturation of the IgG2 mAb by GdnHCl is presented as intrinsic fluorescence intensity at 354 nm with excitation at 295 nm *versus* GdnHCl concentration. The intrinsic fluorescence was measured by using 96-well plate reader. The mAb conc. was 0.2 mg/mL and the experiment was performed at ambient temperature.

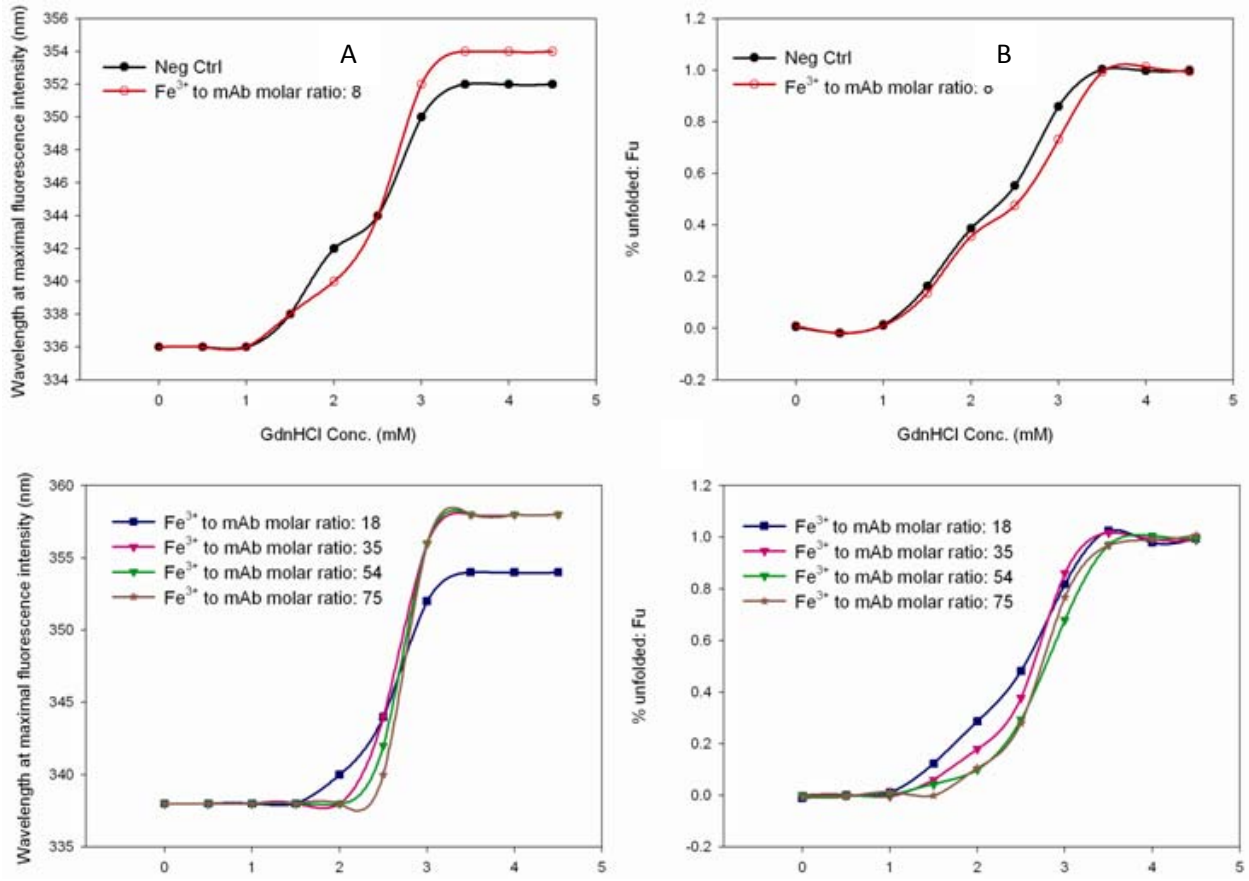

Fig. 7. Chemical denaturation by GdnHCl in the solutions containing different molar ratios of Fe^{3+} to mAb is presented. (A) Wavelength shift in maximal intrinsic fluorescence intensity, and (B) Percentage of unfolded protein. The intrinsic fluorescence was monitored by a plate reader with 96-well plate. The mAb conc. was 0.2 mg/mL and the experiment was performed at ambient temperature.

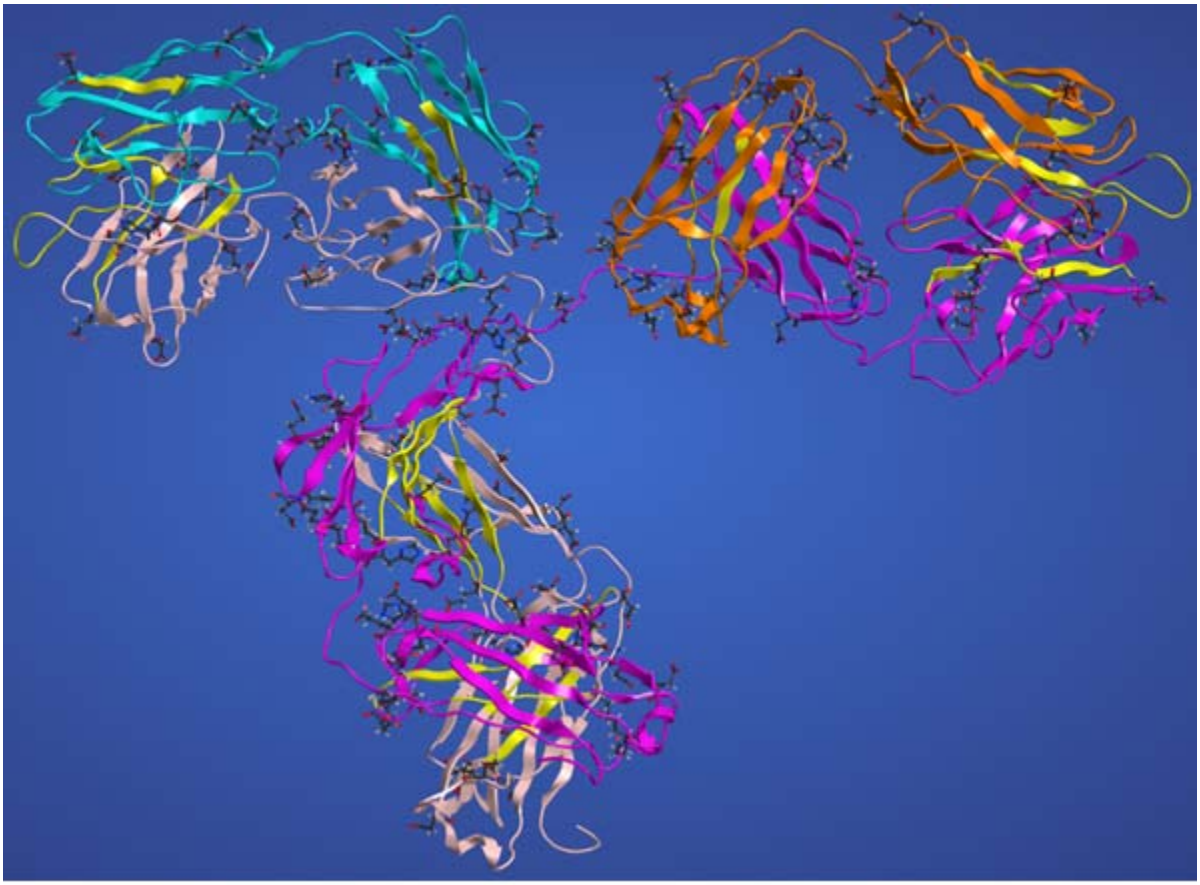

Fig. 8. A three-dimensional homology based model of an IgG2 mAb in this study is shown in ribbon representation. Putative Fe^{3+} chelating sites are shown in CPK. The following color code was used: heavy chains, light pink and magenta; light chains, cyan and orange; predicted aggregation prone regions (APRs), yellow.

>IgG2mAb.LC

DIQMTQSPSSLSASVGDRVTITCRASQSINSYLDWYQQKPGKAPKLLIYAASSLQSGV
PSRFSGSGSGTDFTLTISSLQPEDFATYYCQQYYSTPFTFGPGTKVEIKRTVAAPSV
FIFPPSDEQLKSGTASVVCLLNNFYPREAKVQWKVDNALQSGNSQESVTEQDSKDS
TYSLSSTLTLSKADYEKHKVYACEVTHQGLSSPVTKSFNRGEC

>IgG2mAb.HC

QVQLVESGGGVVQPGRSLRLSCAASGFTFSSYGMHWVRQAPGKGLEWVAVIWY
DGSNKYYADSVKGRFTISRDNSKNTLYLQMNSLRAEDTAVYYCARDPRGATLYY
YYYGMDVWGQGTTVTVSSASTKGPSVFPLAPCSRSTSESTAALGCLVKDYFPEPVT
VSWNSGALTSGVHTFPAVLQSSGLYSLSSVVTVPSSNFGTQTYTCNVDHKPSNTKV
DKTVERKCCVECPPCPAPPVAGPSVFLFPPKPKDTLMISRTPEVTCVVVDVSHEDPEV
QFNWYVDGVEVHNAKTKPREEQFNSTFRVVSVLTVVHQDWLNGKEYKCKVSNK
GLPAPIEKTISKTKGQPREPQVYTLPPSREEMTKNQVSLTCLVKGFYPSDIAVEWESN
GQPENNYKTTPPMLDSDGSFFLYSKLTVDKSRWQQGNVFSCSVMHEALHNHYTQ
KSLSLSPGK

Fig. 9. Potential metal binding residues, aromatic residues, auto / metal catalyzed hydrolysis sites and predicted aggregation prone regions (APRs) are mapped on to heavy and light chain sequences of the IgG2 mAb in this study. Single letter amino acid code is used. Metal binding residues C, D, E, H are shown in bold and red. Potential APRs predicted by Tango/Page and Waltz are shown in yellow and sky blue backgrounds. CDRs are underlined. Auto and metal catalyzed clipping sites, DP, DY, HS, SH and KT, are shown in grey background. Aromatic residues, W, F and Y, are shown in big bold and blue.

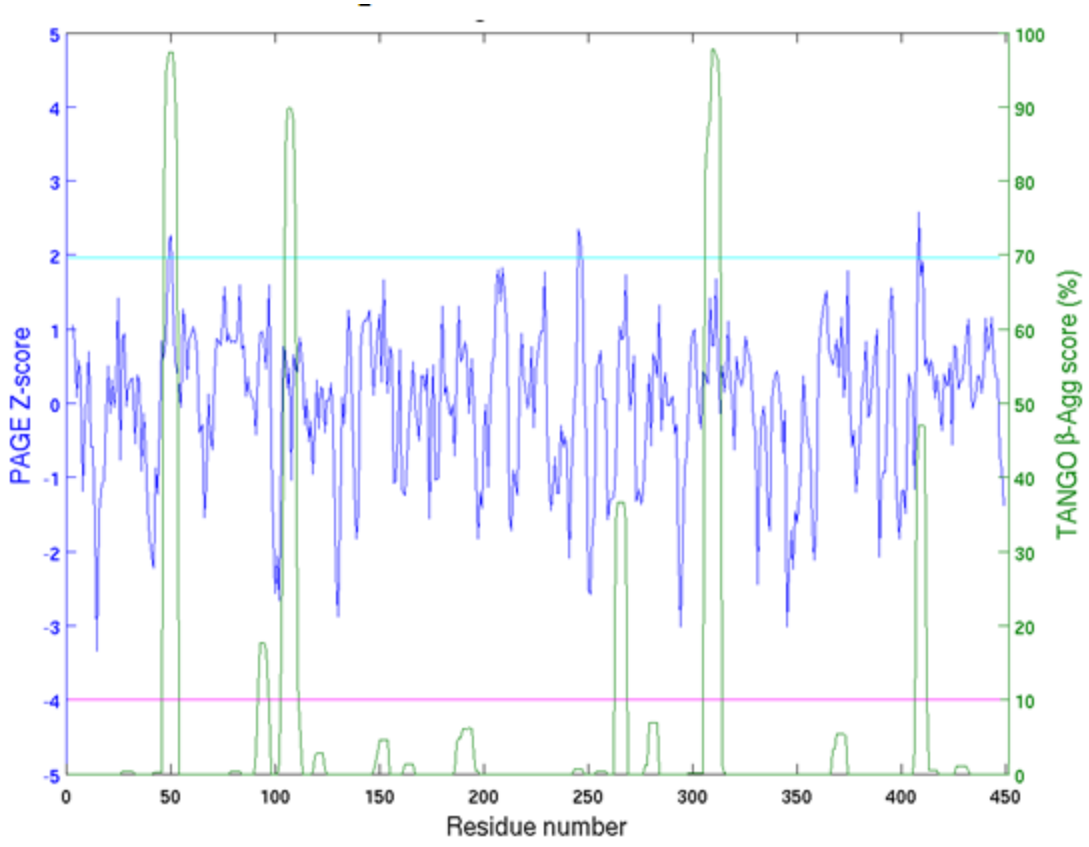

Fig. 10. Potential aggregation prone regions (APRs) in the heavy chain of IgG2 mAb. The APRs were predicted using a combination of Tango and Page. X-axis shows residue number. There are two Y-axes in this figure. The one in blue shows Z-score calculated from PAGE's aggregation propensity values. The horizontal line in cyan shows a cut off value for Z-score (1.96). The Y-axis in green shows Tango's β- aggregation score. The horizontal magenta line shows cut off value for Tango score (10%). These cut off values were used to identify predicted APRs. The APRs detected by this method are: 47-WVAVIWY-53, 92-AVYYC-96, 103-ALTYYYYYG-111, 243-SVFLFP-248, 263-VTCVVV-268, 306-VVSVLTVV-313, 369-LTCLV-373 and 406-GSFFLYS-412. Note that these are not Kabat numbering positions.

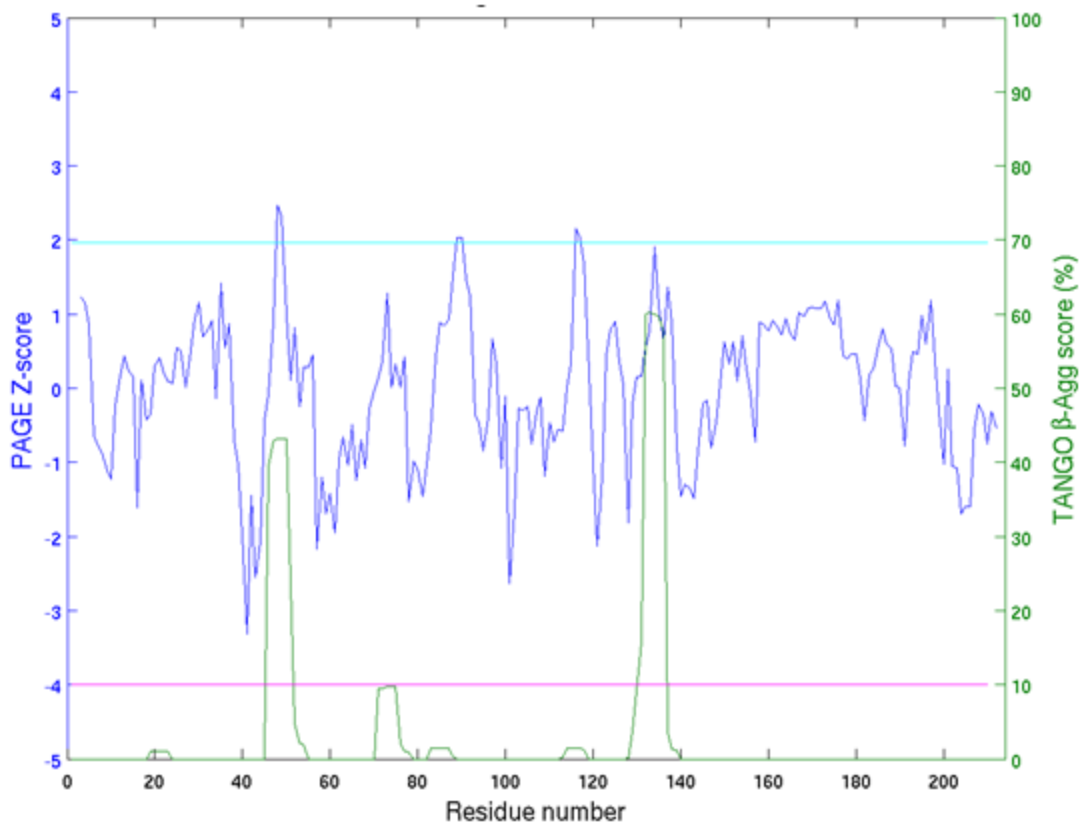

Fig. 11. Potential aggregation prone regions (APRs) in the light chain of IgG2 mAb. The APRs were predicted using a combination of Tango and Page. This figure was plotted in the same was as Fig 10. The APRs detected by this method are: 46-LLIYAA-51, 71-FTLTI-75, 87-YCQQYY-92, 114-SVFIFP-119 and 131-SVVCLL-136. Note that these are not Kabat numbering positions.

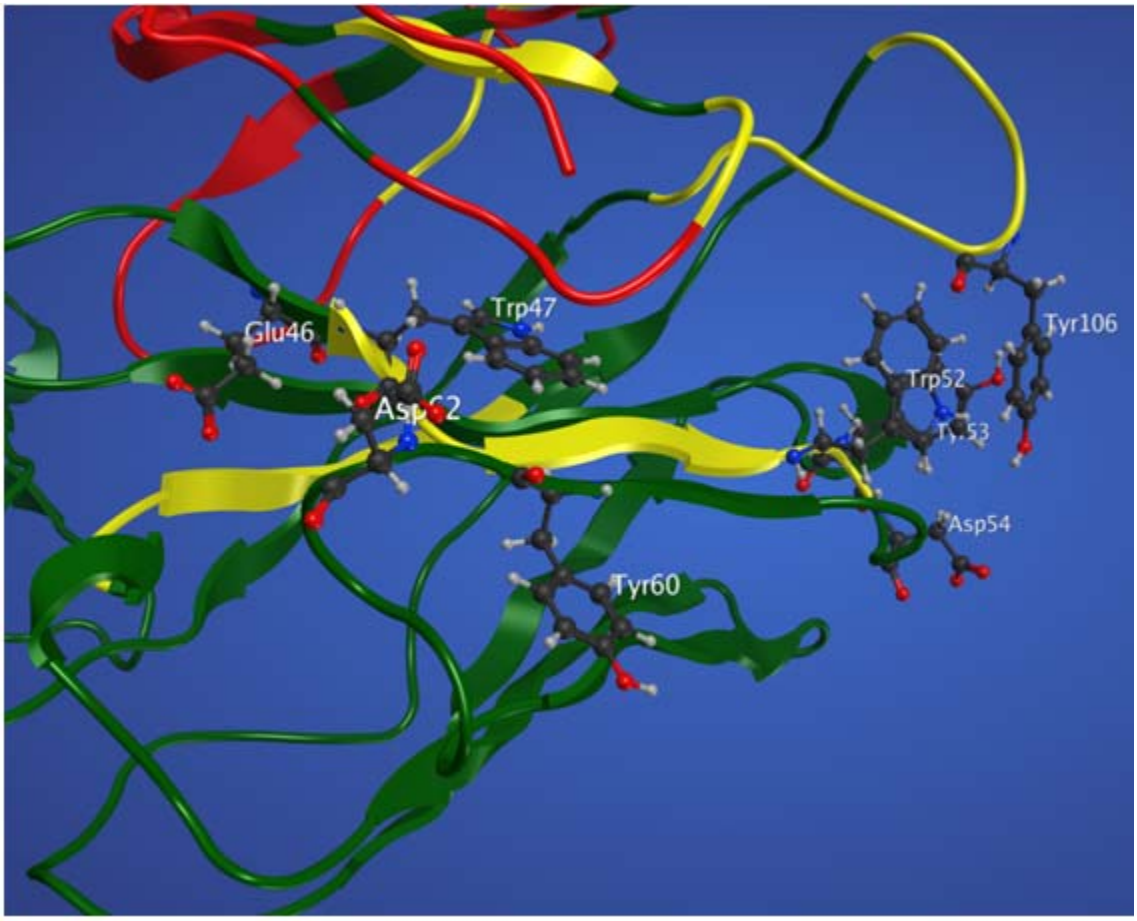

Fig. 12. Co-localization of Fe^{3+} binding residues, aromatic residues and APRs in the Fv portion of the IgG2 mAb is shown. The solvent accessible Fe^{3+} binding residues, Glu46, Asp54 and Asp 62 in the heavy chain, are depicted in ball and stick representation along with their proximal aromatic residues, Trp47, Trp52, Tyr53, Tyr60 and Tyr106. Note the residues are numbered according to their position in the sequences. The following color code was used: green for heavy chain; red for light chain and yellow for APR.

Chapter 5: Thermal Instability of IgG1 Induced by Metal Ions

Table of Contents

5.1 Introduction

Monoclonal antibodies, like other proteins, are generally marginally stable in solution and subject to physical/chemical degradation, such as aggregation, oxidation, fragmentation and deamidation. To gain an understanding of the stability of a biotherapeutic protein candidate, real-time stability studies at various temperatures are generally performed. To save time and resources in protein candidate development, characterization of the conformational stability of a protein using circular dichroism (CD) [1], intrinsic/extrinsic fluorescence [1-2], differential scanning calorimetry (DSC) [3-4], high resolution UV absorbance spectrometry [5], and differential scanning fluorescence (DSF) [3] has gradually gained recognition and acceptance. The acquired information helps the formulation scientist to understand the factors affecting protein stability from the structural perspective and thus provides a basis to identify appropriate components and conditions to stabilize the protein.

During drug substance and/or drug product processing, manufacturing and storage, metal ions, especially iron, are inevitably introduced into the final drug product with the risk for inducing protein degradation [6-8]. One generally accepted degradation mechanism induced by iron is the Fenton reaction [9-13]. However, an alternative degradation mechanism has also been proposed, that is, degradation as a consequence of protein conformational changes induced by metal ion binding to the protein [14-17]. The study in Chapter 4 indicates that ferric ions bind to a therapeutic immunoglobulin monoclonal antibody (IgG2 mAb), and induce mAb degradation. All four major degradation mechanisms, oxidation, aggregation, fragmentation and deamidation were observed. To further characterize and understand the impact of ferric ions on mAb structure and stability, here we focus on investigating the mAb thermal stability. Far-UV CD was

employed to characterize the protein secondary structural change with increasing temperatures. Intrinsic fluorescence was used to study impact on tertiary structure while (bis-ANS) extrinsic fluorescence was utilized to monitor changes in exposure of hydrophobic patches/areas. High-resolution UV second derivative absorbance spectroscopy was used to track the impact of ferric ions on the protein tertiary structure by monitoring peak position thermal shift of six characteristic negative peaks arising from aromatic amino acid residues (Phe, Tyr and Trp) [19]. The impact of ferric ions on protein intrinsic melting points was studied by DSC and the thermal transitional temperature of hydrophobic exposure changes was studied by DSF with SYPRO® Orange dye. SYPRO® Orange dye has been reported to be a sensitive tool to monitor protein unfolding and protein stability under thermal stress because of its distinct fluorescent properties, that is, interactions with hydrophobic regions exposed due to protein conformational changes [19-23]. Our results provide further evidence that the binding of ferric ions perturbs the mAb structure. The gradually decreasing melting points, thermal transition temperature of hydrophobic exposure, and/or SYPRO® Orange intensity with increasing molar ratios of ferric ions to mAb, provide a reasonable explanation for the reduction in protein stability induced by ferric ions from a structural perspective.

The study presented in this chapter was undertaken as part of our ongoing efforts to elucidate the impact of leached metal ions on mAb structure and stability. We used the strategy of "exaggerating" a factor to understand its impact, similar to that used by Hoehne *et al.* [25], when assessing the impact of glass particles, and by Thirumangalathu *et al.* [26] for silicone oil. Metal ions, especially, ferric ion, can be present in raw materials but a primary source is stainless steel manufacturing and storage equipment. Our practical experience suggests that actual levels of metal ions tend to be low (generally less than 1- 5 ppm; i.e. molar rations of approximately

0.6-3 for a mAb with a molecular weight of ca. 150 kDa at 5 mg/mL) when working with well maintained and passivated equipment, especially at large–scale. Higher levels of ferric ions may be obtained when working with surrogate small-scale tanks which present a high surface area compared to the volume parameter. An example where such tanks may be found is in long-term stability studies designed to mimic large-scale bulk solution storage.

5.2 Materials and Methods

5.2.1 Materials

A therapeutic quality immunoglobulin (IgG2) mAb in 20 mM histidine (pH5.5) was obtained from Pfizer Inc. (Saint Louis, MO). USP/EP grade L-histidine, analytical grade ferric chloride ($FeCl_3$), and bis-ANS (4,4'-dianilino-1,1'-binaphthyl-5,5'-disulfonic acid, dipotassium salt) were purchased from Sigma-Aldrich Chemical Co. (St. Louis, MO). The SYPRO® orange dye, supplied as a 5000x concentrated solution in dimethyl sulfoxide (DMSO), was purchased from Invitrogen, Inc. (Carlsbad, CA, USA). The molecular details of SYPRO® orange are not available to users due to intellectual property considerations.

5.2.2 Protein formulations

The mAb solution in 20 mM histidine buffer at pH5.5 was first concentrated to 31.7 mg/mL using a lab-scale tangential flow filtration unit with 50 kDa cut-off membrane (Millipore Inc., Barrington, IL, USA). An appropriate amount of 31.7 mg/mL mAb stock solution and 1 mg/mL $FeCl_3$ stock solutions in 20 mM histidine at pH 5.5 were compounded to obtain a series of test solutions at discrete molar ratios of ferric ions to mAb of 0, 10, 20, 40, 60 and 80. The mAb concentration in all test solutions was 5 mg/mL. Other mAb formulations tested in this study were prepared by diluting the test solutions to appropriate mAb concentration.

5.2.3 Circular dichroism spectroscopy (CD)

Far UV-CD spectra and thermal transition curves for all samples were acquired on a Jasco J-720 spectrophotometer (Tokyo, Japan) with the temperature controlled by a Peltier temperature controller. Samples were diluted to 0.2 mg/mL using milliQ water with similar dilution for the blanks. A 400 µL sample was aliquoted into 1 mm quartz cuvette with a Teflon stopper for measurement. The ellipticity at 218 nm was acquired from 10^{o}C to 80^{o}C with a thermal ramp rate of 1^{o}C per minute. Prior to and post-thermal transition, full spectra from 200 to 260 nm were acquired for the sample and its respective blank with a scan rate of 20 nm/min, step of 0.5 nm, bandwidth of 0.5 nm and sampling time per point of 6s. The reported spectra are the average of three accumulations. Each sample spectrum was corrected by subtracting the respective blank spectra to eliminate buffer contributions.

5.2.4 Intrinsic and extrinsic fluorescence spectroscopy

A Cary Eclipse Fluorescence Spectrometer (Varian Inc, Lake Forest, CA, USA) with a Peltier based cuvette holder was employed to collect both intrinsic and extrinsic fluorescence spectra. A rectangular micro-cuvette (sample volume of 100 µL) with a Teflon stopper was employed with a path length of 1 cm. For both intrinsic and bis-ANS extrinsic fluorescence, the mAb samples were diluted to 0.2 mg/mL using 20 mM histidine (pH5.5) for intrinsic fluorescence or 20 mM histidine (pH5.5) containing 50 µM bis-ANS for extrinsic fluorescence measurement. The Trp-dominated intrinsic fluorescence was acquired by exciting samples at 295 nm and recording the emission from 300 to 450 nm. The bis-ANS extrinsic fluorescence spectra were acquired from 400 to 600 nm with an excitation at 385 nm. The excitation and emission slits were set at 5 nm and full spectra were collected every 2^{o}C from 10^{o}C to 80^{o}C. The respective blanks for both intrinsic and extrinsic fluorescence were collected in the same way as the protein samples and then subtracted from the active samples to eliminate any potential

background interference. Microcal Origin 10.0 (Piscataway, NJ, USA) was employed to process all background-corrected spectra for the maximal wavelengths and corresponding maximal intensities at each temperature.

5.2.5 Derivative UV absorbance spectroscopy

An Agilent 8453 diode array UV- visible spectrometer (Palo Alto, CA, USA) was employed to study the temperature perturbation of UV absorbance. Spectra were collected every 2^{o}C from 20 to 80^{o}C with an equilibration of 2 minutes for each temperature. Prior feasibility experiments had demonstrated that an equilibration time of 2 minutes was sufficient to record a stable spectrum. The samples were diluted to 0.2 mg/mL with 20 mM histidine at pH5.5 in a 1 cm cuvette, sealed with a Teflon stopper (sample volume of 200 µL). Blanks were processed similar to the active samples and their UV absorbance was subtracted from the active spectra to eliminate any potential formulation matrix interference. An Agilent Chem-Station was used to analyze the spectra and the second-derivative was acquired using a nine-point data filter, fifth-degree Savitzky-Golay polynomial. The spectra were subsequently fitted to a cubic function with 99 interpolated points per raw data point as described by Dr. Middaugh [19], permitting 0.01 nm resolution.

5.2.6 Differential scanning calorimetry (DSC)

Differential scanning calorimetry (DSC) (VP-Cap, GE HealthCare, Pittsburgh, PA, USA) was used to monitor the thermal transition temperatures (T_ms) of the mAb at different molar ratios of ferric ions to mAb by measuring the heat capacity associated with gross conformational changes. A scan rate of 200^{o}C/hr was used to record the heat capacity at the temperature of 25 to 110°C. The mAb concentration was diluted to 1.0 mg/ml with the buffer for all samples. The same dilution was used for the corresponding blanks in all experiments.

5.2.7 Differential scanning fluorescence (DSF)

SYPRO® orange dye was supplied in concentrated stock solutions. Prior to use, the dye was diluted into 20 mM histidine buffer at pH5.5. SYPRO orange was first diluted 200 times and then added to the protein solution to achieve a final dilution level of 1:2000 in the assay samples. The final concentration of SYPRO® orange was 2.5 times higher than the recommended gel stain concentration because the fluorescence intensity obtained from an earlier feasibility experiment using a 1:5000 dilution was only 2-fold higher than baseline. To improve the accuracy, a dilution of 1:2000 was utilized for all the tested solutions. The protein solutions were prepared in BioRad multiplate® PCR plates™ low 96-well clear plate (BioRad Laboratories, Hercules, CA, USA). Each cell contained an aliquot of 25 μL solution. The plate was sealed with optically clear adhesive PCR Sealers™ Microseal® 'B' film and the fluorescence monitored by a Bio-Rad CFX™ Real Time System, C1000™ Thermal Cycler (BioRad Laboratories, Hercules, CA, USA). With an excitation at 488 nm using an argon laser, SYPRO® orange was detected with FRET (FÖrster resonance energy transfer) as fluorophore. The sample plate was subjected to thermal stress from 20 to 95^{o}C with an increment of 1^{o}C. At each temperature, the plate was equilibrated for 1 minute prior to measurement. The fluorescence data and the 1st derivatives obtained from the built-in software were exported as CSV file into Microsoft Excel (Microsoft Corporation, Redmond, WA, USA) for further data analysis. The addition of the dye (at 1:5000 to 1:500) did not change the thermal transition points of the proteins determined by DSF using the same thermal stress parameters.

5.3 Results and Discussion

Protein solutions with various molar ratios of ferric ions to mAb of 0, 10, 20, 40, 60 and 80 were prepared. The actual molar ratios of ferric ion to mAb were measured as 0, 8, 18, 35, 54

and 75 due to the compounding deviation. Solution containing no ferric ions served as a negative control.

5.3.1 Far-UV circular dichroism (Far-UV CD)

The impact of ferric ions on the mAb secondary structure was explored by Far-UV CD. The full scan spectra prior to and post melting are presented in Fig. 1. At 10^{o}C, as previously observed, the protein exhibited typical β-sheet pattern with a minimum peak at 218 nm and ferric ions did not produce any impact on the mAb secondary structure. Post melting at 80^{o}C, compared to the spectra prior to melting, the ellipticity decreased and the minimum at 218 nm broadened and shifted to a lower wavelength. However, similar spectra were observed for all the solutions containing different molar ratios of ferric ions to mAb, suggesting ferric ions did not produce any impact on mAb secondary structure observable by this technique. Meanwhile, there was also no significant difference in T_m values and thermal transition patterns observed (data not shown) in the secondary structure at different molar ratios of ferric ions to mAb.

5.3.2 Intrinsic and extrinsic fluorescence

The impact of ferric ions on the protein tertiary structure was studied by intrinsic and extrinsic fluorescence in last Chapter. The same strategy was employed in this study to investigate the impact of ferric ions on mAb tertiary structure thermal stability. No difference in the thermal transitions of maximal fluorescence intensity and wavelength were observed by both intrinsic and bis-ANS extrinsic fluorescence (data not shown), suggesting that either the intrinsic and extrinsic fluorescence are not sufficiently sensitive to detect the subtle changes in thermal transition induced by ferric ions or that ferric ions did not perturb the thermal transition of the mAb tertiary structure.

5.3.3 High resolution derivative UV absorbance spectroscopy

Second-derivative UV absorbance can permit small changes in tertiary structure to be readily detected compared to other spectroscopic approaches since the three aromatic residues, Phe, Trp and Tyr are dispersed throughout the mAb primary sequence [19]. Six distinct negative peaks, three from Phe, and one each from Tyr, Trp/Tyr and Trp were observed in the second-derivative UV absorbance spectra of the test solutions containing different molar ratios of ferric ions to mAb at 20^{o}C. The six peak positions at 20^{o}C for all test solutions are summarized in Table 1 along with the peak position values from the literature [19]. The six peak positions of the negative control solution containing no ferric ions are slightly different from the values reported for bovine granulocyte colony stimulating factor (bGCSF), that is, peak 1 (Phe 1), 2 (Phe 2), 3 (Phe 3), 5 (Trp/Tyr) and 6 (Trp) moved to a higher wavelength while peak 4 (for Tyr) moved to lower wavelength. The differences are possibly induced by the differences in microenvironment between bGCSF and the IgG2 mAb. The peak positions for these six peaks were monitored as a function of temperature, as shown in Fig. 2. At lower temperature, before transition, a quasi-linear continuous wavelength increase with temperature increase was observed for all six negative peaks, reflecting the intrinsic response of the spectra of the aromatic amino acid side-chains to temperature. Similar to bGCSF at pH2 and pH3, three Phe peaks (peak 1, 2 and 3) responded differently to the temperature change. Phe-1 (peak 1, Fig. 2A) and Phe-2 (peak 2, Fig. 2B) exhibited a quasi-linear continuous wavelength increase with temperature without transition. Phe-3 (peak 3, Fig. 2C) and Tyr (peak 4, Fig. 2D) in the negative control solution exhibited a clear transition but in the solutions containing ferric ions no transitions were observed. For Trp/Tyr (peak 5, Fig. 2E) and Trp (peak 6, Fig. 2F), clear transitions were observed for all the solutions. As shown in Fig. 2, the presence of ferric ions in the solutions clearly disturbed two out of three microenvironments that Phe residues are located in, and also the Trp and Tyr

microenvironments. Furthermore, the presence of ferric ions disturbed Phe-3 (Fig. 2C) and Tyr (Fig. 2D) thermal transition pattern. While the negative control solution exhibited a clear transition, the solutions containing ferric ions exhibited continuous wavelength increase with temperature without clear transitions. These observations imply that the mAb tertiary structure is sensitive to the presence of ferric ions.

5.3.4 Differential scanning calorimetry

The melting point of a protein is an indication of its relative thermal stability. DSC was performed on the solutions containing different molar ratios of ferric ions to mAb and two well separated thermal melting transitions (Tm1 and Tm2) were observed, as shown in Fig. 3. The thermal transitions were irreversible. The data indicate that the presence of ferric ions shifts Tm1 (summarized in Table 2) to lower temperatures and broadens the transition at Tm2. An increase in the molar ratios of ferric ion to mAb decreased Tm1 proportionately, as well as the enthalpies of each transition. The DSC profile suggests that Tm1 corresponds to the unfolding or melting of the CH2 domain and Tm2 corresponds to the Fab and CH3 domains [27]. Addition of ferric ions destabilizes the Tm1 melting domains, lowering the onset and peak temperature as well as the melt enthalpy. The Tm2 temperature is not significantly impacted but the melt enthalpy is reduced. Ferric ions destabilize the structure in a domain specific manner with a greater impact on the CH2 domain.

5.3.5 Differential scanning fluorescence

SYPRO® Orange is an environment sensitive probe which on binding to hydrophobic regions shows a significant increase in fluorescence emission [4]. A feasibility experiment suggested that 5 mg/mL stock protein solution containing discrete molar ratios of ferric ions to mAb exhibited reasonable fluorescence intensity. Thus, DSF was performed with 5 mg/mL mAb

instead of diluting to 0.2 mg/mL, as was done for the Far-UV CD, fluorescence and high resolution UV absorbance studies. Since the aggregation rate, one of the major protein degradation pathways, is often directly related to its concentration [5, 28-30], the advantage of using the original solution without dilution is that the acquired properties are more representative of the actual formulation conditions.

As shown in Fig. 4A, the fluorescence spectra of all test solutions exhibited a sigmoid-shape. During the thermal melting process, temperature-dependent unfolding results in increasing exposure of hydrophobic residues and binding of SYPRO® Orange. The fluorescence intensity is maximal when the protein is molten but the hydrophobic residues are still continuous creating a patch for the dye to bind to. Subsequently, the fluorescence intensity decreases, possibly due to the formation of aggregates which could reduce the number of hydrophobic regions available for SYPRO® Orange binding and/or due to completion of denaturation / unfolding such that the hydrophobic residues are moved apart reducing the size of the binding regions. However, simple quenching due to increased temperature has also been shown to be significant and the peak may therefore be a result of the balance between increasing intensity due to hydrophobic exposure and decreasing intensity due to quenching. The spectra in Fig. 4A and the derivative spectra in Fig. 4B clearly show that increasing molar ratios of ferric ions to mAb gradually shift the onset of unfolding to lower temperatures. The hydrophobic-melt temperature (T_h) is taken as the first peak in the derivative spectra, and is summarized in Table 2 [4]. The observed reduction in the T_h indicates that ferric ions destabilize the corresponding domain structure allowing the fluorescence probe to bind at lower temperatures. Increasing the ferric ion to mAb ratio especially above 54, makes the first transition less and less distinct, indicating almost complete destabilization of the corresponding domain structure. The second peak in the

derivative spectra also moves to lower temperatures although the domains corresponding to this peak seem more resistant to unfolding by ferric ions compared to the first. This is in agreement with the DSC results presented above. The reduction in transition temperatures (listed in Table 2) that result from exposure of hydrophobic regions, demonstrates that the different molar ratios of ferric ions to mAb exert significantly different impact on mAb stability, consistent with our previous observations on the protein in real-time stability studies. Furthermore, even though the transition temperatures by DSF for the first transition are consistently lower than the melting transitions obtained by DSC (as shown in Table 2), the trend with ferric ion content is similar. The difference in absolute transition temperatures between DSC and DSF is due to the nature of the techniques, and is in agreement with observations by Goldberg, *et al.* [31]. More importantly, DSF was not only able to detect the impact of ferric ions on the first transition, but also on the second transition corresponding to the melting of more stable domains of the mAb. Other techniques, such as CD, fluorescence and DSC, were not able to detect this effect suggesting that the effect of ferric ions on these more stable domains is quite subtle. The interaction results in changes in surface hydrophobicity or hydration without (appreciable) changes to the tertiary structure and relatively unperturbed secondary structure. Compared to the impact on the less-stable domain represented by the first transition temperature (T_h), the impact on the second transition is thus less significant.

To further explore the impact of increased molar ratios on the mAb stability, a higher protein concentration of 22 mg/mL with the same molar ratios of ferric ions to mAb was prepared and analyzed by DSF. As shown in the fluorescence spectra (Fig. 5A) and the first derivative spectra (Fig. 5B), only one hydrophobic-exposure related transition could be observed. The fact that the transition temperatures are lower than that observed in 5 mg/mL solutions (as

shown in Table 2) indicates that the increased protein concentration also reduced the protein conformational stability. This effect of high protein concentration on T_h has been also reported by He *et al* [4] and Harn *et al*. [1] to increase (secondary structure) stabilization due to molecular crowding (by DSC and CD), but decreased tertiary structure stability (by UV and fluorescence) with increasing concentration. Destabilization of tertiary structure could occur due to increased self-association (reversible and irreversible) resulting in reduction in solvent exposed surface area [31]. Addition of ferric ions to these higher concentrated solutions (22 instead of 5 mg/mL) caused a steeper decline in the T_h (see Table 2), in agreement with the mechanistic explanation that ferric ions destabilize the tertiary structure. The combined effect of ferric ions and higher concentration seems to reduce the onset temperature at which the hydrophobic regions become exposed.

5.4 Conclusions

The impact of ferric ions on the thermal stability of an IgG2 mAb was characterized by Far-UV CD, intrinsic fluorescence and (bis-ANS) extrinsic fluorescence, DSC and DSF using SYPRO® Orange. The results of Far-UV CD and intrinsic/bis-ANS extrinsic fluorescence did not demonstrate any detectable impact of ferric ions on the thermal stability of the mAb. However, the observed impact on the six negative peaks resulting from aromatic residues in the second derivative UV spectra suggested that the presence of ferric ions in the solution disturbed the mAb tertiary structure. This is in agreement with the decreased melting points measured by DSC. The spectra acquired by DSF using SYPRO® Orange dye at high and low protein concentrations provided further evidence that the increased molar ratios of ferric ions to mAb destabilized the mAb, primarily through the less stable domain by perturbing the tertiary structure. At low concentrations, the impact of ferric ions on the more stable domains was small (by DSF).

However, at the higher mAb concentration, a combination of destabilization by possible self-association as well as by ferric ion, resulted in a steep decline in the temperature of hydrophobic exposure. This study of the impact of ferric ions on mAb thermal stability provides further evidence that the earlier observed physical and chemical instability of the studied mAb on long-term storage, was a consequence of the ferric ion binding / interaction.

5.5 References

1. Harn, N., et al., *Highly concentrated monoclonal antibody solutions: direct analysis of physical structure and thermal stability.* J Pharm Sci, 2007. **96**(3): p. 532-46.
2. Taves, C.J., et al., *Human aglycosyl-IgG exhibits increased hydrophobicity. Binding/fluorescence studies with 8-anilinonaphthalene-1-sulfonic acid (ANS).* Biochem Biophys Res Commun, 1984. **124**(2): p. 605-13.
3. Goldberg, D.S., et al., *Formulation development of therapeutic monoclonal antibodies using high-throughput fluorescence and static light scattering techniques: Role of conformational and colloidal stability.* J Pharm Sci, 2011.
4. He, F., et al., *High throughput thermostability screening of monoclonal antibody formulations.* J Pharm Sci, 2009. **99**(4): p. 1707-20.
5. Guo, J., et al., *Stability of helix-rich proteins at high concentrations.* Biochemistry, 2006. **45**(28): p. 8686-96.
6. Zhou, S., et al., *Biologics formulation factors affecting metal leachables from stainless steel.* AAPS PharmSciTech, 2011. **12**(1): p. 411-21.
7. Zhou, S., et al., *Biotherapeutic Formulation Factors Affecting Metal Leachables from Stainless Steel Studies by Design of Experiments.* AAPS PharmSciTech, 2011.

8. Zhou, S., et al., *Metal leachables in therapeutic biologic products: origin, impact and detection.* Am. Pharm. Rev., 2010. **13**(4): p. 76-80.
9. Zhou, S., et al., *Comparative evaluation of disodium edetate and diethylenetriaminepentaacetic acid as iron chelators to prevent metal-catalyzed destabilization of a therapeutic monoclonal antibody.* J Pharm Sci, 2010. **99**(10): p. 4239-50.
10. Bexendale, J.H., et al., *The mechanism and kinetics of the initiation of polymerisation by system containing hydrogen peroxide.* Trans. Faraday Soc., 1946. **42**: p. 155-169.
11. Czapski, G., et al., *The reactions of organic radicals formed by some Fenton reagents.* J. Phys. Chem., 1971. **75**: p. 3271-3280.
12. Davies, G.G., et al., *The kinetics and mechanism of chromium (II) cyanide complexes with hydrogen peroxide in aqueous solution.* J. Am. Chem. So., 1970. **92**: p. 1892-1897.
13. Moorhouse, C.P., et al., *Cobalt (II) ions as a promoter of hydroxyl radical and possible "crypto hydroxyl" radical formation under physiological conditions. Differential effects of hydroxyl radical scavengers.* Biochim. Biophys. Acta, 1985. **843**: p. 261-268.
14. Ponganis, K.V., et al., *Electron transfer reaction of coppper complexes. 1. A kinetic investigation of the oxidation of Bis (1,10-phenanthroline) copper (I) by hydrogen peroxide in aqueous and sodium dodecyl sulfate solution.* Inorg. Chem., 1980. **18**: p. 38-43.
15. Chen, W.T., et al., *Distinct effects of Zn^{2+}, Cu^{2+}, Fe^{3+}, and Al^{3+} on amyloid-beta stability, oligomerization, and aggregation: amyloid-beta destabilization promotes annular protofibril formation.* J Biol Chem, 2011. **286**(11): p. 9646-56.
16. Derrick, T.S., et al., *Effect of metal cations on the conformation and inactivation of recombinant human factor VIII.* J Pharm Sci, 2004. **93**(10): p. 2549-57.

17. Thakurta, P.G., et al., *Tertiary structural changes associated with iron binding and release in hen serum transferrin: a crystallographic and spectroscopic study.* Biochem Biophys Res Commun, 2004. **316**(4): p. 1124-31.
18. Uversky, V.N., et. Al., *Metal-triggered structural transformations, aggregation, and fibrillation of human alpha-synuclein. A possible molecular link between Parkinson's disease and heavy metal exposure.* J Biol Chem, 2001. **276**(47): p. 44284-96.
19. Kueltzo, L.A., et al., *Derivative absorbance spectroscopy and protein phase diagrams as tools for comprehensive protein characterization: a bGCSF case study.* J Pharm Sci, 2003. **92**(9): p. 1805-20.
20. Ericsson, U.B., et al., *Thermofluor-based high-throughput stability optimization of proteins for structural studies.* Anal Biochem, 2006. **357**(2): p. 289-98.
21. He, F., et al., *Detection of IgG aggregation by a high throughput method based on extrinsic fluorescence.* J Pharm Sci, 2009. **99**(6): p. 2598-608.
22. Lavinder, J.J., et al., *High-throughput thermal scanning: a general, rapid dye-binding thermal shift screen for protein engineering.* J Am Chem Soc, 2009. **131**(11): p. 3794-5.
23. Niesen, F.H., eet al., *The use of differential scanning fluorimetry to detect ligand interactions that promote protein stability.* Nat Protoc, 2007. **2**(9): p. 2212-21.
24. Pantoliano, M.W., et al., *High-density miniaturized thermal shift assays as a general strategy for drug discovery.* J Biomol Screen, 2001. **6**(6): p. 429-40.
25. Hoehne, M., et al., *Adsorption of monoclonal antibodies to glass microparticles.* J Pharm Sci, 2011. **100**(1): p. 123-32.
26. Thirumangalathu, R., et al., *Silicone oil- and agitation-induced aggregation of a monoclonal antibody in aqueous solution.* J Pharm Sci, 2009. **98**(9): p. 3167-81.

27. Ionescu, R.M., et al., *Contribution of variable domains to the stability of humanized IgG1 monoclonal antibodies.* J Pharm Sci, 2008. **97**(4): p. 1414-26.

28. Minton, A.P., *Implications of macromolecular crowding for protein assembly.* Curr Opin Struct Biol, 2000. **10**(1): p. 34-9.

29. Minton, A.P., *Protein folding: Thickening the broth.* Curr Biol, 2000. **10**(3): p. R97-9.

30. Tokuriki, N., et al., *Protein folding by the effects of macromolecular crowding.* Protein Sci, 2004. **13**(1): p. 125-33.

Table 1. Second derivative UV-spectra peak positions of aromatic residues in the test solutions containing different molar ratios of ferric ions to mAb at 20^{o}C compared to the reference values in bGCSF at 10^{o}C

		Peak 1: Phe-1	Peak 2: Phe-2	Peak 3: Phe-3	Peak 4: Tyr	Peak 5: Trp/Tyr	Peak 6: Trp
Reference values in bGCSF		252.7	258.8	265.5	277.6	283.9	290.6
Neg Ctrl		253.1	259.1	268.5	276.5	284.5	292.0
Molar ratios of ferric ion to mAb	8	253.2	259.3	269.0	276.9	284.8	292.3
	18	253.2	259.3	268.8	276.8	284.8	292.4
	35	253.2	259.3	268.6	276.8	284.8	292.3
	54	253.1	259.3	268.8	276.8	284.8	292.3
	75	253.2	259.3	268.9	276.8	284.8	292.2

Table 2. First transitional temperatures (Tm1 for DSC and first transition temperature of hydrophobic exposure for DSF) for the test solutions at different molar ratios of ferric ion to mAb

Techniques	mAb conc. (mg/mL)	Neg Ctrl	Molar ratios of ferric ion to mAb				
			8	18	35	54	75
DSF	5	62.0	61.1	59.8	57.8	50.5	46.6
	22	60.0	57.0	46.5	NA	NA	NA
DSC	1	67.97	67.19	67.02	65.93	65.62	65.32

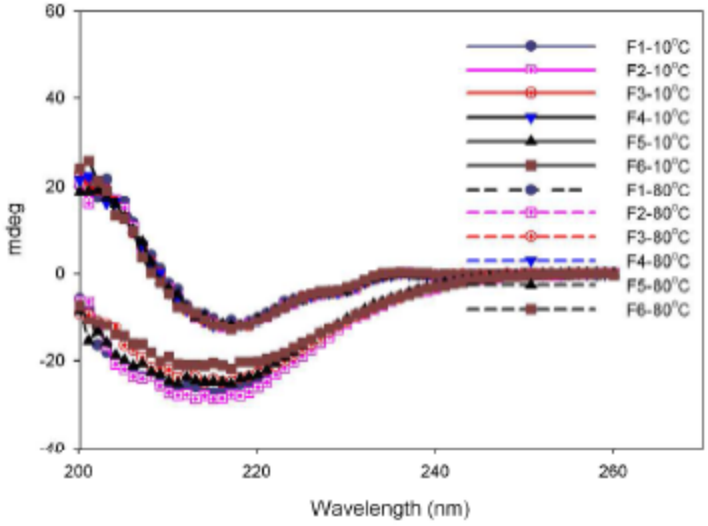

Fig. 1. Secondary structure examined by Far-UV circular dichroism (CD) for the solutions containing discrete molar ratios of ferric ions to protein pre and post melting at 10°C and 80°C: the spectra of upper group represent the secondary structure at 10°C and the spectra in the lower group represent the secondary structure at 80°C.

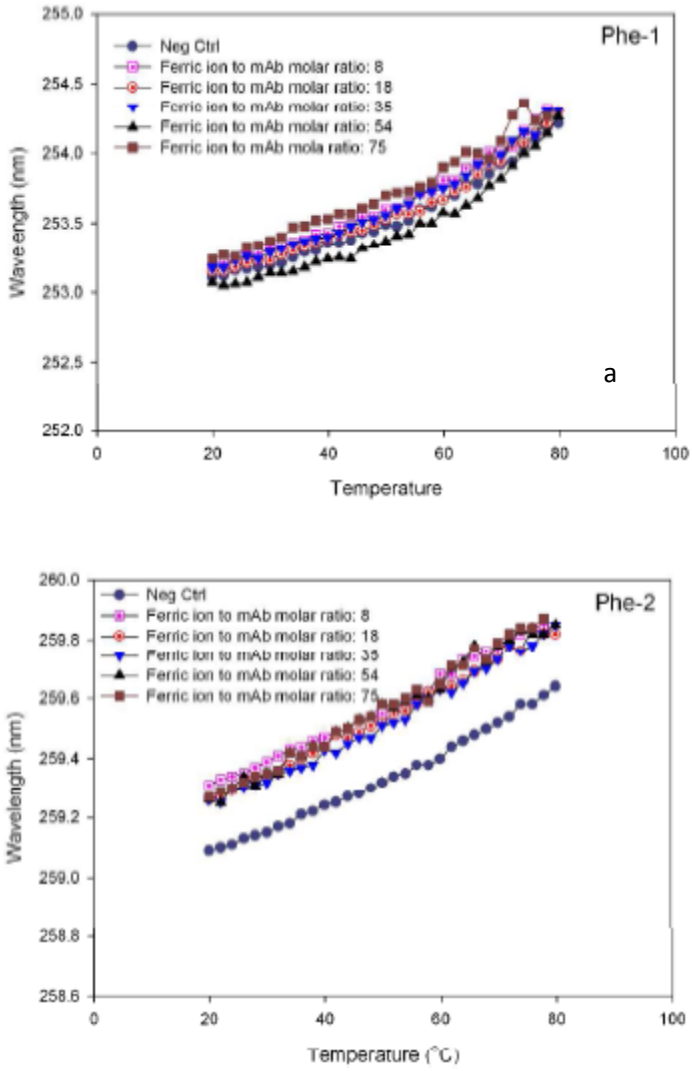

Fig. 2. Comparison of solution thermal stability containing discrete molar ratios of ferric ion to the protein investigated by high-resolution second derivative absorbance at a function of temperature: (a) Phe-1, (b) Phe-2, (c) Phe-3, (d) Tyr, (e) Tyr/Trp, and (f) Trp. The experiment was performed on the diluted solution containing 0.2 mg/mL protein.

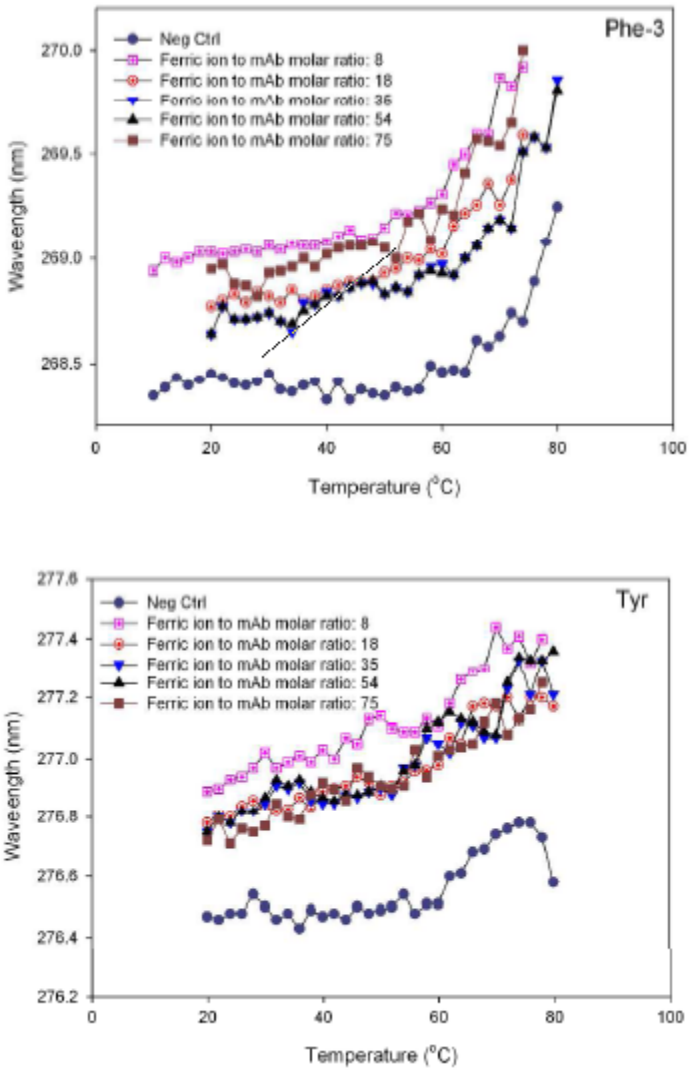

Fig 2. Continued

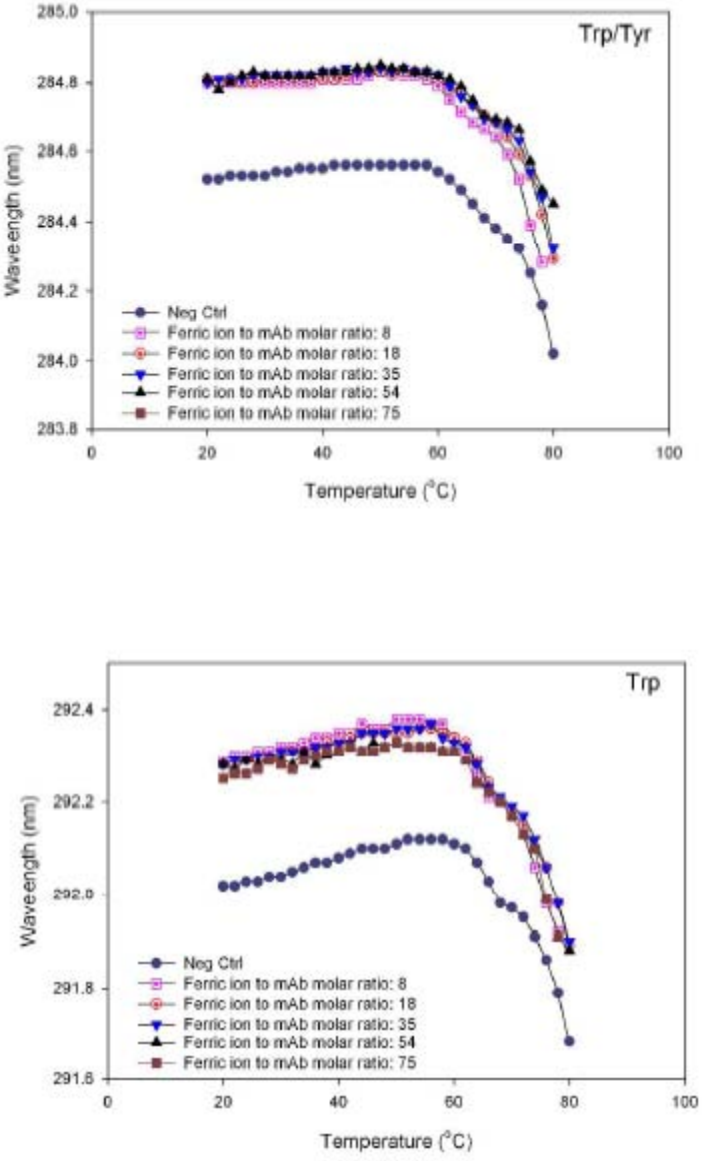

Fig 2. Continued

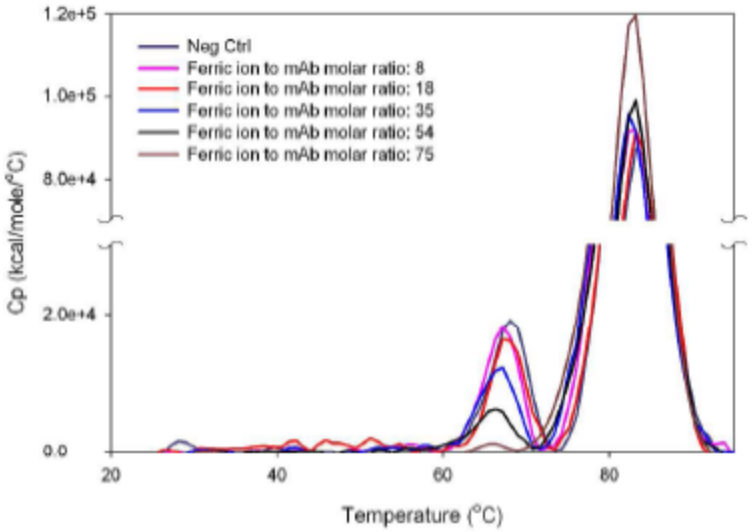

Fig. 3. The impact of ferric ions on the thermal unfolding of the solutions containing discrete molar ratios of ferric ions to the protein investigated by DSC. The experiment was performed on the diluted solution of 1 mg/mL protein in 20 mM histidine at pH5.5 containing discrete molar ratios of ferric ions to mAb at 0, 8, 18, 35, 54 and 75.

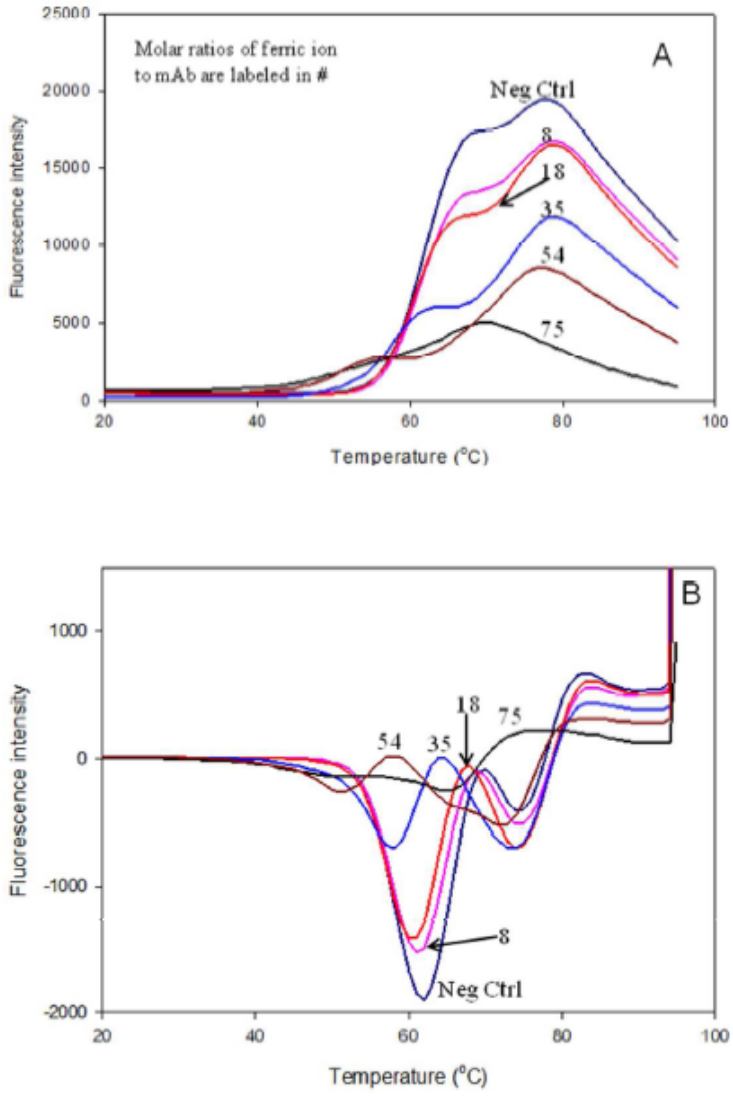

Fig. 4. The impact of ferric ions on the protein thermal stability examined by differential scanning fluorescence (DSF) using SYPRO® Orange dye in the solutions containing discrete levels of molar ratios of ferric ions to protein at 0, 8, 18, 35, 54 and 75. The experiment was performed on the 5 mg/mL stock solutions without dilution: (a) the fluorescence intensity as a function of temperature and (b) the first derivatives of the fluorescence intensity.

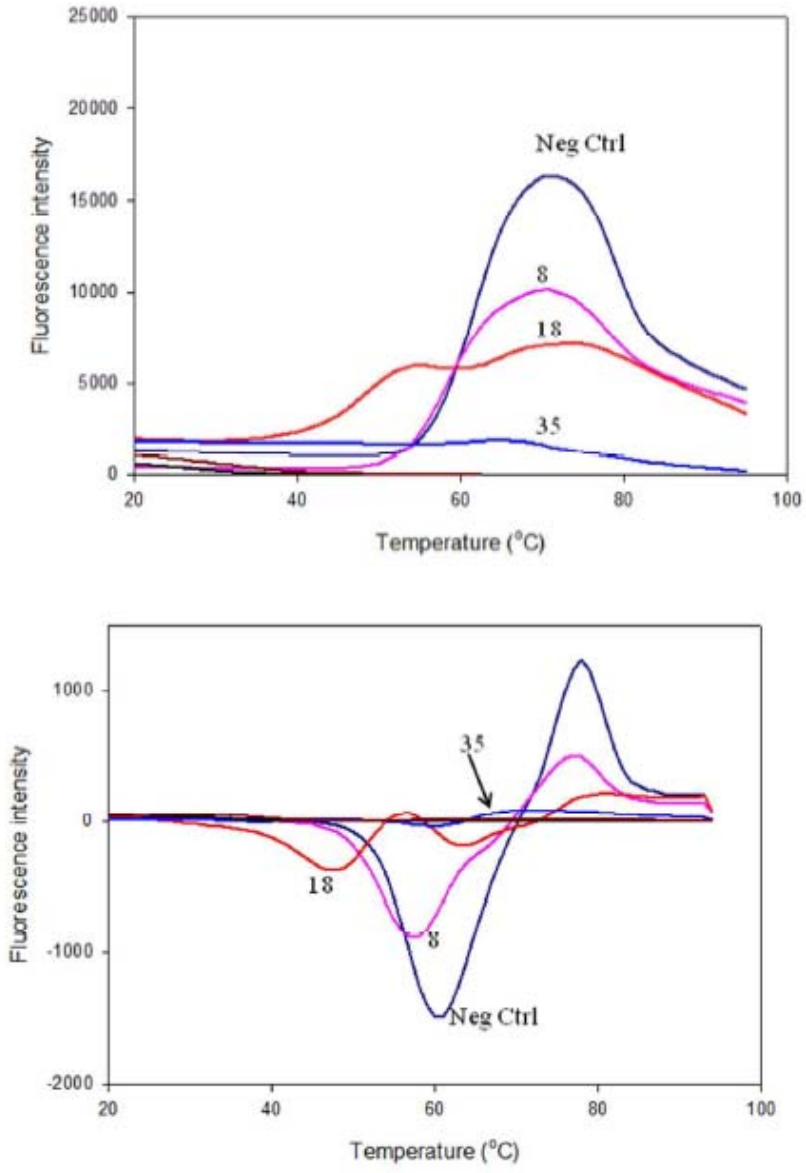

Fig. 5. The impact of ferric ions on the protein thermal stability examined by differential scanning fluorescence (DSF) using SYPRO® Orange dye in the solutions containing discrete levels of molar ratios of ferric ions to protein at 0, 8, 18, 35, 54 and 75. The experiment was performed on the 22 mg/mL stock solutions without dilution: (a) the fluorescence intensity as a function of temperature and (b) the first derivatives of the fluorescence intensity.

Chapter 6: Formulation strategy to prevent metal-catalyzed destabilization of IgG1

Table of Contents

6.1 Introduction

It is well known that transition metal ions such as Fe(II)/(III), Cu(II), Zn(II), Co(II) and Ni(II) etc., can bind to protein molecules to stabilize their structure and play a critical role in modulating physiological functions [1–7]. Iron, an essential constituent of proteins involved in many cellular processes, is crucial for the growth and viability of almost all organisms. However, excessive iron may become toxic or even fatal due to its ability to induce oxidation of lipids and other cellular constituents [8–10]. It has been reported that iron can induce protein degradation via different mechanisms [11–15]. Since iron is only regulated by uptake [6], iron chelators have been introduced into clinical practice to protect patients from toxicity caused by iron overload. Various chelators such as cell-impermeable chelators like ethylenediaminetetraacetic acid (EDTA), dipicolinic acid (DPA), diethylenetriaminepentaacetic acid (DTPA) [16], cell-permeable chelators of hydroxypyridiones such as b-[N-(3-hydroxy-4-pyridone)]-a-aminopropionic acid (L-mimosine) [17], catecholates such as 1,5,10-N, N', N'-tris (5-sulfo-2,3-dihydroxybenzoyl) triazadecane (3,4-LICAMS) [6], and pyrophosphates [6] have been widely studied, although (salts of) EDTA (Fig. 1A) and to a lesser extent DTPA (Fig. 1B) are the most commonly used. EDTA is a hexadentate chelator capable of complexing stoichiometrically with virtually every transition metal in the periodic Table [18]. The effectiveness of EDTA as a chelator for a particular metal ion is governed by the stability constant of the resulting metal complex. The stability constants (log K) of EDTA (acid form) metal complexes for the most commonly observed trace metal ions in parenteral formulations are 25.1 for Fe(III) and 14.6 for Fe(II) [19]. The stability constant for DTPA-Fe (III) is 27.3 and that for DTPA-Fe (II) is 16.0 at 20^{o}C, 0.1M ionic strength [20].

Many parenteral biologics drug products include metal chelators to improve product stability, with salts of EDTA being the most common. These chelators are generally used to complex trace amount of metals (especially iron ions) which may be introduced into the drug solution from formulation excipients and/or leachables from contact with stainless steel equipment utilized in production and storage. Both disodium edetate (Na_2EDTA) and calcium disodium edetate ($CaNa_2EDTA$) have been approved for human use by the FDA [21, 22]. Analysis of drugs approved through the year 2000 reveal that 48 parenteral drugs contain EDTA in various salt forms [23]. Nine contain $CaNa_2EDTA$, 38 contain Na_2EDTA, and 1 product (Folvite®) contains sodium edetate [23].

Na_2EDTA is generally used in pharmaceutical preparations as a chelating agent at concentrations between 0.005 – 0.1% w/v (0.05 – 1mg/mL). $CaNa_2EDTA$ is used in formulations as a chelating agent in the range 0.01% – 0.1% w/v (0.1 – 1 mg/mL). Na_2EDTA readily chelates calcium and can, in large doses, cause calcium depletion (hypocalcemia) if used over an extended period or if administered too rapidly by IV infusion. $CaNa_2EDTA$ does not chelate calcium. For Na_2EDTA the LD50 (mouse, IV) = 0.056 g/kg, and LD50 (rabbit, IV) = 0.047 g/kg. For $CaNa_2EDTA$ the L50 (rat, IV) = 3.0 g/kg. The toxicity is significantly dependent on the salt form used [24].

Disodium edetate is not a first-line agent for any indication; it is approved for use in emergency treatment of severe hypercalcaemia and in the treatment of arrhythmias secondary to digitalis toxicity. In adults with normal renal function, about 50% is excreted in the first hour in the urine and over 95% is excreted with 24 hours. Disodium edetate is almost entirely excreted in the urine unchanged within 24 hours. Therapeutically, a dose of 50 mg/kg Na_2EDTA, as a slow infusion over a 24 hour period, with a maximum daily dose of 3 g, has been used as a treatment

for hypercalcemia. For the treatment of lead poisoning, a dose of 60–80 mg/kg of $CaNa_2EDTA$, as a slow infusion in two daily doses, for 5 days has been used [22, 25].

Use of the generic term EDTA for all its various salt forms has had fatal consequences. Children and adults have died from overdose of disodium edetate mistakenly administered in place of calcium edetate, or when disodium edetate was used for ‘‘chelation therapies’’ [21]. A Public Health Advisory was issued by the FDA in January 2008 concerning this use and the misleading abbreviation EDTA [22, 26].

A recombinant human granulocyte macrophage colony stimulating factor product (Leukine®), was marketed as a lyophilized form without disodium edetate. However, Leukine® was reformulated in 2006 as a liquid containing disodium edetate. An increase in spontaneous reports of adverse events such as syncope and hypotension was noticed, which appeared to coincide with the introduction of the liquid formulation [27]. This increase in adverse event reports was not associated with the lyophilized formulation of Leukine® which did not contain disodium edetate [28]. The liquid Leukine® was voluntarily withdrawn from the market in January 2008 [27]. A new formulation of liquid Leukine® without disodium edetate was approved by the FDA in May 2008 [28]. The dose of disodium edetate through Leukine is about 1.9 mg/day for a 2 m^2 patient via the IV or SC routes. Interestingly, in the same time frame, a new IV formulation of fosaprepitant demelgumine (Emend®) was approved with a disodium edetate dose of up to 14.4 mg per injection. Caution is required when using Na_2EDTA in developing new biopharmaceutical products due to these safety concerns. EDTA also has been reported to accelerate protein oxidation in some cases even though the intention was to stabilize proteins in the presence of iron [12, 13, 29]. Considering the safety and possible stability issues around EDTA, it is important to evaluate the use of alternate chelators.

DTPA is one of the synthetic polyamino polycarboxylic acids that can form stable complexes with a large number of metal ions, such as Cu(II), Ni(II), Co(II), Zn(II), Cd(II), Mn(II) and Ca(II) [30]. Free DTPA contains five carboxylic acid and three amine groups, and five pKa values of 1.79, 2.56, 4.42, 8.76 and 10.42 have been reported [31]. Similar to EDTA, DTPA chelates iron ions at equimolar ratio [31, 32] over pH 2.5–11.0. It has been used in some approved drug products. For example, Magnevist® contains 0.40 mg DTPA/mL (0.04%; dose 0.08 mg DTPA/kg) and Kinevac contains 0.04 mg/mL DTPA (0.004% DTPA; dose 0.008 – 0.048 mg DTPA/kg). Calcium trisodium pentetate is used in the treatment of poisoning by heavy metals while both calcium trisodium pentetate and zinc trisodium pentetate are used in case of poisoning with radioactive metals such as plutonium, americium, and curium. In heavy-metal poisoning, calcium trisodium pentetate has been given in a dose of 1 g daily by intravenous infusion for 3 to 5 days, with further treatment, if necessary, after an interval of 3 days [25, 33–37]. The reported LD50 of DTPA (rat, IP) is 0.59 g/kg [38]. DTPA is hydrophilic and is unlikely to penetrate cells to any great extent [39]. Early pharmacokinetic studies in animals [40-41] and in humans [42] showed that DTPA is very poorly distributed into tissues and is rapidly eliminated from the body via urine excretion after either intravenous injection or inhalation.

The safety profile of DTPA suggests that it can be a viable alternative to the more commonly used (salts of) EDTA in biologics formulations. There is limited information and experience with the use of DTPA in protein formulations. This study therefore focuses on comparing the ability of Na_2EDTA or DTPA (acid form) to influence the physical / chemical stability and biophysical properties of an IgG2 mAb in the presence of various levels of iron.

6.2 Material and Methods

6.2.1 Materials

An IgG2 monoclonal antibody produced by Pfizer Inc. was used as a test molecule in this study. The mAb was formulated in 20 mM histidine buffer at pH 5.5 containing 84 mg/mL trehalose dihydrate, and 0.2 mg/mL polysorbate 80. USP/EP grade L-histidine, L-histidine mono hydrochloride, analytical grade $FeCl_2$, $FeCl_3$, acetate acid (97.7%), disodium EDTA dihydrate and DTPA were obtained from Sigma-Aldrich Chemical Co. (St. Louis, MO, USA). USP/EP grade polysorbate 80 was obtained from J.T. Baker (Meriden, CT, USA).

6.2.2 Preparation of the test solutions and experimental design

The mAb in the formulation buffer was concentrated to 20 mg/mL using a tangential flow filtration (TFF) unit. The protein concentrations were determined using an extinction coefficient of 1.43 (1 mg/mL at 280 nm; 1 cm path-length) determined by the Edelhoch method [43]. The appropriate amounts of Na_2EDTA and DTPA stock solutions were added to mAb in formulation buffer according to the matrix described in Table 1. The pH of the final formulations was controlled to 5.5 using 20 mM histidine /histidine-HCl buffer. At this pH, DTPA (H_5A) exists in equilibrium between $H_2A^{3-}$and H_3A^{2-}; however, in the presence of iron, DTPA forms the complexes of FeA^{3-}/ FeA^{2-} at equimolar ratios [31]. For simplicity, the term DTPA is used in the text, regardless of its ionization form.

Various levels of iron were spiked (as concentrated $FeCl_2$ stock) into the formulated mAb solutions containing the defined molar amount (0.134 mM) of Na_2EDTA or DTPA. Both a negative control (absence of chelator and iron) and a positive control (absence of chelator but presence of iron at a level of 24 ppm) were used. Table 1 summarizes the complete experimental design. The amounts of Na_2EDTA and DTPA in the formulations were confirmed by RP-HPLC. The concentrations of spiked iron were measured by ICP-MS during the evaluation of real time stability data. The formulations were filtered through a 0.22 μm PVDF filter, 1 mL aliquots were

filled into 2-mL type I glass vials, and then placed in stability chambers maintained at either 2–8^{o}C, 25^{o}C, or 40^{o}C. The formulations were stored at various temperatures (5^{o}C, 25^{o}C and 40^{o}C) for thirteen weeks. Biochemical and biophysical data were collected at different time intervals to assess the mAb degradation.

6.2.3 RP-HPLC analysis for mAb oxidation and chelator concentration

RP (reversed phase)-HPLC was employed to monitor the oxidation of the mAb by means of proteolytic mapping with a limit of quantitation of 1.6%. Methionine-containing peptide fragments and their respective oxidized forms (containing methionine sulfoxide) were chromatographically monitored, and their percent oxidation was reported relative to the methionine containing parent peptides. The mAb samples were digested with LysC enzyme for 18±2 hours at 37^{o}C. The oxidized peptide fragments were separated on an Agilent 1100 system equipped with a binary pump and UV detector set at 214 nm. A GraceVydac protein C4 analytical column (5 µm, 4.6 mm x 250 mm) was used to separate peptide fragments with two mobile phases consisting of (A) 0.1% (v/v) TFA (trifluoroacetic acid) in water and (B) 0.085% (v/v) TFA in acetonitrile. The following binary gradient was adjusted at a flow rate of 1 mL/min: (1) 79% mobile phase (mp) A and 21% mobile phase B held for the first 10 mins; (2) mp A decreased to 70% and mp B increased to 30% within 32 mins; (3) mp A decreased to 5% and mp B increased to 95% within 3 mins and held for an additional 4 mins; (4) mp A and B returned to their initial composition (mp A: 79% and mp B: 21%) within 2 mins and held for an additional 8 mins. The final mAb concentration was diluted to 1 mg/mL and 100 µL was injected to separate the oxidative products. Results are reported as % oxidization. The concentrations of both Na_2EDTA and DTPA in the formulations were determined using the Agilent 1100 system coupled to a diode array detector. The separation was achieved isocratically on an Agilent

Eclipse XDB-C18 column (5 µm, 4.6 x 150 mm) at a flow rate of 1 mL/min at ambient temperature. The mobile phase consisted of 30 mM sodium acetate, 2 mM tetrabutylammonium hydroxide, and 5% (v/v) methanol in water (pH 3.15). Excessive $FeCl_3$ (5 mM in final) was added to both samples and standards. External calibration was established with varying levels of Na_2EDTA and DPTA simultaneously. 20 mL of the sample were injected onto the column and the separation was monitored by UV detection at 254 nm.

6.2.4 Size exclusion HPLC

Size exclusion HPLC was employed to monitor mAb aggregation. The chromatography was performed on an Agilent 1100 system equipped with G3000SWXL and G2000SWXL columns (7.8 x 300 mm, Tosoh Biosciences, Montgomeryville, PA, USA or equivalent) in tandem using 200 mM phosphate at pH 7.0 as the mobile phase. An isocratic elution method (0.7 mL/min) was used. The injection volume was adjusted such as to inject 20 mg mAb onto the columns and the elution was monitored at 214 nm. The quantities of the monomer, low molecular weight species (LMMS) and high molecular mass species (HMMS) were reported after integration.

6.2.5 Imaged capillary isoelectric focusing (iCE)

Changes in charge heterogeneity were used to detect deamidation of the mAb. iCE profiles of the monoclonal antibody were obtained using an iCE280 Analyzer equipped with an Alcott 719 AL autosampler (Convergent Bioscience, Toronto, OH, USA). The test solutions were prepared using various amounts of pI markers, Pharmalyte, 1% methyl cellulose, 5 M urea, 20% sucrose and monoclonal antibody samples. A sample volume of 35 µL was injected and the analysis was performed using a sample transfer time of 100 seconds, pre-focusing at 1500 V for duration of 1 min followed by focusing 5 mins at 3000 V. The samples were detected at 280 nm

and the relative abundance of the resolved peaks was calculated. Results are reported as % acidic species.

6.2.6 Sodium dodecyl sulfate-polyacrylamide gel electrophoresis (SDS-PAGE)

SDS-PAGE was employed to quantify the intact and degraded products of the monoclonal antibody. The separation was performed on precast polyacrylamide gels (NuPAGE 4-12% Bis-Tris, Invitrogen, Carlsbad, CA, USA) using a mini-gel apparatus (Invitrogen Cell SureLockTM). The bands were analyzed using the Molecular Dynamics Personal Densitometer (PDQC-90) with FragmeNT software. Results are reported as% Total impurities.

6.2.7 Inductively coupled plasma – mass spectrometry (ICP-MS)

Spiked iron concentrations in the formulations were confirmed by an ICP-MS method which utilized an Agilent 7500 CX ICP-MS system equipped with an autosampler. 50 mL of mAb samples and blanks were digested using 70% nitric acid (Omnitrace-NX0407) (EMD Chemicals Inc, Gibbstown, NJ, USA) at a volume ratio of 1:3 (sample: nitric acid) on a heated water bath (80–90^{o}C) for 15 minutes. Samples were cooled to room temperature after digest completion and diluted to 5 mL with 1% nitric acid before analysis. Samples were analyzed in the ‘‘hydrogen mode’’ and scandium (45) was used as the internal standard. An external calibration curve was established before running the digested samples. A 50 ppb standard was analyzed between every 6 samples to ensure the system performance.

6.2.8 Isothermal titration calorimetry (ITC)

Thermodynamic binding measurements were made using an isothermal titration calorimeter (VP-ITC, GE-Healthcare, Piscataway, NJ, USA) at 25^{o}C. The mAb and $FeCl_3$ samples were degassed at 23^{o}C (Thermo-Vac, GE-Healthcare, Piscataway, NJ) before loading into the ITC cell and syringe. Titration in the presence of chelator anions included mixtures of

equimolar concentrations of either Na_2EDTA or DTPA with mAb in the cell and $FeCl_3$ in the syringe. Reference titrations were carried out by injecting $FeCl_3$ into placebo buffer which did not contain mAb. The reference was subtracted from the heat of interaction with mAb. Iron binding measurements for both DTPA and Na_2EDTA were not feasible via the ITC method due to the very large binding constants ($>10^{12}$M). The concentrations of mAb, $FeCl_3$, Na_2EDTA and DTPA used were 33.5 μM, 6 mM, 268 mM, and 268 mM, respectively. The binding isotherms were best fit to a single class binding site model by Marquardt using non-linear least-squares analysis to obtain stoichiometry and thermodynamic parameters.

6.2.9 Differential scanning calorimetry (DSC)

The thermal stability of the antibody was measured by monitoring the heat capacity associated with gross conformational changes in the antibody using DSC (VP-Cap, GE healthcare). A scan rate of 200^{o}C/hr, scan range of 25–110^{o}C, and a mAb concentration of 1.0 mg/mL was used in all experiments.

6.2.10 Circular dichroism (CD) spectroscopy

Far UV-CD spectra for various samples were acquired by using a Jasco J-810 Spectropolarimeter (Jasco Inc, Easton, MD, USA) equipped with an autosampler. Samples were diluted to 0.25 mg/mL using the formulation buffer. The spectra were acquired for samples and respective buffers from 190 to 260 nm. Sample spectra were subtracted from respective buffer spectra to eliminate buffer contributions. Data acquisition and analyses were performed by using inbuilt Spectra Manager™ software.

6.2.11 Intrinsic fluorescence

Intrinsic fluorescence measurements were performed on a Cary Eclipse Fluorescence Spectrophotometer (Varian Inc, Lake Forest, CA, USA) using 0.2 mg/mL mAb for all iron

concentrations. The mAb was excited at 295 nm and the tryptophan-dominated emission was monitored between 305 to 405 nm to avoid iron interference. The excitation and emission slits were set at 5 nm. All the spectra were analyzed using the Microcal Origin 7.0 (Piscataway, NJ, USA) software. The sample spectra were subtracted from respective blank control spectra to eliminate the formulation matrix contribution.

6.3 Results and Discussion

The ability of Na_2EDTA or DTPA to protect the IgG2 mAb from metal (iron)-induced degradation was studied by holding the formulations at various temperatures and evaluating the physical and chemical changes to the mAb at different time intervals.

6.3.1 Real-time biochemical analysis

Metals, present even in trace amounts in protein solutions, can induce oxidation [12, 44, 45], fragmentation [44–46], aggregation [12], and/or possibly contribute to other pathways of protein degradation such as deamidation or the formation of insoluble particles. Protein oxidation, aggregation, fragmentation and deamidation are major indicators of product stability. There are also concerns for the potential alteration of pharmacology, immunogenicity, and toxicology as a consequence of these degradants [12, 47, 48]. Therefore, these degradation routes serve as indicators of the stability of biologic drug products to support the development of products with adequate shelf life and were closely monitored in this study to differentiate mAb stability among the formulations.

6.3.2 mAb degradation

The real time stability data at 2–8^{o}C for oxidation, soluble aggregates, total impurities and deamidation are shown in Fig. 2–5, respectively. The data for the samples stored at higher temperatures exhibited similar trends (data not shown). For iron concentration less than 4 ppm

(equivalent to 0.0715 mM), the molar ratio of the chelators Na_2EDTA or DTPA to iron is greater than 1:1, i.e. above stoichiometric ratio. Here, both Na_2EDTA and DTPA containing formulations showed stability profiles similar to the negative control. At iron levels more than 15 ppm (equivalent to 0.268 mM), the molar ratio of the chelator to iron is less than 1:1, i.e. sub-stoichiometric ratio. Under such conditions, both Na_2EDTA and DTPA containing formulations exhibited a similar or less severe degree of degradation compared to the positive control but significantly more severe degradation compared to the negative control. At the initial time point, oxidation and aggregation do not correlate directly with the spiked iron levels, probably due to the difference in actual analysis timing for the individual samples since these samples had to wait for a few days to be sequenced for analysis after being stored for two weeks at 2–8^{o}C. Clearly, the iron-catalyzed degradation of mAb can be effectively inhibited at chelator to iron molar ratios of greater than 1:1. Fig. 6 summarizes the degradation data for the thirteen week time point which illustrates again that a molar ratio of chelator to iron above 1:1 leads to efficient stabilization.

6.3.3 Statistical analysis of real-time data

Statistical analyses were performed by using design expert software to gain more insight into the real time stability data obtained and thereby elucidate any subtle differences present. Chelator type, iron levels in the formulations, storage temperature and time were the four major parameters considered in this analysis. The responses from the real-time data analyzed were soluble aggregates (i.e., high molecular mass species - HMMS) and oxidation levels. Analysis of HMMS / oxidation, and two factor interaction response surface model fit to the actual data suggested that un-chelated iron level, time and temperature were major factors to impact the mAb degradation. This observation was in line with the observations in the previous section. No

difference in soluble aggregate levels was observed when comparing formulations containing either DTPA or Na_2EDTA. Fig. 7A and Fig. 7B display response-surface plots for the 13 week time point for Na_2EDTA and DTPA, respectively. These plots demonstrate that higher un-chelated iron levels and higher temperatures increase the amount of soluble aggregates. Furthermore, contour plots (not shown) revealed no notable differences in soluble aggregates for the two chelator types.

Oxidation level analysis for the available data of up to 13 weeks are illustrated in response-surface plots displayed in Fig. 8A (Na_2EDTA) and Fig. 8B (DTPA), respectively. There was no apparent difference between Na_2EDTA and DTPA. Both of them worked effectively at the intended storage condition of 2–8^{o}C. Further analysis of surface plots and contour plots (not shown) suggested that there was a slight difference in the oxidation levels as a function of chelator type at elevated temperature when the chelator to iron molar ratio was less than 1:1. At these sub-stoichiometric levels of chelator, the contour plots (not shown) indicated that Na_2EDTA may be a better stabilizer than DTPA under accelerated storage (40^{o}C) conditions. No significant differences were observed under these accelerated conditions with adequate (greater than stoichiometric) amounts of chelator. Therefore, both DTPA and Na_2EDTA can be effective chelators for the studied mAb as long as an adequate amount of chelator is present.

6.3.4 Biophysical analysis

Biophysical methods were used to evaluate the effect of spiked iron and chelators on mAb structure and stability. The binding of iron ions to the mAb was also measured by ITC in the presence and absence of Na_2EDTA and DTPA. DSC, Far UV circular dichroism (CD) and intrinsic fluorescence were used to probe protein intrinsic thermal stability, secondary structure

and tertiary structure changes using the real time stability samples stored at 2–8^{o}C over eight weeks.

6.3.4.1 ITC evaluation of iron binding to mAb in the presence and absence of chelator

The binding of iron to the mAb was investigated by ITC in the presence and absence of chelator. Analysis of ITC spectra shown in Fig. 9 indicated that there was a stoichiometry of 20:1 ferric ions bound per mAb molecule with a Kd of 0.18 mM in the absence of the chelator. In contrast, no significant binding of iron to the mAb was observed in the presence of chelator of Na_2EDTA or DTPA (spectra not shown). Affinity of iron to mAbs is very weak (Kd in mM) and the stoichiometry of ~20 obtained could vary between antibodies. This affinity is significantly lower than the EDTA/DTPA affinity to iron (Kd's in the nM to fM ranges). We have not explored assigning the binding of iron atoms to different structural regions of the mAb. Combined with the observations from chemical analyses, it is reasonable to believe that the weak binding of free (un-chelated) iron to the mAb, catalyzed the degradation pathways of the mAb by decreasing its intrinsic thermodynamic stability which were further confirmed by other biophysical analysis discussed later.

6.3.4.2 Impact of iron on mAb thermal stability analyzed by DSC

DSC has been used to probe energetics of protein folding/unfolding transitions and thermodynamic mechanisms [49, 50]. The melting point of a protein can be used as an indicator of its relative thermal stability. The DSC data for the real-time stability samples, obtained under non-reducing conditions with the disulfides intact, are shown in Fig. 10. Two thermal melting transitions (Tm1 and Tm2) for this mAb are observed in the DSC scans of the various formulations evaluated. The thermal transitions are irreversible. The data indicate that the formulations with 0.134 mM Na_2EDTA or DTPA and less than or equal to 4 ppm spiked iron,

i.e., with sufficient chelator present to chelate all iron, exhibited comparable sharp transitions. However, a significant shift of Tm1 and broadening for the transition Tm2 were observed for the formulations with spiked iron at the level of greater than or equal to 15 ppm. Due to the difficulty in assigning the melting peaks to specific structural regions/domains on the IgG2, specific explanations for the changes cannot be provided. However, it is clear that addition of iron perturbs the structure such that the Tm1 decreases indicating a destabilization of the structure. Similarly, while Tm2 seems to show an apparent increase most likely due to a broadening of the transition, the heat capacity and enthalpy values of this transition decrease significantly, again illustrating the destabilizing effect of the added iron. A summary of the Tm1 data shown in Fig. 11 was used for the mAb formulation stability comparison. The significant shift of Tm1 to lower temperatures for the formulations with spiked iron levels of $\geq$ 15 ppm indicated that the formulations were less stable than the formulations spiked with $\leq$ 4 ppm iron. Meanwhile, the similarity in values of Tm1 for the formulations with adequate amount of Na_2EDTA or DTPA to chelate iron, suggest that both chelators behaved equivalently in stabilizing the formulations. This observation was consistent with the thirteen week real-time stability data which indicated that the mAb can be protected from degradation with sufficient chelator present in the formulations.

6.3.4.3 Impact of iron on mAb secondary structure analyzed by CD

Circular dichroism has been generally used to probe protein secondary structure since its spectra are sensitive to the protein conformation [49]. Far-UV CD spectroscopy was employed to qualitatively probe the iron induced secondary structure changes of the mAb. Analysis of the spectra obtained for all the samples (not shown) indicate that no significant changes in secondary

structure were observed for any of the real time stability samples stored at 2–8^{o}C over eight weeks.

6.3.4.4 Impact of iron on the mAb tertiary structure analyzed by fluorescence spectroscopy

Fluorescence spectroscopy can be used to probe the effect of additives on protein tertiary structure [50]. Tryptophan fluorescence spectroscopy was used to evaluate the effect of metals and chelators on mAb tertiary structure. A summary of the data is shown in Fig. 12. The fluorescence was monitored over the wavelength range of 300 – 450 nm to eliminate iron interference. There are 22 tryptophan residues in this mAb and the average emission maximum was at the wavelength of 330 nm which suggested that most of them were buried. Identical protein concentrations were used in these experiments with varying concentrations of iron. There was no significant change in the emission intensity at 330 nm for the formulations with ≤ 4ppm iron and Na_2EDTA or DTPA, similar to the negative control. However, the intensity decreased significantly (~58%) for the formulations with ≥ 15 ppm iron. The positive control exhibited an even further decrease in intrinsic fluorescence intensity to 47%. However, no notable red-shift in the emission maximum was observed to indicate mAb gross conformational change for all the formulations studied. The significant intrinsic fluorescence quenching of tryptophan emission without a shift in the emission maximum indicates [49, 51] only subtle changes in the tertiary structure are induced by any un-chelated iron present. The quenching effects could also be local and solvated tryptophan specific. This subtle change in structure was apparently still significant enough to lead to the changes in the thermal melting profiles, and cause the mAb degradation as described in the previous sections, indicating a reduction in the intrinsic thermodynamic stability

of the molecule. A similar phenomenon was observed by Derrick et al. for recombinant human factor VIII which was induced to aggregate in the presence of Al(III) [52].

6.4 Conclusions

This study investigated the ability of metal chelators, Na_2EDTA and DTPA to impact the stability of mAb formulations which were spiked with iron at different levels. A weak binding of the iron to the IgG2 mAb was measured. No gross changes in the secondary or tertiary structure were observable with the techniques employed. The free (un-chelated) iron ions by interacting with the mAb result in a decrease in its intrinsic thermodynamic stability, probably through subtle impact on the folding forces and thereby causing minor perturbations to the tertiary structure. Apart from the expected transition metal-catalyzed oxidative degradation, this decrease in intrinsic stability also resulted in significant increases in soluble aggregate levels, deamidation, and total impurities. Both Na_2EDTA and DTPA exhibited equivalent capacity to inhibit the iron induced mAb degradation when adequate amounts were present to chelate the iron. Analysis of real time and accelerated oxidation data suggested that only in the situation when un-chelated iron ions were present in the formulations stored at higher temperatures, Na_2EDTA performed slightly better. However, the two chelators appeared to be equivalent for solutions stored at the more common mAb storage temperature of 2–8^{o}C. DTPA can therefore be used as an alternative chelator to improve mAb solution formulation stability.

6.5 References

1. Eisenstein, R.S., et al., *Iron-responsive element-binding protein. Phosphorylation by protein kinase C.* J Biol Chem, 1993. **268**(36): p. 27363-70.

2. Hamed, M.Y., *Binding of the ferric uptake regulation repressor protein (Fur) to Mn(II), Fe(II), Co(II), and Cu(II) ions as co-repressors: electronic absorption, equilibrium, and 57Fe Mossbauer studies.* J Inorg Biochem, 1993. **50**(3): p. 193-210.

3. Larson, A.A., et al., *Zinc in the extracellular area of the central nervous system is necessary for the development of kainic acid-induced persistent hyperalgesia in mice.* Pain, 2000. **86**(1-2): p. 177-84.

4. McKee, D.J., et al., *Binding of transition metal ions by ceruloplasmin (ferroxidase).* Biochemistry, 1971. **10**(21): p. 3880-3.

5. Mecklenburg, S.L., et al., *Tertiary structural changes and iron release from human serum transferrin.* J Mol Biol, 1997. **270**(5): p. 739-50.

6. Nguyen, T.H., et al., *Transferrin: the role of conformational changes in iron removal by chelators.* J. Am. Chem. Soc., 1993. **115**: p. 6758-64.

7. Sarkar, B., *Metal protein interactions.* Progress in Food and Nutrition Science, 1987. **11**: p. 363-400.

8. Klausner, R.D., et al., *Regulating the fate of mRNA: the control of cellular iron metabolism.* Cell, 1993. **72**(1): p. 19-28.

9. Leibold, E.A., et al., *Iron-dependent regulation of ferritin and transferrin receptor expression by the iron-responsive element binding protein.* Annu Rev Nutr, 1992. **12**: p. 345-68.

10. Theil, E.C., *Regulation of ferritin and transferrin receptor mRNAs.* J Biol Chem, 1990. **265**(9): p. 4771-4.

11. Hovorka, S.W., et al., *Metal-catalyzed oxidation of human growth hormone: modulation by solvent-induced changes of protein conformation.* J Pharm Sci, 2001. **90**(1): p. 58-69.

12. Li, S., et al., *Aggregation and precipitation of human relaxin induced by metal-catalyzed oxidation.* Biochemistry, 1995. **34**(17): p. 5762-72.

13. Stadtman, E.R., *Metal ion-catalyzed oxidation of proteins: biochemical mechanism and biological consequences.* Free Radic Biol Med, 1990. **9**(4): p. 315-25.

14. Stadtman, E.R. and C.N. Oliver, *Metal-catalyzed oxidation of proteins. Physiological consequences.* J Biol Chem, 1991. **266**(4): p. 2005-8.

15. Uversky, V.N., et al., *Metal-triggered structural transformations, aggregation, and fibrillation of human alpha-synuclein. A possible molecular link between Parkinson's disease and heavy metal exposure.* J Biol Chem, 2001. **276**(47): p. 44284-96.

16. Phan, G., et al., *Predicting plutonium decorporation efficacy after intravenous administration of DTPA formulations: Study of pharmacokinetic-pharmacodynamic relationships in rats.* Pharm Res, 2006. **23**(9): p. 2030-5.

17. Porter, J.B., et al., *Iron mobilization from hepatocyte monolayer cultures by chelators: the importance of membrane permeability and the iron-binding constant.* Blood, 1988. **72**(5): p. 1497-503.

18. Chaberek, S.A., et al., eds. *Organic sequestering agents*. 1st ed. 1959, John Weley & Sons Inc.: New York, NY.

19. West, T.S., et al., eds. *Analytical applications of Diamino-ethane-tetra-acetic acid*. 2nd ed. 1960, The British Drug Houses, Ltd: London.

20. Andergee, G., et al., *Critical evaluation of stability constants of metal complexes of complexones for bimedical and environmental applications.* Pure Appl. Chem., 2005. **77**: p. 1445-95.

21. FDA, *Questions and answers on Edetate Disodium (marketed as Endrate and generic proucts).* 2009.

22. FDA, *Edetate Disodium (marketed as Endrate and generic products).* 2008.

23. Swarbrick, J., et al., *Encyclopedia of Pharmaceutical Technology*. 2000, Marcel Dekker Inc.: New York.

24. Rowe, R., et al., ed. *Handbook of Pharmaceutical Excipients*. 4th ed. 2003, Phamaceutical press: Chicago. 225-228.

25. Sweetman, S.C., ed. *Martidale: the complete drug reference (2 volume set)*. 36 ed. 2009, Pharmaceutical press: Chicago, IL.

26. FDA, *Questions and answers on Edetate Disodium* 2008.

27. *Bayer withdraws liquid formulation of Leukine in US due to adverse reactions*. 2008.

28. *Reformulated liquid Leukine now available in the US: EDTA removed from liquid formulation / restoration of US supplies of Leukine*. 2008.

29. Li, S., et al., *Chemical pathways of peptide degradation. V. Ascorbic acid promotes rather than inhibits the oxidation of methionine to methionine sulfoxide in small model peptides.* Pharm Res, 1993. **10**(11): p. 1572-9.

30. Chaberek, S.A., et al., *Interactions of some divalent metal ions with diethylenetriaminiepentaacetic acid.* J. Inorg. Nucl. Chem., 1959. **11**: p. 184-196.

31. Vandegaer, J., et al., *Iron chelates of diethylenetriaminepentaacetic acid.* J. Inorg. Nucl. Chem., 1959. **11**: p. 210-221.

32. Skochdopole, R., et al., *Iron chelates of N-hydroxyethylethylenediaminetriacetic acid.* J. Inorg. Nucl. Chem., 1959. **11**: p. 222-233.

33. Bhattacharyya, M.H., et al., eds. *Guidebook for hte treatment of accidental internal radionuclide contamination of workers*. 1992, Nuclear Technology Publishing: Ashford.

34. Fisher, D.R., *Decorporation: officially a word.* Health Phys, 2000. **78**(5): p. 563-5.

35. Norwood, W.D., *Therapeutic removal of plutonium in humans.* Health Phys, 1962. **8**: p. 747-50.

36. Crisponi, G., et al., *Iron chelating agents for the treatment of iron overload.* Coordination chemistry Reviews, 2008. **252**: p. 1225-1240.

37. Faa, G., et al., *Iron chelating agents in clinical practice.* Coordination chemistry Reviews, 1999. **184**: p. 291-310.

38. Srivastava, R.C., et al., *Evaluation of LD50 of some polyaminocarboxylic acids used as chelating drugs in metal intoxication.* Toxicol. Lett. FIELD Full Journal Title:Toxicology Letters, 1986. **32**(1-2): p. 37-40.

39. Durbin, P.W., et al., *Development of decorporation agents for the actinides.* Radiat. Prot. Dosim., 1998. **79**: p. 433-443.

40. Crawley, F.E., et al., *The dosimetry of carbon-14 labelled compounds: the metabolism of diethylenetriamine pentaacetic acid (DTPA) in the rat.* Int J Nucl Med Biol, 1979. **6**(1): p. 9-15.

41. Stevens, W., et al., *The retention and distribution of 241Am and 65Zn, given as DTPA chelates in rats and of [14C]DTPA in rats and beagles.* Radiat Res, 1978. **75**(2): p. 397-409.

42. Stather, J.W., et al., *The retention of 14C-DTPA in human volunteers after inhalation or intravenous injection.* Health Phys, 1983. **44**(1): p. 45-52.

43. Pace, C.N., et al., *How to measure and predict the molar absorption coefficient of a protein.* Protein Sci, 1995. **4**(11): p. 2411-23.

44. Marx, G., et al., *Site-specific modification of albumin by free radicals. Reaction with copper(II) and ascorbate.* Biochem J, 1986. **236**(2): p. 397-400.

45. Uchida, K., et al., *Identification of oxidized histidine generated at the active site of Cu,Zn-superoxide dismutase exposed to H2O2. Selective generation of 2-oxo-histidine at the histidine 118.* J Biol Chem, 1994. **269**(4): p. 2405-10.

46. Kim, K., et al., *Nonenzymatic cleavage of proteins by reactive oxygen species generated by dithiothreitol and iron.* J Biol Chem, 1985. **260**(29): p. 15394-7.

47. Cleland, J.L., et al., *The development of stable protein formulations: a close look at protein aggregation, deamidation, and oxidation.* Crit Rev Ther Drug Carrier Syst, 1993. **10**(4): p. 307-77.

48. Manning, M.C., et al., *Stability of protein pharmaceuticals.* Pharmaceutical Research, 1989. **6**: p. 903-918.

49. Shirley, B.A., ed. *Protein stability and folding: theory and practice*. 1995, Human press Inc.: Totowa, New Jersey.

50. Chen, T., *Formulations concerns of protein drugs.* Drug Development and Industrial Pharmacy, 1992. **18**: p. 1311-1354.

51. Lakowicz, J.R., ed. *Principles of fluorescence spectroscopy*. 2nd ed. 1983, Springer: New York.

52. Derrick, T.S., et al., *Effect of metal cations on the conformation and inactivation of recombinant human factor VIII.* J Pharm Sci, 2004. **93**(10): p. 2549-57.

Table 1. Formulations studied with Na_2EDTA or DTPA: the matrix is 5 mg/mL mAb in 20 mM histidine buffer, 0.2 mg/mL polysorbate 80 at pH 5.5

Protein (mg/mL)	Fe^{2+} (ppm)	Na_2EDTA (mg/mL)	Na_2EDTA (mM)	DTPA (mg/mL)	DTPA (mM)
5	0	0	0	0	0
5	0	0.050	0.134	NA	NA
5	4	0.050	0.134	NA	NA
5	15	0.050	0.134	NA	NA
5	24	0.050	0.134	NA	NA
5	0	NA	NA	0.053	0.134
5	4	NA	NA	0.053	0.134
5	15	NA	NA	0.053	0.134
5	24	NA	NA	0.053	0.134
5	24	NA	NA	NA	NA

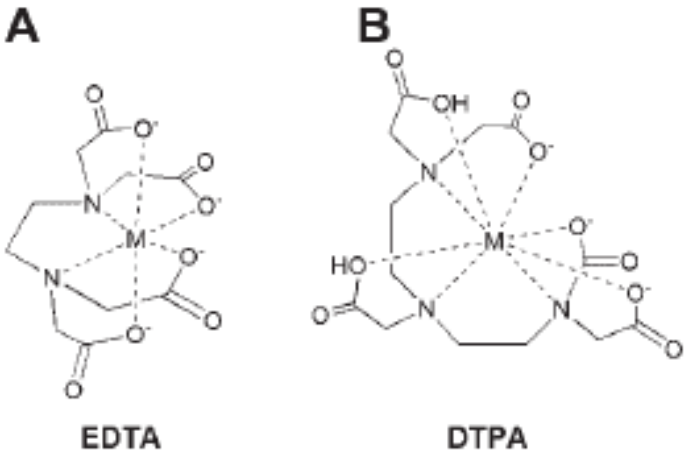

Fig. 1. Schematic structures of (A) EDTA and (B) DTPA and the binding mechanism to metal.

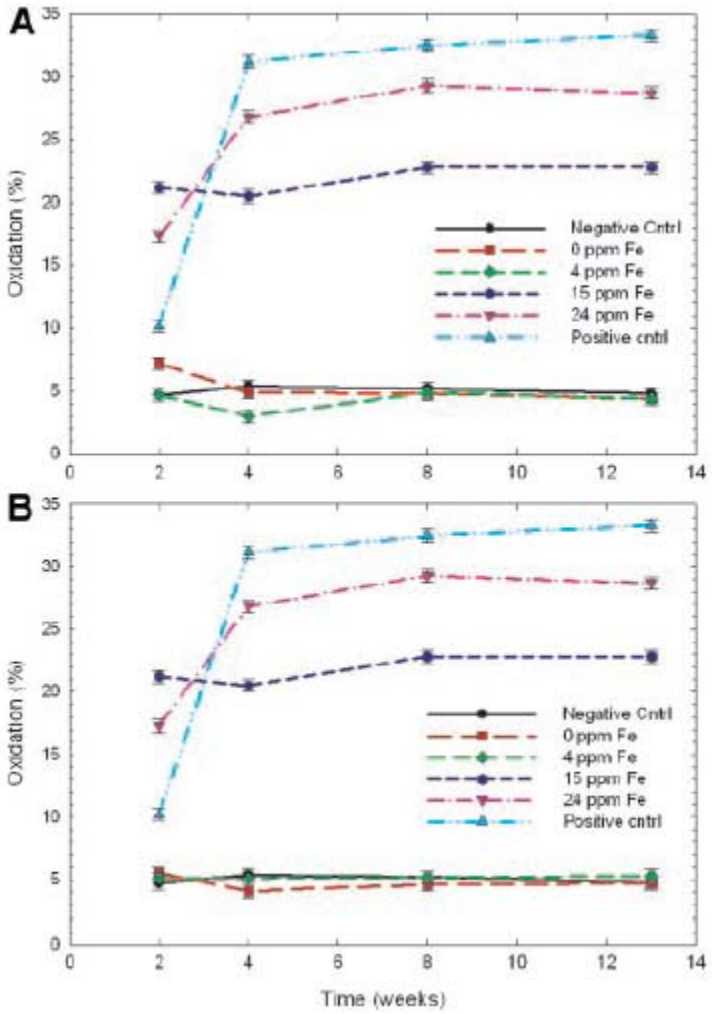

Fig. 2. Oxidation of the mAb over thirteen weeks when stored at 2–8°C for the formulations with (A) Na_2EDTA and (B) DTPA.

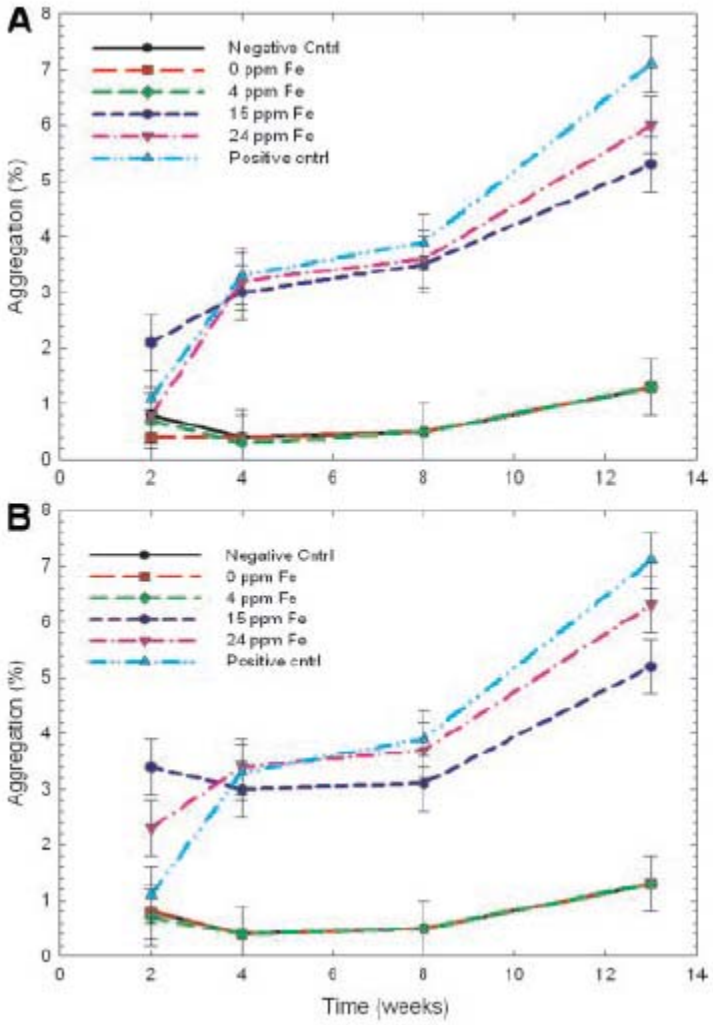

Fig. 3. Aggregate formation in the mAb over thirteen weeks when stored at 2–8°C for the formulations with (A) Na_2EDTA and (B) DTPA.

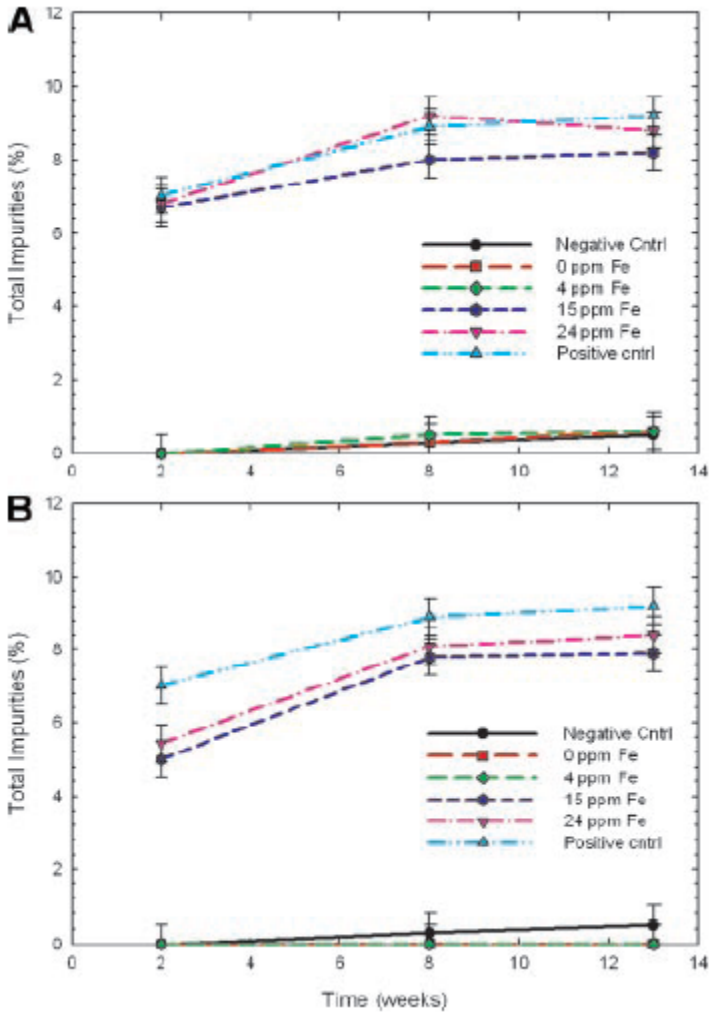

Fig. 4. Total impurities generated in the mAb over thirteen weeks when stored at 2–8°C for the formulations with (A) Na_2EDTA and (B) DTPA.

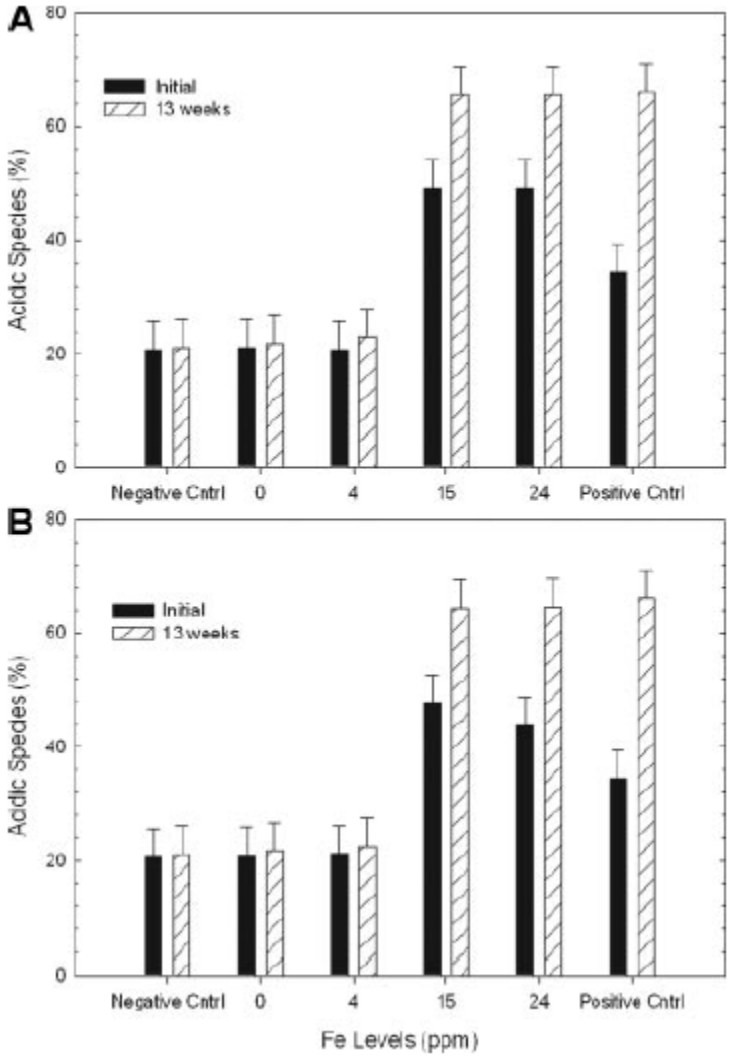

Fig. 5. Acidic species generated in the mAb over thirteen weeks when stored at 2–8^{o}C for the formulations (1st bar for T0 and 2nd bar for T13weeks) with (A) Na_2EDTA and (B) DTPA.

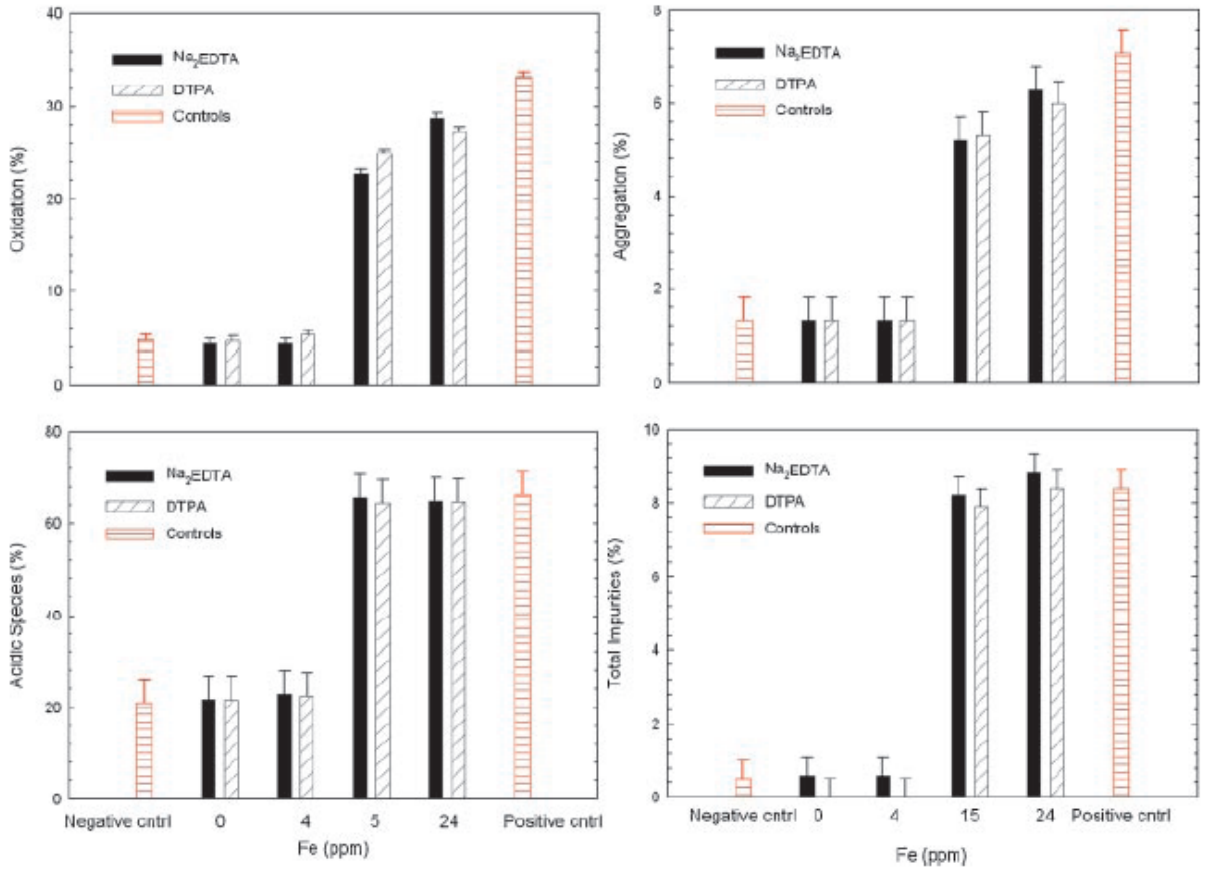

Fig. 6. Comparison of degradation data for the formulations with Na_2EDTA or DTPA when stored at 2–8°C at 13 weeks: oxidation, aggregation, acidic species and total impurities.

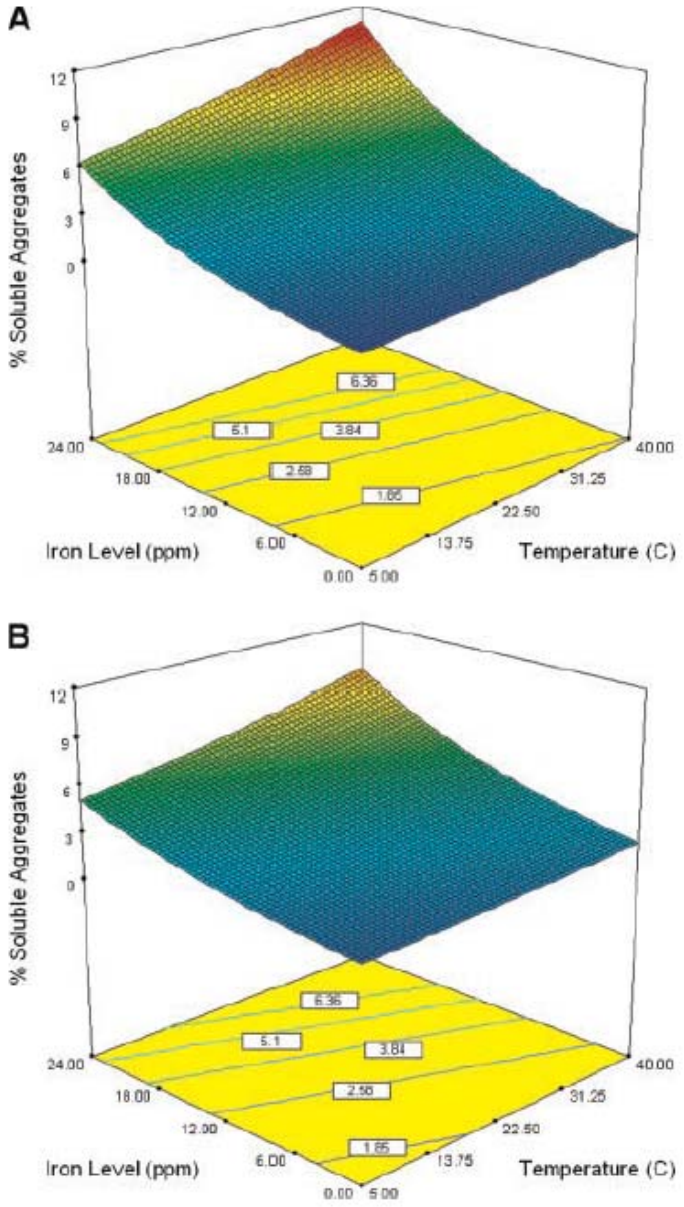

Fig. 7. (A) Response surface plot for soluble aggregate levels for Na_2EDTA at 13 weeks over temperature range of 5–40°C and iron levels of 0–24 ppm. The diagonal line represents contour grid. (B) Response surface plot for soluble aggregate levels for DTPA at 13 weeks over temperature range of 5–40°C and iron levels of 0–24 ppm. The diagonal line represents contour grid.

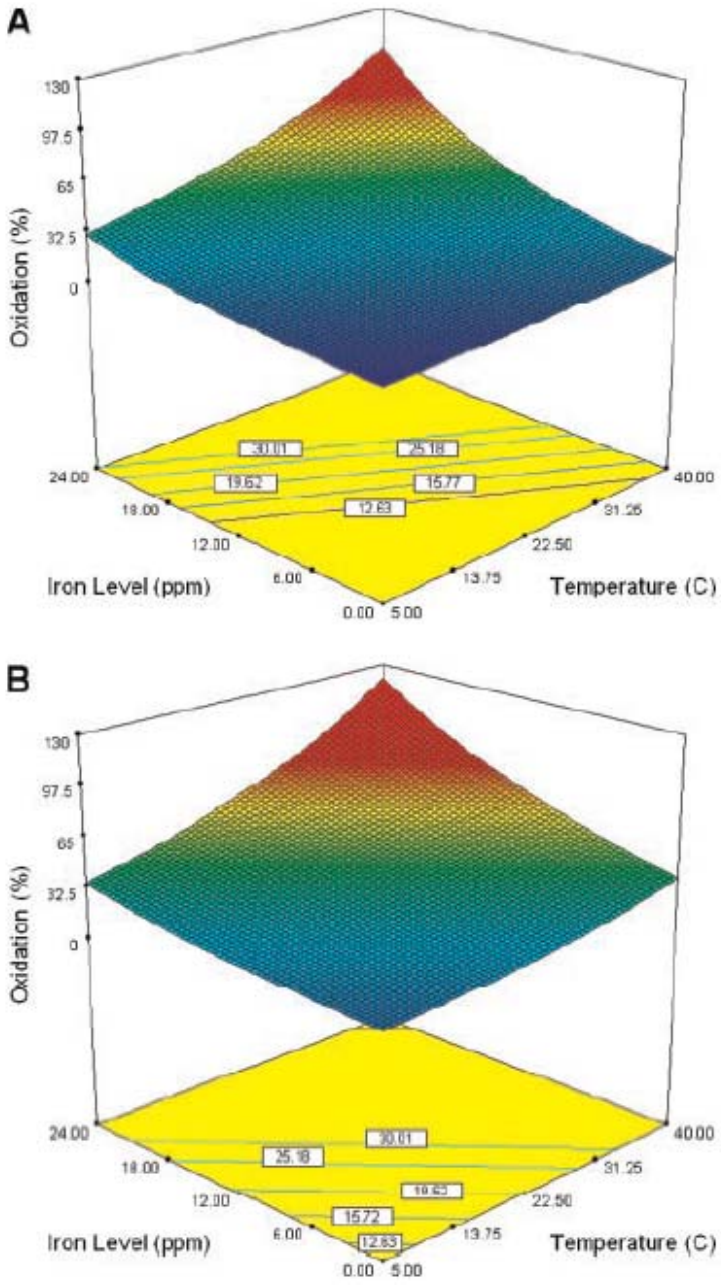

Fig. 8. (A) Response surface plot for oxidation levels for Na_2EDTA at 13 weeks over temperature range of 5–40°C and iron levels of 0-24 ppm. The diagonal line represents contour grid. (B) Response surface plot for oxidation levels for DTPA at 13 weeks over temperature range of 5–40°C and iron levels of 0–24 ppm. The diagonal line represents contour grid.

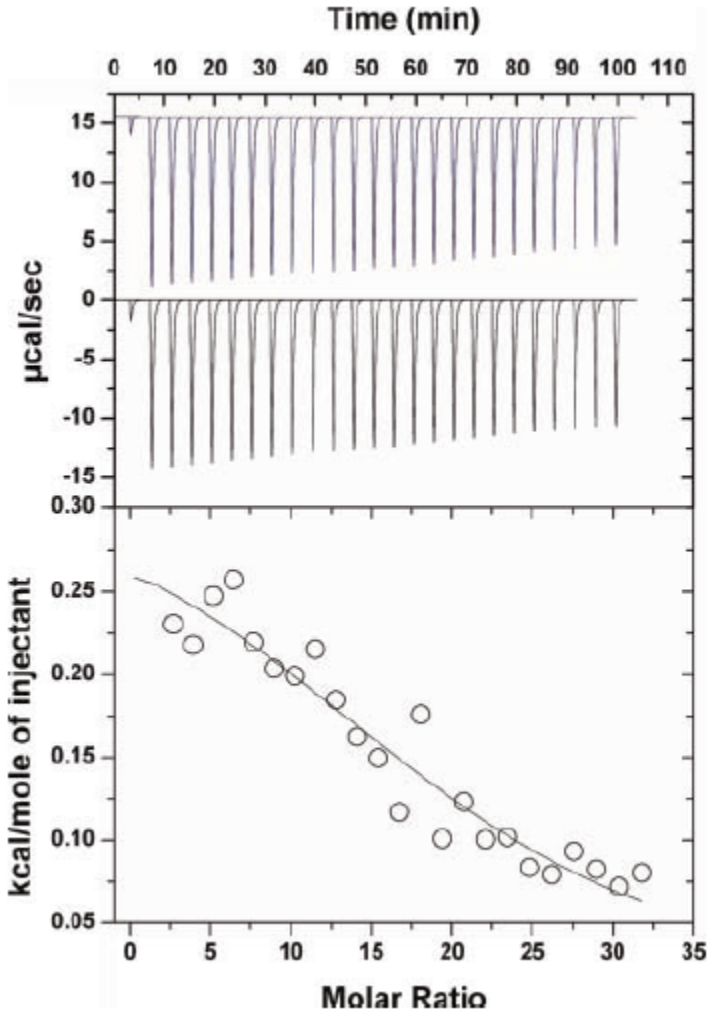

Fig. 9. Iron binding to the mAb by ITC: Iron binding to mAb in absence of chelator, 6 mM of $FeCl_3$ was titrated with 33.5 µM of mAb (blue in upper panel) and 6 mM of $FeCl_3$ was titrated with the placebo (black in upper panel). The resulting binding isotherm is shown in lower panel. Iron binding to mAb was curve fit to obtain thermodynamic parameters.

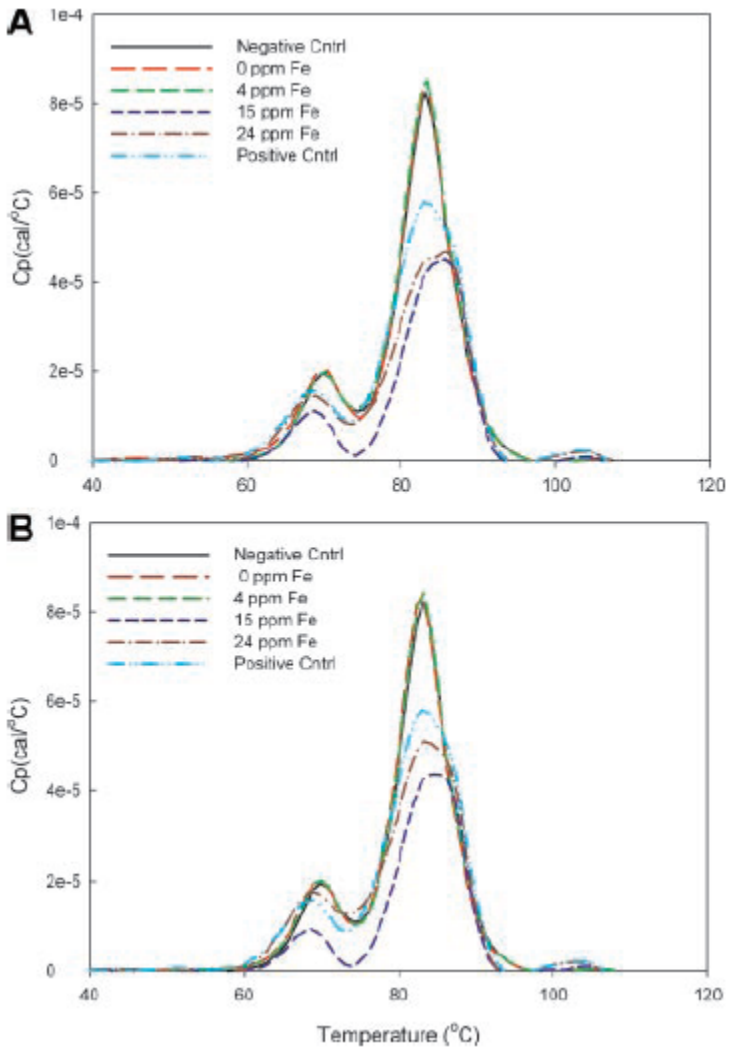

Fig. 10. DSC spectra for the real time stability samples at T8 weeks stored at 2–8°C with A) Na_2EDTA and B) DTPA at spiked iron levels of 0, 4, 15 and 24 ppm, and negative control formulation (absence of chelator and iron), and the positive control formulation (absence of chelator but presence of iron at a level of 24 ppm).

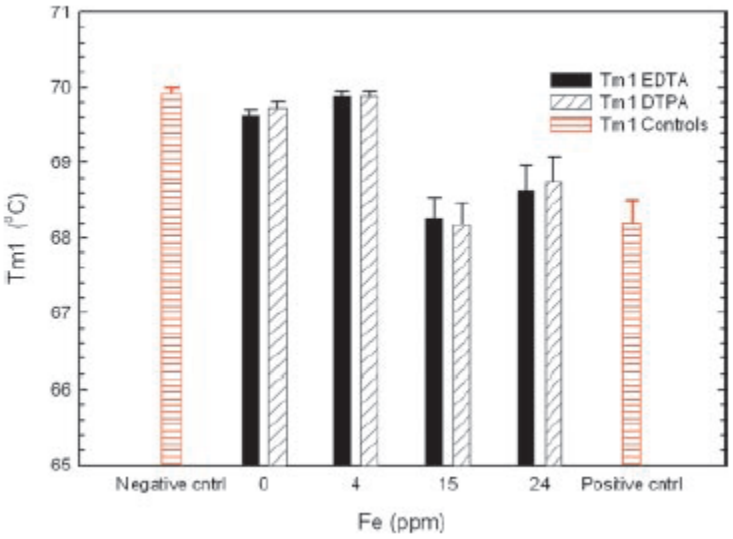

Fig. 11. Tm1 data for the real time stability samples at T8 weeks stored at 2–8°C with Na_2EDTA or DTPA at spiked iron levels of 0, 4, 15 and 24 ppm, the negative control formulation (absence of chelator and iron), and the positive control formulation (absence of chelator but presence of iron at a level of 24 ppm).

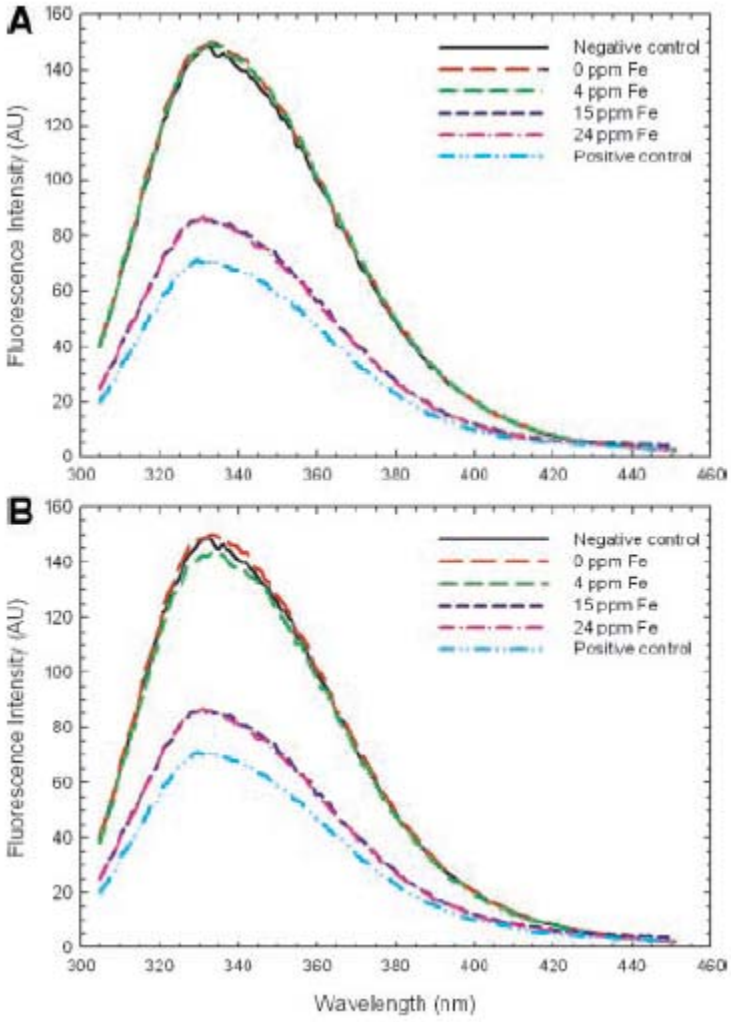

Fig. 12. Fluorescence spectra for the real time stability samples at T8 weeks stored at 2–8^{o}C A) Na_2EDTA and B) DTPA at spiked iron levels of 0, 4, 15 and 24 ppm, negative control formulation (absence of chelator and iron), and the positive control formulation (absence of chelator but presence of iron at a level of 24 ppm).

Part III. Photo-instability

Chapter 7: Mechanisms of IgG photo-degradation:

The Photolysis of Disulfide Bonds in IgG1 and IgG2 Leads to Selective Intramolecular Hydrogen Transfer Reactions of Cysteinyl Thiyl Radicals, Probed by Covalent H/D Exchange and RPLC-MS/MS analysis

Table of Contents

7.1 Introduction

Immunoglobulin G (IgG) monoclonal antibody (mAb) biotherapeutics have gained significant attention and become a fast growing biotherapeutic class in the pharmaceutical industry [1-3]. These protein therapeutics are subject to ultra-violet (UV) and/or visible light exposure during development, manufacturing, transportation, storage and administration to the patients. Antibodies contain multiple disulfide bonds, and, similar to many other proteins, are sensitive to light-induced degradation [4]. Light testing is defined as an integral part of stress testing for submission in registration application for new molecular entities and associated drug products by the Food and Drug Administration (FDA) under The International Conference on Harmonization (ICH) Tripartite guideline [5]. The guideline clearly notes that the intrinsic photostability characteristics of new drug substances and products should be evaluated to demonstrate that, as appropriate, light exposure does not result in unacceptable change. A systematic approach to photostability testing is recommended covering, as appropriate, studies of i) tests on the drug substances, ii) tests on the exposed drug product outside of the immediate packing, and, if necessary, iii) tests on the drug product in the immediate packing, and, if necessary, iv) tests on the drug product in the marketing packing. The resulting instability information is an important element in the quality assurance for drug therapy, e.g., in determining the shelf life, storage instructions, and use life (i.e. stability in an opened container). For photo-labile drug substances and drug products, the formal labeling requirements are established by national/regional requirements.

IgG monoclonal antibodies contain multiple Cys residues, forming inter- and intrachain disulfide bonds. These inter- and intrachain disulfide bonds play an important role for protein

stability. On the other hand, disulfide bonds are subject to light-induced degradation [4, 6, 7]. Photo-irradiation at $\lambda = 253.7$ nm results in the homolytic dissociation of disulfide bonds, leading to the formation of a cysteinyl thiyl radical (CysS•) pair [8-12]. This CysS• radical pair engages in disproportionation (to thiol and thioaldehyde) as well as reversible hydrogen atom transfer reactions with C-H bonds of surrounding amino acids [13-16]. Intramolecular hydrogen transfer reactions were confirmed by the covalent incorporation of deuterium into specific amino acid residues when peptides and protein thiyl radicals were generated in D_2O [15, 16]. These intramolecular hydrogen transfer reactions generate carbon-centered (C-centered) radicals, which ultimately may result in the formation of protein hydroperoxide, protein aggregates and/or protein fragmentation [17]. In specific model peptides and proteins, such as insulin, we have demonstrated that reversible hydrogen transfer reaction between CysS• radicals and C-H bonds led to covalent hydrogen/deuterium (H/D) exchange [16], as outlined in Scheme 1 [15]. Such reversible hydrogen transfer can also result in L- to D-amino acid conversion, as shown for L-Ala in a model peptide [14].

IgG1 and IgG2 represent two important subclasses of IgG. They exhibit differences in the number and connectivity of interchain disulfide bonds. In IgG1, the interchain disulfide bonds link the light chain (LC) and the heavy chain (HC) at the hinge region, whereas in IgG2, the interchain disulfide bonds linking the LC and the HC are located to the junction between the variable and the constant region [18]. Based on these different locations of the disulfide bonds, CysS• radicals generated through disulfide bond photolysis may react selectively with different amino acid residues in different domains of IgG1 and IgG2, generating intermediary carbon-centered protein radicals at different locations. Through covalent H/D exchange, we have probed

in this paper the reactivity of disulfide bonds, and specifically CysS• radicals in IgG1 and IgG2 toward reversible intramolecular hydrogen transfer.

7.2 Experimental

7.2.1 Materials

IgG1 (37 mg/mL) and IgG2 (30 mg/mL) mAb stored as frozen solutions (-80^{o}C) were supplied by Amgen Inc. (Seattle, WA, USA). Dithiothreitol (DTT, >99%) and diethylmaleate (DEM, 97%) were obtained from Sigma-Aldrich (Saint Louis, MO, USA). N-ethylmaleimide (NEM, >99%) and ammonium bicarbonate (NH_4HCO_3) were obtained from Fluka (Saint Louis, MO, USA). Sequencing-grade trypsin and Glu-C were obtained from Promega Corp. (Madison, WI, USA). Deuterium oxide (D_2O, 99.9%) was obtained from Cambridge Isotope Laboratories Inc. (Andover, MA, USA).

7.2.2 Reactions

7.2.2.1 UV irradiation

The IgG1 and IgG2 stock solutions were exchanged into MilliQ H_2O or D_2O at room temperature in a nitrogen (N_2) box using an Amicon® ultra-0.5 centrifugal filter device equipped with a 10 kDa filter membrane (Millipore Inc., Bedford, MA, USA). The samples were centrifuged by means of a mini-centrifuge (Southwest Science, Roebling, NJ, USA) for 15 mins. An aliquot (200 μL) of each protein stock solution in H_2O or D_2O was transferred to a quartz tube and sealed with a rubber stopper. The sealed quartz tubes containing protein solutions were transferred from the N_2 box and irradiated at room temperature for 1 hour with UV light at λ = 253.7 nm by means of four UV lamps (RMA-500, Southern New England, Branford, CT, USA) in a Rayonet Photo-chemical reactor (Southern New England, Branford, CT, USA).

7.2.2.2 Thiol derivation reactions and digestion

The protein solutions in D_2O were exchanged into H_2O by means of an Amicon® ultra-0.5 centrifugal filter device as described above. An aliquot of 100 μL of each protein solution in H_2O was added to 0.9 mL of NH_4HCO_3 buffer (50 mM, pH 7.8). The proteins were denatured by ramping the temperature from 35°C to 80°C using a water bath. Heat denaturing of the proteins was terminated when the solution turned cloudy. Thiol groups produced during photo- irradiation were derivatized with NEM (0.2 mM) for 1 hour at 37°C. The remaining, intact disulfide bonds were reduced by DTT (2 mM) for another 30 mins at 37°C. Then DEM was added at a final concentration of 20 mM to the samples to derivatize the thiol residues resulting from the reduction of disulfide bonds by DTT. That is, the thiol residues produced by photo-irradiation were labeled with NEM whereas DEM was used to alkylate the thiols generated from the disulfide bonds through reduction by DTT. The solutions containing the derivatized proteins were subsequently transferred into 15-mL Falcon™ tubes (BD, Franklin Lakes, NJ, USA) containing 9 mL ethanol and stored at -20°C overnight. The solutions were then centrifuged at 14,000 rpm to precipitate the proteins. After removal of the supernatant, the protein pellet was re-dissolved in 1 mL NH_4HCO_3 buffer (50 mM, pH 7.8). An aliquot of 100 μL of the derivatized protein solutions was digested first with sequencing-grade trypsin (15 μg) (two doses with an interval of 2 hours). Then, the digestion was continued by the addition of sequencing-grade Glu-C (8 μg) by incubating the sample at 37°C overnight.

7.2.2.3 UPLC-MS and nano-ESI-TOF MS analysis

The samples were injected onto a Vydac MS C18 column (25 cm X 1 mm, 3.5 μm) from Grace (Deerfield, IL, USA). The mobile phases A and B were composed of water, acetonitrile and formic acid at 99:1:0.08 (v/v/v, %) for A and 0:99:0.06 (v/v/v) for B. The samples were eluted on an Acquity ultra-performance liquid chromatography (UPLC) system (Waters Corp.,

Milford, MA, USA) by gradient elution at a flow rate of 12 μL. The gradient elution was composed of three segments defined by increasing contents of solvent B: 1% B for 1 min, 10 to 30% B increased within 8 mins, followed by an increase of B to 70% within 3 mins.

ESI mass spectra were acquired on a SYNAPT G2 high definition mass spectrometer (Waters Corp. Milford, MA, USA). Electrospray ionization mass spectra of the proteins were acquired by operating the SYNAPT G2 for maximum resolution with all lenses optimized on the $[M + 2H]^{2+}$ ion from the $[Glu]^1$-fibrinopeptide B and Ar was admitted to the collision cell. The capillary voltage was set at 2.9 kV. The cone voltage was set at 45 V and then ramped to 85 V. The voltage of the extraction cone was maintained at 6 V. Source and desolvation temperatures were set at 95^{o}C and 200^{o}C, respectively. The gas flow at the cone and for desolvation was set at 40 L/h and 250 L/h, respectively. The spectra were acquired within a mass range of 100-2000 amu (amu: atomic mass unit). The data were accumulated for 0.5 sec per cycle and processed using the software MassLynx (Waters Corp. Milford, MA, USA).

7.2.2.4 MS/MS analysis

Collision-induced dissociation (CID) spectra were acquired by setting the MS^1 quadrupole to transmit a precursor mass window of ± 0.2 amu centered on the most abundant isotopomer. MS/MS spectra were acquired with collision energies between 20 eV and 50 eV depending on the mass-to-charge ratio (*m/z*) of the parent ions.

7.2.2.5 Identification of covalent H/D exchange

The covalent incorporation of deuterium into the proteolytic peptides and their fragments was determined by the variation of base peak intensity (BPI) of the isotopic distribution peaks between the covalently deuterated peptide and the corresponding fully protonated peptide. The isotopic distribution peaks were normalized to the most abundant isotopic peak.

7.3 Results

After photo-irradiation, LC-MS analysis of the proteolytic peptides from IgG2 in H_2O and D_2O was performed in order to identify peptides which have covalently incorporated at least one deuterium. Peptide sequence mapping was achieved by searching against a custom-built database of IgG2. A similar analysis was performed for IgG1. The sequence coverage was 87% and 82%, respectively for the HC and LC of IgG2, whereas the sequence coverage was 90% and 92%, respectively, for the HC and LC of IgG1. Two peptides displaying covalent incorporation of deuterium were identified for IgG2, peptide A, VVSVLTVVHQDWLNGK [294:309], located in the constant region (Fc) of the heavy chain (HC), and peptide B, VTVLGQPK [109:116], located in the light chain (LC). For IgG1, only peptide A was identified, which exhibited the same isotopic distribution profile as peptide A originating from IgG2. Therefore, the detailed discussion below will focus on the two peptides A and B originating from IgG2. For simplicity, any peptide analyzed by LC-MS and MS/MS originating from the non-irradiated or the photo-irradiated solutions which were prepared in H_2O, will be referred to as proteo-samples, and the ones prepared in D_2O as deutero-samples.

Peptide A: VVSVLTVVHQDWLNGK [294:309, HC] (m/z = 598.75, z = 3)

The comparison of the isotopic distributions of peptide A after photo-irradiation of IgG2 at λ = 253.7 nm in H_2O or D_2O reveals a mass shift towards higher masses for IgG2 photo-irradiated in D_2O compared to H_2O (Fig. 1A). In contrast, a comparison of the isotopic distributions of peptide A originating from non-irradiated IgG2 in H_2O and D_2O shows a perfect overlap (Fig. 1B). The isotopic distribution of this triply charged peptide ion in H_2O and D_2O, the BPIs and their BPI variations are presented in Table 1. These BPI variations at the same *m/z*

isotopic distribution peaks suggest that during the photo-irradiation of IgG2 in D_2O, peptide A covalently incorporates deuterium.

MS/MS experiments were performed on peptide A originating from the proteo and deutero samples. MS/MS spectra of peptide A generated the following ions: b3-b4 (Fig. 2), and y1-y3, y5, y7-y9 and y11-y14 (Fig. 3). The isotopic distributions of these ions, originating from the UV-irradiated proteo and deutero samples were analyzed. The isotopic distributions of the b3 and b4 fragments overlap (Fig. 2). We, therefore, exclude that the amino acid residues VVSV [294:297, HC] incorporate any deuteron (Fig. 2). A comparison of the isotopic distributions of the y1, y2, y3, and y5 fragment ions of the proteo and deutero samples also shows no difference. Thus, none of the amino acid residues WLNGK [305:309, HC] incorporates a deuteron. Further analysis of the fully protonated fragment ion y7 (QDWLNGK [295:309, HC]) originating from the proteo sample shows that its isotopic distribution displays ions with *m/z* 860.5, *m/z* 861.5 and *m/z* 862.5 with a relative abundance of 82%, 100%, and 21%, respectively. After photo-irradiation of IgG2 in D_2O, the y7 fragment ion of peptide A shows an isotopic distribution composed of the same ions with a relative abundance of 12%, 100% and 36%, respectively. Hence, the relative abundance of the ion with *m/z* 860.5 for the y7 fragment originating from peptide A of the photo-irradiated IgG2 in D_2O is *ca.*15% of that in H_2O, and the relative abundance increased significantly, *ca.* 70%, for the isotopic peak with *m/z* 862.5. This difference in isotopic distributions between the fully protonated peptide A and peptide A originating from photo-irradiated IgG2 in D_2O indicates that deuterium is covalently incorporated into the amino acids composing fragment ion y7. The analysis of the isotopic distributions of the y8, y9, and y11-y14 fragment ions do not reveal any significant shifts toward higher masses. Hence, we

conclude that deuterium incorporation occurred largely in the amino acids Q [303, HC] and/or D [304, HC].

Peptide B: VTVLGQPK [109:116, LC] (m/z = 841.64, z = 2)

Like for peptide A, a comparison of the isotopic distributions of peptide B after photo-irradiation of IgG2 in H_2O and D_2O at λ = 253.7 nm exhibites a mass shift towards higher masses for photo-irradiated IgG2 in D_2O (Fig. 4A). The comparison of the isotopic distributions of peptide B originating from non-irradiated IgG2 in H_2O and D_2O shows no mass shift (Fig. 4B). The isotopic distribution of peptide B in H_2O is composed of ions with *m/z* 421.3, *m/z* 421.8 and *m/z* 422.3 with a relative abundance of 100%, 46% and 13%, whereas the same peptide after irradiation in D_2O is composed of the same ions with a relative abundance of 80%, 100% and 40%, respectively. The most intense peak in D_2O shifts to the ions with *m/z* 421.8, compared to the most intense ion with *m/z* 421.3 in H_2O. The relative abundances of the isotopic peaks for the peptide in D_2O are *ca.* 110% higher for *m/z* 421.8, and *ca.* 200% higher for *m/z* 422.3 compared to the ones in H_2O. These results indicate that during the photo-irradiation of IgG2 in D_2O, peptide B covalently incorporated deuterium.

To specify the location of covalent deuterium incorporation in peptide B, MS/MS analysis was performed (Fig. 5). The isotopic distribution of the fully protonated y1 fragment is composed of ions with *m/z* 147.1 and *m/z* 148.1 with a relative abundance of 100% and *ca.* 10%. After photo-irradiation of IgG2 in D_2O, the corresponding fragment shows an isotopic distribution with a relative abundance of *ca.* 18% and 100%. The fact that the most intense peak shifted from *m/z* 147.1 to *m/z* 148.1 Da for a singly charged fragment ion indicates that nearly 100% of peptide B has covalently incorporated one deuteron into the y1 fragment. Therefore, K [116, LC] represents a site for deuterium incorporation during the photo-irradiation of IgG2 in

D_2O. Further analysis of the fully protonated fragment of y7 (TVLGQPK [110:116]) originating from the proteo sample shows an isotopic distribution for ions with *m/z* 742.5, *m/z* 743.5 and *m/z* 744.5 with a relative abundance of 100%, 42% and 10%, respectively. After photo-irradiation of IgG2 in D_2O, the fragment ion y7 shows an isotopic distribution for ions with *m/z* 743.5, *m/z* 744.5 and *m/z* 745.5, with the same relative abundance of 100%, 42% and 10%, respectively, however 1 Da higher in mass than their corresponding ions in H_2O. This result indicates that one deuterium is incorporated into the sequence TVLGQPK [110:116]. Meanwhile, no significant change is observed for the isotopic distributions of the fragment ion b2 between the proteo and deutero samples. However, the b3-H_2O fragment ion shows an isotopic distribution for the ions with *m/z* 282.2 and *m/z* 283.2 with a relative abundance of 100% and 16%, whereas the fragment b3-H_2O originating from photo-irradiation in D_2O shows a relative abundance of 100% and 60% for the same ions, respectively. Variation of isotopic distributions for the fragment b3-H_2O towards the higher masses is observed for the deutero sample compared to the proteo one. We can, therefore, hypothesize that the residue V [111, LC] has incorporated deuterium during photo-irradiation of IgG2 in D_2O. In conclusion, the MS/MS analyses of the fragment ions of peptide B generated after photo-irradiation of the IgG2 in H_2O and D_2O, allow us to determine that V [111, LC] and K [116, LC] are two amino acid residues which covalently incorporates a deuteron during photo-irradiation of IgG2 in D_2O.

7.4 Discussion

It was recently demonstrated that UV-irradiation (λ = 253.7 nm) of an IgG1 monoclonal antibody could lead to the formation of dithiohemiacetal and thioether products, originating from the photolytic cleavage of selected disulfide bonds [17]. Specifically, the formation of the dithiohemiacetal required disproportionation of a pair of CysS• radicals. An alternative reaction

of CysS• radicals is a hydrogen transfer reaction, as illustrated in Scheme 1 [15], which can generate carbon-centered radicals on surrounding amino acid residues. The intermediary formation of carbon-centered radicals can be monitored by covalent H/D exchange when photolysis reactions are carried out in D_2O. Here, we have identified the selective incorporation of deuterium into two peptides in IgG2 and one peptide in IgG1. These two deuterated sequences are adjacent to disulfide bonds. The difference in deuterium incorporation in IgG1 and IgG2 suggests an influence of IgG structure and sequence on CysS• radical formation and reactivity. Importantly, the observation hydrogen transfer reaction occurs very selectively, i.e., only involve a few amino acids in the HC and LC, respectively. The high sequence coverage of our HPLC-MS/MS analysis, especially for IgG2, ensures that this observed selectivity is not the result of missed peptides but is an inherent feature of IgG conformation and radical reactivity. More importantly, preliminary data on photolytic fragmentation of IgG1 (unpublished results) indicate, that peptide B (VTVLGQPK) is located in a domain of IgG1, which is sensitive to fragmentation. The actual mechanisms of photolytic fragmentation of IgG1 are currently under investigation. However, radical pathway, such as initiated through radical-dependent formation of carbon-centered radicals on specific amino acids of IgG1 may well be at the origin of fragmentation reaction.

7.5 Significance

The intermediary formation of carbon-centered radicals after homolytic disulfide cleavage is critical since it may permit the epimerization of amino acids and, consequently, conformational changes. Moreover, carbon-centered radicals can serve as the origins for the formation of covalent crosslinks and fragmentation of proteins.

7.6 Conclusions

The formation of intermediary carbon-centered radicals in IgG1 and IgG2 after UV-irradiation (λ = 253.7 nm) has been documented through the covalent incorporation of deuterium. This observed covalent deuterium incorporation into IgG1 and IgG2 irradiated in D_2O can be rationalized by intramolecular hydrogen transfer upon the formation of CysS• radicals. The formation of intermediary carbon-centered radicals in IgG monoclonal antibodies may lead to significant degradation, a major concern of biotherapeutic product development. Further understanding of degradation pathways induced by photo-exposure would provide valuable insight for regulatory agency and industry in evaluating protein photo-instability.

7.7 Acknowledgment

We gratefully acknowledge Amgen Inc. for financial support.

7.8 References

1. Brekke, O.H., et al., *Therapeutic antibodies for human diseases at the dawn of the twenty-first century.* Nat Rev Drug Discov, 2003. **2**(1): p. 52-62.
2. Bebbington, C., et al., *Antibodies for the treatment of bacterial infections: current experience and future prospects.* Curr Opin Biotechnol, 2008. **19**(6): p. 613-9.
3. Schrama, D., et al., *Antibody targeted drugs as cancer therapeutics.* Nat Rev Drug Discov, 2006. **5**(2): p. 147-59.
4. Volkin, D.B., et al., *Degradative covalent reactions important to protein stability.* Mol Biotechnol, 1997. **8**(2): p. 105-22.
5. *ICH harmonised tripartite guideline: guideline for the Photostability Testing of New Drug Substances and products.* J Postgrad Med 2001. **47**: p. 264.
6. Ellison, D., et al., *Photoreduction of monoclonal antibodies for conjugation and fragmentation.* Biotechniques, 2000. **28**(2): p. 318-22, 324-6.

7. Lam, X.M., et al., *Antioxidants for prevention of methionine oxidation in recombinant monoclonal antibody HER2.* J Pharm Sci, 1997. **86**(11): p. 1250-5.

8. Bonifačić, M., et al., *Free radical oxidation of organic disulfides.* J. Phys. Chem., 1976. **80**(Copyright (C) 2012 American Chemical Society (ACS). All Rights Reserved.): p. 2426-30.

9. Bonifačić, M., et al., *Radical reactions in aqueous disulphide-thiol systems.* Int J Radiat Biol Relat Stud Phys Chem Med, 1984. **46**(1): p. 35-45.

10. Bonifačić, M., et al., *Primary steps in the reactions of organic disulfides with hydroxyl radicals in aqueous solution.* J. Phys. Chem., 1975. **79**(Copyright (C) 2012 American Chemical Society (ACS). All Rights Reserved.): p. 1496-502.

11. Creed, D., *The photophysics and photochemistry of the near-UV absorbing amino acids. I. Tryptophan and its simple derivatives.* Photochem. Photobiol., 1984. **39**(Copyright (C) 2012 American Chemical Society (ACS). All Rights Reserved.): p. 537-62.

12. Everett, S.A., et al., *Perthiyl radicals, trisulfide radical ions, and sulfate formation: a combined photolysis and radiolysis study on redox processes with organic di- and trisulfides.* J. Phys. Chem., 1992. **96**(Copyright (C) 2012 American Chemical Society (ACS). All Rights Reserved.): p. 306-14.

13. Mozziconacci, O., et al., *Photolysis of an intrachain peptide disulfide bond: primary and secondary processes, formation of H_2S, and hydrogen transfer reactions.* J Phys Chem B, 2010. **114**(10): p. 3668-88.

14. Mozziconacci, O., et al., *Reversible hydrogen transfer between cysteine thiyl radical and glycine and alanine in model peptides: covalent H/D exchange, radical-radical reactions, and L- to D-Ala conversion.* J Phys Chem B, 2010. **114**(19): p. 6751-62.

15. Mozziconacci, O., et al., *Peptide cysteine thiyl radicals abstract hydrogen atoms from surrounding amino acids: the photolysis of a cystine containing model peptide.* J Phys Chem B, 2008. **112**(30): p. 9250-7.

16. Mozziconacci, O., et al., *Reversible intramolecular hydrogen transfer between protein cysteine thiyl radicals and alpha C-H bonds in insulin: control of selectivity by secondary structure.* J Phys Chem B, 2008. **112**(49): p. 15921-32.

17. Mozziconacci, O., et al., *Exposure of a monoclonal antibody, IgG1, to UV-light leads to protein dithiohemiacetal and thioether cross-links: a role for thiyl radicals?* Chem Res Toxicol, 2010. **23**(8): p. 1310-2.

18. Male, D., et al., *Immunology*. Seventh ed2006, Canada: Mosby Elsevier.

Table 1. The isotopic distribution of the identified triply charged peptide A (VVSVLTVVHQDWLNGK [294:309, HC]) originating from IgG2 after photo-irradiation at $\lambda = 253.7$ nm in H_2O or D_2O, and the base peak intensities (BPIs) and their relative variations.

m/z	598.7	599.1	599.4	599.7	600.1
BPI in H_2O (%)	32	100	88	43	16
BPI in D_2O (%)	22	100	97	53	21
BPI variations (%)	-10	0	+11	+10	+5

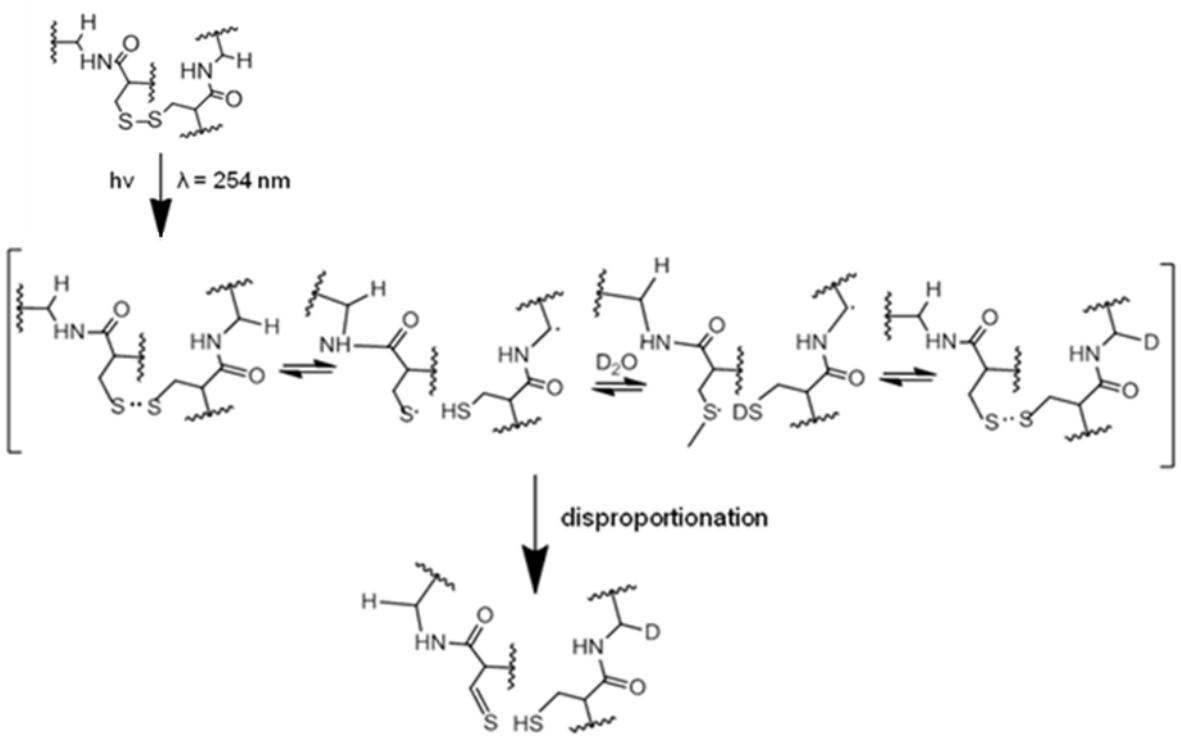

Scheme 1: proposed reaction mechanism to explain the formation of carbon-centered (C-centered) radical. The mechanism proceeds through an intra-molecular hydrogen atom transfer reaction between $^{\alpha}C$ and CysS•.

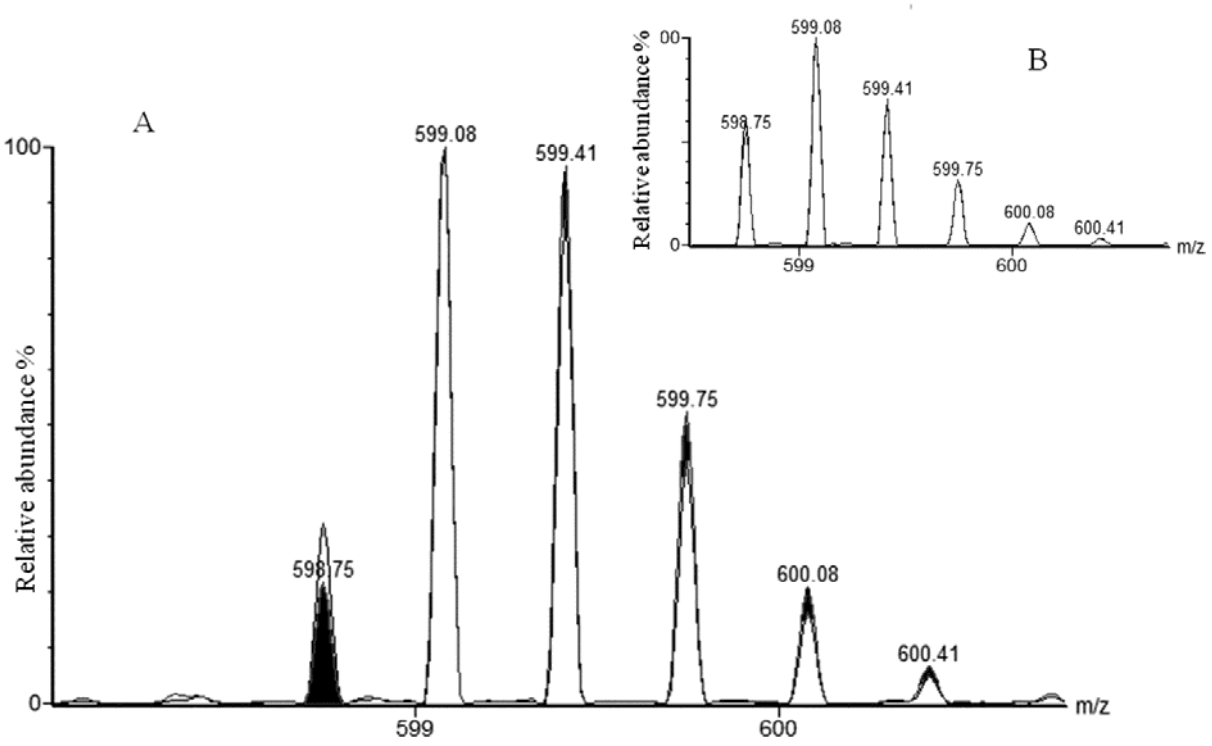

Fig. 1. MS spectra of peptide A, VVSVLTVVHQDWLNGK [294:309, HC], originating from IgG2 after proteolytic digestion: A) photo-irradiated IgG2, B) non photo-irradiated IgG2; IgG2 in H_2O (empty peaks) or in D_2O (filled peaks).

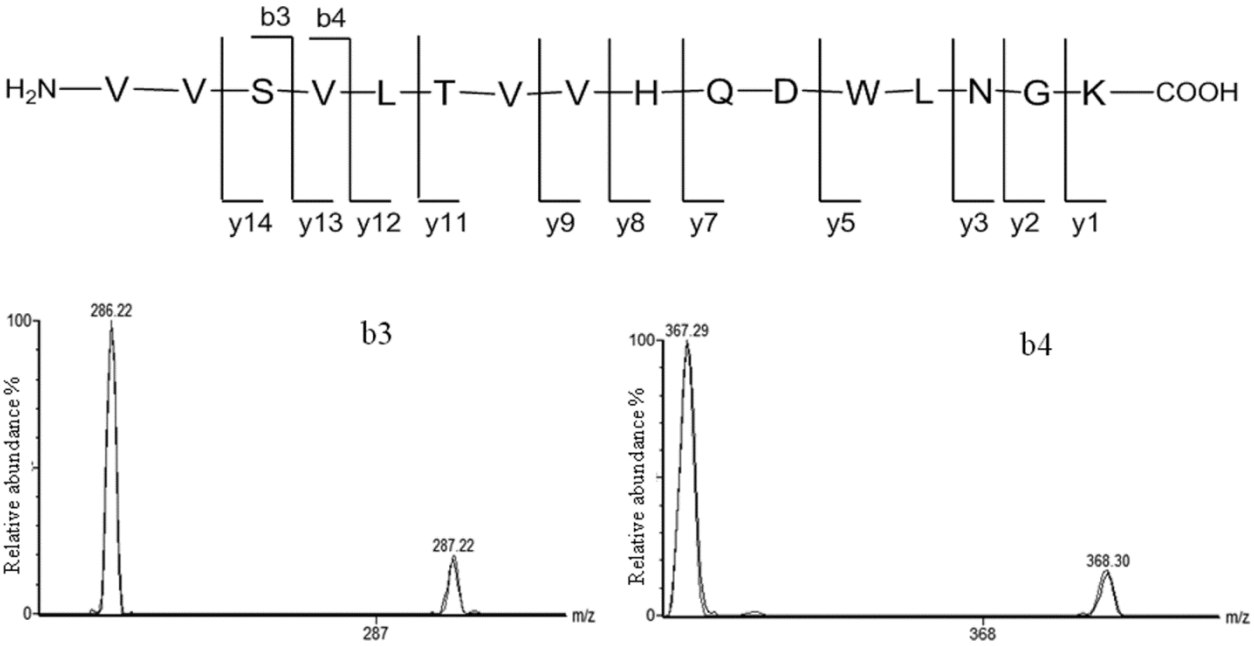

Fig. 2. MS/MS analysis and comparison of the isotopic distributions of the b fragment ions originating from peptide A, VVSVLTVVHQDWLNGK [294:309, HC], to localize the amino acid residues with covalently incorporated deuterium.

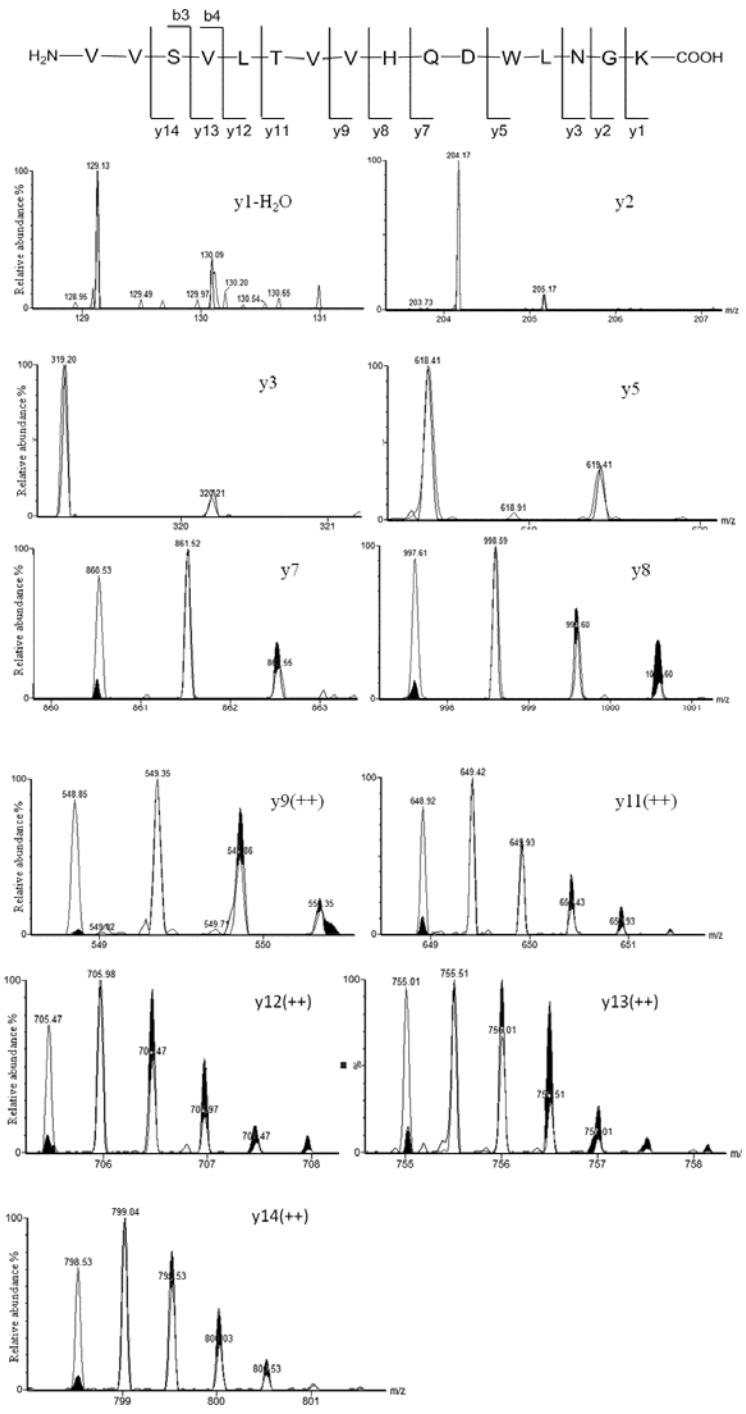

Fig. 3. MS/MS analysis of the y fragment ions originating from peptide A, VVSVLTVVHQDWLNGK [294:309, HC], to localize the amino acid residues with covalently incorporated deuterium.

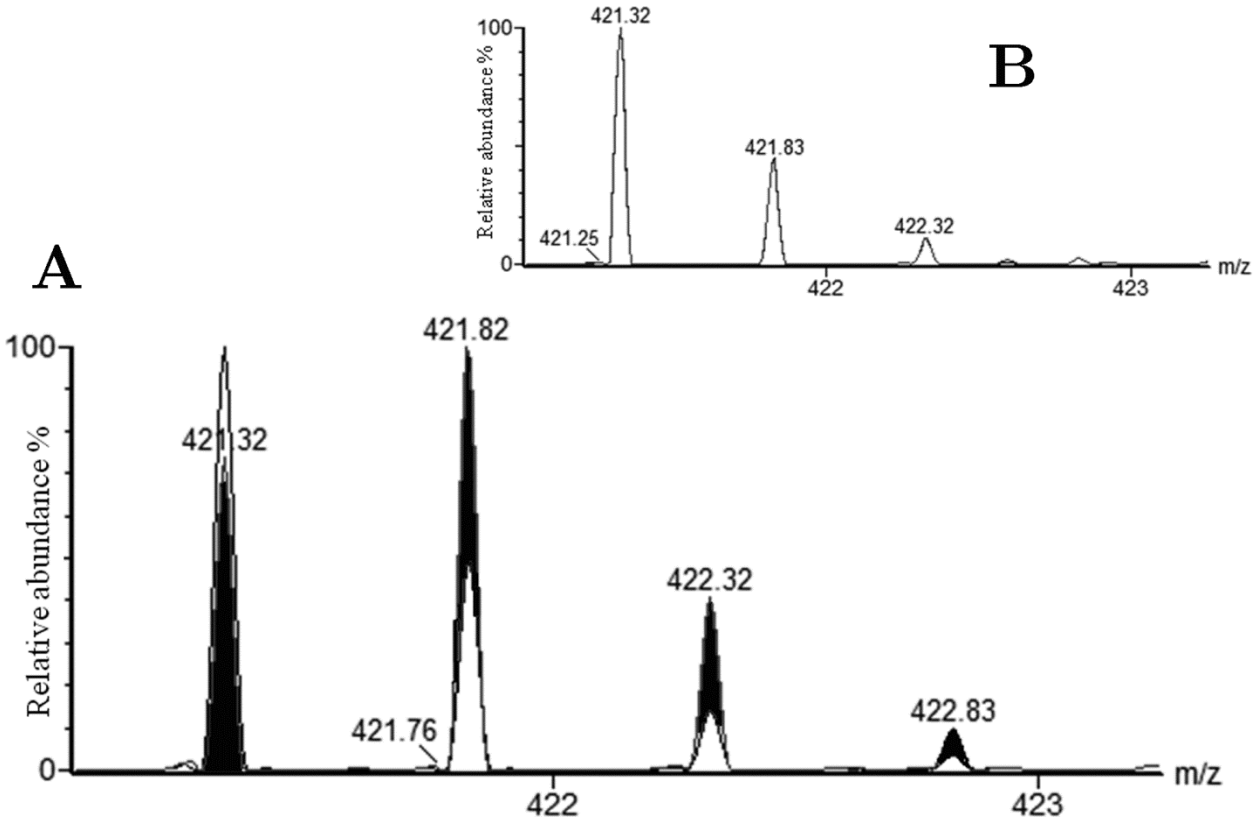

Fig. 4. MS spectra of peptide B, VTVLGQPK [109:116, LC] originating from IgG2 after proteolytic digestion: A) photo-irradiated IgG2, B) non photo-irradiated IgG2; IgG2 in H_2O (empty peaks) or in D_2O (filled peaks).

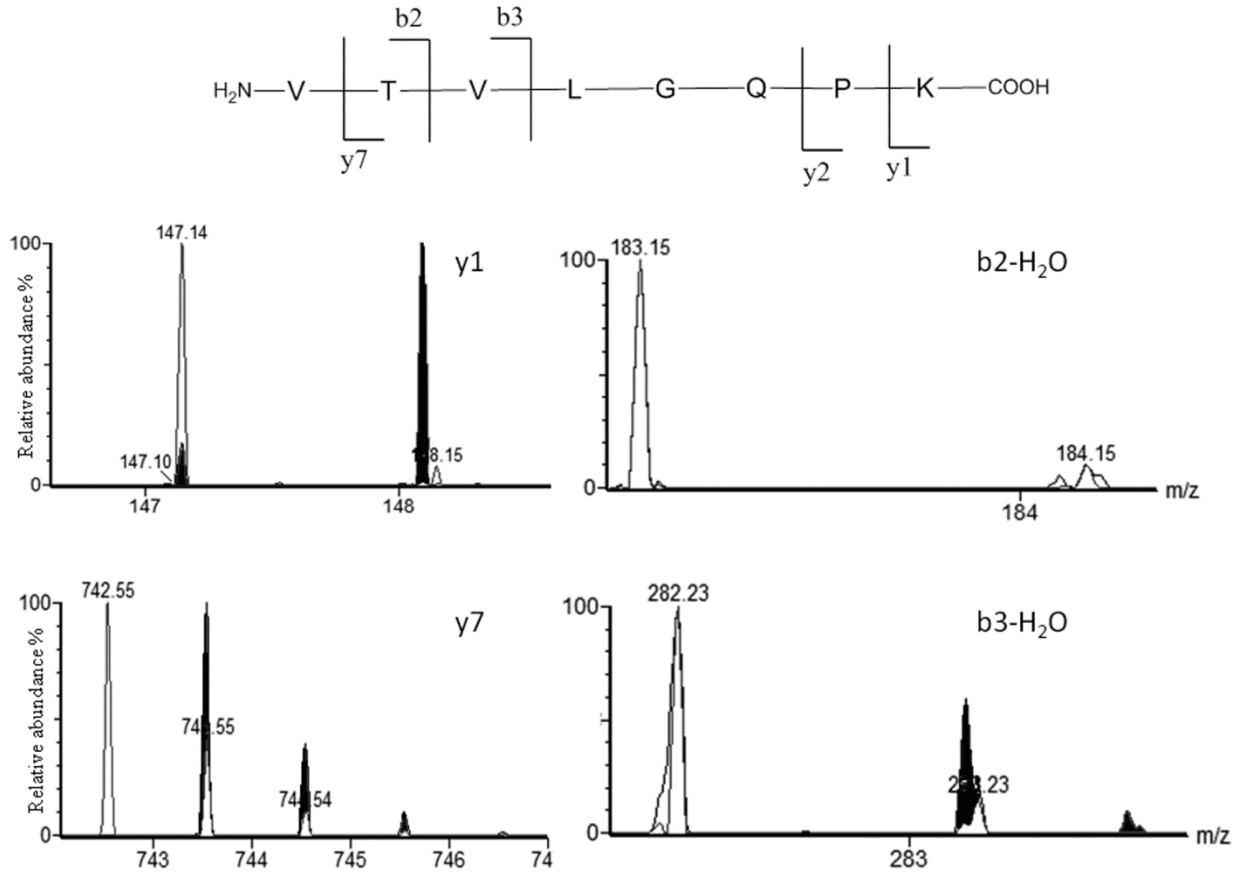

Fig. 5. MS/MS analysis of the b and y fragment ions originating from peptide B, VTVLGQPK [109:116, LC], to localize the amino acid residues with covalently incorporated deuterium.

Chapter 8: Methodology development to detect and characterize IgG1 photo-degradants: Simultaneous Separation and Characterization of IgG1, IgG1 Fragments and Photodegradation Products by Reverse Phase Liquid Chromatography/ Mass Spectrometry (RPLC/MS)

Table of Contents

8.1 Introduction

Reverse phase liquid chromatography (RPLC) combined with mass spectrometry (MS) is an established method to identify and characterize proteins and their degradation products. An increased demand for fast and sensitive analysis has fostered the development of new liquid chromatography techniques accelerating chromatographic separation and reducing the protein amount needed for analysis. Non-porous columns have been utilized for protein separations, especially with particles of 2 μm or less in diameter [1-4] due to their unique advantages. Compared to conventional column stationary phase packing with porous particles, non-porous particles potentially increase the column efficiency by reducing Eddy diffusion, mass-transfer resistance and diffusional broadening due to the lack of pore structures. The use of non-porous packing also reduces the possibility of protein loss inside the pores of the porous packing material, improving resolution and protein recovery.

In current practice, protein separation and the following desalting step are needed prior to protein analysis by LC/MS due to solvent incompatibility and sample complexity. Protein separation is typically achieved by reverse phase liquid chromatography (RPLC), size exclusion chromatograph (SEC), 1-D or 2-D sodium dodecyl sulfate polyacrylamide gel electrophoresis (SDS-PAGE) and/or the combination of these techniques. The separation of intact monoclonal antibodies (mAbs) and their degradation products by traditional RPLC with porous columns has been intractable because of large size, structural complexity and hydrophobicity of the mAb. MAb separation by RPLC with porous columns typically results in low recovery, poor resolution and irreproducibility. The separation and desalting process is very labor-intensive and time-consuming, which also increases risks of introduction of undesired modification(s), degradation

and material loss. Detection and characterization of mAb modifications and/or degradation products has remained a challenging analytical task because of product complexity and low abundance. Separation with online characterization of intact proteins and large fragments will pose an unambiguous advantage in the rapidly developing field of proteomics and biopharmaceutical product analysis.

Non-porous columns have been explored for some time [5-9]. Dauly *et al.* demonstrated that matrix-assisted laser desorption/ionization time-of-flight mass spectrometry (MALDI-TOF-MS) analysis of each collected and desalted fraction of proteins from a non-porous column was a feasible method for sensitive and reproducible protein characterization [2]. Protein profiles of normal and malignant whole cell lysates of human breast cancer cell lines were also generated by using non-porous silica bead packing material, followed by further protein identification of each separated and desalted protein fraction from PRLC [3]. The challenges with the reported application of RPLC/MS for protein analysis are that prior to protein analysis by MS, the proteins of interest had to be separated by RPLC for fraction collection, and desalted.

To the best of our knowledge, the separation with online characterization of an intact mAb and large mAb fragments by RPLC connected to a MS using non-porous columns without the need of pre-separation by other methodologies and desalting has not been reported. Here, we focus on developing a RPLC/MS method capable of separation with online characterization of an IgG1 and its photo-degradation products, especially fragments, without the need for additional separation and desalting. The separation of the proteins and fragments is achieved by RPLC using a non-porous column. The sensitivity and resolution of the mass spectrometer as well as the chromatographic separation were optimized with an in-house prepared mixture containing 12 ng lysozyme, 60 ng bovine serum albumin (BSA), 200 ng IgG1 heavy chain (HC), 600 ng IgG1

light chain (LC), 400 ng IgG1 Fab-HC, 400 ng IgG1 constant HC (Fc-HC) and 800 ng IgG1. Excellent reproducibility in retention time (%RSD < 0.4) and reasonable reproducibility in peak area (total ion counts,) of %RSD < 16 are demonstrated. The limit of detection (LOD) of the proteins and IgG1 fragments ranged between 1.2 and 80 ng dependent on the nature of the analytes. Analysis of IgG1 photo-degradation products further confirmed that this developed RPLC/MS method using a non-porous column is a fast and highly sensitive analytical tool, allowing us to characterize the degradation products, especially fragments, with very limited material of 3 μg IgG1. The detected fragments were confirmed by SDS-PAGE. Combination of the information obtained from our developed RPLC/MS method with in-gel digestion of the fragments resolved by SDS-PAGE allowed us to determine the potential fragment sequence, providing valuable insight into IgG1 photo-instability. Thus, a fast and highly sensitive separation with online characterization method to analyze intact proteins and fragments would provide a novel and powerful approach in proteomic and biopharmaceutical analysis to greatly improve efficiency.

8.2 Experimental

8.2.1 Materials

Recombinant monoclonal immunoglobulin (IgG1, 35 mg/mL) was supplied by Amgen Inc. (Seattle, WA, USA). The purified protein was stored in formulation buffer at -80^{o}C. Other commercially available proteins, such as lysozyme (pI: 11.0, MW: 14.388 kDa) and bovine serum albumin (BSA) (pI: 4.7, MW: 66,463 Da) were purchased from Sigma Aldrich (St. Louis, MO, USA). Dithiothreitol (DTT), iodoacetamide (IAM), sodium phosphate, dibasic (Na_2HPO_4), sodium phosphate, monobasic (NaH_2PO_4) and sodium chloride (NaCl) were also purchased from Sigma Aldrich (St. Louis, MO, USA). FabRICATOR® was purchased from Bulldog Bio, Inc.

(Portsmouth, NH, USA), a distributor of Genovis (Lund, Sweden) in the USA. All organic solvents (analytical and HPLC grade) were purchased from Sigma Aldrich (St. Louis, MO, USA) or VWR Scientific (West Chester, PA, USA). SDS-PAGE running buffer (100 mM tris, 1.92 M glycine and 0.1% (w/v) SDS at pH 8.3) and Precision Plus Protein dual color standards were obtained from Bio-Rad (Hercules, CA, USA). Sequencing grade trypsin and Glu-C were purchased from Promega Corp. (Madison, WI, USA). SYPRO® orange dye, supplied as a 5000x concentrated solution in dimethyl sulfoxide (DMSO), was purchased from Invitrogen, Inc. (Carlsbad, CA, USA).

8.2.2 Sample preparation

8.2.2.1 Formation of light chain (LC) and heavy chain (HC) from IgG1.

The stock solution of IgG1 was dialyzed at 2-8^{o}C in milliQ H_2O using a dialysis cassette with a 10 kDa cut-off membrane (Pierce, Rockford, IL, USA). After dialysis, IgG1 was diluted to 1 mg/mL in milliQ H_2O. 4 µL of a DTT stock solution (100 mM in H_2O) were added into the solution prior to incubation at 37^{o}C for 30 min. The reduction of the disulfide bonds of IgG1 results in the separation of the LC and HC chains. The final concentrations of both LC and HC were 2 µg/µL.

8.2.2.2 Formation of the Fab-HC, Fc-HC, and LC from IgG1

IgG1 was prepared at 1 mg/mL in 50 mM sodium phosphate buffer in the presence of NaCl (150 mM) at pH 6.6. An aliquot of 10 µL reconstituted FabRICATOR® solution in H_2O (20 unit/µL in H_2O) was added to the solution prior to incubation at 37^{o}C for 30 mins. After cleavage of IgG1 between the residues Cys 225 and Cys 257 of the HC, the disulfide bonds present in the resulting protein fragments were reduced according to the procedure described

above to form Fab-HC, Fc-HC and LC as shown in Fig. 1. The final concentrations of LC, Fab-HC and Fc-HC were 2 μg/μL.

8.2.2.3 Preparation of protein mixture standard

BSA, lysozyme, intact IgG1 and its LC, HC, Fab-HC and Fc-HC were mixed to achieve the final concentrations listed in Table 1. The protein mixture was prepared in milliQ H_2O with 0.5% formic acid (v/v).

8.2.2.4 Photo-degradation of IgG1

IgG1 was prepared at 10 mg/mL in 20 mM sodium phosphate buffer at pH 6.5. The sample was placed in a quartz tube and irradiated for either 30 or 45 minutes with ultra-violet (UV) light (λ = 253.7 nm) by means of a Rayonet photochemical equipped with four UV lamps (RMA-500) (Southern New England Ultraviolet Company, Branford, CT, USA). Photo-irradiated IgG1 was cleaved and reduced into LC, Fab-HC, and Fc-HC according to the protocols described in the sections of 8.2.2.1 and 8.2.2.2.

8.2.2.5 Reverse phase liquid chromatography/mass spectrometry (RPLC/MS)

Mass spectrometry data acquisition was achieved on a SYNAPT G2 high definition mass spectrometer (Waters Corp. Milford, MA, USA). Electrospray ionization (ESI) mass spectra of the proteins were acquired by operating the SYNAPT G2 for maximum resolution with all lenses optimized on the $[M + 2H]^{2+}$ ion from the $[Glu]^1$-fibrinopeptide B and Ar was admitted to the collision cell. The capillary voltage was set to 2.9 kV. The cone voltage was set at 45 V and ramped to 85 V. The voltage of the extraction cone was maintained at 6 V. Source and desolvation temperatures were set at 95^{o}C, and 200^{o}C, respectively. Gas flows at the cone and for desolvation were set at 40 L/h, and 250 L/h, respectively. The spectra were acquired using a mass range of 900-3000 amu (amu: atomic mass unit). The data were accumulated for 0.7 sec per

cycle and processed using the software MassLynx (Waters Corp. Milford, MA, USA). ESI generates a series of multiply charged ions for a single protein. To characterize the proteins present, the mass-to-charge *(m/z)* ratio distributions were analyzed by maximum entropy (MaxEnt) processing. MaxEnt disentangled the *m/z* distribution of each mass spectrum produced by the mass spectrometer to present the proteins in the mixture as single peaks on a molecular mass scale [10-12].

The proteins were chromatographically separated after injection of an aliquot of 2 µL of each sample onto a non-porous column, Presto FF-C18 (15 cm x 0.5 mm C18, 2 µm), packed with octadecyl silane (ODS) from Imtakt Corp. (Philadelphia, PA, USA). The column was maintained at 65^{o}C and the solvents were eluted through the column by an Acquity Chromatography System (Waters Corporation, Milford, MA, USA). Mobile phases consisted of H_2O/acetonitrile (ACN)/formic acid at a ratio of 99%, 1%, 0.08% (v/v/v) for solvent A and a ratio of 1%, 99%, 0.06% (v/v/v) for solvent B. The column was equilibrated with 15% B at a flow rate of 5 µL/min. Between 0 - 3 min, and 3 – 20 min the eluent composition was linearly increased to 25% B and 35% B, respectively, at a constant flow rate of 5 µL/min. Between 20 - 35 min and 35 – 45 min, the eluent composition was modified to reach 65% and 95% B, respectively, through a non-linear gradient (chromatographic curve # 3) at a flow rate of 7 µL/min. Elution at 95% B was held for 2 min. After 47 min, the flow rate was gradually increased to 10 µL/min and held for 10 mins with 95% B for column washing. The column was re-equilibrated with 15% B at 5 µL/min for 10 mins.

8.2.2.6 SDS-PAGE

The photo-irradiated IgG1 was treated according to the protocol described in section 1.2. After reduction of the disulfide bonds, the reduced Cys residues were alkylated. An aliquot (100

μL) of the cleaved and reduced photo-irradiated IgG1 sample was mixed with 5 μL of iodoacetamide stock solution (100 mM in H_2O) and incubated at ambient room temperature for 30 mins in the dark. The alkylated sample was mixed with SDS-PAGE sample buffer containing 100 mM Tris, 100 mM Tricine, and 0.1% (w/w) SDS at pH 8.25. The sample was heated at 100^{o}C for 1 min after mixing and subsequently, 20 μL were loaded onto a polyacrylamide gel Novex 4-20% (Invitrogen, Carlsbad, CA, USA). Molecular Weight Standard, precision plus protein dual color standards from Bio-Rad (Hercules, CA, USA), was loaded onto the same gel as a molecular weight reference. The gel electrophoresis was run under a difference of potential of 250 V for 60 min using diluted (1/10) running buffer. During electrophoresis, the temperature was maintained at 6^{o}C.

8.2.2.7 Fluorescence visualization of the IgG1 and its degradants

SYPRO® Orange dye was used as a fluorescence probe to visualize IgG1 and its degradation products. The gel was first rinsed with 2 mM EDTA twice and then incubated in diluted acetic acid (1.7 M) containing 5000x diluted SYPRO® Orange dye for 1.5 hours. The gel was rinsed three times with 1.7 M acetic acid prior to gel imaging. The fluorescence was recorded at 580 nm with the excitation wavelength at 488 nm by TyphoonTM and ImageQuantTM Laser Imager from GE HealthCare (Fairfield, CT, USA).

8.2.2.8 In-gel digestion

The separation of IgG1 and its degradation products was visualized with Coomassie blue (Coomassie R250/acetic acid/MeOH/H_2O (0.2/7.5/30/62.5%, v/v/v/v)) obtained from BioRad (Hercules, CA, USA). Destaining was performed in acetic acid/MeOH/H_2O (10/40/50, v/v/v). The fragments of interest were excised from the Coomassie blue-stained gel. The protein present in the gel slice was digested according to the in-gel digestion protocol described by Shevchenko

et al [13]. Briefly, the gel slice was washed twice with NH_4HCO_3 (100 mM in H_2O) in 50% ACN (v/v) for 15 min at room temperature. After removal of the solvent, the gel slice was washed twice with 100% ACN for 15 mins at room temperature. The gel slice was dried under SpeedVac (Labconco Corp. Kansas City, MO, USA). The dried gel slice was placed in 200 µL of a Promega® reconstitution buffer for trypsin, containing 8 µg of trypsin and 4 µg of Glu-C. The sample was incubated at 4^{o}C for 1 hour for the gel absorption of tryptic enzymes. Prior to digestion incubation 37^{o}C overnight, an aliquot of 300 µL NH_4HCO_3 (100 mM in H_2O) was added to the sample. The solution was transferred into new vials upon the completion of digestion. The gel slice was washed in ACN and centrifuged for 2 mins at 14000 g. The washed solution was transferred into the same new sample vials. Solvent was vacuum dried to reach a final volume of 20 µL.

8.2.2.9 LTQ-FT-MS

The following procedure was applied to analyze the peptides resulting from the proteolytic digestion of the protein isolated by SDS-PAGE. Collision induced dissociation (CID) of fragment ions was performed by means of an LTQ-FT hybrid linear quadrupole ion trap Fourier transform ion cyclotron resonance (FT-ICR) mass spectrometer (ThermoFinnigan, Bremen, Germany) [14]. MS/MS data were acquired with an attenuation of the parent ion in the range of 25%-35%. The mass window to collect the parent ion was fixed to ±0.2 Da.

The data were processed using the ThermoElectron BioWorks 3.2 software followed by peptide identification using the Mascot database-searching program based on the custom-defined IgG1 primary sequence. The peptide assignments obtained were validated using a statistical

method of the Scaffold 1.7 software (Proteome Software Inc., Portland or http://www.proteomesoftware.com).

8.3 Results and Discussion

This work focused on the development of a fast and sensitive analytical tool without the need of additional separation and desalting processes to simultaneously separate and characterize proteins and their fragments. The non-porous packing material of the Presto-FF C18 column allows efficient separation of intact proteins and large protein fragments by reducing mass transfer [1]. The separation of macromolecules on a non-porous column has already been reported [3-8]. However, to the best of our knowledge, simultaneous separation with online characterization of intact proteins and large fragments with RPLC/MS using a non-porous column without having to resort to additional fractionation was never documented. In the present work, we demonstrate that proteins in the range of 14–150 kDa can be well separated with high sensitivity. Analysis of the photo-induced IgG1 degradation products with this developed method further confirmed that it is a highly sensitive and rapid method capable of simultaneous detection and characterization of the degradation products, especially fragments. The acquired structural modifications will also provide valuable insight to understand the possible degradation mechanism and the liable region(s) prone to degradation.

8.3.1 Separation and characterization of proteins by RPLC/MS

BSA, lysozyme, intact IgG1 and its LC, HC, Fab-HC and Fc-HC were separated and identified by mass spectrometry (Fig. 2a-h). The nature of the protein present in each chromatographic peak was determined after MaxEnt processing of the respective mass spectra (Fig. 2b-h, right panels).

8.3.1.1 *Constant heavy chain (Fc-HC) of IgG1*. The mass to charge *(m/z)* distribution pattern (Fig. 2b, left panel) for the first elution peak at 17.28 minutes indicates the presence of two species and the mass deconvolution yielded two main species with a mass of 25,202 Da and 25,364 Da (Fig. 2b, right panel), corresponding to IgG1 Fc-HC which was glycosylated. The number of monosaccharide residues coupled to a protein is estimated by a mass increase of 162 Da per attached monosaccharide [15, 16]. Thus, the observed mass difference between the two Fc-HC species is rationalized by the loss of a monosaccharide.

8.3.1.2 *Lysozyme.* The same approach was used to identify the other chromatographic peaks. Lysozyme eluted after IgG1 Fc-HC at 18.45 min (Fig. 2a). The deconvoluted mass spectrum (Fig. 2c, right panel) shows a mass of 14,306 Da, matching its reported molecular weight of 14,307 Da (from chicken egg white) within an accuracy of 1 Da [17].

8.3.1.3 *Light chain (LC) of IgG1.* The reduced but not alkylated LC eluted at 19.49 min (Fig. 2a). After deconvolution only one mass of 22,927 Da (Fig. 2d right panel) is observed and this mass matches the theoretical molecular weight of the reduced LC. The observation of two sets of charge state distributions centered at *m/z* 1,433.90 and 2,085.20 (Fig. 2d, left panel) for a single species indicates the presence of two different conformational states [17-20]. In a first approximation, we can consider that the distribution of ions centered at *m/z* 2,085.20 characterizes the folded (native) state and the one centered at *m/z* 1,433.90 represented a partially unfolded, or loosely folded, state [21, 22].

8.3.1.4 *Heavy chain (HC) of IgG1.* The reduced but not alkylated HC eluted at 21.57 min (Fig. 2a). The mass spectrum (Fig. 2e, left panel) indicates the presence of two HC with masses of 49,636.04±8.36 Da and 49,475.95±10.57 Da. Based on the uncertainty of ± (8.36-10.57) Da, the variation of mass between the two HC is about 161 Da which would correspond to a

monosaccharide. The latter is confirmed after MaxEnt data processing (Fig. 2e, right panel). Indeed, after deconvolution of the charge state into a mass scale spectrum, the molecular weights of 49,475 Da and 49,636 Da are observed as the most probable components of the charge state ion distribution presented in the mass spectrum (Fig. 2e, left panel). With a difference of mass of 161 Da, we assume that the observation of these two masses is related to the presence of different glycosylation forms of the IgG1. This is consistent also with our observation of two glycosylated forms of IgG1 during the analysis of the IgG1 Fc-HC region (see above). Together, the results are consistent with the fact that the glycosylation site of IgG1 is located in the Fc-HC.

8.3.1.5 *Fab region of IgG1 heavy chain (Fab-HC).* The reduced but not alkylated Fab-HC region eluted at 23.12 min (Fig. 2a). Charge state distributions of the ions were observed analogous to those for the IgG1 LC, centered at *m/z* 1,429.63 and *m/z* 2,024.91 (Fig. 2f, left panel) corresponding to a single species. These two charge state distributions indicate the presence of two different conformational states. The distribution of ions centered at *m/z* 2,024.91 indicates a folded (native) state and the one centered at *m/z* 1,429.63 likely a partially unfolded state, allowing the protonation of more amino acid residues. The sum of the masses of IgG1 Fab-HC and Fc-HC (as reported above) are *ca.* 18-20 Da higher than those observed for intact HC, i.e., 49,636 Da (Fig. 2e). This mass difference of *ca.* 18 Da is rationalized by the additional peptide bond between the IgG1 Fab-HC and the Fc-HC fragments to form the intact HC.

8.3.1.6 *BSA.* BSA eluted at 26.24 min (Fig. 2a). The deconvoluted mass spectrum (Fig. 2g) shows a molecular weight of 66,438 Da, matching its reported molecular weight of *ca.* 66 kDa provided by the supplier.

8.3.1.7 Intact IgG1. Surprisingly, two peaks eluting at 21.96 min and 27.79 min (Fig. 2a) were observed. Both chromatographic peaks show similar charge state distributions (Fig. 2h, left

panel, top and bottom). The deconvoluted mass spectra (Fig. 2h, right panel) show a major mass of *ca.* 144,950 Da along with masses of 142,093 Da and 147,691 Da. The measured mass of 142,093 Da matches the average calculated mass of deglycosylated IgG1 based on its primary sequence. The major species, glycosylated intact IgG1 with a mass of 144,950 Da, is *ca.* 2,726 Da heavier than the theoretical average mass. The mass difference of 2,726 Da matches the average mass of glycans (*ca.* 2,750 Da) reported for such immunoglobulins [23]. The species corresponding to the mass of 147,961 Da likely represents also glycosylated IgG1, demonstrating same glycosylation heterogeneity. The fact that the intact IgG1 was separated into two discrete populations indicates the existence of two conformational states, consistent with our analysis of the Fab-HC and the LC, denoted above. At this point, we cannot conclude that the discussed conformers are originally present in the IgG1 stock solution. Rather, we believe that the use of acetonitrile and elevated temperature during reverse phase chromatography may lead to partial unfolding of the protein. The presence of two conformers of IgG1, and the observation of the combination of two charge state distributions produced during the MS analysis of its LC (Fig. 2d) and Fab-HC (Fig. 2f) indicate that the observed two conformers of IgG1 (Fig 2h) are the result of conformational modifications of its Fab region. Hence, our method is not only capable of allowing simultaneous separation and characterization of proteins and fragments but also capable of providing some information on the conformational stability of the protein. For convenience, we will refer to the two conformers as conformer A (eluted at 21.96 minutes) and conformer B (eluted at 27.79 minutes).

8.3.2 LOD and reproducibility

Each protein in the standard mixture was individually analyzed under the same chromatographic conditions to explore if the presence of other proteins and fragments in the

mixture would interfere with the separation and detection. The consistency in retention time between the chromatograms of the individual components and the mixture (as shown in Fig. 3) demonstrates that the separation and detection of the individual components in the mixture is not compromised by the presence of the other proteins and fragments. The chromatogram of intact IgG1 (Fig. 3e) exhibits two well separated peaks with identical mass spectra, confirming the presence of two conformers.

The reproducibility of the method was evaluated by three consecutive injections of the same protein mixture under identical conditions. Retention time and peak area averages, as well as standard deviation (SD) and relative standard deviations (RSD) were calculated for each analyte as listed in Table 2. Excellent reproducibility in retention time (< 0.4%) with detectable peak area (total ion counts) is demonstrated. Peak area (total ion counts) showed an increased variation with RSDs of < 5% except for IgG1 HC, IgG1 conformer A (6.5% of RSD) and IgG1 Fab-HC (16.26% of RSD). The partial resolution of IgG1 HC, its conformer A, and Fab-HC may contribute to the increased variation in peak area.

The LOD was evaluated by diluting the protein mixture standard by ten-fold and one hundred-fold. The same volume, an aliquot of 2 μL, was injected under identical conditions. An amount of 20.0 ng IgG1 Fc-HC, 1.2 ng lysozyme, 30.0 ng IgG1 LC, 10.0 ng IgG1 HC, 20.0 ng IgG1 Fab-HC, 6.0 ng BSA and 80 ng intact IgG1 in the mixture exhibit acceptable peak intensity for detection and quantification (as shown in Fig. 4). After dilution by 1/100 of the original mixture, the signal-to-noise ratios for 2.0 ng Fc-HC, 0.12 ng lysozyme, 3.0 ng LC, 1.0 ng HC, 2.0 ng Fab-HC, 6.0 ng BSA and 8.0 ng whole IgG, were too low for detection (data not shown here).

8.3.3 Analysis of photo-induced IgG1 degradation

The photo-induced degradation of the IgG1 was analyzed by our developed RPLC/MS method. The photo-irradiated samples were first diluted *ca.* 7-fold to 1.5 mg/mL and then an aliquot of 2 μL was injected. A representative chromatogram of IgG1 after exposure to UV light is displayed in Fig. 5a. The analyte present in each chromatographic peak was analyzed by processing the respective mass spectrum with MaxEnt. A new protein fragment with a mass of 13,210 Da (Fig. 5b), and modified IgG1 Fc-HC with masses of 25,233 Da and 25,396 Da (Fig. 5c) respectively were detected. Each new component is discussed in detail below.

8.3.3.1 *Fragment with a mass of 13,210 Da.* A fragment with the mass of 13,210 Da (Fig. 5b), which is not present in the control (non-photo irradiated IgG1), eluted at 14.95 minutes. A fragment with the same mass was also formed during photo-irradiation of IgG1 under Ar (Fig. 5d). SDS-PAGE analysis followed by Coomassie blue staining did not allow the visualization of this fragment due to its extremely low abundance even after application of a *ca.* 80-fold increased protein load. However, the production of this new protein fragment with a mass of 13,210 Da was confirmed by SDS-PAGE combined with fluorescence imaging using SYPRO® Orange after application of a 15-fold increased protein load. The left panel of Fig. 6 clearly exhibits the IgG1 Fab-HC, Fc-HC, LC and protein species of higher mass (lane 1 and 2 were loaded with IgG1 samples irradiated for 30 and 45 minutes, respectively). The right panel of Fig. 6 generated by lower γ correction using Adobe Photoshop (Adobe, San Jose, CA, USA) enables us to visualize a fragment band with a mass of *ca.* 13 kDa. This further demonstrates that our developed LC/MS method using the non-porous column is highly efficient and sensitive to separate, detect and characterize protein fragments, at least 80-fold more sensitive than SDS-PAGE stained by Coomassie dye. We also note that this new RPLC/MS method only takes 60 minutes instead of at least several hours necessary to complete SDS-PAGE analysis. The

corresponding *ca.*13 kDa band area in the gel stained with Coomassie dye was excised for in-gel digestion and peptide mapping.

After mass determination of the fragment by mass spectrometry (Fig. 5b), we searched the possible peptide sequences which would match any sequence in our IgG1 by using the web-based software FindPept (ExPasy; Bioinformatics Research; http://web.expasy.org/findpept). The search criteria used were: mass variation of ±0.5 Da and oxidation of Trp (+16 and/or 32 Da) and Met (+16 and/or 32 Da). Two candidate peptide sequences located in the IgG1 LC region (Table 3) matched the fragment mass of 13,210 Da within ±0.5 Da. These are overlapping sequences originating from the sequence LC15-LC52. To confirm the sequence of the fragment, peptide mapping by LC/MS/MS of the in-gel digested fragment was performed. The detected peptides for the two candidate fragments (Table 3) are listed in Table 4a-b, respectively. The amino acids in the identified peptide sequences by LC/MS/MS covered 86% and 89% of the amino acids in the respective candidate peptide sequences obtained from FindPept. The formation of the fragment (a mass of *ca.*13,210 Da) in both air-saturated and Ar saturated solution suggests that the fragmentation between Ser and Asn, Val and Ala, Pro and Gly, and Cys and Leu does not involve oxygen and oxygen-centered radicals. Thus, this identified fragment is probably due to hydrolytic cleavage. We also note that during the photo-irradiation of IgG1, the peptide bond between the amino acid residues His [36, LC] and Trp [37, LC] is cleaved leading to the formation of the peptide WYQQLPGTAPL (Table 4a, first entrance). The understanding of the mechanism leading to such hydrolytic cleavage is out of the scope of this study. However, we may hypothesize that during the photo-irradiation of IgG1, the formation of the radical cation of Trp [37, LC] could be at the origin of the fragmentation of the peptide bond [24].

8.3.3.2. *Modified IgG1 Fc-HC.* Mass analysis indicates that the modified IgG1 Fc-HC with masses of 25,233 Da and 25,396 Da (as shown in Fig. 5c) was eluted at 15.21 minutes before the elution of non-modified Fc-HC. A mass increase of 32 Da and 33 Da within *ca.* ±1 Da accuracy compared to their corresponding non-modified ones (Fig. 2b), respectively, indicates the modifications may be due to oxidation. Fc-HC is the region responsible for its biologic properties, which include activation of the complement system which leads to enhanced phagocytosis, placental transfer, and binding to cell-surface receptors [25]. Thus, any modifications to this region may produce impact in its functionality. A detailed analysis of all modifications is currently in progress.

8.4 Conclusions

In this study, we focused on developing a fast and highly sensitive method using RPLC combined to MS for simultaneous separation and characterization of intact proteins and large fragments, eliminating the need of additional fractionation and protein desalting. The separation was achieved by using a non-porous column with a combination of two non-linear gradients of H_2O and ACN. We demonstrate that this method exhibits excellent retention time reproducibility of %RSD < 0.4 and a fair reproducibility in peak area (total ion counts) of %RSD < 16. The LOD of the tested proteins ranged between 1.2 and 80 ng, dependent on the nature of the analyte. In addition, this method was capable of not only separating two conformers of IgG1 but also providing conformational information, that is, identifying the Fab-region responsible for intact IgG1 two conformational states. The analysis of photo-induced IgG1 degradation further demonstrates that this developed RPLC/MS method is a highly sensitive analytical method to detect and characterize fragments, at least 80-fold more sensitive than that of SDS-PAGE stained by Coomassie blue. The information acquired from our developed RPLC/MS method allowed us

to detect and characterize the fragment(s) originating from the IgG1 light chain due to photo-irradiation, providing a valuable tool for studying the photo-instability of antibodies.

8.5 Acknowledgement

We gratefully acknowledge Amgen Inc. for financial support.

8.6 References

1. Banks, J.F., et al., *Rapid peptide mapping by reversed-phase liquid chromatography on nonporous silica with on-line electrospray time-of-flight mass spectrometry.* Anal Chem, 1997. **69**(19): p. 3973-8.
2. Dauly, C., et al., *Protein separation and characterization by np-RP-HPLC followed by intact MALDI-TOF mass spectrometry and peptide mass mapping analyses.* J Proteome Res, 2006. **5**(7): p. 1688-700.
3. Chong, B.E., et al., *Rapid screening of protein profiles of human breast cancer cell lines using non-porous reversed-phase high performance liquid chromatography separation with matrix-assisted laser desorption/ionization time-of-flight mass spectral analysis.* Rapid Commun Mass Spectrom, 1999. **13**(18): p. 1808-12.
4. Koshiyama, A., et al., *Liquid chromatographic separation of proteins derivatized with a fluorogenic reagent at cysteinyl residues on a non-porous column for differential proteomics analysis.* J Chromatogr A, 2011. **1218**(22): p. 3447-52.
5. Chen, Y., et al., *Rapid identification and screening of proteins from whole cell lysates of human erythroleukemia cells in the liquid phase, using non-porous reversed phase high-performance liquid chromatography separations of proteins followed by matrix-assisted [correction of multi-assisted] laser desorption/ionization mass spectrometry analysis and*

sequence database searching. Rapid Commun Mass Spectrom, 1998. **12**(24): p. 1994-2003.

6. Itoh, H., et al., *Fast protein separation by reversed-phase high-performance liquid chromatography on octadecylsilyl-bonded nonporous silica gel. II. Improvement in recovery of hydrophobic proteins.* Anal Biochem, 1991. **199**(1): p. 7-10.
7. Lee, W.C., *Protein separation using non-porous sorbents.* J Chromatogr B Biomed Sci Appl, 1997. **699**(1-2): p. 29-45.
8. O'Neil, K.A., et al., *Profiling the progression of cancer: separation of microsomal proteins in MCF10 breast epithelial cell lines using nonporous chromatophoresis.* Proteomics, 2003. **3**(7): p. 1256-69.
9. Wall, D.B., et al., *Rapid profiling of induced proteins in bacteria using MALDI-TOF mass spectrometric detection of nonporous RP HPLC-separated whole cell lysates.* Anal Chem, 1999. **71**(17): p. 3894-900.
10. Ferrige, A.G., et al., *Disentangling electrospray spectra with maximum entropy.* Rapid Commun. Mass Spectrom., 1992. **6**(Copyright (C) 2012 American Chemical Society (ACS). All Rights Reserved.): p. 707-11.
11. Ferrige, A.G., et al., *Maximum entropy deconvolution in electrospray mass spectrometry.* Rapid Commun. Mass Spectrom., 1991. **5**(Copyright (C) 2012 American Chemical Society (ACS). All Rights Reserved.): p. 374-7.
12. Ferrige, A.G., et al., *The application of MaxEnt to high-resolution mass spectrometry.* Rapid Commun. Mass Spectrom., 1992. **6**(Copyright (C) 2012 American Chemical Society (ACS). All Rights Reserved.): p. 765-70.

13. Shevchenko, A., et al., *Mass spectrometric sequencing of proteins from silver-stained polyacrylamide gels.* Anal. Chem., 1996. **68**(Copyright (C) 2012 American Chemical Society (ACS). All Rights Reserved.): p. 850-8.

14. Ikehata, K., et al., *Protein targets of reactive metabolites of thiobenzamide in rat liver in vivo.* Chem. Res. Toxicol., 2008. **21**(Copyright (C) 2012 American Chemical Society (ACS). All Rights Reserved.): p. 1432-1442.

15. Lapolla, A., et al., *A new effective method for the evaluation of glycated intact plasma proteins in diabetic subjects.* Diabetologia, 1995. **38**(9): p. 1076-81.

16. Lapolla, A., et al., *The role of mass spectrometry in the study of non-enzymatic protein glycation in diabetes.* Mass Spectrom. Rev., 2000. **19**(Copyright (C) 2012 American Chemical Society (ACS). All Rights Reserved.): p. 279-304.

17. Loo, J.A., et al., *Effect of reducing disulfide-containing proteins on electrospray ionization mass spectra.* Anal Chem, 1990. **62**(7): p. 693-8.

18. Babu, K.R., et al., *The methanol-induced conformational transitions of beta-lactoglobulin, cytochrome c, and ubiquitin at low pH: a study by electrospray ionization mass spectrometry.* J Am Soc Mass Spectrom, 2001. **12**(3): p. 317-28.

19. Chowdhury, S.K., et al., *An electrospray-ionization mass spectrometer with new features.* Rapid Commun Mass Spectrom, 1990. **4**(3): p. 81-7.

20. Watt, S.J., et al., *Effect of protein stabilization on charge state distribution in positive- and negative-ion electrospray ionization mass spectra.* J Am Soc Mass Spectrom, 2007. **18**(9): p. 1605-11.

21. Chowdhury, S.K., et al., *Probing conformational changes in proteins by mass spectrometry.* J. Am. Chem. Soc., 1990. **112**: p. 9012-9013.

22. Smith, R.D., et al., *New developments in biochemical mass spectrometry: electrospray ionization.* Anal Chem, 1990. **62**(9): p. 882-99.

23. Chen, R., et al., *Glycoproteomics analysis of human liver tissue by combination of multiple enzyme digestion and hydrazide chemistry.* J. Proteome Res., 2009. **8**(Copyright (C) 2012 American Chemical Society (ACS). All Rights Reserved.): p. 651-661.

24. Hawkins, C.L., et al., *Generation and propagation of radical reactions on proteins.* Biochim Biophys Acta, 2001. **1504**(2-3): p. 196-219.

25. Raju, T.S., et al., *Galactosylation variations in marketed therapeutic antibodies.* MAbs, 2012. **4**(3).

Table 1. Compositions of the protein mixture for RPLC/MS method development using a non-porous column

Compositions	Lysozyme	BSA	LC	Fab-HC	Fc-HC	HC	Intact IgG
Conc. (ng/μL)	6	30	300	200	200	100	400

Table 2. Retention time and peak area (ion counts) reproducibility of RPLC/MS method evaluated by three consecutive injections under identical conditions

Components		Fc-HC	Lysozyme	LC	HC/IgG conformer A	Fab-HC	BSA	IgG conformer B
Retention time (min)	Avg	15.60	16.68	19.14	21.96	22.90	26.41	27.84
	SD	0.00	0.06	0.06	0.00	0.005	0.061	0.05
	% RSD	0.00	0.37	0.32	0.00	0.021	0.23	0.21
Peak area (ion counts)	Avg	2043	5634	7515	1831	2149	732	1616
	SD	73	82	177	119	349	29	68
	% RSD	3.58	1.45	2.35	6.50	16.26	4.02	4.18

Table 3. Identified peptide fragments (highlighted in bold font) by FindPept in the IgG1 sequence for the fragments with a mass of 13,210 Da detected by RPLC/MS using the following criteria: mass variation of ±0.5 Da, oxidation of Trp (+16 and +32 Da) and Met (+16 and +32 Da). (The cleavage sites are indicated by *).

Fragment #	Fragment Mass	Matched peptide mass (Da)	Mass difference (Da)	Peptide sequence	Peptide position in mAb
1	13210.00	13209.56	-0.464	(S)NIGAGYDVH***WYQQLPGTAPK*LLIYGNSNRPSGVPDRF*SGSKSGTSASLAITGLQAEDE*ADYYCQSYDSSLSGLYVFGTGTK*VTVLGQPK*ANPTVTLFPPSSEE*LQANKATLVCLISDF***YPGAVTV(A)	LC 28-152
2	13210.00	13210.49	0.468	(P)GQR***VTISCTGSSSNIGAGYDVHWYQQLPGTAPK*LLIYGNSNRPSGVPDRF*SGSKSGTSASLAITGLQAEDE*ADYYCQSYDSSLSGLYVFGTGTK*VTVLGQPK*ANPTVTLFPPSSEE***LQANKATLVC(L)	LC 15-140

Table 4a. Peptides identified by LC/MS/MS for fragment #1 listed in Table 3 with the PP, PP_2, PP_{tag}, mass accuracy and locations in IgG1 light chain (LC). (PP, PP_2, PP_{tag} are three statistical scores to evaluate the quality of a peptide match. A peptide match with max (PP, PP_2) > 4.5 and PP_{tag} > 1.3 is considered to be significant with p value < 0.05).

Peptide sequence	PP	PP_2	PP_{tag}	±Mass (Da)	Location
WYQQLPGTAPK	22.6	22.7	4.6	-0.0035	LC37-47
LLIYGNSNRPSGVPDR	11.1	12.0	1.8	-0.0121	LC48-63
SGTSASLAITGLQAEDE	25.1	25.2	2.0	-0.0075	LC69-85
ADYYCQSYDSSLSGLYVFGTGTK	20.6	23.9	5.1	-0.0083	LC86-108
VTVLGQPK	28.6	31.5	7.3	0.0007	LC109-116
ANPTVTLFPPSSEE	8.0	11.7	2.2	0.0006	LC117-130
ATLVCLISDF	13.1	16.2	2.1	0.0069	LC136-145

Table 4b. Peptides identified by LC/MS/MS for fragment #2 listed in Table 3 with the PP, PP_2, PP_{tag}, mass accuracy and locations in IgG1 light chain (LC). (PP, PP_2, PP_{tag} are three statistical scores to evaluate the quality of a peptide match. A peptide match with max (PP, PP_2) > 4.5 and PP_{tag} > 1.3 is considered to be significant with p value < 0.05).

Peptide sequence	PP	PP_2	PP_{tag}	±Mass (Da)	Location
VTISCTGSSSNIGAGYDVHWYQQLPGTAPK	10.5	10.3	1.5	-0.0035	LC18-47
LLIYGNSNRPSGVPDR	11.1	12.0	1.8	-0.0121	LC48-63
SGTSASLAITGLQAEDE	25.1	25.2	2.0	-0.0075	LC69-85
ADYYCQSYDSSLSGLYVFGTGTK	20.6	23.9	5.1	-0.0083	LC86-108
VTVLGQPK	28.6	31.5	7.3	0.0007	LC109-116
ANPTVTLFPPSSEE	8.0	11.7	2.2	0.0006	LC117-130

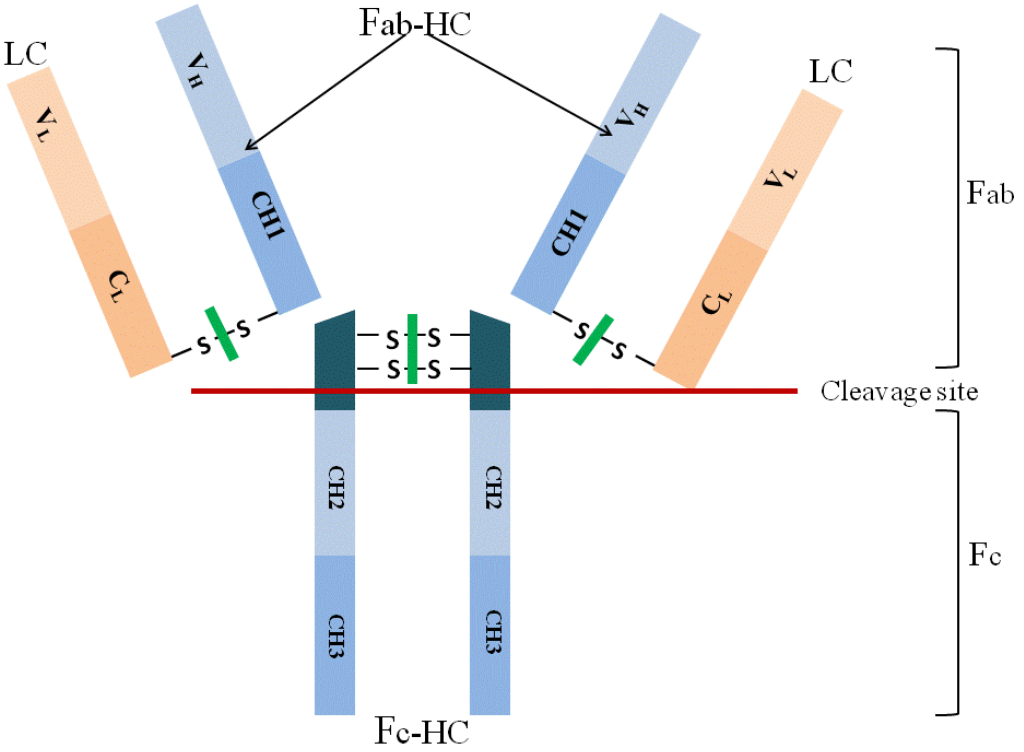

Fig. 1. Cartoon of IgG1 monoclonal antibody structure

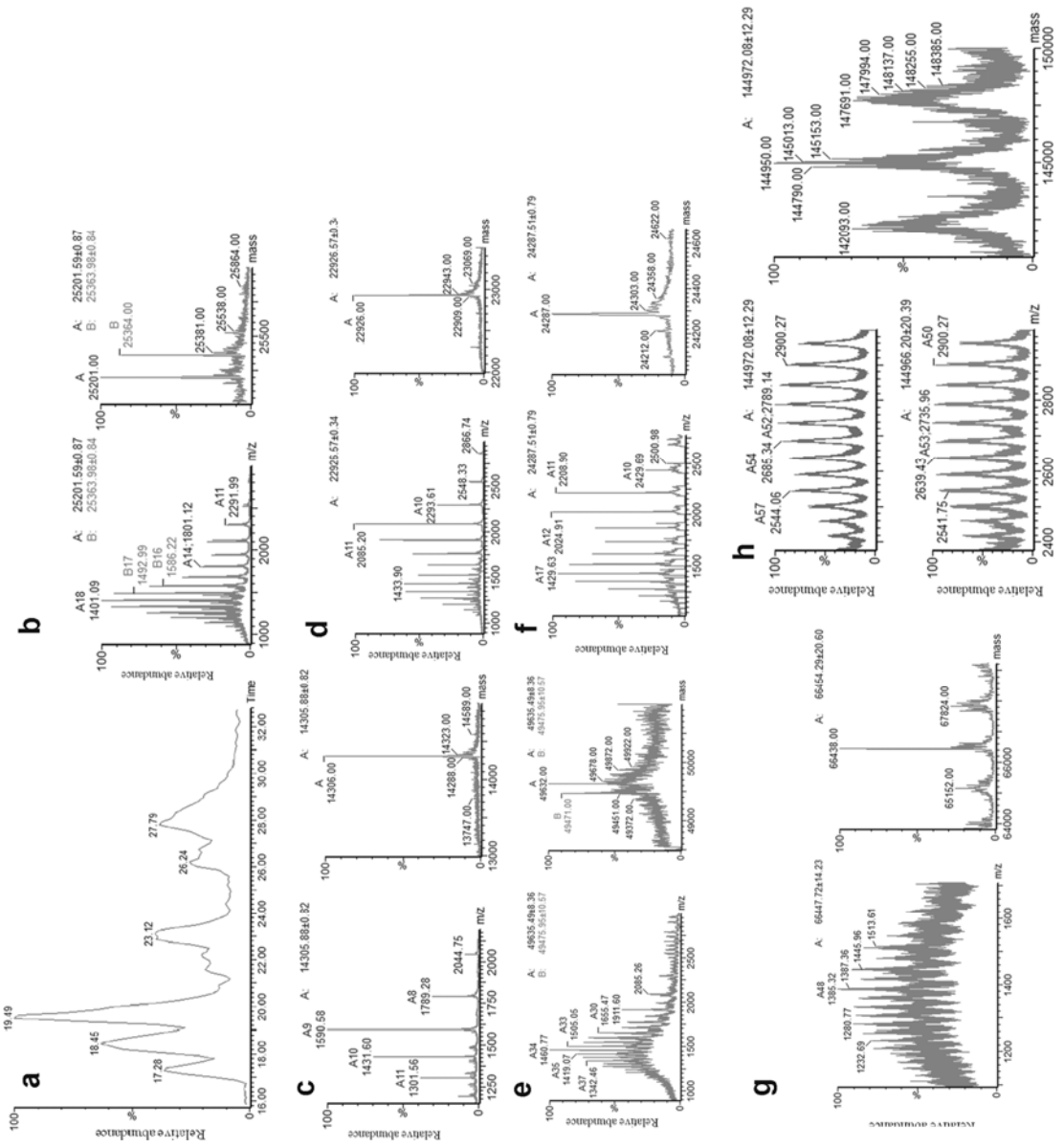

Fig. 2. RPLC/MS analysis of protein mixture standard containing lysozyme (12 ng), bovine serum albumin (BSA) (60 ng), IgG1 LC (600 ng), IgG1 Fab-HC (400 ng), IgG1 Fc-HC (400 ng), IgG1 HC (200 ng) and IgG1 (800 ng). RPLC-MS chromatogram (a), mass spectrum for IgG1 Fc-HC at t_R = 17.28 min (b), lysozyme at t_R = 18.45 min (c), IgG1 LC at t_R = 19.49 min (d), IgG1 HC at t_R = 21.57 min (e), IgG1 Fab-HC at t_R = 23.12 min (f), BSA at t_R = 26.24 min (g) and intact IgG1 at t_R = 21.96 min and t_R = 27.79 min (h)

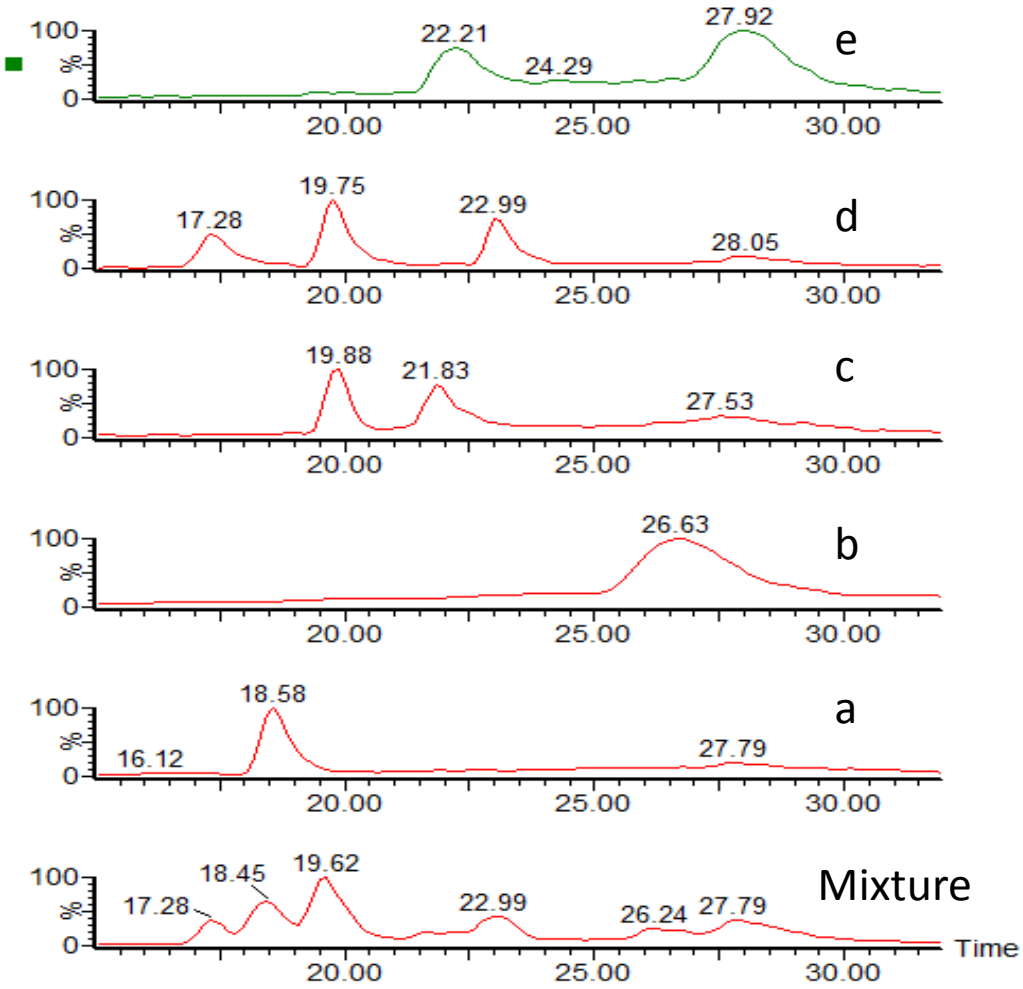

Fig. 3. RPLC/MS chromatograms for individual analyzed lysozyme (12 ng/µL) (a), BSA (60 ng) (b), reduced IgG1 (100 ng) (c), cleaved and reduced IgG1 (200 ng) (d) and intact IgG1 (800 ng) (e)

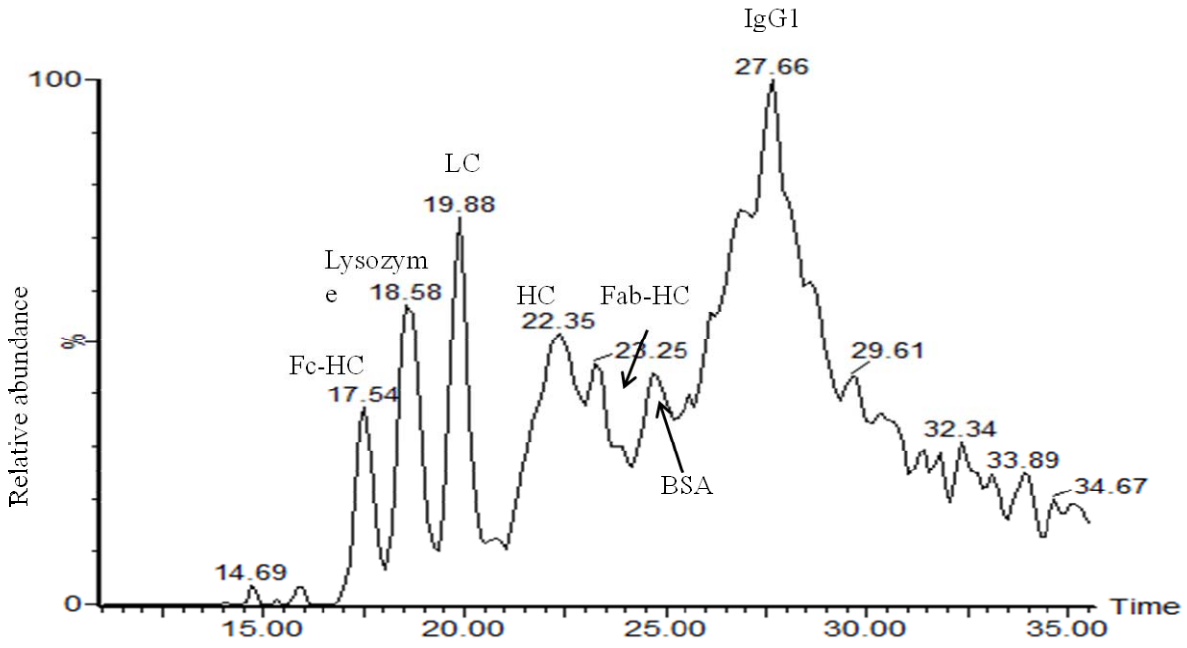

Fig. 4. RPLC/MS chromatogram of the protein mixture standard for limit of quantitation: IgG1 Fc-HC 20 ng, 1.2 ng lysozyme, 30 ng IgG1 LC, 10 ng IgG1 HC, 20 ng IgG1 Fab-HC, 6 ng BSA and 80 intact IgG1

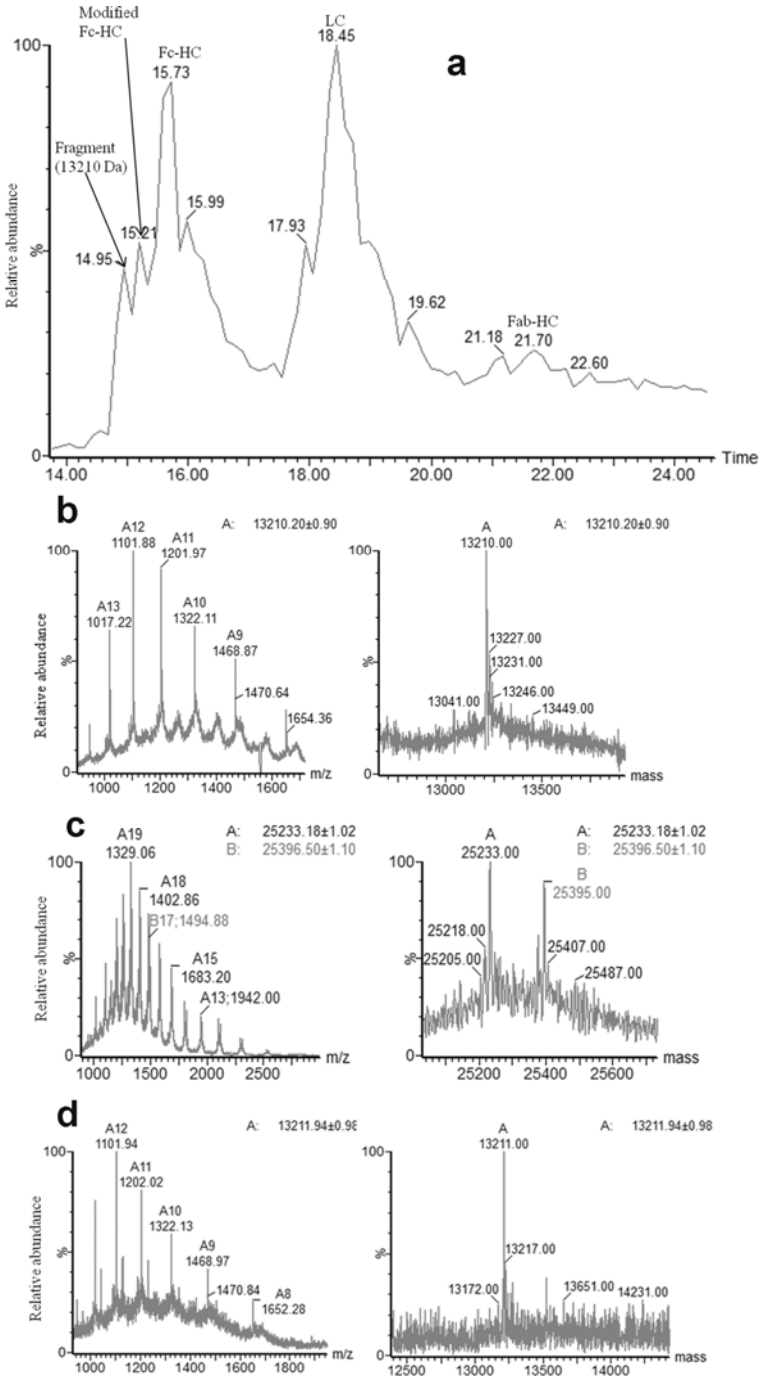

Fig. 5. Analysis of IgG1 photo-degradation products for photo-irradiation in the air: RPLC/MS chromatogram (a), mass spectra for the fragment (b) and mass spectra for modified IgG1 Fc-HC (c), and mass spectra for the fragment when IgG1 photo-irradiation under Ar (d)

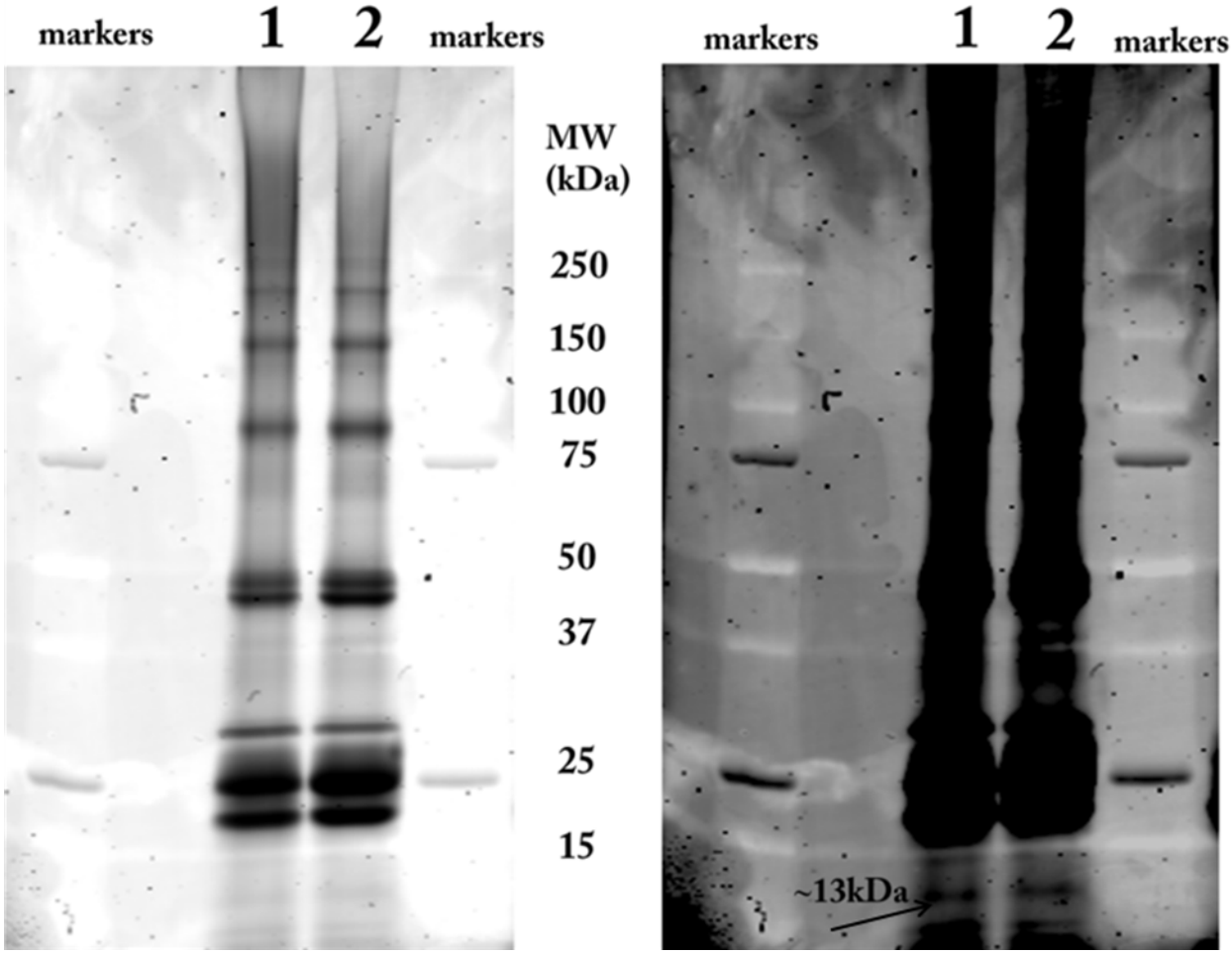

Fig. 6. SYPRO® Orange dye labeled reduced SDS-PAGE gel fluorescence image recorded at emission wavelength of 580 nm with the excitation wavelength at 488 nm by Typhoon™ and ImageQuantTM Laser Imager (left panel at γ correction factor of 2.0 and right panel at γ correction factor of 0.2 by Photoshop). Lane 1 and 2 were loaded with IgG1 samples irradiated for 30 and 45 minutes, respectively.

Part IV: Future Work

In this study, chemical and physical instability of several IgG mAbs due to metal catalyzed oxidation were investigated. The impact of Fe^{3+} on IgG physical instability, conformational change, formation of soluble aggregates, and intrinsic thermal instability was systematically studied. Chemical instability, oxidative modifications of IgG primary sequences by redox-active metal ion (Cu^{2+}) coupled with L-ascorbic acid were investigated. Oxidation of Phe and Tyr in IgG1 was first identified by fluorogenic derivatization using fluorescence spectrometry besides the known oxidation of His, Met and Trp. The oxidation of amino acids in IgG is impacted not only by their intrinsic properties, such as location in primary sequence and high order of structure, but also the external factors, such as temperature, contact materials, etc. The identification of critical determination factor(s) will or should greatly help scientists to design a more and/or robust drug product for patients.

The fluorogenic derivation developed in this study can only qualitatively detect the oxidation of Phe and Tyr residues in antibodies. Quantification of their oxidation using fluorescence is going to be the focus in next study. The oxidized amino acid residues may jeopardize protein function(s). The implication of the oxidized Phe and Tyr residues in IgG1 antibody's bioactivity is not clear which needs investigation. The quantitation of the levels of oxidized Phe and Tyr residues will help us understand the significance of the oxidation in affecting IgG antibody's bioactivity.

Even though both physical and chemical instability of proteins induced by redox-active ions were studied individually, the correlations and inter-relationships between physical and chemical instability pathways of protein degradation due to MCO have not been established. In addition, the metal ions of iron, chromium, nickel and tungsten are often seen in biotherapeutic

products instead of Cu^{2+} due to leaching from the contact materials and/or residues present in excipients. Whether the metal ions behave similarly in inducing IgG chemical and/or physical instability has not be explored.

Besides physical and chemical instability of IgG induced by redox active metal ions, photo-instability of IgG was also studied since photo stability testing is an integral part of the overall stability testing program required by regulatory agencies. The H/D exchange study in this work identified the formation of carbon-centered radical in IgGs due to photo-irradiation, and opens a door to better understand photo-degradation mechanism. With the aid of the developed RPLC-MS method with a non-porous column, we are currently investigating the origin of photolytic fragmentation of IgG.